

rim  
wartz  
rglitt  
TORS

AD-A269 748



Journal of  
Research  
National Bureau of Standards  
Physical and Chemical Division

VOLUME 314

RS

ME 314

# Joining and Adhesion of Advanced Inorganic Materials

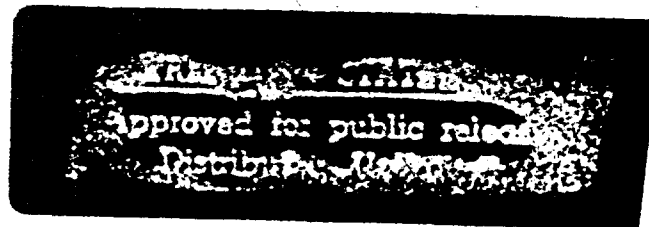
Joining and Adhesion of

EDITORS

A.H. Carim

D.S. Schwartz

R.S. Silberglitt



MRIS

POSTUM  
EDITIONS

①

# Joining and Adhesion of Advanced Inorganic Materials

DTIC QUALITY INSPECTED 1

Accession For	
NTIS CRA&I	<input checked="" type="checkbox"/>
DTIC TAB	<input checked="" type="checkbox"/>
Unannounced	<input type="checkbox"/>
Justification	
By	
Distribution /	
Availability Codes	
Dist	Avail and/or Special
A-1	

Materials Research Society  
9800 McKnight Road  
Pittsburgh, PA 15237  
NWW 9/23/93 \$66.00

DTIC  
ELECTE  
SEP 24 1993  
S E

Approved for public release  
Distribution Unlimited

MATERIALS RESEARCH SOCIETY SYMPOSIUM PROCEEDINGS VOLUME 314

## Joining and Adhesion of Advanced Inorganic Materials

Symposium held April 12-14, 1993, San Francisco, California, U.S.A.

EDITORS:

**A.H. Carim**

The Pennsylvania State University  
University Park, Pennsylvania, U.S.A.

**D.S. Schwartz**

McDonnell Douglas Corporation  
St. Louis, Missouri, U.S.A.

**R.S. Silbergliitt**

FM Technologies, Inc.  
Fairfax, Virginia, U.S.A.

93-21006  
21006

**MRS**

MATERIALS RESEARCH SOCIETY  
Pittsburgh, Pennsylvania

93 9 09 022

This work relates to Department of Navy Grant N00014-93-1-0299 issued by the Office of Naval Research. The United States Government has a royalty-free license throughout the world in all copyrightable material contained herein.

Single article reprints from this publication are available through  
University Microfilms Inc., 300 North Zeeb Road, Ann Arbor, Michigan 48106

CODEN: MRSPDH

Copyright 1993 by Materials Research Society.  
All rights reserved.

This book has been registered with Copyright Clearance Center, Inc. For further information, please contact the Copyright Clearance Center, Salem, Massachusetts.

Published by:

Materials Research Society  
9800 McKnight Road  
Pittsburgh, Pennsylvania 15237  
Telephone (412) 367-3003  
Fax (412) 367-4373

Library of Congress Cataloging in Publication Data

Joining and Adhesion of Advanced Materials Symposium (1st : 1993 : San Francisco, California).

Joining and adhesion of advanced inorganic materials / editors: A.H. Carim, D.S. Schwartz, R.S. Silbergliitt.

p. cm.—(Materials Research Society symposium proceedings ; v. 314).

First Joining and Adhesion of Advanced Inorganic Materials Symposium, held April 12-14, 1993, San Francisco, California, at the 1993 MRS Spring Meeting.

Includes bibliographical references and index.

ISBN 1-55899-212-X.

1. Adhesive joints—Congresses. 2. Sealing (Technology)—Congresses.  
3. Joints (Engineering)—Congresses. 4. Metals—Congresses. 5. Composite materials—Congresses. 6. Ceramic materials—Congresses. I. Carim, A.H.  
II. Schwartz, D.S. III. Silbergliitt, R.S. IV. Materials Research Society Meeting (1993 : San Francisco, Calif.) V. Title VI. Series: Materials Research Society symposium proceedings ; v. 314.

TA492.A3J65 1993  
660'.293—dc20

93-26196  
CIP

Manufactured in the United States of America



## Contents

PREFACE	ix
ACKNOWLEDGMENTS	xi
MATERIALS RESEARCH SOCIETY SYMPOSIUM PROCEEDINGS	xii
<b>PART I: FUNDAMENTALS AND OVERVIEWS OF ADHESION AND BONDING</b>	
*FIRST PRINCIPLES STUDY OF INTERFACIAL ADHESION: THE Mo/MoSi <sub>2</sub> INTERFACE WITH AND WITHOUT IMPURITIES T. Hong, J.R. Smith, and D.J. Srolovitz	3
*MECHANISMS OF WETTING IN REACTIVE METAL/OXIDE SYSTEMS N. Eustathopoulos and B. Drevet	15
*BONDING, STRUCTURE AND PROPERTIES OF METAL/CERAMIC INTERFACES James M. Howe	27
*DIFFUSION BONDING OF ADVANCED AEROSPACE METALLICS David V. Dunford and Andrew Wisbey	39
*RELIABILITY FACTORS IN CERAMIC/METAL JOINING Katsuaki Suganuma	51
INTERFACE SCIENCE OF CONTROLLED METAL/METAL AND METAL/ CERAMIC INTERFACES PREPARED USING ULTRAHIGH VACUUM DIFFUSION BONDING Wayne E. King, G.H. Campbell, A.W. Coombs, G.W. Johnson, B.E. Kelly, T.C. Reitz, S.L. Stoner, W.L. Wien, and D.M. Wilson	61
<b>PART II: INTERFACIAL THERMODYNAMICS, MICROSTRUCTURE, AND MECHANICAL PROPERTIES</b>	
TOWARDS AN UNDERSTANDING OF THE REACTION SEQUENCES IN BRAZED JOINTS: INVESTIGATION OF THE Ti-Cu-O TERNARY AT 945°C G.P. Kelkar, A.H. Carim, and K.E. Spear	71
INTERFACIAL REACTIONS BETWEEN TITANIUM AND BORATE GLASS R.K. Brow, S.K. Saha, and J.I. Goldstein	77
MICROSTRUCTURAL INVESTIGATION OF $\kappa$ -MODIFICATION LAYERS IN CVD $\alpha$ -Al <sub>2</sub> O <sub>3</sub> / $\kappa$ -Al <sub>2</sub> O <sub>3</sub> MULTILAYER COATINGS Mats Halvarsson, Sakari Vuorinen, and Hans Nordén	83
LOCAL MECHANICAL STABILITY OF THE ALUMINUM/CARBON (AMORPHOUS) AND ALUMINUM/SiO <sub>2</sub> (AMORPHOUS) INTERFACE AT EXTRINSIC DISLOCATIONS E.D. McCarty and S.A. Hackney	89
MICROANALYSIS OF A COPPER-TO-GRAPHITE SOLDER BOND James B. Intrater	95

\*Invited Paper

EVALUATION OF ADHESION STRENGTH IN A Ti/Al <sub>2</sub> O <sub>3</sub> COMPOSITE Hsin-Fu Wang, John C. Nelson, Chien-Li Lin, William W. Gerberich, Charles J. Skowronek, and Herve E. Deve	103
--	-----

STRESS-CORROSION CRACKING AT CERAMIC-METAL INTERFACES J.C. Card, R.M. Cannon, R.H. Dauskardt, and R.O. Ritchie	109
---	-----

### PART III: MICROWAVE, LASER, AND INFRARED JOINING

*JOINING CERAMICS USING MICROWAVE ENERGY Iftikhar Ahmad and Richard Silbergliitt	119
---	-----

TEM INVESTIGATION OF MICROWAVE JOINED Si-SiC/Al/Si-SiC AND $\alpha$ -SiC/Al/ $\alpha$ -SiC S. Arunajatesan, A.H. Carim, T.Y. Ylin, and V.K. Varadan	131
---	-----

HIGH SPEED JOINING OF ALUMINUM METAL MATRIX COMPOSITES USING CONTINUOUS WAVE AND PULSED LASERS Parwaz A.A. Khan and Anand J. Paul	137
---	-----

RAPID INFRARED JOINING OF TITANIUM ALLOYS AND TITANIUM MATRIX COMPOSITES Craig A. Blue and Ray Y. Lin	143
---	-----

### PART IV: ADVANCED AND NOVEL JOINING TECHNIQUES I: CAPACITOR DISCHARGE WELDING AND SHS

*CAPACITOR DISCHARGE WELD MODELLING USING ULTRA HIGH SPEED PHOTOGRAPHY R.D. Wilson, J.A. Hawk, and J.H. Devletian	151
---	-----

CAPACITOR DISCHARGE AND FLASH WELDING OF SiC-REINFORCED HIGH TEMPERATURE Al ALLOYS D.S. Schwartz, J.H. Devletian, S.J. Chen, and J. Gould	163
---	-----

CD WELD INTERFACIAL STRUCTURE FOR Al-Fe BASED COUPLES C.P. Dogan, R.D. Wilson, and J.A. Hawk	169
---	-----

FUNDAMENTALS OF THE SHS JOINING PROCESS Robert W. Messler, Jr. and Timothy T. Orling	177
---	-----

*SELF-PROPAGATING, HIGH TEMPERATURE SYNTHESIS AS A TECHNIQUE TO JOIN METALS J.A. Hawk, A.V. Petty, C.P. Dogan, and J.C. Rawers	183
--	-----

### PART V: ADVANCED AND NOVEL JOINING TECHNIQUES II: OTHER APPROACHES

*REACTION PROCESSING AND PROPERTIES OF SiC-TO-SiC JOINTS B.H. Rabin and G.A. Moore	197
---	-----

JOINING OF METAL FILMS TO CARBON-CARBON COMPOSITE MATERIAL BY METAL PLASMA IMMERSION ION IMPLANTATION André Anders, Simone Anders, Ian G. Brown, and Peter Chow	205
---	-----

DIRECT BONDING METHOD OF ALUMINUM TO STAINLESS STEEL BY PRESSURE CASTING OF ALUMINUM Katsuaki Suganuma	209
--	-----

\*Invited Paper

<b>A NOVEL BRAZING TECHNIQUE FOR ALUMINUM AND OTHER METALS</b>	<b>215</b>
Roland S. Timsit and B.J. Janeway	
 <b>PART VI: JOINING AND ADHESION IN ELECTRONIC MATERIALS</b>	
<b>*INDIRECT-BONDED METALLIZATION OF ALUMINUM NITRIDE</b>	<b>223</b>
M. Grant Norton	
<b>A JOINING TECHNIQUE USING MULTILAYER LEAD-INDIUM-GOLD COMPOSITE DEPOSITED IN HIGH VACUUM</b>	<b>235</b>
Chin C. Lee, Chen-Yu Wang, Yi-Chia Chen, and Goran Matijasevic	
<b>WAFER BONDING FOR HYBRID CIRCUIT TECHNOLOGY USING SOLID- STATE REACTIONS</b>	<b>241</b>
Z. Ma, G.L. Zhou, T.C. Shen, M.E. Lin, K.C. Hsieh, L.H. Allen, and H. Morkoç	
<b>AUTHOR INDEX</b>	<b>247</b>
<b>SUBJECT INDEX</b>	<b>249</b>

\*Invited Paper

## Preface

This volume is a record of the first Joining and Adhesion of Advanced Inorganic Materials Symposium, held on April 12-14 at the 1993 MRS Spring Meeting in San Francisco, California. We brought together for this symposium an international group of researchers working in every aspect of materials joining and adhesion, from fundamental theoretical aspects of adhesion to joining techniques being applied in the commercial world. Adhesion of thin films and coatings was discussed at the atomic/electronic level, as well as on the practical level of coatings for wear resistance. Joining of a broad range of materials was discussed, including ceramics and ceramic matrix composites, metals and metal matrix composites, and semiconductors. A variety of novel joining techniques were described, many of which are destined to become commercially important technologies in the near future.

Funding for this symposium was provided by the U.S. Office of Naval Research and the U.S. Department of Energy, Assistant Secretary for Energy Efficiency and Renewable Energy, Advanced Industrial Materials Program. The encouragement and support of these institutions is gratefully acknowledged. The organizers would like to thank Dr. R. Lochman at Sandia National Laboratories for help with promoting the symposium, and Mr. S. Johnson at Penn State University for help with preparation of the proceedings.

Altat Carim  
Dan Schwartz  
Richard Silbergliit

June 1993

## Acknowledgments

No MRS symposium would flow smoothly, nor could the proceedings be published in a timely fashion, without the combined efforts of a large number of people. The symposium organizers would like to thank the following people for graciously contributing their time and expertise to the manuscript peer review process and/or helping with the symposium by serving as Session Chairs.

I. Ahmad  
W. Baeslack  
R. Brow  
D. Dunford  
N. Eustathopoulos  
M. Halvarsson  
J. Hawk  
A. Houssais  
J. Howe  
C. Lee  
R. Lin  
Z. Ma  
M.G. Norton  
T. Orling  
G. Pinneo  
B. Rabin  
J. Smith  
K. Suganuma  
R. Timsit  
R. Wilson

---

MATERIALS RESEARCH SOCIETY SYMPOSIUM PROCEEDINGS

---

- Volume 279—Beam-Solid Interactions—Fundamentals and Applications, M.A. Nastasi, N. Herbots, L.R. Harriott, R.S. Averback, 1993, ISBN: 1-55899-174-3
- Volume 280—Evolution of Surface and Thin Film Microstructure, H.A. Atwater, E. Chason, M. Grabow, M. Lagally, 1993, ISBN: 1-55899-175-1
- Volume 281—Semiconductor Heterostructures for Photonic and Electronic Applications, D.C. Houghton, C.W. Tu, R.T. Tung, 1993, ISBN: 1-55899-176-X
- Volume 282—Chemical Perspectives of Microelectronic Materials III, C.R. Abernathy, C.W. Bates, D.A. Bohling, W.S. Hobson, 1993, ISBN: 1-55899-177-8
- Volume 283—Microcrystalline Semiconductors—Materials Science & Devices, Y. Aoyagi, L.T. Canham, P.M. Fauchet, I. Shimizu, C.C. Tsai, 1993, ISBN: 1-55899-178-6
- Volume 284—Amorphous Insulating Thin Films, J. Kanicki, R.A.B. Devine, W.L. Warren, M. Matsumura, 1993, ISBN: 1-55899-179-4
- Volume 285—Laser Ablation in Materials Processing—Fundamentals and Applications, B. Braren, J. Dubowski, D. Norton, 1993, ISBN: 1-55899-180-8
- Volume 286—Nanophase and Nanocomposite Materials, S. Komarneni, J.C. Parker, G.J. Thomas, 1993, ISBN: 1-55899-181-6
- Volume 287—Silicon Nitride Ceramics—Scientific and Technological Advances, I-W. Chen, P.F. Becher, M. Mitomo, G. Petzow, T-S. Yen, 1993, ISBN: 1-55899-182-4
- Volume 288—High-Temperature Ordered Intermetallic Alloys V, I. Baker, J.D. Whittenberger, R. Darolia, M.H. Yoo, 1993, ISBN: 1-55899-183-2
- Volume 289—Flow and Microstructure of Dense Suspensions, L.J. Struble, C.F. Zukoski, G. Maitland, 1993, ISBN: 1-55899-184-0
- Volume 290—Dynamics in Small Confining Systems, J.M. Drake, D.D. Awschalom, J. Klafter, R. Kopelman, 1993, ISBN: 1-55899-185-9
- Volume 291—Materials Theory and Modelling, P.D. Bristowe, J. Broughton, J.M. Newsam, 1993, ISBN: 1-55899-186-7
- Volume 292—Biomolecular Materials, S.T. Case, J.H. Waite, C. Viney, 1993, ISBN: 1-55899-187-5
- Volume 293—Solid State Ionics III, G-A. Nazri, J-M. Tarascon, M. Armand, 1993, ISBN: 1-55899-188-3
- Volume 294—Scientific Basis for Nuclear Waste Management XVI, C.G. Interrante, R.T. Pabalan, 1993, ISBN: 1-55899-189-1
- Volume 295—Atomic-Scale Imaging of Surfaces and Interfaces, D.K. Biegelson, D.S.Y. Tong, D.J. Smith, 1993, ISBN: 1-55899-190-5
- Volume 296—Structure and Properties of Energetic Materials, R.W. Armstrong, J.J. Gilman, 1993, ISBN: 1-55899-191-3

---

MATERIALS RESEARCH SOCIETY SYMPOSIUM PROCEEDINGS

---

- Volume 297—Amorphous Silicon Technology—1993, E.A. Schiff, M.J. Thompson, P.G. LeComber, A. Madan, K. Tanaka, 1993, ISBN: 1-55899-193-X
- Volume 298—Silicon-Based Optoelectronic Materials, R.T. Collins, M.A. Tischler, G. Abstreiter, M.L. Thewalt, 1993, ISBN: 1-55899-194-8
- Volume 299—Infrared Detectors—Materials, Processing, and Devices, A. Appelbaum, L.R. Dawson, 1993, ISBN: 1-55899-195-6
- Volume 300—III-V Electronic and Photonic Device Fabrication and Performance, K.S. Jones, S.J. Pearton, H. Kanber, 1993, ISBN: 1-55899-196-4
- Volume 301—Rare-Earth Doped Semiconductors, G.S. Pomrenke, P.B. Klein, D.W. Langer, 1993, ISBN: 1-55899-197-2
- Volume 302—Semiconductors for Room-Temperature Radiation Detector Applications, R.B. James, P. Siffert, T.E. Schlesinger, L. Franks, 1993, ISBN: 1-55899-198-0
- Volume 303—Rapid Thermal and Integrated Processing II, J.C. Gelpey, J.K. Elliott, J.J. Wortman, A. Ajmera, 1993, ISBN: 1-55899-199-9
- Volume 304—Polymer/Inorganic Interfaces, R.L. Opila, A.W. Czanderna, F.J. Boerio, 1993, ISBN: 1-55899-200-6
- Volume 305—High-Performance Polymers and Polymer Matrix Composites, R.K. Eby, R.C. Evers, D. Wilson, M.A. Meador, 1993, ISBN: 1-55899-201-4
- Volume 306—Materials Aspects of X-Ray Lithography, G.K. Celler, J.R. Maldonado, 1993, ISBN: 1-55899-202-2
- Volume 307—Applications of Synchrotron Radiation Techniques to Materials Science, D.L. Perry, R. Stockbauer, N. Shinn, K. D'Amico, L. Terminello, 1993, ISBN: 1-55899-203-0
- Volume 308—Thin Films—Stresses and Mechanical Properties IV, P.H. Townsend, J. Sanchez, C.-Y. Li, T.P. Weihs, 1993, ISBN: 1-55899-204-9
- Volume 309—Materials Reliability in Microelectronics III, K. Rodbell, B. Filter, P. Ho, H. Frost, 1993, ISBN: 1-55899-205-7
- Volume 310—Ferroelectric Thin Films III, E.R. Myers, B.A. Tuttle, S.B. Desu, P.K. Larsen, 1993, ISBN: 1-55899-206-5
- Volume 311—Phase Transformations in Thin Films—Thermodynamics and Kinetics, M. Atzmon, J.M.E. Harper, A.L. Greer, M.R. Libera, 1993, ISBN: 1-55899-207-3
- Volume 312—Common Themes and Mechanisms of Epitaxial Growth, P. Fuoss, J. Tsao, D.W. Kisker, A. Zangwill, T.F. Kuech, 1993, ISBN: 1-55899-208-1
- Volume 313—Magnetic Ultrathin Films, Multilayers and Surfaces/Magnetic Interfaces—Physics and Characterization (2 Volume Set), C. Chappert, R.F.C. Farrow, B.T. Jonker, R. Clarke, P. Grünberg, K.M. Krishnan, S. Tsunashima/E.E. Marinero, T. Egami, C. Rau, S.A. Chambers, 1993, ISBN: 1-55899-211-1
- Volume 314—Joining and Adhesion of Advanced Inorganic Materials, A.H. Carim, D.S. Schwartz, R.S. Silbergliitt, R.E. Loehman, 1993, ISBN: 1-55899-212-X
- Volume 315—Surface Chemical Cleaning and Passivation for Semiconductor Processing, G.S. Higashi, E.A. Irene, T. Ohmi, 1993, ISBN: 1-55899-213-8

---

## PART I

---

### **Fundamentals and Overviews of Adhesion and Bonding**



## FIRST PRINCIPLES STUDY OF INTERFACIAL ADHESION: THE Mo/MoSi<sub>2</sub> INTERFACE WITH AND WITHOUT IMPURITIES

T. Hong\*, J. R. Smith\*\* and D. J. Srolovitz\*

\*Department of Materials Science and Eng., University of Michigan, Ann Arbor, MI 48109

\*\*Physics Departments, General Motors Research and Development Center, Warren, MI 48090

### ABSTRACT

Adhesive properties of the Mo(001)/MoSi<sub>2</sub>(001) heterophase interface with and without C, O, B, S, and Nb impurities are calculated using a first principles local density functional approach. The adhesive energy and interfacial strength of the impurity-free interface are 10% to 15% smaller than the respective values for cleavage along the (001) planes of Mo and MoSi<sub>2</sub>. All of the impurities were found to decrease the Mo/MoSi<sub>2</sub> adhesive energy. The substitutional impurities S and Nb decrease the interfacial strength, while the interstitial impurities C, O, and B increase it. All of the impurities increase the interfacial spacing in proportion to their covalent radii. The impurity effects on adhesion may be described in terms of competing bonding and strain effects.

### INTRODUCTION

The adhesive energy or work of adhesion of an interface is the energy required to separate the two materials that meet at the interface, in the absence of any dissipative processes (such as dislocation motion). In this sense, the adhesive energy is the fundamental quantity which describes the strength of the bond between two materials. It is this adhesive energy that determines the fracture properties of materials within the simple thermodynamic model of brittle fracture due to Griffith.<sup>1</sup> While more modern theories of interfacial fracture are capable of including a range of other physical phenomena (e.g. plasticity, segregation, etc.), they all require, at their most fundamental level, a description of the energy or force required to separate the material at the interface - i.e., the adhesive energy. As a result of the centrality of the adhesive properties in fracture, the adhesive energy becomes a focal point of an increasing number of studies involving physicists, chemists, and materials scientists. As the search for high performance materials continues, it is common to combine two or more materials with complementary properties in order to optimize properties. This has led to considerable interest in the fracture behavior of composites and the interfaces between the dissimilar materials within them. The present study focuses on the adhesive energetics of heterophase interfaces in a metal/intermetallic composite. This work is part of an ongoing effort to obtain a microscopic understanding of the mechanisms that control adhesion in order to provide a rational basis for the design of increasingly complex materials.

In this paper, we report the results of a fully three dimensional, first-principles study of adhesion at a heterophase interface. The electronic structure and total energy of the Mo(001)//MoSi<sub>2</sub>(001) interface is calculated as a function of interfacial spacing by using the first principles, self-consistent local orbital (SCLO) method.<sup>2</sup> To determine the adhesive energetics, the recently proposed four-point method<sup>3</sup> is then employed to fit the calculated energy values at different interfacial separations to a universal-binding-energy relation (UBER).<sup>4</sup> The ideal work of adhesion (or adhesive energy), the peak interfacial strength (the peak derivative of the energy with respect to the separation of the solids at the interface), and the full adhesion curve are all obtained by performing calculations at as few as four interfacial separations. The adhesive energy and the pertinent surface energies are combined to analyze the relative configurational stability of different possible interfacial geometries.

MoSi<sub>2</sub> is of particular interest for high-temperature structural applications.<sup>5</sup> The inherently low ductility of pure MoSi<sub>2</sub> has led several groups<sup>6</sup> to create a composite of MoSi<sub>2</sub> and other tougher metals (such as Mo and Nb) in order to achieve higher ductility through ductile phase toughening. MoSi<sub>2</sub> crystallizes in the body-centered tetragonal structure with experimental lattice constants<sup>6</sup>  $a=3.202\text{\AA}$ ,  $c=7.851\text{\AA}$ . The experimental lattice constant of bcc

Mo is  $a=3.14\text{\AA}$  and, hence, the lattice mismatch for the  $[100]//[100]$  (001) planes of the two materials is then less than 2%. In this configuration, little atomic relaxation is expected (other than the formation of a grid of dislocations spaced approximately  $160\text{\AA}$  apart) and hence this is an ideal candidate metal/intermetallic system for studying heterophase interfaces using first principles methods.

In addition to examining a clean heterophase interface, the aim of the present work is also to determine how impurities affect interfacial bonding and adhesion between two different solids. The SCLO method<sup>2</sup> is again employed to compute the total energies, the electronic structure, and the electron density distribution of the  $\text{Mo}(001) // \text{MoSi}_2(001)$  heterophase interface with representative impurities, namely, interstitial C, O, and B, and substitutional S and Nb. The impurity atoms C, O, B, and S were chosen because they represent some of the more common interfacial impurities in metallic alloys. Nb is of interest also because it has been found<sup>8</sup> to facilitate bonding between  $\text{MoSi}_2$  and another metal, Cu. Because of its relatively large size, Nb was taken to be a substitutional impurity. Various studies have shown that C and B occupy the octahedral sites in bcc Fe.<sup>9-10</sup> As the local environment at the Mo/MoSi<sub>2</sub> interface resembles that in a bcc solid (in the absence of experimental data), it is reasonable to assume that these same sites would be occupied at the Mo/MoSi<sub>2</sub> interface by these non-metal impurities. These are the 4-fold symmetric surface sites on the Mo(001) surface. The impurities were introduced above these sites at a monolayer coverage and at a height that was determined by minimizing the energy with respect to the separation between the clean Mo surface and the impurity monolayer. To determine the relative stability of the substitutional and the interstitial configurations for non-metal impurities, total energies were computed for both configurations for B and S, which are the larger non-metal impurities.<sup>11</sup> We found that the lower energy configuration for S is substitutional, whereas B strongly favors the interstitial configuration. This suggests that the smaller C and O impurities are also interstitial. Detailed results will be discussed later in this paper. To simplify discussions, results from only the lower energy configuration (i.e., substitutional for Nb and S and interstitial for C, O, B) are included in the results presented below, except as otherwise noted.

## METHOD

As mentioned earlier, we employ the first principles SCLO method<sup>2</sup>, based on the local-density approximation<sup>12</sup>, in the present study. This method has been successfully applied to explain and, in some cases, to predict surface phenomena involving transition metals. The localized basis set includes all core orbitals, and for the valence orbitals a minimum basis set is augmented by more diffuse orbitals - containing much of the flexibility of the quantum chemist's double-zeta-plus-polarization basis sets. The Ceperley-Alder<sup>13</sup> form of the exchange-correlation potential is used. Self-consistent iterations are continued until changes in the electron eigenvalues are less than 5 meV.

Details on the optimization of the outermost s, p, and d orbital parameters for Mo and Si are discussed in Ref. 14. Because of the similarity between Mo and Nb, the optimized orbital parameters for Mo were also used for the Nb impurity atom. The procedure for optimizing orbital parameters of non-metal impurities is somewhat more complicated, however. It was presumed important to optimize the impurities in a solid-state environment. Thus slabs consisting of three layers of Mo with a monolayer of impurity atoms chemisorbed on each surface (maintaining inversion symmetry) were chosen for the optimization procedure. The distance between the impurity monolayer and the Mo layers is initially chosen to make the nearest impurity-Mo distance equal to the sum of the covalent radius<sup>11</sup> of the impurity and the metallic radius of Mo. The total energy of slabs containing each impurity atom is then minimized with respect to the parameters determining the outermost impurity s and p orbitals. These are the 3s and 3p orbitals for C, O, and B and the 4s and 4p orbitals for S. This is referred to as step 1.

While keeping the orbital parameters of impurity atoms fixed at these optimized values, the total energy of each system is then minimized with respect to the distance between the impurity and the Mo layers (referred to as step 2). Using these optimized distances, step 1 is repeated for all impurities. Fortunately, the new optimized orbital parameters are either the same as or very close to those from step 1 for all of the impurities. This saves us from further iterations of step 1 and step 2. The key to avoiding numerous iterations of step 1 and step 2 is apparently a good initial value of interfacial separation between the impurity layer and the Mo layers. It appears that the sum of the respective radii is a good approximation. The 3d orbital

of S is constructed following the same prescription as that for the 3d orbital of Si.<sup>14</sup> These optimized orbital parameters are then used in the calculations of the impurity-doped Mo/MoSi<sub>2</sub> heterophase interface. Although the optimization of the separation between the impurity layer and Mo layers is conducted without the presence of the MoSi<sub>2</sub>, test calculations were also performed for cases where MoSi<sub>2</sub> was present. We found that the equilibrium impurity-Mo distance in the absence of the silicide was within 0.1 Å of the value with the silicide. This is due to the steep repulsive potential for Mo-impurity distances less than the equilibrium separation and the fact that the Mo/MoSi<sub>2</sub> adhesion tends to force the impurity layer closer to the Mo film. For the undoped and each impurity-containing cases, total energies from different Mo-MoSi<sub>2</sub> interfacial separations are fitted to the universal binding energy relation, as discussed in Ref. 3. This leads to the following expression for the adhesive energy per unit surface area (E) as a function of interfacial separation

$$E = -E_0(1+u^*)e^{-u^*} \quad (1)$$

where

$$u^* = (d - d_0) / l \quad (2)$$

The equilibrium interfacial separation is denoted by  $d_0$  and the corresponding adhesive energy is  $-E_0$  ( $E_0$  will be referred to as the ideal adhesive energy hereafter). The scaling length  $l$  is a fitting parameter which provides a measure of the elastic characteristics of the material. The stress  $\sigma$  is defined as the derivative of the energy  $E$  with respect to the interfacial separation  $d$ . The stress-separation relation is of the form

$$\sigma = \sigma_{\max} u^* e^{(1-u^*)} \quad (3)$$

where the ideal peak interfacial strength (per unit area of interface)  $\sigma_{\max}$  is related to the ideal adhesive energy  $E_0$  by

$$\sigma_{\max} = \frac{2E_0}{cl} \quad (4)$$

and where  $e$  is the base of the natural logarithm. As mentioned earlier, these parameters play a key role in determining interfacial adhesive properties.

## RESULTS

### Impurity Free Mo/MoSi<sub>2</sub> Interface

Depending upon the stacking sequence near the interface, three distinct interfacial arrangements are possible. These arrangements can be represented by MoMo//MoSiSi, MoMo//SiMoSi, and MoMo//SiSiMo, where the double slashes are used to denote the interface. While only those atomic layers closest to the interface that are needed to distinguish the interfacial arrangements are listed, one might also wonder how thick the films should be to adequately represent adhesion. Both Mo and MoSi<sub>2</sub> are metallic. Since short electronic screening lengths are characteristic of metallic systems, effectively limiting interfacial electronic effects to one or two layers of the interface, it is reasonable to model the interface by slabs containing a few atomic layers.

In order to examine the dependence of interfacial properties upon the thickness of the slabs and interfacial arrangement, four different Mo-MoSi<sub>2</sub> interfacial configurations are considered in this study. To simplify the calculation, reflection symmetry in the direction perpendicular to the interface is maintained in all configurations. The stacking sequences of the four configurations starting from the mirror plane are MoMo//SiMoSi, MoMo//SiMoSiSi, MoMoMo//SiMoSiSiSi, and MoMoMo//SiSiMoSi, respectively. The first three configurations all correspond to arrangement where the first MoSi<sub>2</sub> layer is Si and the second is Mo but with different Mo and MoSi<sub>2</sub> slab thicknesses. The last configuration corresponds to the

arrangement in which the first two MoSi<sub>2</sub> layers adjacent to the interface are Si. For purposes of comparison, results for ideal adhesion in pure MoSi<sub>2</sub>, cleaved along a (001) plane are also reported. The two possible MoSi<sub>2</sub> (001) cleavage planes are MoSi//SiMoSi and MoSiSi//MoSiSi. The MoMo//MoSiSi interfacial arrangement is not included in this study since this case will be nearly indistinguishable from that of cleavage in pure Mo.

The calculated values of the ideal adhesive energy ( $E_0$ ), the peak interfacial strength ( $\sigma_{\max}$ ), the equilibrium interfacial separation ( $d_0$ ), and the scaling length ( $l$ ) for all six interfacial geometries described above are reported in Table I. By comparing the adhesion results for the three geometries in which a single Si layer is at the interface, it is clear that the thickness of slabs does not substantially affect the ideal adhesive energy, the peak interfacial strength, or the equilibrium interfacial separation. The MoMo//SiMoSiSi and MoMoMo//SiMoSiSi  $E_0$ ,  $\sigma_{\max}$ , and  $d_0$  all agree to within 3%. This indicates that a three layer slab is adequate for modeling bulk Mo. This is a direct manifestation of the very short screening length in metals. The somewhat larger differences between the results with two different MoSi<sub>2</sub> slab thicknesses, on the other hand, are largely due to the smaller interplanar spacing in MoSi<sub>2</sub> than in Mo (approximately 15%) in the [001] direction. Based upon the above discussion, we assume that a slab of MoSi<sub>2</sub> of four layers is sufficient to represent the bulk MoSi<sub>2</sub>.

TABLE I. Calculated ideal adhesive energy ( $E_0$ ), peak interfacial strength ( $\sigma_{\max}$ ), equilibrium separation ( $d_0$ ), and the scaling length ( $l$ ) for four different Mo-MoSi<sub>2</sub> configurations and for perfect MoSi<sub>2</sub> crystals. Stacking configurations all start at the mirror plane, while actual slabs contain twice the number of layers shown.

	MoMo/ /SiMoSi	MoMo/ /SiMoSiSi	MoMoMo/ /SiMoSiSi	MoMo/ /SiSiMoSi	MoSi/ /SiMoSi	MoSiSi/ /MoSiSi
$E_0$ (mJ/m <sup>2</sup> )	4100	3590	3500	4610	3860	4600
$\sigma_{\max}$ (GPa)	51.6	40.8	39.6	53.0	43.8	49.4
$d_0$ (Å)	1.37	1.44	1.44	1.36	1.28	1.36
$l$ (Å)	0.59	0.65	0.65	0.64	0.65	0.68

It is not possible, based upon the data in Table I, to unequivocally establish which Mo(001)//MoSi<sub>2</sub>(001) interface (i.e. MoMo//SiMoSiSi or MoMo//SiSiMoSi) has the lowest energy and hence is thermodynamically stable. This is because the energies are sufficiently close that we would have to guarantee the same stoichiometry for all of the silicide segments considered. That would necessitate the treatment of thicker films, which is beyond our current computational capabilities. A comparison of results for the MoSi//SiMoSi and MoSiSi//MoSiSi interfaces shows that the MoSi//SiMoSi represents the lower energy configuration for the free MoSi<sub>2</sub>. If we were to bring this equilibrium MoSi<sub>2</sub> surface in contact with a Mo surface at sufficiently low temperatures, then we would expect the stacking to remain unchanged, i.e., MoMoMo//SiMoSiSi. If the energy difference between MoMoMo//SiMoSiSi and MoMoMo//SiSiMoSi were sufficiently small, then it would be likely that in any Mo(001)//MoSi<sub>2</sub>(001) composite both interfaces would be present. This assertion is based upon the non-equilibrium nature of composite processing and the manner in which interfaces migrate. Therefore, when the composite is subjected to an external stress which tends to pull the interface apart, it is the weaker interface which would dominate the adhesion properties of material. Examination of Table I demonstrates that the MoMoMo//SiMoSiSi interface is substantially weaker than the MoMoMo//SiSiMoSi interface, based on both the adhesive energy  $E_0$  and the peak interfacial strength  $\sigma_{\max}$ . For all of these reasons we will focus on the MoMoMo//SiMoSiSi interface for the remainder of the present study.

The ideal adhesive energy and peak interfacial strength for the MoMo//SiMoSiSi interface are between 10% and 15% smaller than those for crystalline Mo(001) and MoSi<sub>2</sub>(001). This suggests that the Mo/MoSi<sub>2</sub> interface will fail under stress before either the Mo or MoSi<sub>2</sub> crystals. However, since this comparison was made on the basis of ideal adhesion, it is only conclusive in the absence of plasticity.

In order to examine the validity of the universal binding energy relation (UBER) (Eq. 1) for adhesion between two dissimilar metallic materials, the UBER form is fitted to the calculated

energy values at different interfacial separations and plotted in Fig. 1 for the six interfaces analyzed in Table I. In all cases, the UBER provides an excellent fit to the data. The MoMo/SiMoSiSi and the MoMoMo/SiMoSiSi adhesion curves are very close over the entire range of the interfacial separation, reflecting the short-screening effect in Mo, as discussed earlier. Strikingly, the adhesion curves for the MoMo/SiSiMoSi and MoSiSi/MoSiSi interfaces are nearly the same over a wide range of the interfacial separation. This suggests that the /MoSiSi surface energy is similar to that of the pure Mo (001) regarding adhesion.

A detailed analysis of the bonding at the Mo/MoSi<sub>2</sub> interface has been presented in Ref. 14, where both electron density and interfacial density of states results may be found. The interfacial adhesive bonding is attributable to the combination of a nearly uniform band of charge accumulation at the interface and directional charge accumulation between atoms across the interface.

#### Mo/MoSi<sub>2</sub> Interface with Impurities: Adhesion

As discussed in the Introduction, we assume that the impurities are either fixed at a 4-fold symmetric, interstitial site or as a substitutional site (see Fig. 2). Our total energy calculations show that the largest (covalent radii) impurities, Nb and S are in substitutional sites, while the smaller C, O, and B impurities occupy interstitial sites. When the heterophase interface is formed (or cleaved), we explicitly assume that the impurity remains bound to the Mo crystal.

Calculated values of the ideal adhesive energy ( $E_0$ ), the peak interfacial strength ( $\sigma_{\max}$ ), and the equilibrium interfacial separation ( $d_0$ ) are listed in Table II for the undoped (MoMo/SiMoSiSi) and all of the impurity-doped cases. In all cases,  $d_0$  is the equilibrium distance between the plane through the nuclei of the surface transition-metal atomic layer and the plane through the nuclei of the surface Si layer. The transition-metal surface atomic layer is Mo except for the Nb substitutional case.

TABLE II. Calculated ideal adhesive energy ( $E_0$ ), peak interfacial strength ( $\sigma_{\max}$ ), equilibrium interfacial separation ( $d_0$ ), and scaling length ( $l$ ) for the undoped and all the impurity-doped cases. Also listed are the chemical energy ( $E_c$ ) and strain energy ( $E_s$ ), which are defined in the text.

	undoped	Nb	C	O	B	S
$E_0$ (mJ/m <sup>2</sup> )	3500	3230	3160	2860	2700	1770
$\sigma_{\max}$ (GPa)	39.6	33.2	39.0	50.2	40.8	20.6
$d_0$ (Å)	1.44	1.60	2.26	2.17	2.37	2.72
$l$ (Å)	0.65	0.72	0.39	0.42	0.49	0.63
$E_c$ (mJ/m <sup>2</sup> )	---	180	-920	-430	-660	-320
$E_s$ (mJ/m <sup>2</sup> )	---	90	1260	1070	1460	2050

It is evident from the data in Table II that all of the impurities reduce the adhesive energy and increase the equilibrium interfacial separation. The reduction of the ideal adhesive energy upon doping is a very strong effect. S doping reduces the ideal adhesive energy of the Mo/MoSi<sub>2</sub> interface by nearly a factor of two. Comparison of results for different dopants shows that, among the non-metal impurities, larger reductions in the ideal adhesive energy are caused by atoms of larger atomic size. The magnitude of the increase in the equilibrium spacing  $d_0$  or local strain is simply related to the covalent radius<sup>11</sup>, as may be seen in Fig. 3. Note that the value of  $d_0$  in Fig. 3 for the Nb-doped case is the value from Table II plus the Mo(2)-Nb interplanar spacing, where the labeling of the atomic planes is as per Fig. 2. This corresponds to the equilibrium interfacial separation between the Mo(2) atom and the Si(1) atom, i.e., the Nb-doped case is treated here on an equal footing with the cases involving non-metal impurities. The interfacial spacing is, to a good approximation, a linear function of the covalent radius of the atoms of the impurity layer. This suggests a rather simple picture of the effects of the non-metal impurities. That is, the impurities act as spacers at the interface, pushing the two surfaces apart. The bonds across the interface are presumably stretched and weakened as the

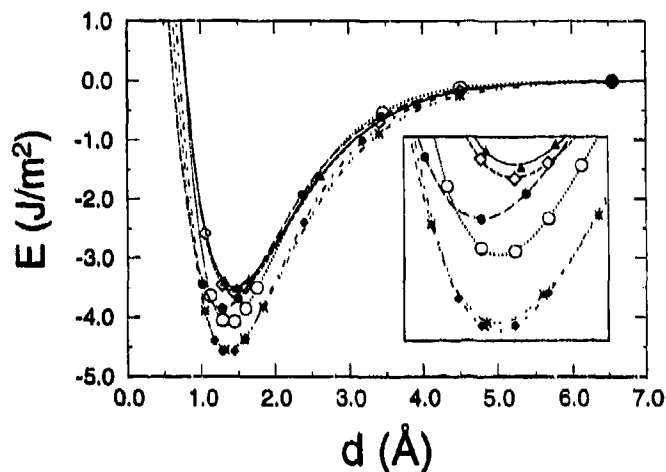
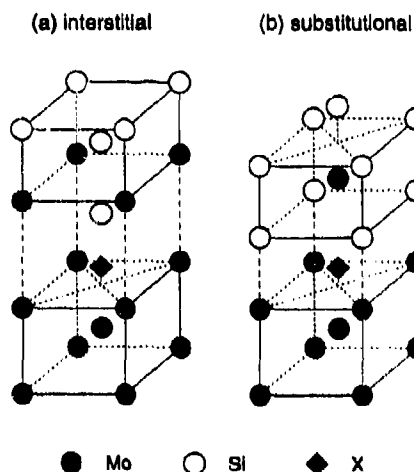


Figure 1. The calculated total energy  $E$  (per unit surface area) at different interfacial separations and the corresponding universal-binding-energy relation (UBER) versus interfacial separation  $d$  for all the cases. The inset shows the details in the vicinity of the minima. The  $\circ$ 's correspond to MoMo//SiMoSi,  $\diamond$ 's to MoMo//SiMoSiSi,  $\triangle$ 's to MoMoMo//SiMoSiSi,  $\blacklozenge$ 's to MoMo//SiSiMoSi,  $\bullet$ 's to MoSi//SiMoSi, and  $\times$ 's to MoSiSi//MoSiSi. Stacking configurations all start at the mirror plane. Actual slabs contain twice the number of layers listed.

Figure 2. The half unit cells employed to study systems containing (a) interstitial and (b) substitutional impurities. The interstitial impurity locations are denoted by the X. There is inversion symmetry about the center of the Mo(1) atomic layer. The layers are numbered by element and in order of their distance from the center (Mo(1)) layer. The undoped interface is equivalent to that shown in (a) but with the interstitial site unoccupied. The Nb-doped interface employs the same unit cell as for the undoped interface except that Nb is substituted for the Mo(3) atoms.



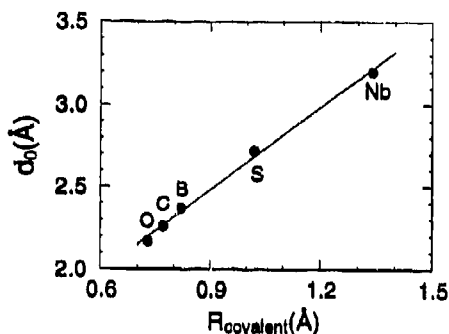


Figure 3. Interfacial separation  $d_0$  between the Mo and MoSi<sub>2</sub> crystals versus the covalent radii<sup>11</sup> of the impurities.

two crystals move apart. Consequently, the adhesive energy is reduced. This is consistent with the apparent weakening of the Mo-Mo bond (the electron charge accumulation between the Mo(3) and Mo(4) atoms when the interface is formed) across the interface in the impurity-doped cases compared with the undoped case, as discussed below. Since Nb is an element which is similar in nature to Mo, its effect on the adhesive bonding is somewhat different than that for the non-metal impurities. While Fig. 3 shows that Nb increases the Mo(2)-Si(1) spacing the most, the charge density plots (see below) show that a Nb-Mo(4) bond is established which is quite similar to the Mo(2)-Mo(4) bond for the undoped interface. This was the rationale for taking the equilibrium spacing in Table II to be the Nb-Si(1) spacing, putting the Nb-doped interface on the same footing as the undoped interface.

In Fig. 4, the calculated adhesive energy ( $E$ ) as a function of interfacial separation  $d$  is plotted for the undoped and doped interface cases. Since the increase in the equilibrium interfacial spacing can be thought of as a local strain, the  $E$  versus  $d$  curve may be used in dividing the dopant effects into strain energy and chemical energy terms. Since the presence of impurities increases the equilibrium Mo-MoSi<sub>2</sub> crystal spacings  $d_0$ , we define the strain energy ( $E_s$ , cf. Table II) as the energy difference between  $E(d_{0,\text{undoped}})$  and  $E(d_{0,\text{doped}})$ , where  $E(d)$  is the undoped Mo/MoSi<sub>2</sub> adhesion curve. In other words, we define the dopant contribution to the strain energy  $E_s$  as the change in energy of the undoped Mo/MoSi<sub>2</sub> system when the spacing between the Mo and MoSi<sub>2</sub> crystals is increased to the extent caused by the dopants,  $d_{0,\text{doped}}$  - the minimum of the impurity adhesion curves. The strain energy is found to be positive definite. One could define a chemical energy as the difference between two energies at the strained spacing, i.e., at the spacing corresponding to the minimum of the doped curve. We define the chemical energy as the difference in energy between the minimum of the impurity-doped curve and the Mo/MoSi<sub>2</sub> curve at the same spacing -  $d_{0,\text{doped}}$ . The sum of the strain and chemical energies is then the adhesive energy difference between the minima of the impurity-doped curve and the Mo/MoSi<sub>2</sub> curve. This is not a unique definition of the strain and chemical energies, but one which greatly simplifies our understanding of the adhesion energetics. Larger strain energies  $E_s$  correspond to smaller adhesive energies, while larger chemical energies  $E_c$  are correlated with larger adhesive energies, both as expected.

Examination of each impurity-doped case reveals the distinctive roles played by the different types of impurities. The Nb-Si(1) spacing ( $d_0$  in the Nb column of Table II) is somewhat larger than the Mo-Si(1) spacing in the undoped interface. This is consistent with the fact that the lattice constant of bcc Nb (3.29 Å) is larger than that of bcc Mo (3.14 Å). Both the strain energy and the chemical energy in the Nb-doped case are small, reflecting the similarity between Mo and Nb. The small positive chemical energy term indicates that Nb atoms form slightly weaker bonds with MoSi<sub>2</sub> atoms across the interface than do the Mo atoms. This is consistent with the surface energy of Nb(100) being smaller than the surface energy of Mo(100).<sup>3</sup>

For the non-metal impurities, some interesting trends can be deduced from Table I. The ordering of the strain energies  $E_s$  caused by the different impurities at the interface is  $O < C < B < S$ , whereas the ordering of the absolute value of the chemical energies  $E_c$  is  $S < O < B < C$ . These two energies along with the  $E_c + E_s$  are plotted in Fig. 5 as a function of the covalent radius of the non-metal impurities. It is perhaps not surprising to find that the strain energy is a

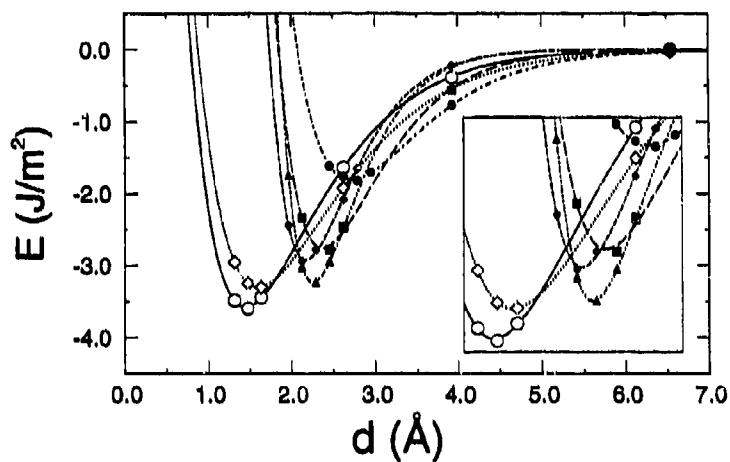


Figure 4. The calculated energy  $E$  (per unit surface area) of the doped and undoped interfaces versus interfacial separation  $d$ . The undoped interface is represented by the open circles, the Nb doped interface by open diamonds, the O doped interface by filled diamonds, the C doped interface by filled triangles, the B doped interface by filled squares and the S doped interface by filled circles.

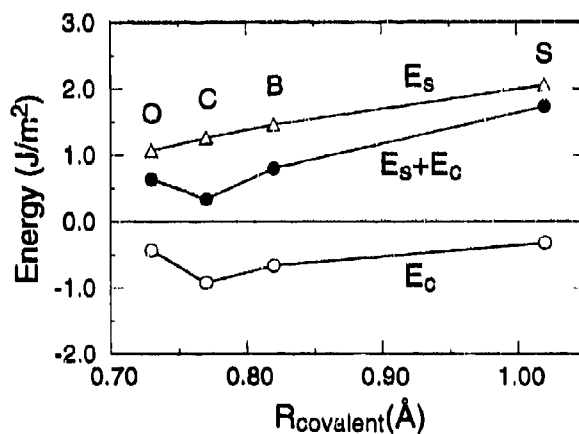


Figure 5. The strain energy (triangles), chemical energy (open circles), and sum of the two (solid circles) versus the covalent radii of the impurities.



monotonic function of the covalent radius, as the effects of impurity size are expected to be incorporated in the strain energy. However, the linear dependence of  $E_a$  on the covalent radius may be attributed to the nearly linear form of the undoped Mo/MoSi<sub>2</sub> adhesive energy versus separation  $d$  curve (Fig. 4) over the range of separations corresponding to the equilibrium separations of the impurity doped interfaces. The chemical energy is a more complicated function of the covalent radius. This is because the chemical interaction between atoms is not directly related to the atomic sizes, rather it is a function of chemical parameters such as electronegativity. As discussed above, the sum of the chemical and strain energies gives the net effect of an impurity on the adhesive energy  $E_0(\text{undoped}) - E_0(\text{doped})$ . It is clear from Fig. 5 that the effects of non-metal impurities can be best described as a strong strain effect modulated by a modest chemical interaction. This supports the concept proposed earlier that the non-metal impurities act as spacers of the Mo and MoSi<sub>2</sub> crystals.

It turns out that a complete picture of the impurity effects on adhesion is not that simple, however. This becomes evident after comparing the peak interfacial strength (cf.  $\sigma_{\text{max}}$  in Table II) for all of the interfacial impurities. Although all impurities reduce the ideal adhesive energy, B slightly increases the interfacial strength, and O and C significantly strengthen the interface. On the other hand, both substitutional Nb and S decrease the interfacial strength. In particular, S causes the largest reduction (by almost a factor of 2) in both the ideal adhesive energy and the peak interfacial strength. Recalling the dependence of the peak interfacial strength on the ideal adhesive energy  $E_0$  and the scaling length  $l$  (Eq. 4), it is not difficult to see that the increase of the peak interfacial strength in the C-, O-, and B-doped cases is primarily due to small scaling lengths in those cases, whereas the low peak interfacial strengths of the S-doped interfaces is attributable to the low  $E_0$  value. The reduced  $\sigma_{\text{max}}$  value associated with the Nb doped interface is attributable to both an increase in  $l$  and a decrease in  $E_0$ .

#### Mo/MoSi<sub>2</sub> Interface with Impurities: Charge Density

Impurities are expected to affect electron charge distributions. Nevertheless, it is still quite striking to the degree to which they bring about dramatic changes in the electron charge arrangement at the Mo and MoSi<sub>2</sub> interface. Since the focus of the present study is interfacial adhesion, we focus on the changes in the electron charge profiles when the Mo/MoSi<sub>2</sub> interface is formed by bringing the Mo and MoSi<sub>2</sub> crystals together from large separations (i.e.,  $d$  is changed from effectively  $d=\infty$  to  $d_0$ ). In Figs. 6(a-d) the electron charge density rearrangement due to the formation of the interface is plotted for the undoped Mo/MoSi<sub>2</sub> interface and that interface with Nb, C, and S respectively. The electron charge density plots for the O and B impurities are very similar to that of C and may be found in Ref. 15. These plots are generated by subtracting the electron charge density distributions at large interfacial separation from those at the equilibrium separation so they represent the net effects of charge rearrangement caused by the ideal adhesion. In all cases, electron charge rearrangement becomes quite small at distances larger than one or two atomic layers from the interface. This again demonstrates that the metallic screening length is quite small.

Comparison of the charge rearrangement for the undoped Mo/MoSi<sub>2</sub> interface plot (Fig. 6a) with that for the Nb-doped case (Fig. 6b) shows that the two cases bear a strong resemblance to each other. This reflects the similarity in physical properties between elemental Mo and Nb. In both cases, a substantial accumulation of electrons is found to spread over all parts of the interface between Mo (or Nb) and MoSi<sub>2</sub> atoms when the interface is formed. This is indicative of the adhesive nature of the interfacial bonding.<sup>16</sup> In addition to a uniform "band" of electron accumulation at the interface, there also exists contributions from strong directional electron accumulations localized along the lines connecting atoms across the interface in the direction normal to the interface (i.e., the  $z$ -direction) in both cases. This part of electron charge accumulation between atoms surrounding the interface is reminiscent of covalent bonding in diatomic molecules. The parallel between the diatomic molecular bond and the bimetallic interfacial bond has been pointed out earlier.<sup>4</sup> Note especially the relatively large accumulation of electrons between the surface atoms of the Mo crystal (Mo(3) or Nb, Fig. 2) and the second-layer Mo atoms (Mo(4)) in the MoSi<sub>2</sub> film.

In the non-metal impurity-doped interface cases, the band of interfacial electron charge accumulation at the interface is reduced, or even totally eliminated in some instances as compared with the undoped or Nb-doped interface cases. Additionally the strong accumulation between the Mo(3) and Mo(4) atoms is greatly reduced. This suggests that the adhesive bonding between the Mo and MoSi<sub>2</sub> crystals is significantly weakened due to the introduction

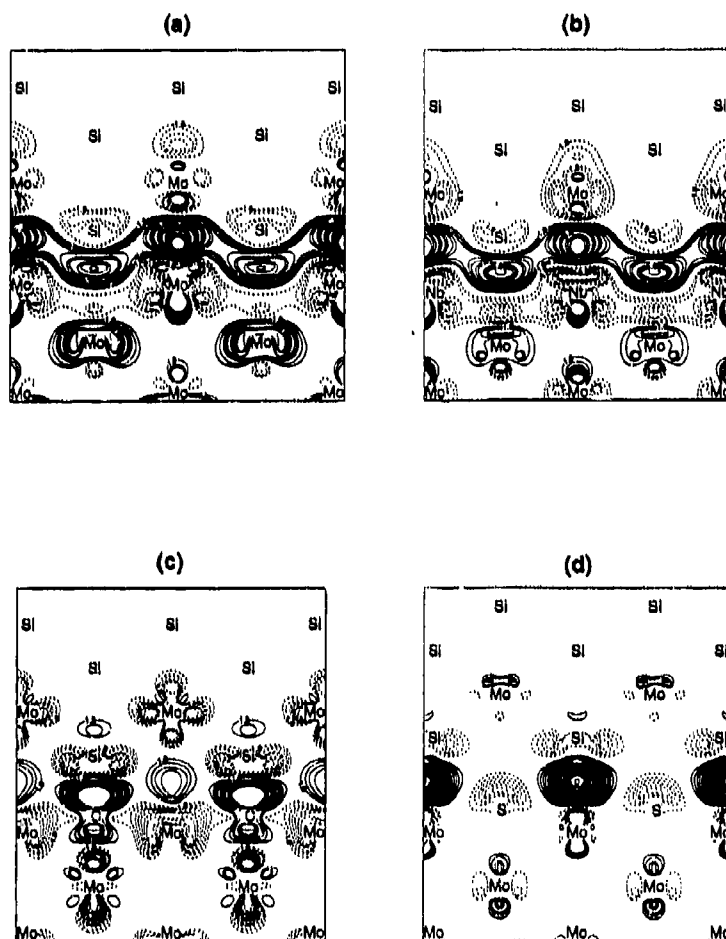


Figure 6. Charge density rearrangements due to adhesion between the (001) surfaces of Mo and  $\text{MoSi}_2$ : (a) the undoped case (denoted by  $\text{Mo}/\text{MoSi}_2$ ), (b) the Nb-doped case (denoted by  $\text{Mo}/\text{Nb}/\text{MoSi}_2$ ), (c)  $\text{Mo}/\text{C}/\text{MoSi}_2$ , (d)  $\text{Mo}/\text{S}/\text{MoSi}_2$ . These contours were determined by subtracting the charge densities of the system with the interface from those at effectively infinite separation. Positive contours (solid lines) denote electron accumulation due to ideal adhesion and negative contours (dashed lines) indicate electron depletion.

of the non-metal impurities. In the C, O, and B doped interface cases, there is a relatively large accumulation of electrons around the impurity atoms in the  $z$ -direction. This is due to the strong chemical bonds formed across the interface by the impurity atoms and to the reduced atomic bond lengths associated with the interstitial nature of the impurity atoms. Although the main features of adhesive bonding in systems doped by these three impurities are similar, there do exist some differences. For example, the Mo atoms one layer away from the interface in the Mo crystal (Mo(2)) in the C- and O-doped cases lose  $d$ -electrons with  $z^2-r^2$  symmetry, while gaining some with  $xz$  and  $yz$  symmetry. In the B-doped case, meanwhile, a gain of electrons with  $z^2-r^2$  and  $xy$  symmetry is evident at those sites. Because of the different local interfacial geometry in the substitutional S-doped case, examination of effects due to S suggests yet another picture. Both the uniform band of electron charge accumulation and the charge accumulation between Mo atoms are completely absent in the S-doped case. Instead, owing to the shorter distance between the Mo(3) and the Si(1) atoms (compared with the Mo(3)-interstitial impurity distance), the electron charge accumulation between these atoms is even enhanced relative to its counterpart in the undoped case. When the interface between the Mo and MoSi<sub>2</sub> crystals is formed, there is a net charge depletion surrounding the S sites. This is in contrast to the substantial charge accumulation at impurity sites in the C-, O-, and B-doped cases. The charge rearrangement around the Mo(2) and Mo(4) sites in the S-doped case appears weaker than the undoped and C-, O-, and B-doped cases. All these results suggest that there is a weaker interfacial adhesion in the S-doped case than in either the undoped or interstitial-doped interface cases.

## CONCLUSIONS

The likely equilibrium stacking of atomic planes at the Mo(001)/MoSi<sub>2</sub>(001) interface is MoMo/SiMoSiSi stacking. Both the ideal adhesive energy and peak interfacial strength for the MoMo/SiMoSiSi interface are between 10% and 15% smaller than those for crystalline Mo(001) and MoSi<sub>2</sub>(001). The equilibrium interlayer separation between Mo and MoSi<sub>2</sub> in the interfacial arrangement was found to be intermediate between those in crystalline Mo and MoSi<sub>2</sub>. The adhesive bonding at the stable interface was identified to be a combination of a uniform band of charge accumulation at the interface and directional charge accumulation between atoms across the interface.

Our first principles electronic structure calculations show that all of the impurities considered (Nb, C, O, B, and S) decreased the adhesive energy of the Mo/MoSi<sub>2</sub> heterophase interface. The Nb-doped case resembles the undoped case in many aspects and differences between the two cases are attributable to the differences between elemental Mo and Nb. The non-metallic impurities C, B, O, and S have a much stronger effect on adhesive energies. S was shown to have the largest effect, with a monolayer at the Mo/MoSi<sub>2</sub> interface decreasing the adhesive energy by approximately a factor of 2. It was found that the impurities increase the interfacial spacing in proportion to the impurity covalent radius. Electron-density-difference plots show that the adhesive bonding across the interface in the undoped case is weakened by all of the non-metal impurities. Impurity effects were analyzed in terms of the competition between strain and chemical energetics. A simple picture emerged in which the impurities lower the Mo/MoSi<sub>2</sub> adhesive energy by stretching and therefore weakening the bonds across the interface. No such simple picture was found to explain the effects of impurities on peak interfacial strengths. The interstitial impurities C, O, and B increased the interfacial strength, while the substitutional impurities Nb and S decreased it. We note that for those impurities which increase the peak interfacial strength (C, B, and O), the equilibrium interfacial separation falls near the point of peak interfacial strength of the corresponding undoped case.

## ACKNOWLEDGMENTS

T. H. and D. J. S. gratefully acknowledge the support of the Air Force Office of Scientific Research, Grant AFOSR-90-0112, under whose auspices this work was performed. The authors wish to thank the excellent support and service of the San Diego Supercomputer Center and the Wright-Patterson Air Force Base Supercomputer Center.

## REFERENCES

1. A.A. Griffith, Phil. Trans. R. Soc. A221, 163 (1920).

2. J. R. Smith, J. G. Gay, and F. J. Arlinghaus, *Phys. Rev. B* **21**, 2201 (1980).
3. T. Hong, J. R. Smith, D. J. Srolovitz, J. G. Gay, and R. Richter, *Phys. Rev. B* **45**, 8775 (1992).
4. A. Banerjee and J. R. Smith, *Phys. Rev. B* **37**, 6632 (1988); see also P. Vinet, J. H. Rose, J. Ferrante, and J. R. Smith, *J. Phys.: Condens. Matter* **1**, 1941 (1989).
5. *Intermetallic Matrix Composites II*, edited by D. Miracle, J. Graves, and D. Anton (Materials Research Society, Pittsburgh, 1992).
6. P. Villars and L. D. Calvert, *Pearson's Handbook of Crystallographic Data for Intermetallic Phases* (American Society for Metals, Metals Park, Ohio, 1985).
7. C. Kittel, *Introduction to Solid State Physics*, 6th ed. (Wiley, New York, 1986), p. 57.
8. A. K. Ghosh (private communication).
9. W. G. Hartwock and H. J. Grabke, *Acta Metallurgica* **29**, 1237 (1981). See also H. J. Grabke, *Steel Research* **57**, 180 (1986); *ibid.*, in *Chemistry and Physics of Fracture*, edited by R. M. Latanision and R. H. Jones, NATO ASI Series, Series F: Applied Sciences, No. 130 (Nijhoff, Boston, 1987), p.338.
10. M. Morinaga, N. Yukiawa, H. Adachi, and T. Mura, *J. Phys. F* **17**, 2147 (1987).
11. Covalent radii are taken to be the single-bond radii listed by Linus Pauling, *The Nature of the Chemical Bond* (Cornell University Press, Ithaca, 1960), pp. 225-8.
12. P. Hohenberg and W. Kohn, *Phys. Rev.* **136**, 864 (1964); W. Kohn and L. J. Sham, *Phys. Rev.* **140**, A1133 (1965).
13. S. H. Vosko, L. Wilk, M. Nusair, *Can. J. Phys.* **58**, 1700 (1980); D. M. Ceperley and D. J. Alder, *Phys. Rev. Lett.* **45**, 566 (1980).
14. T. Hong, J. R. Smith, D. J. Srolovitz (to be published).
15. T. Hong, J. R. Smith, D. J. Srolovitz, *Phys. Rev. B* **47**, 13615 (1993); *ibid.* *Phys. Rev. Lett.* **70**, 615 (1993).
16. R. P. Feynman, *Phys. Rev.* **56**, 340 (1939).

## MECHANISMS OF WETTING IN REACTIVE METAL/OXIDE SYSTEMS

N. EUSTATHOPOULOS, B. DREVET

LTPCM, URA 29, INPG, DU, ENSEEG, BP 75, 38402 Saint Martin d'Hères Cedex, France

### ABSTRACT

It is shown that for metal/oxide systems with weak or moderate reactivity, wetting depends mainly on parameters related with the detailed chemistry and structure of interfacial reaction products rather than on parameters related with the intensity of interfacial reactions. Consequently, wetting can be promoted by alloying a metal matrix M with a reactive solute B capable of modifying in a favourable sense the metal/oxide interface. This can be achieved via two mechanisms depending on the value of the Wagner's interaction parameter  $e_O^B$ . When  $e_O^B < 0$  (moderate interactions between solute B and dissolved oxygen), the solute B can modify the liquid-side of the interface by adsorption, an effect that can be strongly enhanced by oxygen coming from dissolution of the oxide substrate. When  $e_O^B \ll 0$  (strong O-B interactions in M), the solute B can lead to the formation, at the solid-side of the interface, of a new phase. When this new phase features metallic bonding wetting can be strongly improved.

### 1 INTRODUCTION

Wettability of solids by liquids is generally described by the angle  $\theta$  formed at the line of contact of three phases, solid (S), liquid (L) and vapour (V).  $\theta$  is related with the characteristic interfacial energies  $\sigma$  of the system by Young's equation :

$$\cos \theta = (\sigma_{SV} - \sigma_{SL}) / \sigma_{LV} \quad (1)$$

At high temperatures, the surface tension of the liquid  $\sigma_{LV}$  and the contact angle are usually measured by the sessile drop technique. From these quantities, the following two parameters, very important in joint processing and properties, can be evaluated : the work of immersion

$$W_i = \sigma_{SV} - \sigma_{SL} = \sigma_{LV} \cos \theta \quad (2)$$

a quantity which is needed for describing infiltration of capillaries by liquids, and the work of adhesion

$$W_a = \sigma_{SV} + \sigma_{LV} - \sigma_{SL} = \sigma_{LV} (1 + \cos \theta) \quad (3)$$

a parameter which quantifies the strength of the interfacial bond between the solid and the liquid.

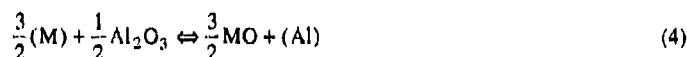
For pure non-reactive metal/ionocovalent oxide systems in reducing or neutral atmospheres, bonding is brought about by weak interactions, which have been attributed either to Van der Waals [1,2] or chemical interactions [3,4] localized at the interface. Non-wetting ( $\theta > 90^\circ$ ) is generally observed in this case and  $W_a$  represents only a few tens of percent of the work of cohesion of the metal equal to  $2\sigma_{LV}$  [1,5].

Both wetting and bonding can be affected by trace elements, especially oxygen even at partial pressure levels as low as  $10^{-5}$ - $10^{-10}$  Pa. It is now well established that when dissolved oxygen is present in a metal M, the contact angle decreases and the adhesion energy increases [1,6]. This is due to the fact that dissolved oxygen combines with metal atoms and forms OM clusters which acquire a partially ionic character as a result of charge transfer from the metal to oxygen. Such clusters can develop coulombic interactions with any ionocovalent ceramic and, as a consequence, they adsorb at the metal/oxide interface [1]. The resulting increase in adhesion energy is significant but rather limited (a few tens of percent).

The simplest way to enhance wettability in a non-reactive metal M/oxide system is via the composition of the metallic phase. Using a non-reactive alloying element B, it is possible to produce a significant decrease in  $\theta$  resulting from pure adsorption of B at the M/oxide interface [7]. The conditions to be satisfied by the metal B are a high work of adhesion, a low surface tension and weak B-M interactions in the alloy [7]. But even in the most favourable cases, the contact angles remain above  $60^\circ$ . In principle, lower contact angles, which are needed in some cases (e.g. in joining of ceramics by brazing alloys), can be expected using a reactive solute B. However, the central question is how to select B, no model of general acceptance being available relating wettability to reactivity. In the following section, experimental results of reactive wetting will be reviewed in order to identify the governing thermodynamic and physico-chemical parameters.

## 2 EXPERIMENTAL RESULTS ON PURE METAL/OXIDE SYSTEMS

In pure metal/oxide systems, the oxido-reduction reaction is generally used to discuss reactivity [1,8]. In order to simplify notations, we will now focus on the case of the reduction of alumina by a metal M with the formation of a MO oxide, according to a reaction of the type :



An approximate criterion for reactivity is the degree of progress of the interfacial reaction,  $\alpha_{eq}$ , which can be obtained by calculating the equilibrium concentration of Al in liquid M, coming from the dissolution of  $Al_2O_3$ .  $\alpha_{eq}$  is thus equal to the difference between final and initial (that is zero in our case) mole fraction of Al,  $X_{Al}$ . In the case  $X_{Al} \ll 1$ , the equilibrium  $X_{Al}$  for reaction (4) is written as follows [9] :

$$X_{Al} = \exp - \left( \frac{\Delta G_R^0 + \bar{\Delta}H_{Al(M)}}{RT} \right) = \exp - \left( \frac{\Delta G_R^*}{RT} \right) \quad (5)$$

where  $\bar{\Delta}H_{Al(M)}$  is the partial enthalpy of mixing of Al at infinite dilution in M and  $\Delta G_R^0$  the standard Gibbs free energy of reaction (4). Note that, at moderate or high values of the quantity  $\Delta G_R^* / RT$ , the real reactivity consists in a simple dissolution of the oxide substrate in the liquid metal and not in an oxido-reduction reaction. Thus, the term  $\Delta G_R^* / RT$  will not be used to quantify the real reactivity for a given system, but only to establish a rough scale of relative reactivity for different systems.

Experimental contact angles  $\theta$  taken from compilations [1,9,10,11] are represented in Figure 1 as a function of the parameter  $\Delta G_R^* / RT$  calculated for a number of pure metal/oxide couples (see [9] for more details). We observe that an increase of  $\Delta G_R^* / RT$  is

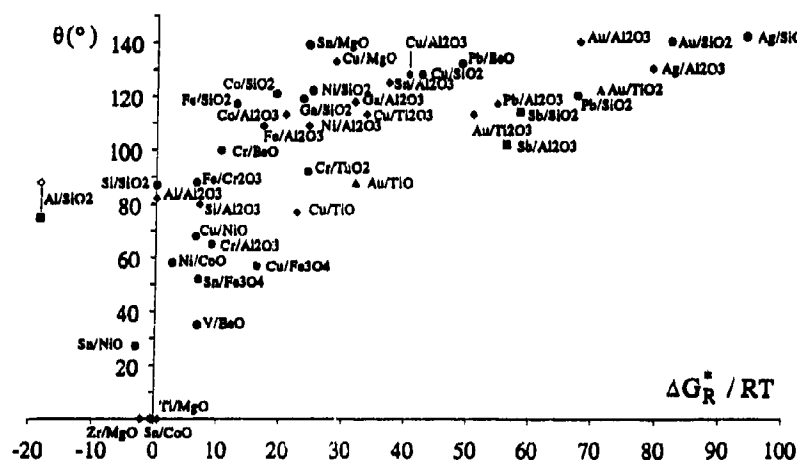


Figure 1 : Experimental contact angles versus  $\Delta G_R^* / RT$  for pure M/oxide systems. The reactivity increases from right to left. From [9].

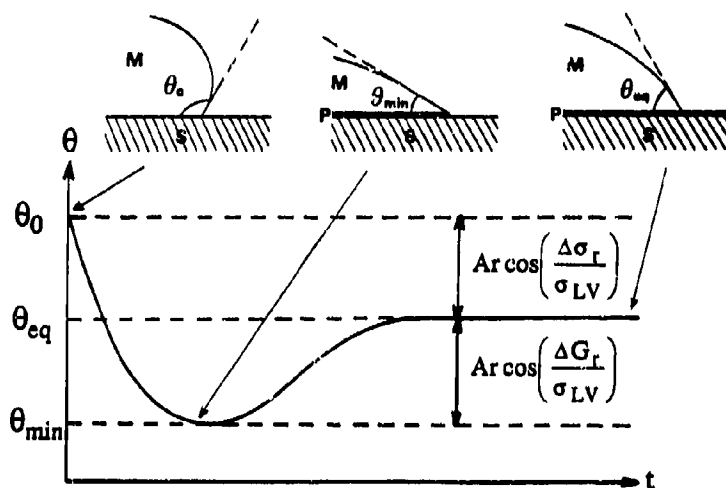


Figure 2 : Schematic representation of the reactive wetting of a metal M on a solid S with the formation of a reaction product P according to the model of Aksay et al. [13] : variation of the contact angle with time at a constant temperature and corresponding sessile drops.

correlated with an increase of  $\theta$ . Moreover, at high values of  $\Delta G_R^0 / RT$ ,  $\theta$  tends towards a limit,  $\theta \approx 140^\circ$ , a value typical of noble metals (e.g. Au and Ag) on alumina and silica. In the same way, when  $\Delta G_R^0 / RT \rightarrow 0$ ,  $\theta$  decreases steeply and perfect wetting can be reached (ex : Ti, Zr/MgO). A similar correlation between reactivity and wettability has already been observed by Naidich [1] and by Nicholas [8] using the function  $\Delta G_R^0$ .

In the next section, the different attempts of interpretation of reactive wetting will be briefly presented.

### 3 ATTEMPTS OF THEORETICAL DESCRIPTION OF REACTIVE WETTING

Despite some progress, reviewed by Laurent [12], there is at the present time no theory of general acceptance capable of describing satisfactorily reactive wetting, that is wetting followed by material transfer at the solid/liquid interface. According to Laurent, the smallest contact angle possible in a reactive system is given by :

$$\cos \theta_{\min} = \cos \theta_0 - \frac{\Delta \sigma_r}{\sigma_{LV}} - \frac{\Delta G_r}{\sigma_{LV}} \quad (6)$$

where  $\theta_0$  is the contact angle of the liquid on the substrate in the absence of any reaction.  $\Delta \sigma_r$  takes into account the change in interfacial energies brought about by the interfacial reaction.  $\Delta G_r$  is the change in free energy per unit area, released by the reaction of the material contained in the "immediate vicinity of the metal/substrate interface" [13].

Two different interpretations of reactive wetting exist, based (i) on the assumption that the predominant contribution is the Gibbs free energy term  $\Delta G_r$  [1,13,14], i.e. a parameter related with the intensity of interfacial reactions, and (ii) on the assumption that the predominant contribution is the interface energy term  $\Delta \sigma_r$  [15,16,17], i.e. a parameter related with the detailed chemistry and structure of interfacial reaction products.

#### 3.1 Models based on the $\Delta G_r$ term

This contribution to reactive wetting was first proposed by Aksay et al. [13] and by Naidich [1] who considered that the reaction between the liquid and a fresh, unreacted, solid surface at the periphery of the drop increases the driving force for wetting. Aksay et al. argued that, because the rate of interfacial reaction is maximum at the very first instants of contact between the liquid and the solid, the effect of the  $\Delta G_r$  term is strongest during these early instants of contact. Thereafter, the interface becomes saturated in reaction products and the overall reaction is controlled by diffusion. Consequently, the reaction kinetics slow down and the contact angle would increase and gradually approach the equilibrium value (Figure 2). Note that, in practice, such a dewetting would be difficult to observe as the triple line can be blocked by asperities (roughness) created by the reaction itself in the course of wetting.

However, major difficulties lie in the calculation of the  $\Delta G_r$  term. Indeed, the coupling conditions of the time-dependent interfacial reaction with the kinetics of wetting are unknown. As a consequence, a rigorous calculation of the thickness of the reaction zone in "the immediate vicinity of the interface" is still not possible and choices differing by a factor of ten have been made. Clearly, such calculations can only provide order of magnitude estimates of  $\Delta G_r$ .

Despite these difficulties, Naidich [1] performed calculations of  $\Delta G_r$  assuming that the "reactive" interface consists of two monolayers, one at the liquid-side of the interface, the



other at the solid-side. Supposing that chemical equilibrium in this region is reached rapidly,  $\Delta G_r$  is estimated by :

$$\Delta G_r = \int_0^{\alpha_{eq}} \frac{d(\Delta G_R)}{d\alpha} d\alpha \quad (7)$$

where  $\alpha$  and  $\alpha_{eq}$  are respectively the current and equilibrium degrees of progress of the reaction and  $\Delta G_R$  the Gibbs free energy of the reaction per unit area. Using this model, Naidich calculated  $\Delta G_r$  for some M/oxide reactive systems like Sn/NiO, Ti/MgO and Zr/MgO and found that the calculated values of  $W_a$  agree, within a factor two, with the experimental ones [1]. This agreement suggests that  $\Delta G_r$  represents the predominant contribution to reactive wetting and that an intense reaction is required to obtain a good wetting of a liquid on a solid [18,19]. Thus, neglecting the  $\Delta\sigma_r$  term, this model provides an explicit relation between wettability and reactivity (equations (6) and (7)), relation which seems to confirm the empirical correlation of Figure 1.

### 3.2 Models based on the $\Delta\sigma_r$ term

However, using such a purely energetical model, it is not possible to explain many experimental results in which wettability does not correlate with reactivity via the  $\Delta G_r$  term. To illustrate it, two types of experiments will be now presented, each of the  $\Delta\sigma_r$  and  $\Delta G_r$  terms being successively kept constant.

- a) A series of experiments was recently carried out in which the  $\Delta G_r$  term varied while the  $\Delta\sigma_r$  term was kept constant [17]. In these experiments, the wetting of a CuPd-Ti alloy of fixed composition has been studied on three oxide substrates of different thermodynamic stability (alumina, mullite and silica). In these systems, Ti reacts with all oxides leading to the same interfacial product (Ti-O<sub>3</sub>) but reactivity, as evidenced by the thickness of the Ti<sub>2</sub>O<sub>3</sub> layer, differed from one oxide to other by one to two orders of magnitude. Despite this great difference, wettability on the three substrates is nearly the same (Table 1). In this example, wettability correlates with interfacial chemistry, not with the intensity of interfacial reactions.
- b) In another discriminant experiment, the inverse situation has been obtained, i.e. a change of interfacial chemistry occurs at a fixed value of the Gibbs free energy of the metal/ceramic reaction. Adding Ti to NiPd alloys placed on alumina substrates, a series of wetting transitions is observed at particular values  $X_{Ti}^*$ , with a change in the type of Ti-oxide formed at the interface (Figure 3) [20]. Since when  $X_{Ti} = X_{Ti}^*$  the thermodynamic driving forces for the interfacial reactions are the same, the change  $\Delta\theta$  can only be explained by a change in  $\Delta\sigma_r$ .

substrate	$\theta$ (°)	interfacial product	thickness ( $\mu\text{m}$ )
alumina	34	Ti <sub>2</sub> O <sub>3</sub>	≈ 0.5
mullite	32	Ti <sub>2</sub> O <sub>3</sub>	≈ 1
silica	35	Ti <sub>2</sub> O <sub>3</sub>	≈ 10

Table 1 : Wettability and interfacial chemistry of CuPd-Ti ( $X_{Ti}=0.15$ )/oxide sessile drop experiments at  $T=1473\text{K}$  [17].

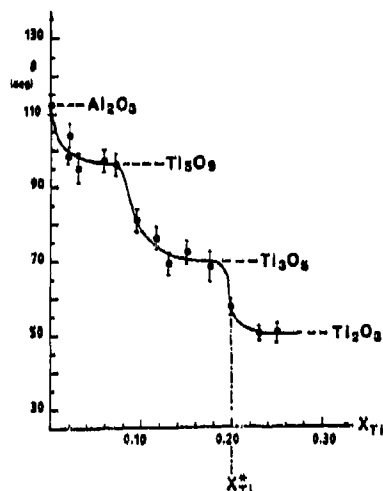


Figure 3 : Wetting transitions observed at particular values of the molar fraction of Ti for the reactive NiPd-Ti/alumina system at  $T=1523K$ . Each plateau corresponds to a particular Ti oxide identified at the interface by microprobe analysis. From [20].

From these two studies and other experiments (on Cu-Ti/ $Al_2O_3$  [15] and NiPd-Ti/C [16]), one can conclude that at least in metal/ceramic systems with a weak or moderate reactivity, the predominant contribution to reactive wetting is the term  $\Delta\sigma_r$ , reflecting interface energy change during the reaction, rather than the transient  $\Delta G_r$  term. Accordingly, an interfacial reaction could be only a way to modify in-situ the metal/ceramic interface. In practice, to exploit interfacial reactions as a means of promoting wetting without causing massive reactions between the metal and the ceramic, one can alloy a non-reactive base metal with controlled quantities of reactive solute additions, leading to the optimum relation between wettability and reactivity. Let us thus consider, at a given temperature, a reactive solute B dissolved in a non-reactive matrix M on an oxide substrate, for instance an alumina substrate. The chemical interaction in this system can be described by the dissolution of alumina in the alloy [15,21] :



possibly followed by the precipitation of a B oxide at the interface, for example :



For small values of the mole fractions of B and Al, the equilibrium mole fraction of dissolved oxygen  $X_O^D$  for reaction (9) (the superscript D stands for dissolution) will be given by the equation :

$$X_O^D = K \exp\left(-\frac{3}{5} e_O^B X_B\right) \quad (11)$$

where K is a constant [21] and  $e_O^B$  Wagner's first-order interaction parameter between the O and B solutes defined by the equation :

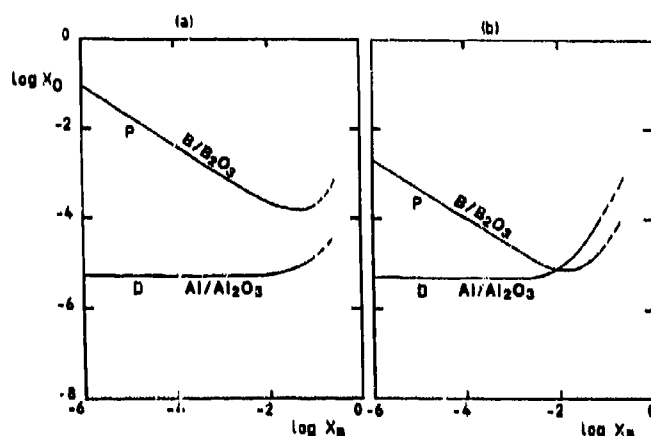


Figure 4 : Thermodynamics of matrix M-solute B/ $\text{Al}_2\text{O}_3$  systems ( $\epsilon_O^B < 0$ ).

- curve D gives the logarithm of the mole fraction of oxygen from stoichiometric dissolution of alumina in MB alloys as a function of  $\log X_B$ .
- curve P describes logarithmically the variation of  $X_O$  in equilibrium with  $\text{B}_2\text{O}_3$  as a function of  $X_B$ .

a) Only dissolution of alumina in the melt occurs. This is the case of Ni-Cr alloys at  $T=1773\text{K}$  [28].

b) The solute B reduces alumina on the right of the intersection point of the two curves. This occurs for Ni-Ti at  $T=1773\text{K}$  [29,30].

$$\ln \gamma_O = \ln \gamma_{O(M)} + \epsilon_O^B X_B + \dots \quad (12)$$

where  $\gamma_{O(M)}$  and  $\gamma_O$  are the activity coefficients of oxygen in pure M and in the M-B alloy respectively, and  $X_B$  the molar fraction of B in M. The more highly negative  $\epsilon_O^B$ , the stronger the interaction between B and O, and for sufficiently high values of  $X_B$ ,  $X_O^D$  increases rapidly (equation (11)) : strong O-B interactions will promote alumina dissolution in the melt, as expected (curves D in Figure 4).

Moreover, a solute B satisfying the condition  $\epsilon_O^B < 0$  can also lead to precipitation of an oxide  $\text{B}_2\text{O}_3$  by reaction with the excess oxygen in the alloy. The mole fraction of dissolved oxygen in equilibrium with the  $\text{B}_2\text{O}_3$  precipitate (reaction (10)), denoted  $X_O^P$ , is given by :

$$X_O^P = K' X_B^{-2/3} \exp(-\epsilon_O^B X_B) \quad (13)$$

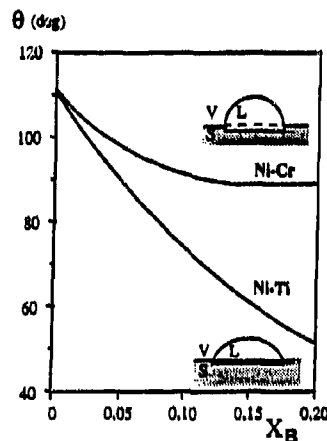


Figure 5 : Contact angles of Ni-based alloys on alumina as a function of Cr or Ti mole fraction for Ni-Cr [28] (simple dissolution of alumina) and Ni-Ti [29,30] (dissolution+precipitation of a Ti oxide) at 1773K.

where  $K'$  is a constant [21]. When  $X_B \rightarrow 0$ ,  $X_O^P$  varies as  $X_B^{-2/3}$ , i.e. it is a decreasing function of  $X_B$ . However, at higher  $X_B$  values, the exponential term in equation (13) predominates and  $X_O^P$  increases rapidly with increasing  $X_B$  (curves P in Figure 4). Thus, in both cases of dissolution and precipitation, the concentration of dissolved oxygen increases above a certain value of  $X_B$ .

If for the same value of  $X_B$  the inequality  $X_O^D > X_O^P$  holds, the solute B will reduce the alumina, forming  $B_2O_3$  :



This condition is verified for the Ni-Ti alloy, interactions between oxygen and titanium solutes being very strong ( $\epsilon_O^{Ti} = -100$ ), but not for the Ni-Cr alloy ( $\epsilon_O^{Cr} \approx -25$ ). Indeed, additions of Cr up to 20 at.% in Ni do not lead to the formation of a chromium oxide : the only effect of Cr in this matrix is to increase the dissolution of alumina in the alloy. As shown in Figure 5, Cr additions in Ni considerably decrease the contact angle of Ni on alumina. The influence of chromium would result from two effects :

a) an increased concentration of dissolved oxygen due to interfacial reactions, i.e. an increased concentration of OM clusters which can be adsorbed at the metal/oxide interface,  
b) an increased adsorption capability of the OCr clusters as compared with the ONi clusters. Indeed, as chromium is more electropositive than nickel, the charge transfer from chromium to oxygen (or, in other terms, the degree of ionicity of OCr clusters) would be greater than in the case of nickel (on this point, see also [22]).

Note that for a solute B, the thermodynamic requirements for both a and b effects are the same, i.e.  $\epsilon_O^B < 0$ .

In the Ni-Ti/ $Al_2O_3$  system, due to strong O-Ti interactions, OTi clusters in Ni must be very tensioactive at metal/oxide interfaces. However, in this case, one must also take into account the effect on wettability of the formation of a continuous  $Ti_2O_3$  layer at the nickel/alumina interface by reduction of alumina. Currently, it is generally accepted that the more metallic in character an oxide is, the more it will be wetted by molten metals [1,8].

This effect clearly appears in the results of Table 2, concerning non-reactive Cu/oxide systems, the metallic-like oxide TiO being more wettable than an ionic-covalent oxide like  $\text{Al}_2\text{O}_3$ . Thus, in the Ni-Ti/ $\text{Al}_2\text{O}_3$  system, the replacement of  $\text{Al}_2\text{O}_3$  by the semi-metallic oxide  $\text{Ti}_2\text{O}_3$  must increase  $W_a$  and decrease  $\theta$ . The combination of these two effects, i.e. (a) adsorption of OTI clusters at the liquid-side of the interface and (b) formation of a semi-metallic oxide such as  $\text{Ti}_2\text{O}_3$  at the solid-side of the interface can explain the strong decrease in contact angle caused by Ti additions in Ni (Figure 5).

This influence of Ti is even greater in the case of Cu-Ti alloys on alumina [15,19] where, due to the higher thermodynamic activity of Ti, the metallic-like TiO oxide is formed at the interface. In that case, wetting becomes nearly perfect (Figure 6-curve 2), as opposed to the Cu-Ti/ $\text{Y}_2\text{O}_3$  system [19] (Figure 6-curve 1) where only dissolution of  $\text{Y}_2\text{O}_3$  into Cu-Ti alloys occurs, producing a significant but limited decrease of  $\theta$  (from  $140^\circ$  to  $80^\circ$ ).

Unlike the effect of Ti additions, adding Ca to Al on  $\text{Al}_2\text{O}_3$  or  $\text{SiO}_2$  substrates has no effect on wetting, in spite of the formation of CaO at the interface [23]. Indeed, the ionic-covalent substrate is now replaced by an oxide of the same type.

Oxide	Conduction type	$\theta$ ( $^\circ$ )	$W_a$ (mJ/m $^2$ )
$\text{Al}_2\text{O}_3$	insulator	128	460
$\text{Ti}_2\text{O}_3$	semi-metallic	113	740
$\text{TiO}_{1.14}$	metallic	82	1460
$\text{TiO}_{0.86}$	metallic	72	1650

Table 2 : Contact angle and work of adhesion of copper on different oxides at  $T=1423\text{K}$  [1].

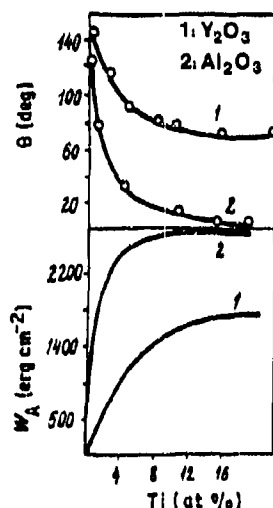


Figure 6 : Wetting and work of adhesion of Cu-Ti melts on  $\text{Y}_2\text{O}_3$  and  $\text{Al}_2\text{O}_3$  at  $T=1423\text{K}$  from [19]. Reactivity consists in a simple dissolution of the oxide substrate in the first case, and in a dissolution+precipitation of a Ti oxide at the interface in the second case.

#### 4 INTERPRETATION OF RESULTS ON PURE M/OXIDE SYSTEMS

Based on the conclusion that the predominant contribution to reactive wetting is the  $\Delta\sigma_r$  term, three kinds of behaviour can be distinguished on the curve of Figure 1 :

1) For  $\Delta G_R^* / RT \gg 0$ , that is typically for values of 20 or more, M/oxide couples can be considered, with regard to wettability, as non-reactive systems (i.e.  $\Delta\sigma_r \approx 0$ ). In that case, non-wetting is observed ( $\theta \approx 120^\circ$ ) and the work of adhesion  $W_a$  comes from metal/oxide interactions localized at a sharp interface and represents only a small fraction of the work of cohesion of the corresponding metal (typically 25%).

2) For positive but low values of  $\Delta G_R^* / RT$  (of the order of 10), the corresponding contact angles lie between  $60^\circ$  and  $100^\circ$ . A typical example is Cu/NiO ( $\theta = 68^\circ$  at 1473K) ( $e_O^{Ni} \approx -7$ ). Thermodynamic calculations performed at equilibrium lead to the following value of the molar fraction of oxygen coming from the dissolution of NiO [9] :  $X_O^D = X_{Ni}^D = 1.5 \cdot 10^{-2}$ .  $X_O^D$  is not high enough to produce precipitation of the copper oxide  $Cu_2O$  ( $X_O^D \approx 4 \cdot 10^{-2}$ ). Thus, the only possible effect in the Cu/NiO system is the adsorption of dissolved oxygen. This adsorption leads to a much lower contact angle than for the Cu/ $Al_2O_3$  system [6] for the same value of  $X_O$  ( $68^\circ$  against  $100^\circ$ ). This can be explained by an increased adsorption capability of ONi clusters with respect to OCu clusters, as indicated by the negative value of  $e_O^{Ni}$ .

Wettability in systems like Sn/ $Fe_3O_4$  ( $e_O^{Fe} \approx -50$  [24]), Cu/ $Fe_3O_4$  ( $e_O^{Fe} \approx -540$  [24]) or Fe/ $Cr_2O_3$  ( $e_O^{Cr} \approx -10$  [25]) can be interpreted in the same way. Moreover, the positions of the Al/ $Al_2O_3$  and Si/ $Al_2O_3$  systems on Figure 1 suggest that these couples, considered previously as non-reactive systems [10], fall into the same category, in spite of the very low solubility of oxygen in Al and Si respectively.

3) For values of  $\Delta G_R^* / RT$  close to zero or negative, reaction produces a new phase at the interface. Nevertheless, wettability will depend on the bonding character of this interfacial layer and two cases can be distinguished :

3.a) The first case corresponds to the replacement at the interface of an ionic-covalent oxide by another of the same type. For this kind of systems, no important improvement of wetting is expected. Al on  $SiO_2$  provides an example of intense reactivity, involving the reduction of  $SiO_2$  to form  $Al_2O_3$  at the interface, and a slight liquid enrichment in Si. As the ionic-covalent oxide  $SiO_2$  is replaced by an oxide of the same type, the contact angle of Al on  $SiO_2$  ( $\theta = 80 \pm 5^\circ$  at 1073K) is therefore close to that of Al on  $Al_2O_3$  [26,27]. The same explanation is valid for the Al-Ca on  $Al_2O_3$  or  $SiO_2$  systems previously mentioned, for which Ca additions do not improve wetting because the interfacial product (CaO) has roughly the same bonding character than the substrate.

3.b) The second case corresponds to the replacement at the interface of an ionic-covalent oxide by a metallic one. A typical example of this situation is Ti/MgO [1]. Liquid titanium can dissolve a large quantity of oxygen (a few at.% O) and form a metallic-like oxide, such as  $TiO$ , even solid solutions of Ti with high oxygen contents. The perfect wetting observed for this system (Figure 1) can be explained by the double in-situ modification of the interface : the adsorption of oxygen at the liquid-side and the formation of a metallic-bonded phase at the solid-side.

These features can also explain the excellent wetting obtained for Sn on NiO or CoO (Figure 1). The reduction of these substrates by liquid Sn is possible and the amount of dissolved Ni or Co produced by this reaction is greater than that needed to precipitate the intermetallics  $Ni_3Sn$  or  $Co_3Sn_2$  at the temperature of the experiment.

## 5 CONCLUSION

For systems with weak or moderate reactivity, the governing parameter of reactive wetting appears to be the term reflecting interfacial energy change  $\Delta\sigma_r$ , rather than the transient Gibbs free energy term  $\Delta G_r$ . However, the importance -and even the predominance- of this last term must not be excluded in some cases, for instance when an intense reaction strongly localized at the triple line occurs.

Pure metal/oxide systems can be divided into three categories :

- 1) In systems for which  $\Delta G_R^* / RT \gg 0$  (typically greater than 20),  $\theta$  is about  $120^\circ$ . Weak metal/oxide interactions are localized at a sharp interface.
- 2) In systems characterized by  $\Delta G_R^* / RT \approx 10$ , an improvement of wetting is obtained with regard to the preceding case ( $\theta \approx 80^\circ$ ), due to the effect of adsorption at the interface of oxygen, produced by the dissolution of the oxide substrate. This effect, which is greatly enhanced by the formation of metal-oxygen clusters, leads to energetically moderate interfaces.
- 3) When  $\Delta G_R^* / RT \leq 0$ , both dissolution of the oxide substrate and precipitation of a new phase at the interface occur. Wetting will depend on the nature of this new phase : for lono-covalent compounds, a case 2) behaviour will be observed whereas for metallic compounds (metallic-like oxides or intermetallics), nearly perfect wetting can be expected associated with energetically strong interfaces.

In order to produce a strong improvement of wetting of a non-reactive metal by an alloying element B, two conditions have to be satisfied :

- a) The thermodynamic parameter  $\epsilon_B^B$  must be very negative. Then, the solute B can modify both liquid and solid sides of the interface, forming at the liquid-side an adsorption layer rich in OB clusters and at the solid-side a new phase.
- b) This new phase must be at least partially metallic-bonded.

Despite the significant improvements in our knowledge of reactive wetting in metal/ceramic systems gained in the last few years, further work is needed, especially for the very reactive couples in order to evidence experimentally and to model theoretically the transient contribution to the wetting driving force,  $\Delta G_r$ , predicted by general considerations.

## REFERENCES

- [1] Ju. V. Naidich, *Prog. Surface Membrane Sci.* **14**, 353 (1981).
- [2] P. W. Tasker, A. M. Stoneham, *J. Chimie Physique (F)* **84**(2), 149 (1987).
- [3] K. H. Johnson, S. V. Pepper, *J. Appl. Phys.* **53**, 6634 (1982).
- [4] P. Hicter, D. Chatain, A. Pasturel, N. Eustathopoulos, *J. Chimie Physique* **85**(10), 941 (1988).
- [5] N. Eustathopoulos, D. Chatain, L. Coudurier, *Mater. Sci. Engineering A* **135**, 83 (1991).
- [6] P. D. Ownby, J. Liu, *J. Adhesion Sci. Technol.* **2**(4), 255 (1988).
- [7] J. G. Li, L. Coudurier, N. Eustathopoulos, *J. Mater. Sci.* **24**, 1109 (1989).
- [8] M. G. Nicholas, *Joining Ceramic, Glass and Metal*, edited by W. Kraft (DGM, Rutesheim, 1989), p. 3.
- [9] N. Eustathopoulos, B. Drevet, *J. Physique III (F)* (to be published).
- [10] D. Chatain, I. Rivollet, N. Eustathopoulos, *J. Chimie Physique (F)* **83**(9), 561 (1986).
- [11] R. Sangiorgi, M. L. Muolo, D. Chatain, N. Eustathopoulos, *J. Amer. Ceram. Soc.* **71**(9), 742 (1988).

- [12] V. Laurent, PhD thesis, Grenoble, France, 1988.
- [13] L. A. Aksay, C. E. Hoge, J. A. Pask, *J. of Phys. Chem.* **78**, 1178 (1974).
- [14] P. R. Chidambaram, G. R. Edwards, D. L. Olson, *Metall. Trans. B* **23B**, 215 (1992).
- [15] P. Kritsallis, L. Coudurier, N. Eustathopoulos, *J. Mater. Sci.* **26**, 3400 (1991).
- [16] P. Kritsallis, L. Coudurier, C. Parayre, N. Eustathopoulos, *J. Less-Common Metals* **175**, 13 (1991).
- [17] L. Espié, DEA report, INP Grenoble, France, 1992.  
L. Espié, B. Drevet, N. Eustathopoulos, submitted to *Metall. Trans.*
- [18] Ju. V. Naidich, Ju. N. Chuvashov, *J. Mater. Sci.* **18**, 2071 (1983).
- [19] Ju. V. Naidich, V. S. Zhuravljov, N. I. Frumina, *J. Mater. Sci.* **25**, 1895 (1990).
- [20] P. Kritsallis, PhD thesis, Technical University of Athens, Greece, 1990.
- [21] N. Eustathopoulos, L. Coudurier, *J. Adhesion Sci. Technol.* **6**, 1011 (1992).
- [22] P. Kritsallis, J. G. Li, L. Coudurier, N. Eustathopoulos, *J. Mater. Sci. Letters* **9**, 1332 (1990).
- [23] N. Mori, H. Sorano, A. Kitahara, K. Ogi, K. Matsuda, *J. Japan Inst. Metals* **47**, 1132 (1983).
- [24] Y. Austin Chang, K. Fitzner, Min-Xian Zhang, *Progress in Materials Science* **32**, 97 (1988).
- [25] M. Heinz, K. Koch, D. Janke, *Steel Res.* **60**, 246 (1989).
- [26] Yu. V. Naidich, Yu. N. Chubashov, N. F. Ishchuk, V. P. Krasovskii, *Poroshkovaya Metallurgiya* **246**(6), 67 (1983).
- [27] V. Laurent, D. Chatain, N. Eustathopoulos, *Mater. Sci. Engineering A135*, 89 (1991).
- [28] P. Kritsallis, V. Merlin, L. Coudurier, N. Eustathopoulos, *Acta Metall. Mater.* **40**(6), 1167 (1992).
- [29] V. Merlin, P. Kritsallis, L. Coudurier, N. Eustathopoulos, *Mat. Res. Soc. Symp. Proc.* **238**, 511 (1992).
- [30] Yu. V. Naidich, V. S. Zhuravlev, V. G. Chuprina, *Sov. Powd. Metall. and Met. Ceramics* **13**(3), 236 (1974).



## BONDING, STRUCTURE AND PROPERTIES OF METAL/CERAMIC INTERFACES

JAMES M. HOWE

Department of Materials Science and Engineering, University of Virginia, Charlottesville, VA 22903

### ABSTRACT

This paper reviews the effects of chemical bonding, reaction, interfacial structure, fabrication, specimen geometry and testing conditions on the strength and fracture behavior of metal/ceramic interfaces. It is shown that a number of important properties of metal/ceramic interfaces such as the wetting behavior and work of adhesion can be qualitatively predicted from simple bonding models based on the elements in the metal and ceramic. In addition, the interfacial structure can often be predicted from principles of equilibrium thermodynamics and minimization of interfacial energy for relatively thick metal/ceramic layers. More quantitative description of interfacial structure employing atomistic calculations has been performed for simple interfaces and this area is progressing. The fracture behavior of metal/ceramic interfaces is a complicated process which depends on many factors such as the specimen geometry and loading conditions, strength of the interfacial bond, thermal, elastic and fracture properties of the metal and ceramic, thickness of the metal layer and testing environment. Advances in this area include the development of favorable specimen geometries for measuring interface properties and an understanding of the relationship among the phase angle of loading, crack trajectory and interface fracture energy for these geometries. Conversely, little is known about the stress corrosion and fatigue behavior of metal/ceramic interfaces although data on these time dependent failure modes are beginning to appear in the literature. Much progress has been made but considerably more work is needed to understand the properties of metal/ceramic interfaces.

### INTRODUCTION

Understanding the relationship among the processing, structure and properties of metal/ceramic interfaces is becoming increasingly important as performance requirements demand a combination of these materials in applications ranging from electronic packaging to high-temperature aircraft structures [1]. The purpose of this review is to assess the current understanding of the relationship among the processing, structure and properties of metal/ceramic interfaces, emphasizing work on planar metal/ceramic interfaces produced by diffusion bonding. This particular area was chosen in order to focus the review and because considerable work has been performed on this type of interface. However, it is important to note that many of the topics that are discussed in this review apply to other types of metal/ceramic interfaces.

Table I lists some of the main factors that are involved in fabricating, testing and understanding the behavior of metal/ceramic interfaces. There are sixteen subheadings in this list, and it is not all inclusive, which serves to illustrate the complexity of the problem. The topics in Table I were divided into three categories for convenience and this review largely follows the order of topics shown in Table I.

### CHEMICAL BONDING

Chemical bonding is defined as bonding in which there is only charge transport as opposed to mass transport across a metal/ceramic interface. Excellent reviews of this subject with regard to metal/ceramic interfaces have been published [2,3]. The purpose of the following discussion is to outline some physical principles which can be used to understand chemical bonding at metal/ceramic interfaces.

Table I. Some factors involved in the behavior of diffusion bonded metal/ceramic interfaces.

---

### I. Chemical Bonding

- a. Surface energies of metal and ceramic
- b. Interfacial energy and work of adhesion
- c. Experimental measurement and calculation of work of adhesion
- d. Orientation relationships across metal/ceramic interfaces
- e. Segregation to metal/ceramic interfaces
- f. Effect of the above on interface properties

### II. Chemical Reaction

- a. Thermodynamics of reaction
- b. Kinetics of reaction
- c. Bonding conditions - time temperature, pressure, surface roughness
- d. Effect of reaction layer on properties

### III. Fracture Behavior

- a. Geometry of test specimen
  - b. Fracture energy (toughness) of interface
  - c. Dependence of crack path on mode of loading, elastic properties of metal and ceramic, metal thickness, reaction layer, etc.
  - d. Residual stresses
  - e. Stress corrosion cracking
  - f. Fatigue
- 

### Surface Energies of Metals and Ceramics

Energy is required to create a solid or liquid surface because the surface atoms or ions experience unbalanced bonding forces. This imbalance is reflected in a number of phenomena which allow experimental measurement of surface energies [4]. Experimental values for the surface energies of solid metals have been correlated with physical property data such as the heat of sublimation and modulus of elasticity [5,6]. Surface energies of metals generally increase linearly with the heat of sublimation ranging from about 1-3 J/m<sup>2</sup> and decrease linearly with temperature at about 0.02%/K. Experimental measurements of the surface energies of ceramics are less abundant than those of metals but they tend to range from about 0.5-1 J/m<sup>2</sup> and display a similar correlation with the modulus of elasticity [3].

### Metal/Ceramic Interfacial Energy and Work of Adhesion

The driving force for the formation of a metal/ceramic interface is the decrease in free energy  $\Delta G$  that occurs when intimate contact is established between the metal and ceramic. In the case where only chemical bonding occurs at the interface and interfacial separation proceeds without plastic deformation of the metal or ceramic, the change in free energy  $\Delta G$  is identical to the work of adhesion  $W_{ad}$  required to separate a unit area of interface into the two original surfaces. In this case the relationship between the interfacial energy  $\gamma_{mc}$  and work of adhesion is given by the equation [4,7]:

$$\gamma_{mc} = \gamma_m + \gamma_c - W_{ad} \quad (1)$$

where  $\gamma_m$  and  $\gamma_c$  are the surface energies of the metal and ceramic, respectively. Equation (1) shows that  $\gamma_{mc}$  decreases as  $W_{ad}$  increases and that strong metal/ceramic interfaces are generally low energy interfaces. Another useful relationship is given by the equation:

$$W_{ad} = \gamma_m (1 + \cos \theta) \quad (2)$$

where  $\theta$  is the contact angle between the metal and ceramic. Equations (1) and (2) provide a number of useful insights into the behavior of metal/ceramic interfaces. For example, Eqn. (2) indicates that the work of adhesion increases with the surface energy or melting point of the metal and this is observed experimentally [2,3]. Equation (1) also shows that there is little chance of producing a strong metal/ceramic interface when both  $\gamma_m$  and  $\gamma_c$  are low and that a high value of  $\gamma_m$  may be necessary to produce a strong interface if  $\gamma_c$  is very low.

Further qualitative estimates of the wetting characteristics of ceramics by metals can be obtained by using a relationship such as that of Pauling [8] between the ionicity and electronegativities of the component elements. In general, highly ionic ceramics should be difficult to wet since their electrons are tightly bound and their surfaces represent large discontinuities in charge. Such behavior is supported by experiment [3,9], where the contact angle tends to increase in proportion to the ionicity (heat of formation) of the ceramic. Metallic and covalent bonds are similar in character and covalently bonded ceramics should be more easily wet by metals than highly ionic ceramics and this is also supported by experiment [10]. Some fairly simple relationships to estimate the work of adhesion of both oxide and non-oxide ceramics have been developed [11-13]. More quantitative data has recently been obtained for some model metal/ceramic interfaces such as Ag/MgO and Ti/MgO using *ab initio* local density-functional calculations and image potentials [14] and this area of research is advancing rapidly.

#### Orientation Relationships at Metal/Ceramic Interfaces

Orientation relationships have been observed to form across many chemically bonded metal/ceramic interfaces [15-17] similar to the case of metal/metal interfaces [18-20]. The orientation relationships result from interfacial energy minimization, including the effects of strain, and low-energy close-packed planes and directions are often found to align between the metal and ceramic across the interface. Exceptions to this have been found in the case of some noble metals on ionic crystals, where alignment of close-packed rows of atoms dominate the interfacial structure [16]. Slight deviation of an interface away from a perfect low-index interface plane can be accommodated by periodic steps in the interface and misfit dislocations can also form at metal/ceramic interfaces to accommodate differences in lattice parameters or orientation across the interface [21]. To first approximation, it appears that prediction of the interfacial structures of a number of metal/ceramic interfaces can be approached using some of the same geometrical techniques that have been established for interphase boundaries in metal/metal systems with appropriate consideration for the possibly dominant influence of the nonmetallic component in the ceramic [22-24]. Exceptions to this do occur, and in these cases predictions must employ other models or atomistic calculations.

#### Segregation

The theory of impurity segregation to surfaces and grain boundaries in metals is well understood and several different models have been proposed to predict segregation behavior [4-6,25-27]. The theory is less well developed for ceramics but considerable progress has been made [28]. In contrast, the theory of impurity segregation to heterophase interfaces in metals has just recently been developed [29] and there are currently no quantitative theories to predict segregation behavior to metal/ceramic interfaces, which is even more complicated due to the nature of the metal/ceramic bond. Segregation is known to occur, as demonstrated by the formation of various reaction products at interfaces in metal/ceramic composites [30] and by the addition of Ti to Ag-braze alloys [31], for example. Segregation should occur to metal/ceramic interfaces when it results in a decrease in the interfacial energy. In the case of metals, segregation has been found to depend on the bond energy, the elastic strain energy and the enthalpy of mixing of the impurity element, and similar factors may be important in understanding the segregation of impurities to metal/ceramic interfaces. Considerably more work is needed to understand this area.

### Effect on Interface Properties

Evaluation of the correlation between the interfacial strength and bonding reported for many metal/ceramic systems is difficult because the interfacial structure, extent of reaction at the interface and the testing techniques used to measure the interface strength vary considerably. There have been very few studies where all of these features have been sufficiently controlled to fully establish this correlation. However, some data on reasonably well-characterized metal/ $\text{Al}_2\text{O}_3$  systems support the bonding/strength relationships discussed above. For example, work on Nb/ $\text{Al}_2\text{O}_3$  single-crystal interfaces [32,33] has shown that the interface fracture energy is highest when the metal/ceramic interface parallels the close-packed planes and directions and that it decreases for other orientations, as expected from the viewpoint of interfacial energy minimization. Further, room-temperature tensile data on various metal/ $\text{Al}_2\text{O}_3$  systems indicates that the interfacial strengths increase with the work of adhesion and melting points of the metals as predicted from Eqn. (2). Lastly, data for the maximum strengths of several pure metals and Ni alloys versus the O affinity of the metals or alloying elements shows that the chemical affinities of the elements across the interface can be used to estimate the strengths of metal/ceramic interfaces in some systems [34], again in agreement with the principles described previously. In summary, it appears that the qualitative bonding arguments presented above are generally useful for estimating the behavior of many metal/ceramic interfaces although it is much more difficult to be quantitative about such relationships.

### CHEMICAL REACTION

Chemical reaction occurs when there is mass transfer across an interface and this often leads to the formation of interfacial reaction layers with properties that differ from those of either the metal or ceramic components. Such reaction products can have a drastic effect on the interface properties. Whether or not new phases form depends on the thermodynamic properties of the metal/ceramic system and on the reaction conditions such as time, temperature, pressure and atmosphere. This section begins with discussion of the thermodynamic and kinetic aspects of chemical reaction, and this is followed by the effects of bonding conditions and reaction layers on interface properties.

#### Thermodynamics of Chemical Reaction

The driving force for chemical reaction is the chemical potential of the atomic species involved. Although chemical reaction is an irreversible process, chemical reaction at metal/ceramic interfaces is usually considered from the viewpoint of equilibrium thermodynamics, where the possible reaction products and conditions for chemical reaction are determined from equilibrium thermodynamic data available for various systems as a function of time, temperature and pressure [35]. Excellent reviews of chemical reaction at metal/ceramic interfaces have been published by Klomp [2,33,36] with emphasis on two important cases of reaction; namely, when there is a reduction-oxidation reaction with accompanying dissolution of one or both of the ceramic elements into the metal and when there is a highly reactive metal and ceramic. Several important points that arise from these analyses are that in metal/ceramic systems where the ceramic contains a gaseous species, such as  $\text{Al}_2\text{O}_3$  and  $\text{Si}_3\text{N}_4$ , the reaction can be controlled by changing the activity of the gaseous species in the surroundings. In addition, in many situations, the compressive loads applied during fabrication of metal/ceramic interfaces establishes intimate contact at the interface which can prevent gaseous species from reaching the interface. Lastly, the thermodynamics of some systems predict reaction under all conditions so that the reaction cannot be controlled by outside means.

Warren and Andersson [37] have reviewed the equilibrium thermodynamics of SiC with a number of common metals and they provide a simple scheme to divide metal/ceramic interfaces into two classes, reactive and stable, based on the phase diagrams of the systems. In reactive systems, SiC reacts with the metal to form silicides and/or carbides and C, with reactive metals including Ni, B, Ti, Cr, Fe, Zr, Nb, Mo, Ta and W. The most important characteristic associated with the phase diagram of a reactive system is that a two-phase field, which shows SiC in equilibrium with the metal, does not exist in the ternary phase diagrams for these

elements. In contrast, for stable systems, SiC and a metal can coexist thermodynamically and a two-phase field exists in the ternary diagram. Examples of this are SiC with the metals Al, Au, Ag, Cu, Mg, Pb, Sn, and Zn. Thus, equilibrium thermodynamics are quite useful for determining whether or not reaction is likely in relatively thick metal/ceramic couples. However, the effects of stress on the thermodynamics of thin films and interfaces are just beginning to be understood [38] and this is an area associated with reaction at metal/ceramic interfaces that has not been examined.

#### Kinetics of Reaction

Most kinetic data on relatively thick (greater than one micrometer) reactive metal/ceramic interfaces indicate that reaction can usually be described by a simple parabolic growth law [37,39-42]. Parabolic growth indicates that the reaction is diffusion controlled and the parabolic rate equation is:

$$x = kt^{1/2} \quad (3)$$

where  $x$  is the average thickness of the reaction layer,  $k$  is the parabolic rate constant and  $t$  is the reaction time at a particular temperature [43]. Certain alloying additions to Ti in Ti/TiB<sub>2</sub> composites were found to reduce the parabolic rate constant by more than an order of magnitude and this is one way to control chemical reaction [42]. Kinetic data for reaction layers which are discontinuous or only tens of nanometers thick have not been studied systematically and it is not known if these initial reaction layers display parabolic growth behavior.

#### Bonding Conditions

In many metal systems such as Al, it is not possible to reduce the stable oxide film at the metal/ceramic interface in a reasonable time below the melting temperature and the solubility is too low to effect dissolution into the metal. Hence, in order to present a nascent metal surface to the ceramic for bonding, it is necessary to destroy the oxide film by plastic deformation of the metal during the bonding process. The main variables in the bonding process are the pressure, temperature, time and surface roughness. These variables are not independent, but they are discussed separately below in order to emphasize the most important factors associated with each one.

In addition to establishing contact between the metal and ceramic, an important role of pressure is to destroy the surface oxide on the metal and this has a large effect on the integrity of the metal/ceramic bond [44-47]. The exact pressure that is needed depends on the metal/ceramic system, thickness of the metal layer and on the bonding temperature. In general, good bonding is favored by a relatively high pressure which reduces the thickness of the metal layer by at least a factor of four [46].

Temperature increases interaction across a metal/ceramic interface by increasing the mobility of atoms and also the mobility of dislocations in the metal during bonding. Since the mobility of dislocations increases with temperature and the flow stress correspondingly decreases, the pressure required for bonding decreases with increasing temperature [45,46]. Therefore, an increase in bonding temperature should generally enhance bonding of a metal/ceramic interface for a given pressure and time, provided that the time is sufficiently short to prevent development of detrimental reaction products at the metal/ceramic interface. Data on various metal/Al<sub>2</sub>O<sub>3</sub> systems shows that there is a direct correlation between the percent of bonded interface on the temperature and deformability of the metals and that in most cases a temperature of at least 0.9 of the melting point of the metal is necessary for good bonding (strength) at the interface [2,3,45].

A relatively short bonding time is usually required to form a strong bond between a metal and ceramic under temperature and pressure conditions that are sufficiently high to cause rapid deformation of the metal [47]. In the case of chemical bonding, the time required to deform the metal is often the limiting parameter. For the case of chemical reaction, the time that the

temperature and pressure are applied can have a great effect on the interface properties and a high deformation rate and short bonding time help to limit the formation of thick reaction layers.

When a surface is rough, deformation of the metal differs greatly from the case of a smooth surface, which was assumed above. In general, asperities prevent large-scale plastic deformation at the surface because the metal is anchored between the asperities. This greatly limits the development of nascent metal/ceramic contact and adversely affects the strength of the interface [44,46]. Techniques such as friction and ultrasonic bonding [48] tend to break up surface oxides and fill in holes and defects in the surface and these techniques show potential for minimizing chemical reaction and breaking up tenacious surface oxides in chemically reactive systems.

#### Effect of Reaction Layer on Properties

The effect of a reaction layer on the interface strength depends on a number of factors such as the mechanical properties of the reaction layer, its thickness and morphology, the strength of the interfacial bond and the mode of loading at the interface. Many of these factors are discussed in the following section so that only the effect of the thickness of the reaction layer is emphasized here. Reactions formed at metal/ceramic interfaces include solid solutions, amorphous phases, crystalline phases with low-energy orientation relationships with the metal and ceramic as well as crystalline phases with no apparent orientation relationship [47,49-51]. Each of these reaction products produces a different type of interface between the metal and ceramic and the relative effectiveness of these various types of reaction products on the strength of metal/ceramic interfaces is not fully understood. However, most reaction layers are brittle and therefore potentially detrimental to the interface properties.

Metcalf [42] established a theoretical framework for understanding the effect of reaction layer thickness and properties on the fracture behavior of Ti-B filament composites and some of the fracture mechanics concepts associated with these results are pertinent. In this system, reaction resulted in growth of a  $TiB_2$  layer at the interface and the mechanical properties were analyzed assuming that the flaw size for crack initiation is proportional to the reaction layer thickness, that cracks do not initiate in the matrix and that the distribution of flaws in the B filament is constant as the reaction layer thickens. When the reaction layer is thin, the size and quantity of flaws in this layer is less than the existing population in the filament and fracture is controlled by the filament. As the reaction layer thickens, a point is reached where the stress intensity associated with a reaction zone cracks exceeds that in the filament and the filament fails at a stress that decreases as the thickness of the layer increases. With increasing reaction, a second critical thickness is reached where the filament fails the instant the reaction layer cracks. This type of behavior was verified experimentally [42] and demonstrates the detrimental effect of thick, brittle reaction layers on interface properties. Although there are limited data of this type for diffusion bonded metal/ceramic interfaces, data on other types of interfaces generally show that relatively thin reaction layers (less than one micrometer, perhaps less than a tenth of a micrometer) may have a beneficial effect on interface properties by forming a strong interfacial bond, while relatively thick (greater than about one micrometer) reaction layers usually degrade the interface properties [42,47,49,52,53].

#### **FRACTURE BEHAVIOR**

The mechanical properties of a metal/ceramic interface depend upon many factors such as the elastic properties of the metal and ceramic, the thickness of the metal layer, the specimen geometry and the mode of loading. In addition, residual strains due to elastic and thermal mismatch are associated with most metal/ceramic interfaces and these must be minimized in order to optimize the properties of the interface. It is particularly important for design purposes to know not only the fracture strength but also the fracture resistance and fracture energy of an interface, and the effects of cyclic loading and environment on the fracture behavior. These topics are discussed below.

### Geometry of Test Specimen

In the past, interface strengths have often been assessed by pull-off or shear-off tests, which yield the load at which the bond is ruptured. In these tests, failure occurs by spreading of a crack from the most severe flaw in the bonded interface. These tests depend on the flaw size distribution, which varies with processing conditions, and thus do not provide a good measurement of the inherent bond strength or toughness of a metal/ceramic interface. In order to avoid crack nucleation as the critical event, several notched or precracked specimens have been developed with different modes of loading. Some of the most popular specimens currently include a double-cantilever-beam (DCB) specimen with nominally mode I loading and sandwich-type 3- or 4-point bend specimens with mixed mode loading [54-57]. With these specimens, it is possible to quantify the mode of loading as well as to assess the interface strength in terms of an interface fracture energy  $G_0$ , also called the generalized critical energy release rate [54,55].

### Fracture Energy

Since the reversible fraction of the interface fracture energy  $G_0$  is equal to the work of adhesion  $W_{ad}$  in Eqn. (1), fracture energy measurements can be used to determine the amount of irreversibly dissipated energy accompanying interface fracture if  $W_{ad}$  is known. Only a few such studies have been performed [54,58], but the results of these studies indicate that the work of adhesion in Eqn. (1) represents only a small fraction of the interface fracture energy, with the fraction of irreversibly dissipated energy typically comprising more than 98%. Most of the irreversibly dissipated energy is due to plastic deformation of the metal during fracture. Since a large part of the interface fracture energy is due to plastic deformation processes in the metal, it is important to understand the effect of metal layer thickness on the interface fracture energy. This effect was examined by Reimann et al. [59] using thin Au foils diffusion bonded between two thicker  $Al_2O_3$  layers in a flexure specimen geometry with mixed mode loading. In this study, both the fracture initiation resistance and the subsequent growth resistance were found to increase with the metal layer thickness. This behavior was largely attributed to crack shielding caused by bridging metal ligaments in the crack wake during fracture. These investigators also developed a semi-empirical expression which includes the role of the work of adhesion, the metal flow stress and the metal layer thickness on the fracture resistance.

The effects of interface toughening due to crack-tip shielding mechanisms was clearly demonstrated in a set of experiments where controlled arrays of implanted microcracks were used to induce crack bridging by Cu at a Cu/glass interface and increase the toughness by a factor of 8-80 times over that of a plain Cu/glass interface [60,61]. The contribution to toughening was also shown to depend on a compromise between the spacing of the microcracks and the thickness of the bridging metal ligaments, and emphasizes the importance of metal ductility on interfacial toughness. These results demonstrate that the interface fracture energy is enhanced by interfacial microcracks which are out-of-plane with respect to the main interface crack and that the toughness of such interfaces can greatly exceed the toughness of the brittle ceramic component.

### Crack Path Versus Mode of Loading

The previous section emphasized the important contributions of the crack path, including crack bridging, crack deflection and metal ductility to the interfacial fracture energy. The path that a crack follows along a metal/ceramic interface is determined by a number of factors including the mode of loading, the elastic properties of the metal and ceramic, the metal layer thickness and the presence of a reaction layer. Rigorous analytical treatment of the relationship between crack path selection and the interfacial fracture energy for several model interfaces has been performed by Evans [62] and others [63,64], and these studies show that the crack trajectory depends on the phase angle of loading  $\psi$ , which is a function of the ratio of the interface fracture energy to the fracture energy of the brittle component of the interface and the relative shear  $v$  to opening  $u$  experienced by the interface crack. In the case of two brittle solids where the elastic Dundurs parameter  $\beta = 0$  [65], the phase angle of loading is given as:

$$\Psi = \tan^{-1} (u/v) = \tan^{-1} (K_{II}/K_I) \quad (4)$$

where  $K_I$  and  $K_{II}$  are the mode I and mode II stress intensity factors. Since  $\Psi = 0$  for mode I loading and  $\pi/2$  for pure mode II loading, the value of  $\Psi$  is a direct measure of the relative amount of mode II loading (mixity of loading) on the interface crack [62,65]. For this type of interface, cracking out of the interface is most likely to occur into the lower modulus material (say the metal) when the phase angle  $\Psi = 70^\circ$  [62].

A second situation of importance in metal/ceramic systems occurs when one of the materials is ductile and the other is brittle. In this case, the fracture behavior and the interface fracture energy are highly sensitive to the sign of the phase angle and different types of behavior are predicted [62]. When the phase angle has a positive sign and the fracture energy of the brittle component is much less than that of the interface, the relative incidence of cracking out of the interface is identical to that of the all-brittle system just described. However, when the phase angle is negative, the large fracture energy of the ductile material compared to the interface prohibits crack propagation out of the interface. In this situation, one of two possibilities should occur depending on the yield strength of the ductile material. For a low yield-strength material, plastic blunting of the interface crack occurs and failure proceeds by ductile mechanisms involving hole nucleation at the interface. Alternatively, for a high yield-strength material, the stress field of the interface crack interacts with preexisting flaws in the brittle material causing cracks to grow from these flaws back toward the interface, resulting in chips of brittle material attached to the fracture surface. All of these types of cracking have been reported in the literature and summaries of possible crack paths as a function of variables such as the mode of loading, interface strength and reaction layer strength are provided by Evans [56,62] and Suga and Elmsner [66].

Since the test configuration determines the sign and magnitude of the phase angle of loading, which in turn governs the crack path and thus the mechanisms that contribute to the interface fracture energy, it is essential that the test geometry, mode of loading and mechanisms of cracking be considered in interpreting values of the interface fracture energy.

### Residual Stresses

Edges and corners are a major source of failure for metal/ceramic interfaces when there is a mismatch in either the thermal expansion or elastic modulus of the metal and ceramic [67]. When a metal has either a larger thermal expansion coefficient or a lower modulus than the ceramic or both (which is often the case), the unconstrained metal develops a smaller lateral dimension at the interface than the ceramic. In order to maintain continuity at the interface, the metal must be uniformly extended by the application of edge tractions. Surface forces which are equal in magnitude but opposite in sign must then be applied to the metal in the bonded state to achieve stress-free conditions at the surface and this introduces large normal and shear stresses near the edge of the metal/ceramic joint [68]. Thermal expansion mismatch usually induces tensile stresses in the ceramic adjacent to the interface that promote failure of the ceramic. In addition, large shear stresses also exist near the edge along the interface for both thermal and elastic mismatch so that a substantial mode II contribution to edge failure should occur in all situations. It is important to note that for the case of thermal expansion mismatch, the stresses decrease in magnitude as the relative metal thickness decreases so that thin metal layers can be used to reduce thermal expansion mismatch [68]. Conversely, a mismatch in modulus generates interfacial tensile stresses at the edge regardless of the sign of the mismatch and thus always enhances the propensity to fracture.

Suga et al. [66] used finite element calculations to investigate the effects of thermal and elastic mismatch on interface stresses and they found that the local tensile and shear stresses at the edge of a bonded interface can be described by the stress intensity factors  $K_I^*$  and  $K_{II}^*$  which are proportional to the thermoelastic parameters  $\Delta\alpha\Delta E\Delta T$  and  $\Delta\alpha\Delta E^*\Delta T$ , respectively, where  $\Delta\alpha$ ,  $\Delta E$  (and  $\Delta E^*$ ) and  $\Delta T$  represent the differences in thermal expansion coefficients and elastic moduli of the metal and ceramic, and the temperature, respectively. Thus, once the



thermoelastic constants and size of the components in a metal/ceramic joint are given, the local stress field in the edge region can be estimated without any calculation using the data provide in the paper. These results are quite useful for estimating residual stresses at metal/ceramic joints.

### Stress Corrosion Cracking

The susceptibility of metal/ceramic interfaces to stress corrosion cracking is important in structural applications where some water is present in the environment, such as in air or combustion gases, since most ceramics are susceptible to stress corrosion by water [59,60,69]. There are two possible cases for stress corrosion cracking of a metal/ceramic interface, one is related to direct attack of the interatomic bonding at the interface and the other involves damage to the interfacial region, including some volume of the metal, ceramic or both. Few studies have been performed on the stress corrosion behavior of metal/ceramic interfaces but recent work by Oh et al. [60,70] indicates some behavior that may be observed.

Oh et al. [60,70] performed subcritical crack-growth studies on DCB specimens containing a thin Cu film between glass substrates with and without patterned microcracks, similar to the specimens described previously [61]. Subcritical crack-growth testing was performed under constant displacement conditions in various gaseous atmospheres spanning a range of relative humidities. The Cu/glass interfaces were found to display three regimes of behavior, similar to environmentally assisted crack-growth behavior in metal and ceramics [69,71]. Interfacial crack-growth rates were much higher and apparent crack-growth thresholds were much lower in a moist environment than in a dry one. Additionally, crack velocities along the interface were found to be more sensitive to the stress intensity and greater than three orders of magnitude faster than subcritical crack-growth data for bulk soda-lime glass tested in water vapor. Comparison of the plain and patterned Cu/glass interfaces in both wet and dry environments showed that the subcritical growth rates are many orders of magnitude slower for the patterned interfaces and that the patterned interfaces displayed threshold interfacial fracture energies that are increased by a factor of six to seven over those of the plain interfaces. Although detailed microstructural investigations of the mechanisms of interfacial crack growth were not performed in these studies the increased resistance of the patterned interfaces appears to be attributable to crack bridging as discussed in the section on fracture energy.

### Fatigue

It appears that only one study has been performed to examine the fracture behavior of metal/ceramic interfaces under cyclic loading (fatigue) conditions [72], again using the plain and patterned Cu/glass interfaces mentioned above and also an Al-Mg/Al<sub>2</sub>O<sub>3</sub> interface. These interfaces displayed markedly different fracture behavior with failure occurring at the metal/ceramic interface under a relatively low load for the Cu/glass specimen and generally within the ceramic under a much higher load for the Al-Mg/Al<sub>2</sub>O<sub>3</sub> interface. The limited data indicate that fatigue crack-growth rates can be many orders of magnitude faster than subcritical crack-growth rates at equivalent levels of crack extension force and occur at much lower thresholds than under monotonic loading but this behavior may vary widely depending on the particular metal/ceramic interface. The presence of implanted microcracks led to much improved crack-growth resistance due to crack bridging of the interface by metal-film ligaments. While the fracture behavior of the two types of interface was much different, in both cases, plastic deformation appeared to constitute most of the fracture energy with crack bridging playing an important role in the fracture process.

### CONCLUSIONS

Many factors are involved in determining the relationship among the bonding, structure and properties of diffusion bonded metal/ceramic interfaces. The effects of some factors, such as the thermodynamics and kinetics of reaction, on the behavior of diffusion bonded metal/ceramic interfaces are reasonably well understood. The effects of other factors, such as segregation, stress corrosion and cyclic loading, on the properties of metal/ceramic interfaces are just beginning to be understood.

## ACKNOWLEDGEMENT

This research was supported by the National Science Foundation under Grant DMR-9107550.

## REFERENCES

1. K. K. Chawla, Composite Materials. Science and Engineering (Springer-Verlag Publishers, New York, 1987).
2. J. T. Klomp, in Surfaces and Interfaces of Ceramic Materials, edited by L.-C. Dufour et al. (Kluwer Academic Publishers, New York, 1989) p. 375; M. G. Nicholas, *ibid.*, p. 393.
3. M. G. Nicholas, *Mater. Sci. Forum*, **29**, 127 (1988).
4. L. E. Murr, Interfacial Phenomena in Metals and Alloys (Addison-Wesley Publishing Company, Reading, MA, 1975) p. 34.
5. E. D. Hondros, in Precipitation Processes in Solids (The Metallurgical Society of AIME, Warrendale, PA, 1978) p. 1.
6. J. A. Alonso and N. H. March, Electrons in Metals and Alloys (Academic Press, London, 1989) p. 473.
7. A. W. Adamson, Physical Chemistry of Surfaces (Interscience Publishers, New York, 1960) p. 265.
8. L. Pauling, The Nature of the Chemical Bond, 2 ed. (Cornell University Press, New York, 1948) p. 69.
9. Y. Naidich, *Progress in Surface and Membrane Science*, **14**, 353 (1981).
10. L. Ramqvist, *Inter. J. Powder Met.*, **1**(4), 2 (1965).
11. M. Humenik and W. D. Kingery, *J. Amer. Cer. Soc.*, **37**, 18 (1954).
12. J. A. McDonald and J. G. Eberhart, *Trans. AIME*, **233**, 512 (1965).
13. Y. Naidich and G. A. Kolesnichenko, *Russ. Met.*, **4**, 141 (1968).
14. U. Schonberger, O. K. Andersen and M. Methfessel, *Acta Metall. Mater.*, **40**, S1 (1992); D. M. Duffy, J. H. Harding and A. M. Stoneham, *ibid.*, S11.
15. J. T. Klomp, in Ceramic Microstructures '86. Role of Interfaces, edited by J. A. Pask and A. G. Evans (Plenum Press, New York, 1987) p. 307.
16. H. J. Fecht and H. Gleiter, *Acta Metall.*, **33**, 557 (1985).
17. W. Mader, in Structure and Properties of Interfaces in Materials, edited by W. A. T. Clark et al. (*Mater. Res. Soc. Proc.* **238**, Pittsburgh, PA, 1992) p. 763.
18. M. Kato, *Mater. Sci. Eng.*, **A146**, 205 (1991).
19. H. I. Aaronson, T. Furuhara, J. M. Rigsbee, W. T. Reynolds, Jr. and J. M. Howe, *Metall. Trans.*, **21A**, 2369 (1990).
20. U. Dahmen, *Acta Metall.*, **30**, 63 (1982).
21. H. F. Fischmeister, G. Elsner, B. Gibbesch and W. Mader, in Proc. MRS Inter. Meeting on Adv. Mater. Vol. 8 - Metal-Ceramic Joints, edited by M. Doyama et al. (MRS, Pittsburgh, PA, 1989) p. 227.
22. W. Bollmann, *Surf. Sci.*, **31**, 1 (1972).
23. R. W. Balluffi, A. Brockman and A. H. King, *Acta Metall.*, **30**, 1453 (1982).
24. H. J. Fecht, *Acta Metall. Mater.*, **40**, S39 (1992).
25. E. D. Hondros and M. P. Seah, in Physical Metallurgy, edited by R. W. Cahn and P. Haasen (North-Holland Publishing Company, Amsterdam, 1983) p. 888.
26. R. Chelikowsky, *Surf. Sci.*, **139**, L197 (1984).
27. P. Wynblatt and R. C. Ku, *Surf. Sci.*, **65**, 511 (1977).
28. W. C. Mackrodt, in Ceramic Microstructures '86. Role of Interfaces, edited by J. A. Pask and A. G. Evans (Plenum Press, New York, 1987) p. 271; W. D. Kingery, *ibid.*, p. 281.
29. S. A. Dregia and P. Wynblatt, *Acta Metall. Mater.*, **39**, 771 (1991); P. Bachan, P. Wynblatt and S. M. Foiles, *ibid.*, p. 2681.
30. S. R. Nutt, in Aluminum Alloys- Contemporary Research and Applications, edited by A. K. Vasudevan and R. D. Doherty (Academic Press, Inc., San Diego, CA, 1989) p. 389.
31. M. G. Nicholas, in Proc. MRS Inter. Meeting on Adv. Mater. Vol. 8 - Metal-Ceramic Joints, edited by M. Doyama et al. (MRS, Pittsburgh, PA, 1989) p. 54.
32. G. Elsner, T. Suga and M. Turwitt, *J. de Physique*, **46**, C4-597 (1985).
33. J. T. Klomp, in Ceramic Microstructures '86. Role of Interfaces, edited by J. A. Pask and A. G. Evans (Plenum Press, New York, 1987) p. 307.

34. R. M. Crispin and M. G. Nicholas, *J. Mater. Sci.*, **11**, 17 (1976).
35. C. H. P. Lupis, Chemical Thermodynamics of Materials (North-Holland Publishing Company, Amsterdam, 1983).
36. J. T. Klomp, *Colloque de Physique*, **51**, C1-745 (1990).
37. R. Warren and C-H. Andersson, *Composites*, **15**, 101 (1984).
38. J. Y. Huh, Ph.D. Thesis, Carnegie Mellon University, 1993.
39. R. E. Tressler, T. L. Moore and R. L. Crane, *J. Mater. Sci.*, **8**, 151 (1973).
40. D. B. Gundel and F. E. Wawner, *Scripta Metall. Mater.*, **25**, 437 (1991).
41. M. Backhaus-Ricoult, *Acta Metall. Mater.*, **40**, S95 (1992).
42. A. G. Metcalfe, in Composite Materials, Vol. 4 - Metallic Matrix Composites, edited by K. G. Kreider (Academic Press, New York, 1974) p. 269.
43. C. Zener, *J. Appl. Phys.*, **20**, 950 (1949).
44. B. Darby: in Ceramic Microstructures '86, Role of Interfaces, edited by J. A. Pask and A. G. Evans (Plenum Press, New York, 1987) p. 319.
45. B. Gibbsch and G. Elssner, *Acta Metall. Mater.*, **40**, S89 (1992).
46. J. T. Klomp, *J. Mater. Sci.*, **15**, 2483 (1980).
47. S. Morozumi, M. Kikuchi and T. Nishino, *J. Mater. Sci.*, **16**, 2137 (1981).
48. A. Suzumura, T. Onzawa, S. K. Budhil, A. Ohmori and Y. Arata, in Proc. MRS Inter. Meeting on Adv. Mater. Vol. 8 - Metal-Ceramic Joints, edited by M. Doyama et al. (MRS, Pittsburgh, PA, 1989) p. 269; K. Miyazawa, S. Matsuoka, T. Fujii and T. Suga, *ibid.*, p. 275.
49. P. L. Ratnaparkhi and J. M. Howe, *Acta Metall. Mater.* (in press).
50. S. D. Peteves, P. Tambyser, P. Helbach, M. Audier, V. Laurent and D. Chatain, *J. Mater. Sci.*, **25**, 3765 (1990).
51. X. S. Ning, T. Okamoto, Y. Miyamoto, A. Koreeda and K. Suganuma, *J. Mater. Sci.*, **26**, 4142 (1991).
52. P. M. Scott, M. Nicholas and B. Dewar, *J. Mater. Sci.*, **10**, 1833 (1975).
53. K. Miura, T. Narita and T. Ishikawa, in Proc. MRS Inter. Meeting on Adv. Mater. Vol. 8 - Metal-Ceramic Joints, edited by M. Doyama et al. (MRS, Pittsburgh, PA, 1989) p. 29; S-I. Tanaka, *ibid.*, p. 91.
54. G. Ellsner, T. Suga and M. Turwitt, *J. de Physique*, **46**, C4-597 (1985).
55. T. Suga and G. Ellsner, *J. de Physique*, **46**, C4-657 (1985).
56. A. G. Evans and B. J. Dalgleish, *Acta Metall. Mater.*, **40**, S295 (1992).
57. R. M. Cannon, B. J. Dalgleish, R. H. Dauskardt, J. M. McNancy and R. O. Ritchie, *J. Amer. Cer. Soc.* (in press).
58. I. E. Reimanis, B. J. Dalgleish, M. Brahy, M. Ruhle and A. G. Evans, *Acta Metall. Mater.*, **38**, 2645 (1990).
59. I. E. Reimanis, B. J. Dalgleish and A. G. Evans, *Acta Metall. Mater.*, **39**, 3133 (1991).
60. T. S. Oh, J. Rodel, R. M. Cannon and R. O. Ritchie, *Acta Metall.*, **36**, 2083 (1988).
61. T. S. Oh, R. M. Cannon and R. O. Ritchie, in Proc. MRS Inter. Meeting on Adv. Mater. Vol. 8 - Metal-Ceramic Joints, edited by M. Doyama et al. (MRS, Pittsburgh, PA, 1989) p. 105.
62. A. G. Evans, B. J. Dalgleish, M. He and J. W. Hutchinson, *Acta Metall.*, **37**, 3249 (1989).
63. Z. Suo and J. W. Hutchinson, *Mater. Sci. Eng.*, **A107**, 135 (1989).
64. J. Rice, *J. Appl. Mech.*, **55**, 98 (1988).
65. J. Dundurs, *J. Appl. Phys.*, **36**, 650 (1969).
66. T. Suga and G. Ellsner, in Proc. MRS Inter. Meeting on Adv. Mater. Vol. 8 - Metal-Ceramic Joints, edited by M. Doyama et al. (MRS, Pittsburgh, PA, 1989) p. 99.
67. H. C. Cao, M. D. Thouless and A. G. Evans, *Acta Metall.*, **36**, 2037 (1988).
68. A. G. Evans, M. Ruhle and M. Turwitt, *J. de Physique*, **46**, C4-613 (1985).
69. A. G. Evans and S. M. Wiederhorn, *Inter. J. Fracture*, **10**, 379 (1974).
70. T. S. Oh, R. M. Cannon and R. O. Ritchie, *J. Amer. Cer. Soc.*, **70**, C352 (1987).
71. R. P. Wei, S. R. Novak and D. P. Williams, *Mater. Res. Stand.*, **12**, 25 (1972).
72. R. M. Cannon, B. J. Dalgleish, R. H. Dauskardt, T. S. Oh and R. O. Ritchie, *Acta Metall. Mater.*, **39**, 2145 (1991).

## DIFFUSION BONDING OF ADVANCED AEROSPACE METALLICS

DAVID V. DUNFORD AND ANDREW WISBEY

Materials and Structures Dept., Defence Research Agency, Farnborough, Hants. UK

### ABSTRACT

Advanced aluminium and titanium alloys, metal matrix composites (MMC's) and intermetallic compounds are of considerable interest to the aerospace industry. These materials offer significant mechanical improvements over many conventional materials. Appropriate joining technologies are being developed to utilise the advantages these materials offer in aerospace applications. Diffusion bonding offers considerable potential as a joining process. This keynote paper will review diffusion bonding with reference to these advanced metallic systems.

### INTRODUCTION

Considerable advances in metallic systems pertinent to the aerospace community have been made in recent decades. The goals of lighter and stiffer airframe structures have led to potential applications for lower density aluminium - lithium alloys and the rapid development of both continuous fibre and particulate reinforced metal matrix composite systems. Higher temperature and lower density metallic systems are being developed for gas turbine applications to improve thrust to weight ratios and engine efficiency. The development of improved manufacturing technologies, such as superplastic forming, has enabled complex structures to be fabricated from expensive materials cost effectively by maximising material utilisation. To preserve these improvements and allow successful incorporation into aerospace structures, advanced joining techniques are required. Conventional fusion welding may cause unacceptable microstructural damage and poor mechanical properties. Solid state joining can offer significant advantages for some advanced materials. Several solid state processes depend on high pressures and large scale deformation; for example pressure welding, roll bonding and explosive bonding for example. These processes are used to produce semi-finished products such as clad sheet or plate but are generally unsuitable for MMC's. In friction and ultrasonic welding, intense deformation confined to the bond interface region raises the temperature and disrupts and disperses the oxide films before welding. These processes are discussed in detail in reference 1.

In diffusion bonding (DB), through thickness deformation is usually small (5% or less), low pressures (much less than the macroscopic yield stress) and high temperatures ( $> 0.5 T_m$ , where  $T_m$  is the absolute melting point) are typical. Hence the deformation is confined primarily to surface asperities [2]. DB by hot isostatic pressing (HIP) under inert gas pressure has the unique advantages of high pressure (up to 300 MPa) and temperatures (up to 2000°C) with minimum total deformation giving greater flexibility in component shape. This process is used extensively for consolidating powders. Compared with other joining processes, diffusion bonding offers [3]:

- i) joint strengths approach or equal parent material strength
- ii) low deformation and distortion lead to accurate dimensional control
- iii) joints can be fabricated between thick and thin sections
- iv) large bond areas lead to lower service stresses
- v) corrosion resistance is the same as the base material or selected interlayer, with no fluxes required.
- vi) dissimilar materials, metastable alloys and MMC's may be joined

In this paper the mechanisms of diffusion bonding will be discussed together with the development of diffusion bonding processes for advanced metallics currently of interest to the aerospace industry.

## MECHANISMS

The various diffusion bonding techniques available are summarised in Fig. 1[4]. Diffusion bonding can take place either in the solid state or via a transient liquid phase (TLP). Stable surface films (present on aluminium alloys) or brittle intermetallic compounds (formed between dissimilar materials) can lead to low joint strengths. To permit DB of such materials, interface coatings or foils may be employed.

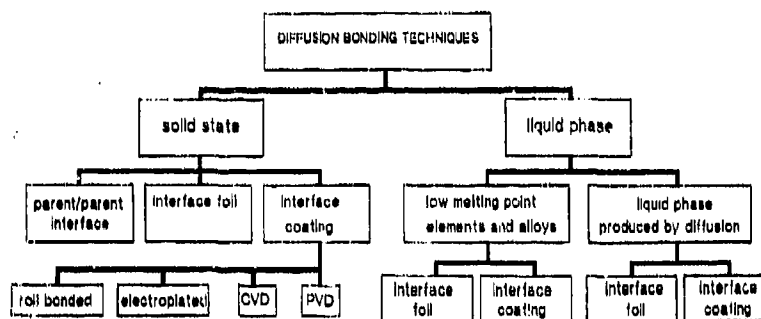


Figure 1. Summary of diffusion bonding techniques [4]

The solid state bonding process can be divided into two stages corresponding to a stress dependent stage 1 and stress independent stage 2. The sequential operative mechanisms in these stages are:

- |   |           |
|---|-----------|
| a) instantaneous plastic deformation on loading, associated with surface asperities | } Stage 1 |
| b) creep deformation  |           |
| c) diffusion across the bond interface  | } Stage 2 |
| d) recrystallisation and grain boundary migration                                   |           |

Modelling of stage 1 is based on the relationship;

$$\dot{\epsilon} = A \sigma^n \exp \left( -\frac{Q_c}{RT} \right) \quad \dots (1)$$

where  $\dot{\epsilon}$  = creep rate,  $\sigma$  = applied stress,  $Q_c$  = activation energy for diffusion,  $A$  and  $n$  are constants with  $n$  in the range 3-4 for a typical titanium alloy. For a fine grained superplastic alloy  $n$  is in the range 1.5 - 2, indicating a lower temperature stress dependence and strain hardening rate which aids bonding in stage 1. At the onset of stage 2 the bond interface consists of bonded areas and residual voids. Hydrostatic pressure can accelerate plastic deformation and the closure of large voids, but elimination of small voids ( $< 20 \mu\text{m}$ ) depends only on surface, volume, or grain boundary diffusion. Stage 2 is therefore diffusion controlled and is accelerated by a fine grain size and high temperature. Recrystallisation and grain boundary migration leading to a non-planar bond interface is desirable for maximum strength, but does not always occur. The time required is usually much greater for stage 2 than for stage 1. Diffusion bonding models based upon idealised surface geometries and the above mechanisms have been successful in predicting the effect of pressure on time to produce a 95% parent metal bond strength in both titanium and copper [5-8]. More complex models are required to explain bonding in the presence of oxide films and for dissimilar materials.

In diffusion bonding the major bonding parameters (pressure, temperature and time) are interdependent and control the deformation. These variables are optimised to reduce bonding time and therefore cost. In practice the maximum temperature is limited by the onset of liquation or excessive grain growth, and bonding pressure is limited by safety (gas pressure bonding), cost considerations, or excessive deformation (thick section and platen pressure bonding).

When the temperature or pressure required to obtain good surface contact prohibits solid state DB, liquid phase (LP) DB offers an alternative joining method. This process relies on interlayers or coatings at the bond interface. These either melt, or diffuse into the base metal to create a transient liquid phase (TLP), at a temperature well below the melting point of the base metal. This process has some advantages of conventional brazing (low pressures, short times) and of diffusion bonding (base metal microstructure and strength).

### DB TECHNIQUES

Diffusion bonds in components can be divided into those made by massive DB and those made between thin sheet; DB in thin sheet is frequently associated with subsequent superplastic forming (SPF) [9]. DB of thin sheet prior to SPF is often performed using argon gas pressure (2-3.5 MPa (300-500 psi)) for Ti alloys, but similar platen pressures may also be used. Massive DB involves the joining of thick section machined parts under higher pressure (e.g. 14 MPa, 2000 psi) applied by mechanical means or by hot isostatic pressing (HIPing). For HIPing the component is sealed in an evacuated can before the pressure is applied. After DB the can is removed, unless it is an integral part of the component.

### DB TEST METHODS

For successful exploitation of DB in structural component design strength data (eg. tensile, shear, impact, fatigue) have to be obtained. Strengths reported for DB joints can show a wide variation depending on bonding parameters, bonding techniques and test piece design. The latter being particularly important since the test piece must provide meaningful strength data to enable the effects of metallurgical and processing variables on bond strength to be assessed. To measure the strength of a diffusion bond it is essential that failure occurs in the bond interfacial region. Failure in the base metal away from the bond interface may provide information on joint design, but does not help in the evaluation of the bonding process. Tensile tests are used for thick section diffusion bonds, but have been shown to be insensitive to the presence of voids in the bond interface [10]. However, impact tests appear particularly sensitive to bond quality [10]. For thin sheet, shear tests are used. Unfortunately, these test pieces experience large out of plane bending or peel stresses, with large stress concentrations at the ends of the joint [11]. Constrained tensile [11] and compressive [12] shear tests have been developed to prevent out of plane bending. Peel tests have also been used, particularly at elevated temperatures for aluminium alloys [13], to assess the quality of DB in thin sheet regarding potential DB/SPF processing. Corrosion and oxidation studies on DB joints may also be required.

### TITANIUM ALLOYS

Titanium absorbs its own surface oxide film above about 750°C and alloys are readily bonded in vacuum or inert gas. Figure 2 shows the microstructure of a DB joint in the high temperature Ti alloy IMI 834. The mechanical properties of DB joints in IMI 834 (Table 1)[12] show that parent metal tensile, shear and impact strengths are attainable even in this creep resistant alloy. As the  $\beta$ -transus temperature for titanium is approached, rapid grain growth occurs, the creep rate decreases and the bonding time may increase. For example in Ti-6Al-4V alloy, at a typical bonding pressure for this alloy (300 psi, 2 MPa), the time to produce a pore free bond increased six fold when the grain size increased from 6.4  $\mu$ m to 20  $\mu$ m [9]. Other product forms, such as plate or forgings, have a coarser grain size when compared to sheet, consequently different bonding parameters are required. The enhanced bonding associated with fine grain materials can be exploited using fine grain interlayer foil(s) for bonding thick sections of coarser microstructure, or by surface working, which induces



Figure 2. Diffusion bond in IMI 834, 990°C (0.5 hour) 5 MPa. Bond line at arrows.

Table I. The tensile, shear and impact properties of IMI 834 and DB joints produced under various conditions [12]

Material condition/Bonding parameters	Bulk Defm. %	Tensile Properties			Shear Strength MPa	Impact Energy J
		0.2% PS MPa	UTS MPa	Elong. %		
1. As received	0	946	1083	14.3	-	4.2
2. Thermal cycle 990°C 0.5 hr	0	870	1029	16	663	5.4
3. DB 950°C (0.5 hr) 5MPa	0.2	928	1022	2.3	284-438	2.2
4. DB 990°C (0.5 hr) 5MPa	1.0	884	1039	17.1	675	4.9
5. DB as 3. + 1020°C (6 hr) + 700°C (2 hr).	0.2	913	1032	16.5		4.5

fine recrystallised grains at the bond interface when heated to the DB temperature. Accelerated bonding is also achieved under superplastic conditions, reducing the bonding pressure by a factor of 4, welding time by a factor 6-30 and the temperature required by 50-150°C [14]. Crystallographic texture and microstructure morphology may also affect the rate of bond formation [15]. For example, an acicular microstructure requires longer bonding times or higher pressures than an equiaxed microstructure.

Small bond defects may not affect the tensile or shear strength of the bond but may greatly affect other mechanical properties such as fatigue or impact strength. Impact properties are most sensitive to bond quality. Fine pores, as small as 1µm, can reduce the

impact strength. The distribution of pores is known to affect both impact and fatigue properties, for example clusters of pores reduce fatigue properties [16].

For near net shape components, low bulk deformation during DB is required. Joints may be made at low temperatures and for short times (eg 800°C, 15 minutes and 5 MPa for Ti-6Al-4V) to produce a partially bonded interface with high porosity and then annealed at temperatures just below the  $\beta$  transus for extended times. Voids are eliminated and parent metal tensile strength and increased impact values obtained (Table II)[12].

Table II. Mechanical properties of DB joints in Ti - 6Al - 4V. (ND - none detected)

Bonding Conditions	Bulk defn. %	Condition	UTS (MPa)	Elong %	Impact strength J	Void density %
850°C, 5MPa, 0.25h	0.43	As bonded	791	0	0	7-17
		After 24hrs at 950°C	950	19	17	ND

Liquid phase DB of Ti alloys using Cu, Cu base and other alloy interlayers can produce almost parent metal mechanical properties. A  $\beta$  titanium alloy, Ti-21V-4Al, bonded with a Ti-20Zr-20Cu-20Ni interlayer had a tensile strength of ~700 MPa. Subsequent ageing increased this to 1400 MPa [17].

Diffusion bonding of Ti alloy sheet can be conveniently combined with superplastic forming (SPF) to produce structures with significant cost and weight savings compared to conventional manufacturing routes. Complex three and four sheet structures may be made using stop-off compounds to prevent bonding in predetermined areas and, after bonding, formed into shaped dies to produce honeycomb type structures (Fig 3) [18]. Some bonds may also be made after SPF, giving great flexibility to this manufacturing route. However, surfaces for DB after SPF are exposed to the gaseous environment longer than the primary bonds with a greater risk of surface contamination; oxygen and water must therefore be removed from the argon pressurising gas. Several thousand Ti alloy DB/SPF components are in service, for example wing access panels on Airbus aircraft [19] and other civil and military applications [20]. A critical DB/SPF component is the fan blade for civil gas turbine engines [21].

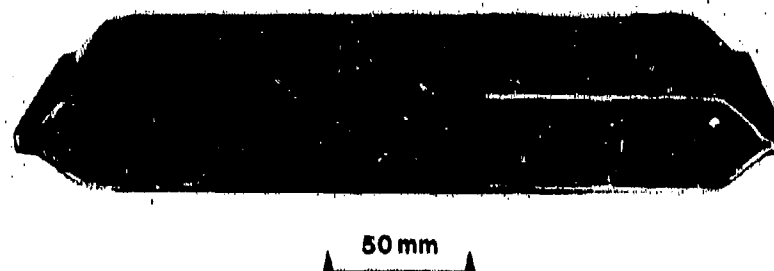


Figure 3. Four sheet diffusion bonded / superplastically formed Ti - 6Al - 4V structure, showing diffusion bonded joints between skin and core sheet at A, and between core sheets at B. (Courtesy of British Aerospace Warton).



Ordered intermetallic Ti alloys for use at temperatures above those for conventional Ti alloys ( $> 600^{\circ}\text{C}$ ) are of particular interest currently. There is little quantitative published data available, but the  $\text{Ti}_3\text{Al}$  based alloys seem to diffusion bond readily at temperatures of  $100\text{--}150^{\circ}\text{C}$  below the alloy  $\beta$  transus ( $1065\text{--}1130^{\circ}\text{C}$ ) to give parent metal microstructures [22]. It is expected that parent metal mechanical properties should be obtained. Higher pressures, compared to Ti alloys, are required for DB of titanium aluminides due to the higher flow stresses of these intermetallics. DB of the  $\text{TiAl}$  based alloys is more difficult than the  $\text{Ti}_3\text{Al}$  based alloys since aluminium modified titanium oxides are formed and these may restrict grain boundary migration at the bond interface. Bonds in a  $\text{TiAl}$  alloy with a planar interface had a tensile strength of  $\sim 40$  MPa less than the parent metal at  $800^{\circ}\text{C}$  and  $1000^{\circ}\text{C}$  test temperatures. Plastic deformation of the surface before bonding can cause recrystallisation at the bond interface and enhance bond strength [23].

### ALUMINIUM ALLOYS

The diffusion bonding of aluminium alloys is primarily under consideration for sheet applications, especially with the development of superplastic aluminium alloys. Massive DB of aluminium alloys, as used with titanium alloys, is virtually unknown. Aluminium alloys, unlike titanium alloys, are difficult to diffusion bond because of their stable oxide film. This alumina rich film even forms in inert gas atmospheres or in vacuum and can be stable up to the alloy melting point. At bonding temperatures this film is a barrier to the diffusion of solute elements. Removal or disruption of surface oxide films is necessary for successful bonding. Fracture and dispersion of the oxide, as occurs during roll bonding, is precluded at low deformations. High strength diffusion bonded joints have been obtained using surface coatings or interlayers. For example, after argon ion sputter cleaning and ion plating with  $1\text{ }\mu\text{m}$  thick silver layers, clad aluminium alloys have been diffusion bonded in the solid state at temperatures of  $300\text{--}450^{\circ}\text{C}$  [24]. The reduced concentration of silver within the clad layer during subsequent diffusion, prevented the formation of silver rich intermetallics. This bonding route may be also suitable for rapidly quenched metastable alloys where low bonding temperatures ( $< 350^{\circ}\text{C}$ ) are required; for example, continuous SiC fibres coated with an Al-Cr-Fe metastable alloy matrix have been consolidated to form an MMC via a surface coating of silver [25]. Transient liquid phase bonds have been made using zinc and copper interlayers to form a eutectic phase at  $420^{\circ}\text{C}$  and  $548^{\circ}\text{C}$ , respectively. The solubility of these elements in aluminium at the bonding temperature allows interlayer element concentrations at the bond interface to be reduced to low values ( $< 2\text{ wt}\%$ ) by a post bond anneal.

Superplastic Al-Zn-Mg 7475E alloy has been bonded successfully in the solid state at  $500^{\circ}\text{C}$  and  $2.76\text{ MPa}$  using 5052 Al-Mg alloy as an interlayer [26]. Bond shear strength was found to improve with increased deformation from 3 to 15% and increased bonding times of 60 minutes. Studies without interlayers at bonding temperatures of  $516^{\circ}\text{C}$  for 4 hours using  $0.7\text{ MPa}$  pressure gave parent metal shear strengths ( $331\text{ MPa}$ ) [27]. This was due to recrystallisation at the bond interface (induced by prior surface peening) leading to a non-planar interface.

Diffusion bonding of aluminium-lithium alloys has been reviewed [28] and is particularly attractive because these alloys combine high specific stiffness and strength with superplastic behaviour. Aluminium-lithium alloys may be bonded without interlayers since lithium compounds disrupt the surface oxide. However, because of the more rapid thermal oxidation of these alloys, particular care is required to avoid surface contamination during heating to the bonding temperature. A DB joint made in vacuum without interlayers is shown in Fig. 4. This joint exhibited parent metal compressive shear strength in the T6 condition ( $\sim 230\text{ MPa}$ ) and a  $90^{\circ}$  room temperature peel strength of  $54\text{ Nmm}^{-1}$  (peak) and  $18\text{ Nmm}^{-1}$  (plateau); this can be compared with corresponding strength values for adhesive joints of  $30\text{--}40\text{ MPa}$  (shear) and  $8\text{ Nmm}^{-1}$  (peel). Careful control of solid state bonding parameters is required for joint reproducibility and consequently TLP DB may be attractive. Studies using Cu, Zn or complex multilayer systems utilising Al-Cu-Si as the melting phase, have reported strengths approaching those of the base metal [28,29]. A TLP bond in 8090 Al-Li alloy is shown in Fig. 5. Care must be taken to ensure that the interlayer can be diffused away from the bond interface. For both solid state and TLP diffusion bonds joint stiffening gave peel strengths



Figure 4 Section (optical) through solid state diffusion bond in Al - Li 8090 alloy. Bond interface is at A - A.

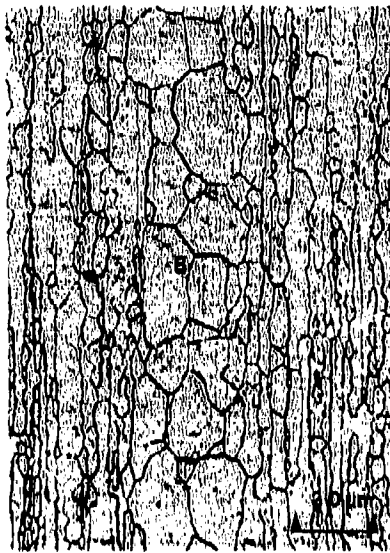


Figure 5. Section (optical) through TLP diffusion bond in Al - Li 8090 alloy. Bond interface in coarse grained region B.

at superplastic forming temperatures sufficient to allow combined DB and SPF [30].

In comparison with titanium alloys DB of aluminium requires procedures of greater complexity and any process deviation can lead to poor reproducibility of joint quality. The potential advantages for weight saving and structural efficiency when combined with SPF are however very attractive.

#### DISSIMILAR MATERIALS

The need to combine high strength with high toughness, to provide surfaces with corrosion, wear or oxidation resistance and to conserve expensive materials, has led to growing interest in dissimilar material joints. Diffusion bonding is particularly suited for such joints because it provides close control of the process variables. Metal/metal, metal/ceramic or ceramic/ceramic joints are possible via DB. It is difficult to obtain sufficient interface contact or diffusion for ceramic/ceramic bonding below about 1000°C. However many ceramics can now be bonded either to themselves or to thicker metallic supports using reactive metal interlayers (containing Mg, Li, Zr or Ti) and either solid state or liquid phase techniques [31]. Mismatch of thermal expansion coefficients (CTE), which can give rise to high thermal stresses and cracking at the bond interface. This problem is particularly pronounced for ceramic/metal joints. To overcome this mismatch an interlayer, or combination of interlayers, may be used to decrease the stress gradient across the interface. The laminated interfaces may be several millimetres thick.

In dissimilar metal joints the greater stress relaxation available means that thermal stresses due to CTE mismatch may be less severe than in metal/ceramic joints. Care must be taken to ensure chemical compatibility and minimum adverse reactions between the materials to maximise joint strength. The mechanical properties are particularly important, since dissimilar metal joints may be heavily loaded. The interlayers should ideally exhibit mutual solid solubility without intermetallic formation, a wide temperature range for bonding and

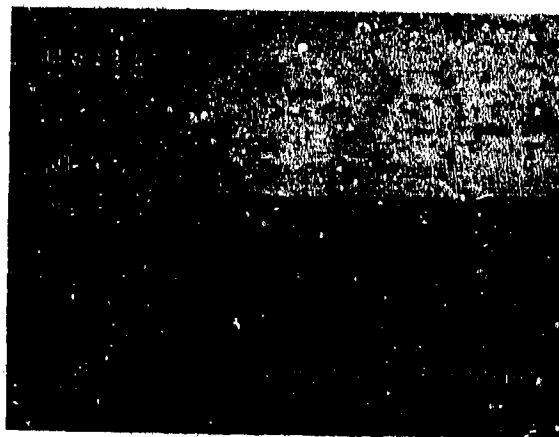


Figure 6 Section (optical) through a  $Ti_3Al$  (Super  $\alpha_2$ ) - nickel alloy (HS 242) DB joint, using tantalum and nickel interlayers to aid bonding.

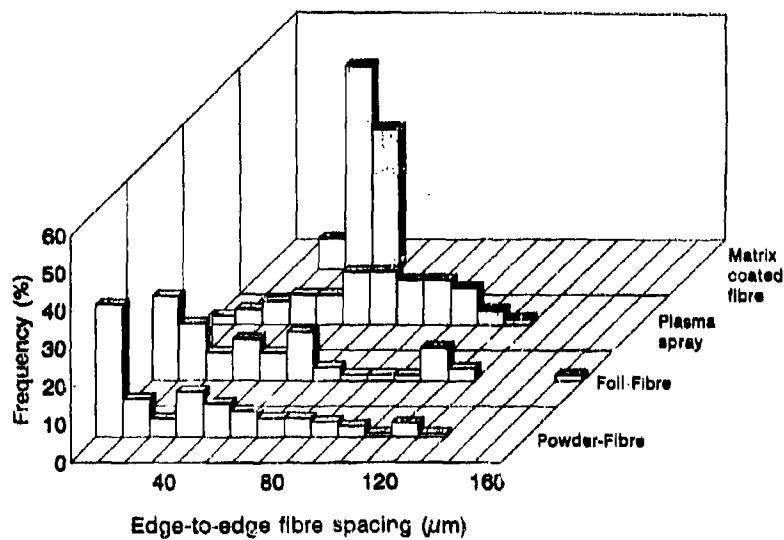


Figure 7 Frequency v. magnitude of edge-to-edge inter-SiC fibre spacing for composites made by different routes.

compatible CTE and Young's modulus. An example of this type of joint is shown in Fig. 6. The  $Ti_3Al$  alloy (Super  $\alpha_2$ ) has been diffusion bonded to the wear resistant Ni base HS 242 alloy using 25  $\mu m$  thick Ta and Ni interlayers. This joint had a compressive shear strength of ~480 MPa (compared to ~390 MPa without interlayers) despite the formation of a  $Ni_3Ta$  inter-metallic. Joints between Ti-6Al-4V alloy and Co-based Stellite HS6 using similar interlayers had tensile strengths of ~800 MPa, compared to ~600 MPa without interlayers. Ductile interlayers may also enhance the toughness of joint interfaces. Many alloy combinations have been joined by diffusion bonding, for example; titanium alloys to stainless steels and Ni alloys, and steels to Co base alloys [3].

Different alloys of the same base element may be diffusion bonded, for example a high temperature Ti alloy IMI 834 has been diffusion bonded to a  $Ti_3Al$  alloy. This is a relatively straightforward procedure for titanium alloys and steels using DB parameters for the lower temperature alloy of the couple. Future developments may exploit the potential of bulk macro and micro-laminates produced by the bonding of stacked sheets or foils of dissimilar materials.

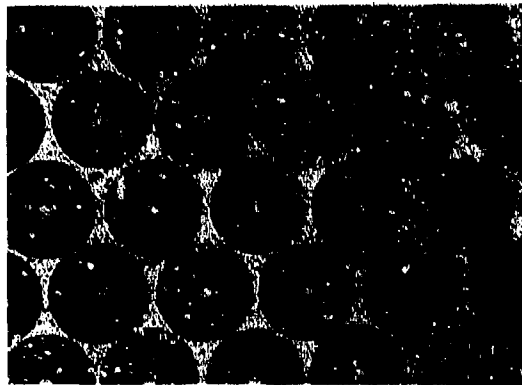


Figure 8 Ti - 6Al - 4V / 80 vol. % SiC fibre composite made by MCF process [25].

## METAL MATRIX COMPOSITES

Advanced continuous fibre or particulate reinforced metal matrix composites can lead to increased strength and stiffness at ambient and elevated temperatures. Aluminium MMC's can be made by melt infiltration but reactive metals are restricted to solid state processing. Diffusion bonding has an important role in both solid state processing and joining.

Processing of continuous fibre materials is extremely important since any fibre/fibre contact can drastically reduce the mechanical properties [32]. This is especially true for large diameter fibres (eg. ~100  $\mu m$  SiC). Commercial processing routes for titanium based MMC's have been reviewed [33]. All of the processing routes require DB to affect final consolidation. DB has been carried out using conditions similar to those for bulk titanium alloys. The most widely used method is the foil-fibre (F-F) lay-up in which unidirectional mats of SiC fibre are sandwiched between foils of the required alloy. Titanium alloy and Ti aluminide MMC's are currently being produced. Many matrix systems are precluded by the

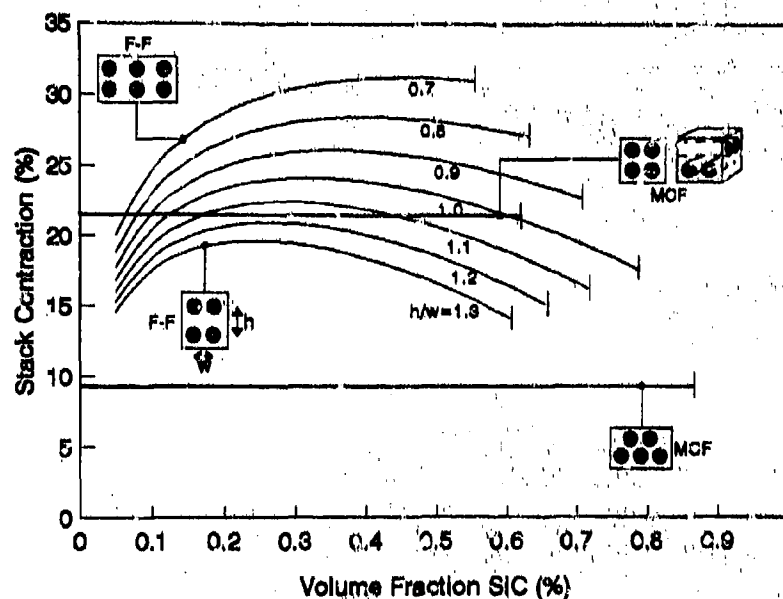


Figure 9 Vertical contraction normal to fibre axes during composite consolidation of sheet when no displacement allowed in sheet plane v. SiC volume fraction. MCF = metal coated fibre, F-F = foil - fibre. The effect of fibre spacing ( $w$ ) and foil thickness ( $h$ ) on contraction in F - F composite are also shown.



Figure 10 Section (optical) through a solid state diffusion bond between 8090 / 20 wt% SiC particulate reinforced metal matrix composite (MMC) sheet. Bond interface at A - A, particle / particle contact at B.

unavailability of alloy foils. During consolidation, fibres move giving non uniform fibre distribution in the finished composite (Fig. 7). Similar problems with uniform fibre distribution occur for the powder-fibre process, in which the foil is replaced by a cloth like material, produced by rolling a mixture of the alloy powder and an organic binder. For both processes the maximum practical fibre content is about 45% by volume. Plasma spraying has been used to introduce the matrix material onto the fibres. Although a more uniform fibre distribution is achieved (when compared to the F-F process), the fibres or their thin protective coatings may be damaged by impact of the plasma spray droplets. The matrix coated fibre (MCF) route involves coating the fibre with the matrix alloy using physical vapour deposition (PVD) processes such as evaporation or sputtering. A composite made by DB of MCF is shown in Fig. 8. SiC fibres were pre-coated by electron beam evaporation and vapour deposition (EBEVD). Composites produced by the MCF route have uniform fibre distribution (Fig. 7, 8) with no fibre-fibre contact. Numerous alloy systems, including metastable alloys, can be used as the matrix and fibre volume fraction is controlled by varying the coating thickness. Fibre volume fractions as high as 80% have been reported (Fig. 8) [25]. Another advantage of the MCF process, when compared to the F-F process, is that shrinkage during consolidation is independent of volume fraction and can be predicted, depending only on fibre packing/lay-up (Fig. 9). This is particularly important where near net shape processing to final component size is required. DB, either solid state or liquid phase may also prove to be the best means of incorporating titanium MMC components into structures.

Joining MMC's, particularly for elevated temperature applications, to preserve advantageous mechanical properties will require DB. For example solid state and TLP DB processes have been used for particulate reinforced aluminium MMC's [34]. Higher bond strengths were obtained when particle/particle contact (B in Fig. 10) at the bond interface was avoided, either by the insertion of an interlayer (solid state) to create particle-matrix interfaces and provide a ductile interlayer, or by TLP melting at the bond interface.

## CONCLUSIONS

The selection of appropriate joining processes depend on the materials, the joint, strength and quality requirements, and cost. For demanding applications, or advanced materials, diffusion bonding offers many advantages and may be the only option for MMC's. Increased application of DB/SPF technology will depend upon accurate and reproducible process control and the greater availability of large vacuum hot presses and HIP pressure vessels for manufacturing large components. This is particularly important if DB is to be considered for mass production applications, eg. in the automotive industry.

## ACKNOWLEDGEMENTS

The authors wish to acknowledge the support of their colleagues within Materials and Structures Department, especially Prof. Peter Partridge and Dr. Malcolm Ward-Close. The authors are grateful for the support of MOD.

(C) British Crown Copyright 1993 - published under license

## REFERENCES

1. M.M.Schwartz, *Metals Joining Manual*, (McGraw-Hill Publishers, 1979).
2. M.M.Schwartz in *Welding Technology for the Aerospace Industry*, (Amer.Weld.Soc., 1981) pp. 1 - 40.
3. P.G.Partridge in *Superplasticity*, (AGARD lecture series no.168, 1989) pp 5.1 - 5.29.
4. P.G.Partridge and C.M.Ward-Close, *Metals and Materials*, 5 (6), 334 - 339 (1989).
5. A.Hill and E.R.Wallach, *Acta Metall.*, 37 (9), 2425 (1989).
6. J.Pilling, D.W.Livesey, J.B.Hawkyard and N.Ridley, *Met. Sci.*, 18 (3), 117 - 122 (1984).
7. Z.X.Guo and N.Ridley, *Mater. Sci. & Technol.*, 3 (11), 945 - 953 (1987).
8. Y.Takahashi and K.Nishiguchi, *Welding World*, 27 (3-4), 100 (1989).

9. J.R. Williamson in Welding Technology for the Aerospace Industry, (Amer. Weld. Soc., 1981) pp. 55 - 83.
10. T.S. Baker and P.G. Partridge in Diffusion Bonding, edited by R. Pearce (SIS, (Cranfield, UK) Publishers, 1987) pp 73 - 90.
11. P.G. Partridge and D.V. Dunford, *J. Mater. Sci.*, **22**, 1597 - 1608 (1987).
12. A. Wisbey and P.G. Partridge, *Mater. Sci. & Technol.*, **9** (3), (in press) (1993).
13. D.V. Dunford and P.G. Partridge, *J. Mater. Sci.*, **27**, 5769 - 5776 (1992).
14. M.Kh. Shorshorov et al., *Svar. Proiz.*, **10**, 20 - 22 (1975).
15. E.S. Karakozov, A.P. Ternovskii and B.A. Lavrov, *Svar. Proiz.*, **7**, 29 - 31 (1983).
16. A. Gunderson, H.L. Gegel, S.R. Lyon in Titanium Science and Technology, edited by R.I. Jaffe and H.M. Burte (Plenum Press Publishers, 1973) pp. 649 - 664.
17. T. Onzawa, A. Suzumura and M.W. Ko, *J. Jpn. Weld. Soc.*, **7** (4), 38 - 45 (1989).
18. D. Stephen in Designing with Titanium, (Institute of Metals (London) Publishers, 1986) pp. 108 - 124.
19. M.H. Mansbridge in Advanced Materials: Looking ahead to the 21st Century, (proc. 22nd Int. SAMPE Tech. Conf., Boston, 1990) pp. 224 - 236.
20. H.E. Freidrich, R. Furlan, M. Kullick in Superplasticity and Superplastic Forming, edited by C.H. Hamilton and N.E. Paton (TMS Publishers, 1988) pp 649 - 664.
21. Rolls Royce plc (private communication).
22. N. Ridley, D.W. Livesey and M.T. Salehi, High Temperature Intermetallics, (Institute of Metals (London) Publishers, 1991) pp. 198 - 200.
23. Y. Nakao, K. Shinozaki and M. Hamada, *ISIJ International*, **31** (10), 1260 - 1266 (1991).
24. J. Harvey, P.G. Partridge and A. Lurshay, *Mater. Sci. Eng.*, **79**, 151 (1986).
25. C.M. Ward-Close and P.G. Partridge, *J. Mater. Sci.*, **23**, 4315 - 4323 (1990).
26. T.D. Byun and R.B. Vastava in Welding, Bonding & Fastening, (NASA Conf. Pub. 2387, 1985) 231.
27. J. Kennedy in Superplasticity and Superplastic Forming, edited by C.H. Hamilton and N.E. Paton (TMS Publishers, 1988) pp 523 - 528.
28. D.V. Dunford and P.G. Partridge, *Mater. Sci. & Tech.*, **8** (5), 385 - 398 (1992).
29. P.-J. Winkler, T. Heinrich, R. Keyte, G. Mahon and R.A. Ricks in Aluminium - Lithium, edited by M. Peters and P.-J. Winkler (DGM (Germany) Publishers, 1992) pp. 1069 - 1074.
30. D.V. Dunford and P.G. Partridge, *Mater. Sci. & Tech.*, **8** (12), 1131 - 1140 (1992).
31. C.M. Akselsen, *J. Mater. Sci.*, **27**, 569 - 579 (1992).
32. P.K. Brindley, S.L. Draper, M.V. Nathal and J.I. Eidridge in Fundamental relationships between microstructures and mechanical properties of metal - matrix composites, edited by P.K. Liaw and M.N. Gungor (TMS Publishers, 1990) pp. 387 - 401.
33. P.G. Partridge and C.M. Ward-Close, *Int. Mater. Rev.*, **38** (1), 1 - 24 (1993).
34. P.G. Partridge and D.V. Dunford, *J. Mater. Sci.*, **26**, 2255 - 2258 (1991).

## RELIABILITY FACTORS IN CERAMIC/METAL JOINING

KATSUAKI SUGANUMA

National Defense Academy, Department of Materials Science and Engineering,  
Hashirimizu 1-10-20, Yokosuka 239, Japan.

### ABSTRACT

This paper reviews the processing factors in joining ceramics to metals concerning the reliability. Thermal expansion mismatch has a great influence not only on the absolute value of strength but also on the reliability of joints. Large thermal stress increases the scatter of joint strength because of the presence of defects induced during joining process. One should insert an appropriate interlayer to relax the stress between a ceramic and a metal. Surface roughness also has some influence on the reliability. A roughly ground bond face leads large scatter in strength. Scratches must be removed before joining. Unjoined area reduces joint strength especially in solid-state joining. In brazing, the homogeneity in the braze layer should be also controlled carefully. A slight applied pressure during brazing can preserve the integrity of joints.

### INTRODUCTION

Ceramics have been gradually expanding their applications into structural materials replacing the conventional metallic materials since the beginning of the 1980's. In fact, one can find several establishments using ceramic parts in the commercial fields as shown in Fig.1. Silicon ceramics, especially  $\text{Si}_3\text{N}_4$ , have been intensively examined and developed for the structural uses because of its high toughness in addition to light weight character, good wear resistance, high strength and modulus up to 1000 °C, etc. The establishment of ceramics as structural materials has been not only dependent on the improvement of their properties but also greatly on the advances in joining technology of ceramics to metallic materials. Even though properties of ceramics have been improved drastically, they still have problems of hard workability and of poor reliability compared with metallic materials. Inevitably, they are used in a small volume combined with metallic parts. Then, in practical adoption of ceramic products, it frequently becomes one of the major interests whether the reliability of a joint structure is adequate for a certain requirement or not.

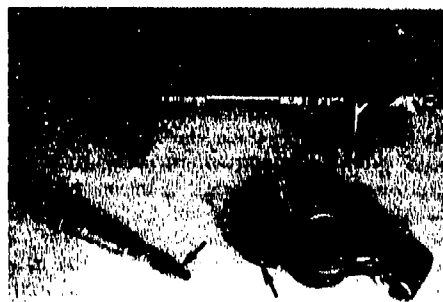


Fig.1  $\text{Si}_3\text{N}_4$  products for automobile engine components (Courtesy to Nissan Motor, Co.Ltd.). The arrows point to  $\text{Si}_3\text{N}_4$ .

The reliability of a ceramic/metal joint structure has not been surveyed consistently yet. Because most ceramic/metal joints fracture in a quite brittle manner, the scatter in strength can be treated by the Weibull statistics. The statistical treatment of strength data has provided us useful information on joining parameters. Factors influencing the reliability of a joint can be classified into several categories. Fig.2 shows the schematic illustration of several important defect categories, which may



cause scatter in strength directly. From the microscopic view, the reaction structure caused by wetting or by chemical and physical bond-ability between two faces may be of concern. These factors will reflect the distribution of unjoined or weakly bonded island-like defects on interfaces resulting in substantial reduction in joint strength. From the more macroscopic view, when a reaction layer grows thick, cracking in the layer frequently influences joint strength to a great extent. Thermal or residual stress in a joint becomes another important factor. The final goal for joining research will be in establishing a technique producing a tightly bound interface by eliminating these defects and by accommodating thermal stress.

The present paper concentrates on reviewing the factors affecting the structural integrity of a ceramic/metal joint. Especially, processing parameters influencing structural reliability will be discussed. Processing parameters such as interface reaction will be considered initially. Next is the physical contact and the surface damage effect. Then the effect of thermal stress on strength will be discussed in the last section.

### INTERFACE CHEMISTRY

Interface formation of a ceramic/metal system has been discussed for many decades on the basis of reaction chemistry<sup>1</sup>. Interface characterization has been carried out with various microstructural observation methods and, especially, with the wetting experiment with the assist of thermodynamic considerations. Successful results have been achieved from such semi-empirical works. The active metal brazing method is one of the fruitful establishments. In a recent few years, the research has also directed towards the lattice structure<sup>2</sup> and the atomic binding at the dissimilar materials interfaces<sup>3</sup>. These works are, however, still at the beginning and more time will be required to obtain the comprehensive explanation of ceramic/metal interfaces.

Turning our interests to the influence of interface chemistry on the reliability of a joint, fewer works have been reported on this subject. There seems to be some close relation between interface chemistry and scatter in strength. The points are not on the absolute strength of an interface but on the homogeneity of interface bonding. If homogeneous bonding is achieved over the whole interface, the scatter in strength is expected to be small even though the binding at an atomic scale is weak. Then, from the view point of the scatter in strength, one should think about the homogeneity of interface bonding and this is influenced by reaction and wetting behavior.

In the metal/metal brazing systems, it is easy to get homogeneous wetting between

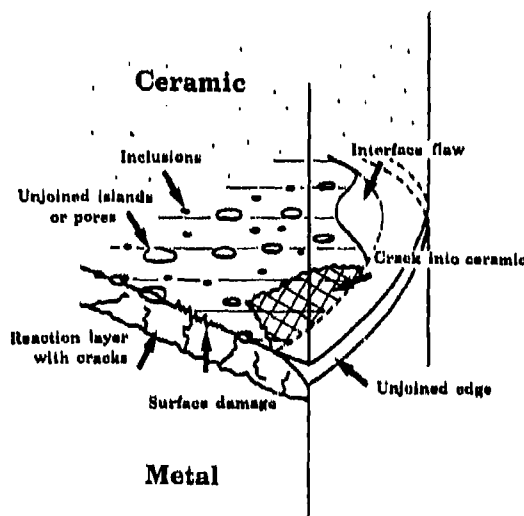


Fig.2 Schematic illustration of various defect structures in ceramic/metal joint.

metal substrates and brazing metals such as the Cu/solder system. In the ceramic/metal brazing systems, it is also possible to obtain similar wetting behavior by using the active metal brazees for most ceramics. There are, however, some exceptional brazing systems. The Al based alloys are regarded as one of the active metals since Al itself is quite active against most ceramics. These alloys are useful to braze ceramics/metals in lower temperature range than Ag-Cu-Ti alloys.

Fig.3 shows Weibull plots of the  $\text{Si}_3\text{N}_4$  joints brazed with pure Al and Al-X (X=Si, Mg) binary dilute alloys<sup>4</sup>. The scatter in strength of the  $\text{Si}_3\text{N}_4/\text{Al}/\text{Si}_3\text{N}_4$  joint is small and the addition of small amount of Si does not influence it so much. However, a similar amount of Mg addition to the braze made the scatter very large. These changes in strength are closely related to the change in fracture mode. Fig.4 shows the Weibull modulus of joint strength for various brazing alloys as a function of the fraction of an interface fracture area against the whole interface area. As the fraction of interface fracture area increases, the Weibull modulus decreases. The addition of Mg increases interface fracture. From TEM observation, it was revealed that the Mg addition changed the interface microstructure. Fig.5 shows a schematic illustration of the  $\text{Si}_3\text{N}_4/\text{Al}$  alloy interface and the fracture path. When Mg was not in the braze alloy, a nanocrystalline  $\beta$ -sialon layer and an Al-Si-O amorphous layer were formed at the interface. In the case of the  $\text{Si}_3\text{N}_4/\text{Al-Mg}$  interface, Mg concentrated at the interface and oxide products, i.e.,  $\alpha\text{-Al}_2\text{O}_3$  and  $\gamma\text{-Al}_2\text{O}_3$  with Si, were discretely formed along the interface. The fracture path primarily runs along the oxide layer. Thus, the addition of a small amount of Mg to the Al braze promotes the oxidation of Al and the oxide layer at the interface grows thick. This microstructural change increases the scatter in strength of the joint drastically. The reason for the increased scatter in the presence of the stable thick oxide products can be ascribed primarily both to the weak bonding between the

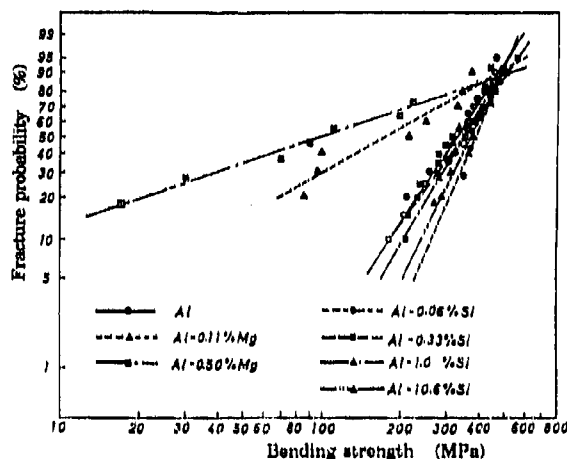


Fig.3 Weibull plots of bending strengths of  $\text{Si}_3\text{N}_4/\text{Al-X}$  (X=Si, Mg)/ $\text{Si}_3\text{N}_4$  joints<sup>4</sup>.

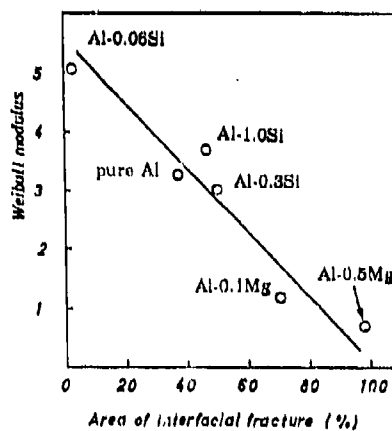


Fig.4 Weibull moduli of  $\text{Si}_3\text{N}_4$  joints brazed with various Al alloys as a function of fraction of interface fracture<sup>4</sup>.

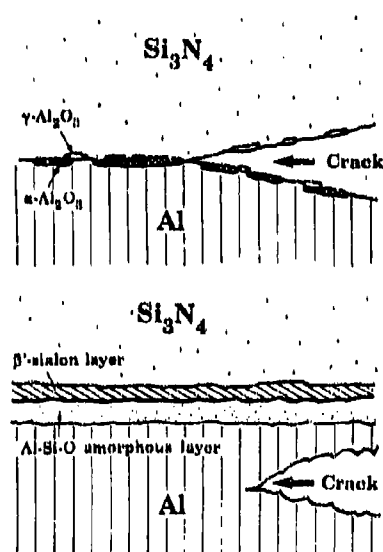


Fig. 5 Schematic illustrations of interface microstructure and fracture paths of  $\text{Si}_3\text{N}_4$  joints brazed with Al-Mg alloy (top) and with pure Al (bottom).

Al oxides and  $\text{Si}_3\text{N}_4/\text{Al}$  and the thermal expansion mismatch between  $\text{Si}_3\text{N}_4$  and the Al oxides which will be discussed later.

The presence of additives in ceramics may also influence the interface chemistry and then the reliability.  $\text{Si}_3\text{N}_4$  with or without the additives  $\text{Al}_2\text{O}_3$  and  $\text{Y}_2\text{O}_3$  were brazed with pure Al and the strengths of these joints were evaluated<sup>6</sup>. TEM observation revealed that the  $\text{Si}_3\text{N}_4$  with the additives formed a thick Al-Si-O layer reaching 1000 nm while that without any additive formed the layer 400 nm thick. Fig. 6 shows the Weibull plots of strength. The joint of  $\text{Si}_3\text{N}_4$  with the additive has higher strength and smaller scatter in strength than the joint without any additive. XFS analysis showed that fracture of the additive free  $\text{Si}_3\text{N}_4$  joint occurred at the Al/reaction layer interface while the joint with the additive fractured in the Al layer. These results imply that the thick Al-Si-O layer can cover the

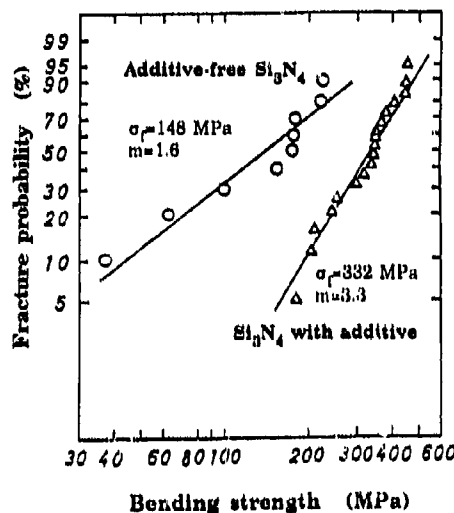


Fig. 6 Weibull plots of bending strength of  $\text{Si}_3\text{N}_4$  joints with or without additive brazed with  $\text{Al}^6$ .

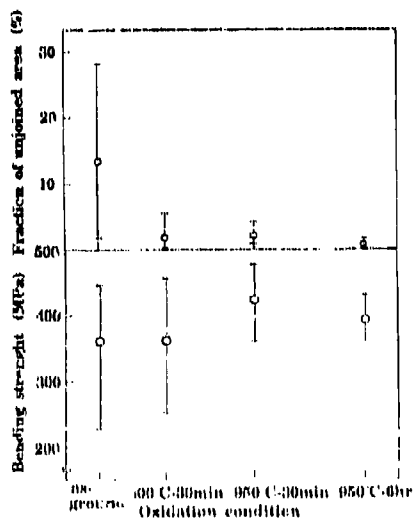


Fig. 7 Effect of pre-oxidation of  $\text{Si}_3\text{N}_4$  on the fraction of unjoined area formed on an interface of  $\text{Si}_3\text{N}_4$  joint brazed with  $\text{Al}^6$ .

interface between the substrate  $\text{Si}_3\text{N}_4$  and the Al braze layer much more uniformly than the thin formation of the layer. This microstructural difference seems to result in changing the scatter in strength between the two cases. A similar result has been obtained by a pre-oxidation-treatment of  $\text{Si}_3\text{N}_4$  before brazing<sup>8</sup>. The oxidized treatment of  $\text{Si}_3\text{N}_4$  promoted wetting between  $\text{Si}_3\text{N}_4$  and Al resulting in decreasing the unjoined area as shown in Fig.7. The oxidized interface had a thick Al-Si-O layer as one of the two reaction layers<sup>7</sup>.

It has been known that the ion mixing of a ceramic/metal interface can provide good interface adhesion<sup>6,9</sup>. Petevan reported the influence of ion beam mixing on scatter in strength of the Cr-coated  $\text{Si}_3\text{N}_4/\text{Ni-Cr}$  alloy joint<sup>9</sup>. By Xe ion irradiation on the Cr-coated surface, a two-fold improvement in Weibull modulus was achieved with the improvement of the absolute strength. Though a definite reason for the improvement in Weibull modulus has not been proposed yet, the improvement of the adhesion of Cr film to  $\text{Si}_3\text{N}_4$ , the chemistry change due to the enhanced diffusion, and the annealing out of some of the residual surface damage of  $\text{Si}_3\text{N}_4$  seem to be have some role.

#### PHYSICAL CONTACT AT INTERFACE

In the actual joining sequences, a perfect interface connection over the whole interface is hardly achieved within a certain joining period and temperature limited by the progress of interface reaction. Then the initial surface roughness and the applied pressure have two of the critical parameters which have great influence on achieving interfacial contact not only in solid-state bonding but also in brazing. In solid-state bonding, interfacial contact is promoted by plastic deformation in the early stage following by

creep deformation and diffusion in the later stage. Pressure primarily influences achieving contact by plastic deformation in the first stage. Unjoined islands are inevitably formed on the interface under a limited pressure. It will be dependent on the amplitude of pressure, period, temperature and various material's factors such as flow stress. Fig.8 shows the relationship between the fracture stress and the unjoined area of the solid-state bonded  $\text{Al}_2\text{O}_3/\text{Nb}$  joint<sup>10</sup>. Apparently, the increase in unjoined area decreases the strength of the specimen. Fig.9 shows the influence of the unjoined area on the scatter in strength, of which data were obtained by changing the roughness of the Nb bond face. The large fraction decreased the average joint strength but the Weibull modulus did not change. These facts imply that the joint fracture initiated from the same origin, i.e., the unjoined island on the interface. The importance of the contact pressure during joining on the scatter in strength has been reported by Gottalig, et al<sup>11</sup>. They showed that the high pressure joining promoted the substantial reduction of the scatter in strength.

If interface reaction releases gas as the reaction product, the pores filled with the gas may be left on the interface resulting in the inhibition of contact. The  $\text{Si}_3\text{N}_4/\text{Ni}$

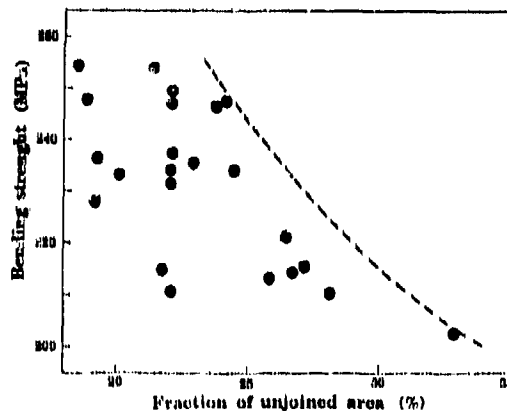


Fig.8 Bending strength of individual  $\text{Al}_2\text{O}_3/\text{Nb}$  joints as a function of unjoined area formed on interface<sup>10</sup>.

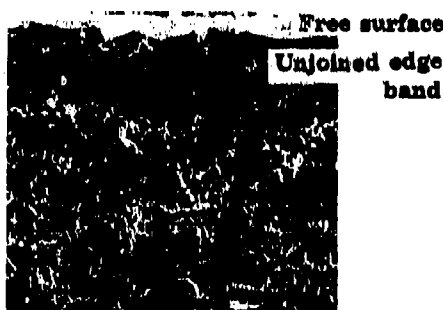
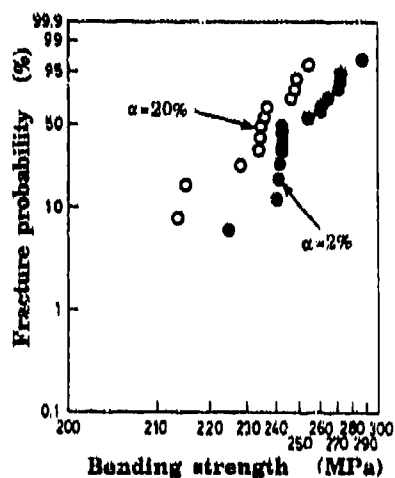


Fig.10 Unjoined edge band found on the fracture surface of an  $\text{Al}_2\text{O}_3/\text{Nb}$  joint<sup>10</sup>.

Fig.9 Influence of unjoined areal fraction ( $\alpha$ ) on bending strength of  $\text{Al}_2\text{O}_3/\text{Nb}$  joints<sup>10</sup>.

interface is considered to be primarily one of this case. This interface is weak due to the presence of pores on the interface<sup>12</sup>. When Ni contains nitride forming elements such as Cr, no pore is formed at an interface and the strength is improved<sup>8,13</sup>.

Unjoined area is frequently formed at the edge of a joint as the banded region as shown in Fig.10. This edge defect weakens the joint extremely as it works as a notch induced on the interface. Fig.11 shows the typical position dependent strength data obtained for the  $\text{Si}_3\text{N}_4/\text{Fe}$  foil/ $\text{Si}_3\text{N}_4$  joint<sup>14</sup>. The interface strength was quite high reaching 500 MPa but it was obtained only in the central area of the joint. Such a phenomenon has been reported for various systems. The edge unjoined defect originates from several reasons. One is the flatness of the interface. Mechanical finishing of bond faces inevitably cuts extra volume away from the edge region.

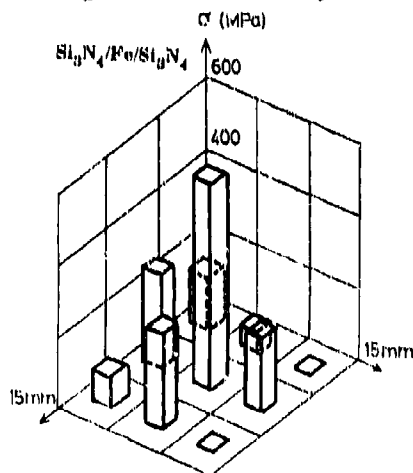


Fig.11 Position dependence of bending strength of  $\text{Si}_3\text{N}_4/\text{Fe}$  jointed at  $1300^\circ\text{C}$  for 30 min under a pressure of 20 MPa<sup>14</sup>.

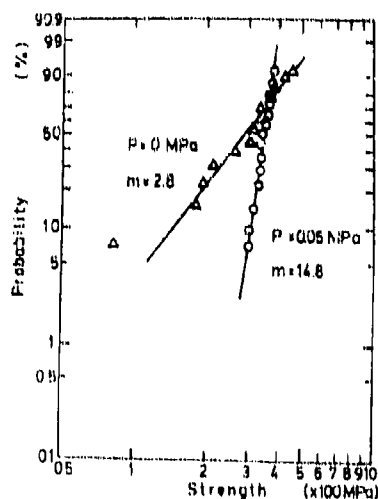


Fig.12 Effect of applied pressure on bending strength of  $\text{Si}_3\text{N}_4$  joints brazed with Al<sup>10</sup>.

The inhomogeneity in deformation of the metal layer will also reflect the phenomenon. In the case of the reaction gas releasing system, the reaction in the outer region may be promoted by continuous evacuation<sup>11</sup>. This will cause excess thinning of the ceramic at the edge region.

In brazing, pressure also has great effect on strength and its scatter. The changes in interlayer thickness and uniformity seem to be responsible for the influence. Fig.12 shows the effect of brazing pressure on the strength of the  $\text{Si}_3\text{N}_4$  joint with an Al braze<sup>15</sup>. Only slight applied pressure is enough to produce a sound joint with little scatter in strength. Johnson reported the influence of the braze layer thickness effect on the strength of the  $\text{Si}_3\text{N}_4$  joint brazed with the Ag-Cu-Ti braze<sup>16</sup>. The strength of the joint was proportional to the inverse of the square root of joint thickness when the thickness was below 50  $\mu\text{m}$ . This indicates that the joint layer becomes one of the defects of which size is taken as the thickness. Further work is required to prove this effect.

Thus, from the processing stand point, an appropriate pressure both for solid-state bonding and for brazing should be determined together with the other processing and materials parameters. To remove the edge unjoined region, hydrostatic pressing such as HIPing becomes one of the powerful methods. Utilizing the roughness effect of a metal is also useful<sup>10</sup>.

#### DAMAGE ON BOND FACE OF CERAMIC

Surface roughness has several effects on the strength of a ceramic/metal joint. Rough surface will prevent completing contact at an interface under a limited pressure and may have the damaged layer in a ceramic near an interface which has deep scratches and severe residual stress. On the other hand, an irregular bond face may have an anchoring effect which promotes joining by mechanical interlocking. In the actual case, these effects influence the mechanical properties of a joint in a competing way.

Fig.13 shows the Weibull plots of the strength of the  $\text{Si}_3\text{N}_4$  joint brazed with pure Al varying the surface grinding condition<sup>17</sup>. Clearly the rougher bond face made the joint weaker. This is because the roughly ground bond face has a damaged layer and it remains in the joint even after joining treatment. The fracture of the joint occurs in the damaged layers along the joining interface. Thus, a roughly ground bond face can weaken the ceramic/metal joint if the damaged layer remains in the joint. The surface finishing methods also have important influence on the roughness effects. To make a certain rough surface by polishing is one of the promising conditions for metal ceramic interfaces<sup>18</sup>.

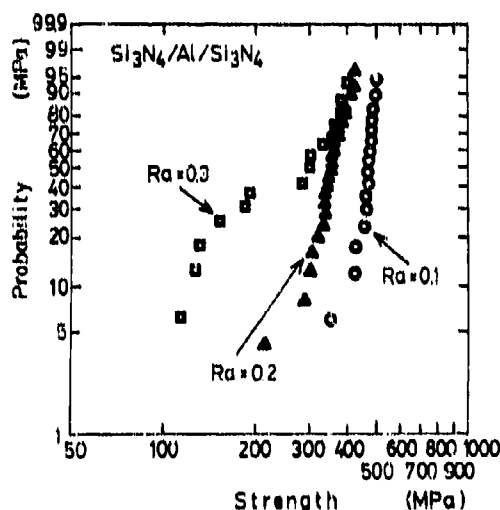


Fig.13 Influence of surface roughness of a bond face on bending strength of  $\text{Si}_3\text{N}_4$  joints brazed with Al<sup>17</sup>.

## THERMAL STRESS

The distribution of thermal (or residual) stress is not uniform in a ceramic/metal joint even along the interface. Concentration of thermal stress becomes more severe with proximity to the interface and to the free surface. The most harmful effect is caused by the tensile part of the thermal stress at the interface or in the ceramic. The maximum tensile stress concentrates on or near the interface and on the free surface. Since this stress acts almost vertical to the interface, the apparent interfacial strength measured by tensile or bending tests is substantially reduced. The amplitude of residual stress depends on the shape and dimension of the interface<sup>19</sup>. Fig.14 shows the diameter dependence of the thermal stress of the  $\text{Si}_3\text{N}_4$ /invar alloy joint measured on the surface near the interface. The larger diameter made the larger residual stress. It is also noteworthy that stress concentration at the corner of the rectangular bond face joint is more serious.

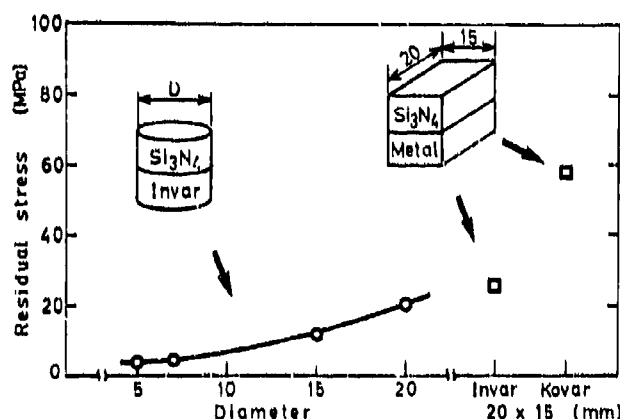


Fig. 14 Effect of size and shape of bond face on residual stress of  $\text{Si}_3\text{N}_4$ /invar alloy joints<sup>19</sup>. The residual stress was vertical to the interface on the  $\text{Si}_3\text{N}_4$  surface.

The joint with large thermal expansion mismatch decreases strength. However, it occasionally happens that some specimen is strong but the other is weak even if they are the same kind. This depends on the presence and distribution of internal flaws induced by thermal stress during joining treatment. The strengths of the  $\text{Si}_3\text{N}_4$ /invar and  $\text{Si}_3\text{N}_4$ /kovar joints, which are differing in the amplitude of thermal stress, were examined statistically<sup>20</sup>. The latter joint had larger thermal stress than the former as seen in Fig.14. The strengths of the joints are shown in Fig.15. The  $\text{Si}_3\text{N}_4$ /invar joint exhibited good strength with small scatter. On the other hand, the  $\text{Si}_3\text{N}_4$ /kovar joint had distinguished two parts in the distribution of strength. While one was high strength with small scatter, the other was weak with large scatter. The latter joint always had the interfacial flaw which was formed on cooling from the joining temperature. Thus, large thermal stress occasionally induces flaws into a joint, which do not only weaken the joint but also may make the scatter in strength large. In other words, it is very important to evaluate the scatter in strength especially for joints with large expansion mismatches. Several effective methods to relax the influence of thermal stress has been reviewed in ref.[21].

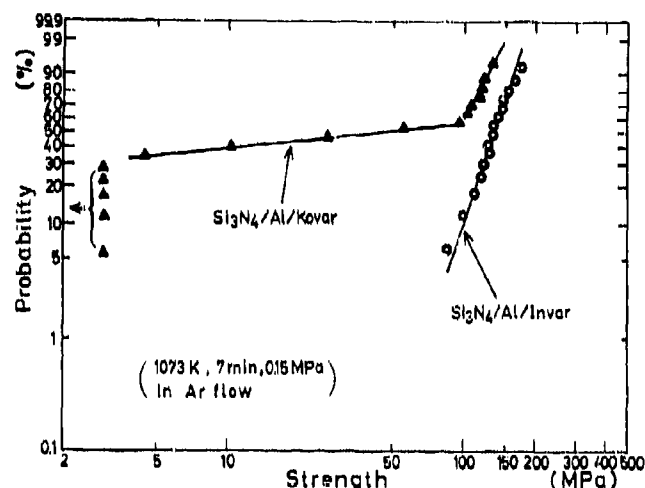


Fig.15 Weibull plots of bending strengths of  $\text{Si}_3\text{N}_4/\text{Invar}$  and  $\text{Si}_3\text{N}_4/\text{Kovar}$  joints brazed with  $\text{Al}^{20}$

## SUMMARY

This paper has focused on the reliability of joining ceramics and metals especially on the scatter in strength. The influences of several important processing factors have been made clearer. No mention, however, has been made on the reliability during the operation of joint products, i.e., the time dependent change in the reliability. In practical application, a ceramic/metal joined component is used not only under an external stress but under the internal stress originating from the elastic and expansion mismatch. Since most of engineering ceramics such as  $\text{Si}_3\text{N}_4$  and  $\text{SiC}$  usually suffer from severe thermal stress during operation because of their extremely small thermal expansion coefficients against metal components, then thermal stress will be one of the most dominant factors to restrict the life time of joints. There are other important factors in determining the life time, i.e., environmentally induced degradation such as oxidation, corrosion, stress assisted corrosion and also fatigue. Up to this moment, only a few works have been carried out on these subjects<sup>22-24</sup>. Further intensive works are required for a full understanding of the mechanisms by which joint strength decreases in certain environments and also for establishing the design technology for a ceramic/metal joining system. Such efforts are expected to accompany both the development of new techniques and the refinements of existing techniques.

## REFERENCES

1. For example, M.G. Nicholas, *Mater. Sci. Technol.* **1**, 657 (1985).
2. For example, G. LeLay, *Surface Sci.* **132**, 169 (1983); M. Rülhe and A.G. Evans, *Mater. Sci. Engineer.* **A107**, 187 (1989).
3. For example, F.S. Ohuchi and M. Kohyama, *J. Am. Ceram. Soc.* **74**, 1163 (1991).
4. X.S. Ning, T. Okamoto, Y. Miyamoto, A. Koreeda, K. Suganuma and S. Ghoda, *J. Mater. Sci.* **26**, 2050 (1991).
5. X.S. Ning, T. Okamoto, Y. Miyamoto, A. Koreeda and K. Suganuma, *J. Mater. Sci.* **24**, 2865 (1989).
6. M. Morita, K. Suganuma and T. Okamoto, *J. Mater. Sci. Letters* **6**, 474 (1987).



7. X.S. Ning, K. Suganuma, T. Okamoto, A. Koreeda and Y. Miyamoto, *J. Mater. Sci.* **24**, 2879 (1989).
8. S. Noda, H. Doi and O. Kamigaito, *J. Mater. Sci. Letters* **5**, 381 (1986).
9. S.D. Peteves, *Mater. Sci. Monogr.* **66B**, 1469 (1991).
10. K. Suganuma, T. Okamoto, M. Koizumi and S. Gohda, *Ceram. Eng. Sci. Proc.* **10**, 1919 (1989).
11. B. Gottselig, E. Gyarmati, A. Naoumides and H. Nickel, *J. European Ceram. Soc.* **6**, 153 (1990).
12. M.E. Brito, H. Yokoyama, Y. Hirotsu and Y. Mutoh, in *Advanced Materials*, vol.8, edited by M.Doyama and S.Somiya (Mater. Res. Soc. International Meeting, Tokyo, 1989) pp.23-28.
13. M. Takamura and S.D. Peteves, *J. Am. Ceram. Soc.* **73**, 1221 (1990).
14. K. Suganuma, unpublished work, (1985).
15. K. Suganuma, T. Okamoto, M. Koizumi and M. Shimada, *J. Mater. Sci.* **22**, 1359 (1987).
16. S.M. Johnson, *Ceram. Eng. Sci. Proc.* **10**, 1846 (1989).
17. K. Suganuma, T. Okamoto, M. Koizumi and M. Shimada, *Adv. Ceram. Mater.* **1**, 356 (1986).
18. C. Beraud, M. Courvire, C. Esnouf, L. Juve and D. Treheux, *J. Mater. Sci.* **24**, 4545 (1989).
19. K. Suganuma, T. Okamoto, M. Koizumi and K. Kamachi, *J. Mater. Sci.* **22**, 3561 (1987).
20. K. Suganuma, T. Okamoto, M. Shimada and M. Koizumi, *Am. Ceram. Soc. Bull.* **65**, 1060 (1986).
21. K. Suganuma, Y. Miyamoto and M. Koizumi, *Ann. Rev. Mater. Sci.* **13**, 47 (1988); K. Suganuma, *I.S.I.J. International* **30**, 1046 (1990).
22. K. Suganuma, M. Morita, T. Okamoto and M. Koizumi, *Ceram. Eng. Sci. Proc.* **10**, 190<sup>R</sup> (1989).
23. T.S. Oh, R.M. Cannon and R.O. Riche, *J. Am. Ceram. Soc.* **70**, C352 (1987).
24. P.F. Becher and M.K. Ferber, *J. Mater. Sci.* **19**, 3778 (1984).

## INTERFACE SCIENCE OF CONTROLLED METAL/METAL AND METAL/CERAMIC INTERFACES PREPARED USING ULTRAHIGH VACUUM DIFFUSION BONDING

WAYNE E. KING, G. H. CAMPBELL, A. W. COOMBS, G. W. JOHNSON, B. E. KELLY, T. C. REITZ, S. L. STONER, W. L. WIEN, AND D. M. WILSON

Chemistry and Materials Science Department, University of California, Lawrence Livermore National Laboratory, Livermore, CA 94550

### ABSTRACT

We have designed, constructed, and are operating a unique capability for the production of highly controlled homophase and heterophase interfaces: an ultrahigh vacuum diffusion bonding machine. This machine is based on a previous design which is operating at the Max Planck Institut für Metallforschung, Institut für Werkstoffwissenschaft, Stuttgart, FRG. In this method, flat-polished single or polycrystals of materials with controlled surface topography can be heat treated up to 1500°C in ultrahigh vacuum. Surfaces of annealed samples can be sputter cleaned and characterized prior to bonding. Samples can then be precisely aligned crystallographically to obtain desired grain boundary misorientations. Material couples can then be bonded at temperatures up to 1500°C and pressures up to 10 MPa. Results are presented from our initial work on Mo grain boundaries and Cu/Al<sub>2</sub>O<sub>3</sub> interfaces.

### INTRODUCTION

The lack of well characterized, precisely oriented interfaces has been identified as limiting the capability of the Interface Science community to make progress in the study of structure and properties of interfaces. Lawrence Livermore National Laboratory and Sandia National Laboratories are developing a multi-disciplinary, multi-institutional research effort in interface science. This research, which focuses on the influence of impurities, flaws, and inclusions on adhesion and bonding at internal interfaces will rely on the availability of bicrystals with well defined interfacial chemistry and highly reproducible misorientations. The capability to produce such bicrystals did not exist within the United States although it is critical to further advancement of interface science and technology.

### BACKGROUND

To address this need we have selected the diffusion bonding approach, which was successfully demonstrated at the Max Planck Institut in Stuttgart, for application to the class of interface problems of interest.<sup>1,2</sup> Figure 1 shows a rendering of the design of the UHV diffusion bonding machine. It comprises four chambers: a surface analysis chamber, a diffusion bonding chamber, an annealing chamber, and a surface modification chamber (not shown). typically, a sample is first introduced into the annealing chamber via either an airlock chamber (Figure 2). The sample is annealed in ultrahigh vacuum to 1500°C to stabilize the microstructure.

After annealing, a rail system transports the sample to the surface analysis chamber, to the surface modification chamber, or to the bonding chamber. A special manipulator (see the Figure 3) moves the sample to the railroad car. In the surface analysis chamber (Figure 4), sample surfaces are sputter-cleaned with a 500 eV ion beam at an incidence of 15 deg. The sample can be rotated during sputtering to ensure that material is removed uniformly. The sample can be heated at the same time to about 1000°C to purify its near-surface region. Surface cleanliness and levels of surface doping are assessed with Auger electron spectroscopy, low-energy electron diffraction, and static secondary-ion mass spectrometry.

In the surface modification chamber (planned for 1994), the sample can be rotated to face a low-energy ion implanter. The implanter has two ion sources to provide both gas and other ions. The sample can be further rotated to face an electron-beam evaporator or a magnetron sputtering source, where it can be

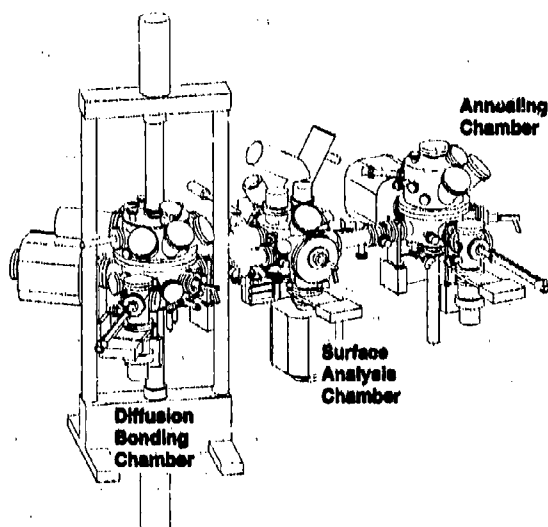


Figure 1. Rendering of the Lawrence Livermore National Laboratory UHV Diffusion Bonding Machine.



Figure 2. Cut-away view of the annealing chamber. Air-lock chamber is shown at right. Radio frequency (RF) furnace is shown at top center.



Figure 3. Multi-articulated manipulator for manipulating samples in vacuum without sample holder. The mechanical hand at the end of the arm is shown grasping a coin.

loaded onto a heated sample holder. An airlock is included in the surface-modification chamber for loading and unloading samples.

In the bonding chamber (Figure 5), samples are stacked on the lower ram of the diffusion bonding press. A spacer is first placed on the ram and fixed with a set of fingers on a precision crystal-orientation device (Figure 6). The first sample is stacked onto the spacer, and another set of fingers is driven in to hold the sample. The next sample is placed on top of the first sample and fixed with a third set of fingers. Finally, a second spacer is stacked on the top of the samples and positioned by a final set of fingers.



Figure 4. Cut-away view of the surface analysis chamber. SIMS ion gun is shown at top left. SIMS quadrupole mass spectrometer is shown at top right.

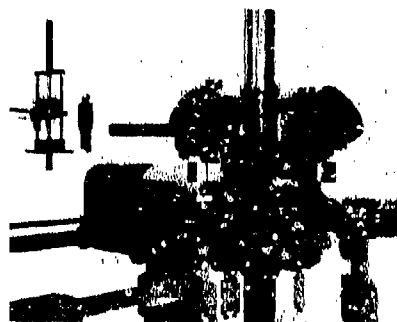


Figure 5. Cut-away view of the diffusion bonding chamber. Bonding chamber and press are shown at top left.

A laser beam is then reflected off the edge of the bottom sample in the stack. The sample is rotated with the precision crystal orientation device until a prepolished optical flat reflects the laser beam through a port of the diffusion bonding chamber onto a screen. The position of the reflection is noted, and the laser beam is then raised to intersect the upper sample. This sample is rotated so that the reflection from its optical flat coincides with the reflection from the bottom sample. The rotation gears of the precision crystal orientation device are locked, and the upper ram is brought to bear upon the sample stack. A small load is added, and the fingers are withdrawn. The entire stack is then raised into the furnace for bonding. An airlock is also incorporated in the diffusion bonding chamber to facilitate removal of bonded samples.

## RESULTS AND DISCUSSION

### Fracture of the Cu/Alumina interface

We have fabricated samples intended for fracture testing using the Ultrahigh Vacuum Diffusion Bonding Machine. These samples were diffusion bonds of polycrystalline high purity copper foils, ~200  $\mu\text{m}$  thick, to high purity polycrystalline alumina rods, 2.0 cm long. The foil geometry was selected to minimize the contribution of bulk plasticity to the fracture-resistance measurements. Surfaces of the

copper foils and alumina rods were sputter cleaned in-situ prior to bonding. Bonding was carried out as a function of temperature (800, 875, or 960°C) and time (1 or 2 hours) at a bonding load of 1.5 MPa. Resultant bonded samples yielded seven 4-point bend test samples.

Figure 7 demonstrates how this geometry was fabricated such that it could be bonded in ultrahigh vacuum where the samples are handled remotely without sample holders. The pieces at left are the starting materials, flat-polished alumina rods, a thin Cu foil, and a support ring for the copper foil. Two support rings are spot welded to the rim of the Cu foil. This support ring facilitates the remote handling of the samples in the ultrahigh vacuum. The bonding process proceeded as follows: First an alumina rod was loaded into the

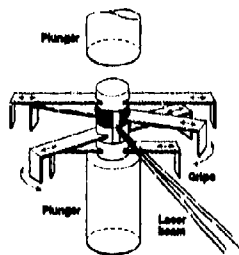


Figure 6. Schematic diagram of precision crystal orientation device.

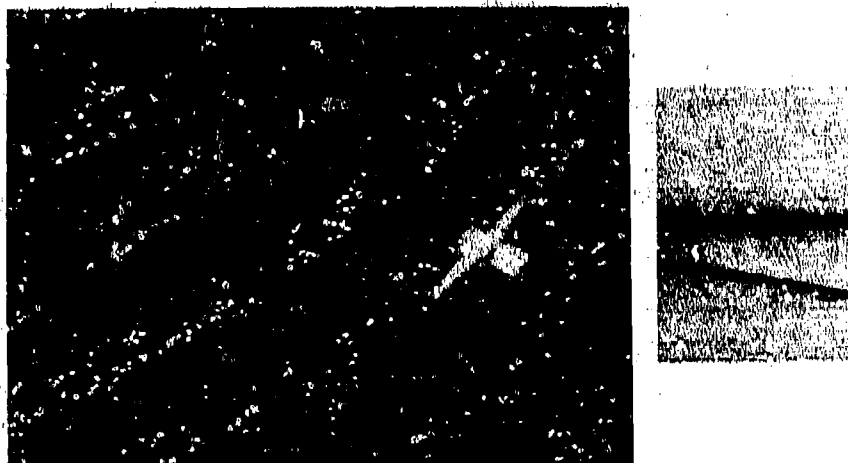


Figure 7. Fabrication of 4-point bend samples. Alumina rod, Cu foil, and Cu ring at left. As-bonded samples at center. One of seven bend test samples cut from a single sample at right. Magnified image of bond line at far right.

surface-analysis chamber of the ultrahigh vacuum diffusion bonding machine. The alumina was sputter cleaned using  $\sim 2 \times 10^{18} \text{ Xe}^{+}/\text{cm}^2$ . In order to reduce the hillock formation that is typical in sputtering, the ion beam was incident at  $15^\circ$  from horizontal and the sample was rotated during sputtering. After cleaning, the alumina was transferred to the diffusion bonding chamber and loaded on the lower ram of the diffusion-bonding press. The Cu foil was then sputter cleaned on both sides using a procedure similar to that used for the alumina except that the Cu was heated to  $\sim 400^\circ\text{C}$  during sputtering. The Cu foil was stacked atop the first alumina rod in the diffusion bonding chamber. Finally, the second alumina bar was cleaned and the sample stack was completed. A load of 1.6 MPa was applied to the stack and the stack was raised into the radio-frequency heater in the diffusion bonding chamber. The temperature was ramped to the set point over 25 min followed by the soak time and then ramped back to room temperature over 15 min. During the bonding process, the vacuum in the diffusion bonding chamber typically did not exceed  $5 \times 10^{-9}$  torr. The samples at center in Figure 7 show the as-bonded configuration. It is possible to produce 1-2 samples per day of this type. After removal from the bonding machine, each sample was cut into seven  $3 \times 3 \times 40$  mm bars for 4-point bend testing. This bend-test sample configuration is shown at right. The inset figure shows a micrograph of the Cu foil bonded between two alumina bars. A human hair is included in the micrograph illustrating the thinness of the Cu foil.

Samples were notched for 4-point bend testing using a high-speed saw. Notches were cut 0.5 mm deep with a kerf of  $\sim 87 \mu\text{m}$ . Samples were loaded on a 4-point bend fixture. The mid-point deflection was monitored using a spring-loaded probe fitted with two opposing clip gauges. Load and mid-point displacement were monitored as a function of time for a constant cross-head displacement rate. Figure 8 shows a typical load vs time curve.

#### Bonding Kinetics of Cu with Sapphire

To determine the conditions under which completely dense interfaces form, we are studying the evolution of bonded interfacial area as a function of bonding temperature and time. The system under investigation is copper/sapphire. Insight will be gained from this study into the appropriate bonding

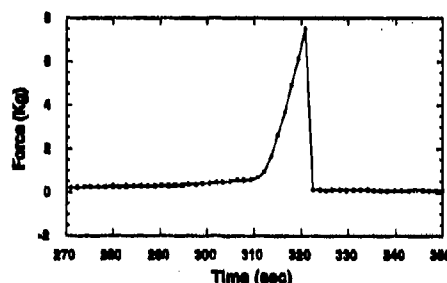


Figure 8. Typical load vs. time data for 4-point bend sample shown in Figure 7.

conditions for copper/alumina mechanical test specimens and data will be obtained on a model system in diffusion bonding.

In the analysis chamber of the UHV Diffusion Bonding Machine, the surfaces of the specimens to be bonded were cleaned by ion sputtering with  $\text{Xe}^+$  ions at 1 keV. The samples were rotated during sputtering to maintain an even surface finish. The cleaned surfaces were placed together in the bonding chamber and high purity alumina spacer blocks inserted between the specimens and the rams of the hydraulic press. To ensure proper alignment of the specimen stack so that the applied force is distributed as an uniform pressure on the bond area, the top spacer block had a spherical radius

of curvature ground on one end to allow point contact with the top ram. The applied force resulted in a pressure of 1 MPa at the bonding interface in all cases studied here.

The bonding temperature and times were varied to study their effects. The temperatures chosen were 800, 900, and 1000°C and the times were 1, 2, and 4 hr. During the diffusion bonding heat cycle the pressure in the bonding chamber never exceeded  $1 \times 10^{-8}$  torr. The heating and cooling rates were 20 and 15°C/min, respectively.

The characterization of the bonded area at the interface was done by optical microscopy through the sapphire. Under normal incidence light conditions, as in the micrograph shown in Figure 9, the bonded areas are light in contrast because the copper is conforming to the polished surface of the sapphire and reflecting light back into the objective. The micrographs were digitized and a brightness threshold was chosen for each micrograph which corresponded with the bonded area. The number of pixels above this brightness was summed and an area fraction was calculated.

Some results are shown in the in Figure 10a and b. The average measured bonded area is shown along with the high and low measures indicating the variability in bonded area density across the entire interface. The results indicate that achieving a fully dense interface in the copper/alumina system requires lengthy bonding times, probably 6 to 12 hr, at 1000°C or higher.

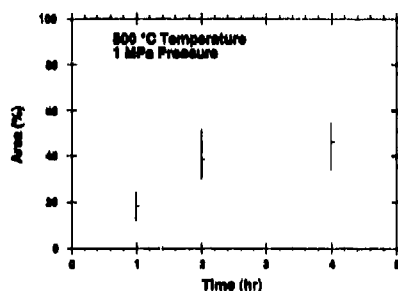


Figure 9a. Fractional bonded area as a function of time for constant temperature and pressure.

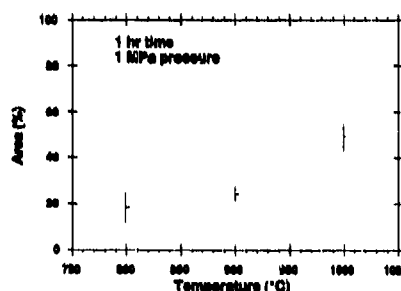


Figure 9b. Fractional bonded area as a function of temperature for constant time and pressure.

### Cu/Ti/Alumina Interface

In this experiment,  $\sim 30\text{\AA}$  of Ti was sputter deposited on a piece of sapphire. The Ti was then covered with  $\sim 2\text{ }\mu\text{m}$  of Cu. The samples were removed from the sputter deposition machine and loaded into the ultrahigh vacuum diffusion bonding machine. Bulk polycrystalline oxygen-free high conductivity copper was bonded to the coated sapphire. Surfaces of the copper and coated sapphire were sputter cleaned in-situ prior to bonding. Bonding was carried out as at  $200^\circ\text{C}$  for 1 hour at a bonding load of 1.0 MPa. Resultant bonded sample was cut into the appropriate geometry for analytical electron optical observation. The Figure 11 shows a cross-section electron micrograph of the bonded interface inset within the x-ray energy dispersive spectroscopy profile.

### Mo Bicrystals

We have fabricated two bicrystals intended for grain boundary atomic-structure determination using the Ultrahigh Vacuum Diffusion Bonding Machine. This sample was a diffusion bond of a pair of Mo single crystals. The Mo single crystals were oriented along  $\langle 310 \rangle$ , sliced parallel to the (310) plane, and flat polished and precisely oriented to within  $0.1^\circ$  of (310).

The rate of diffusion bonding is controlled by surface diffusion which is a function of temperature and pressure. We seek interfaces with controlled geometries (usually planar) and chemistries. Such interfaces can only be obtained by minimizing the temperature, pressure, and time for diffusion bonding in order to discourage boundary migration, deformation, and segregation of impurities to the interface. A key to reducing bonding temperature, pressure, and time is the minimization of the volume of materials that must be transported by surface diffusion in order to eliminate porosity at the interface. This has been accomplished by controlling the flatness of the surface of the samples to be bonded. Typical metallographic preparation methods yield samples with peak-to-valley deviations from flatness of  $\sim 1000\text{ nm}$ . This flatness has been significantly improved,  $< 100\text{ nm}$ , by using techniques used in the polishing of precision optics, namely pitch polishing.

Surfaces of the Mo single crystals were sputter cleaned in-situ prior to bonding. Bonding was carried out at  $1400^\circ\text{C}$  for four hours at a bonding load of 1.0 MPa. The bicrystal was aligned and bonded as described above. Resultant samples were be cut into the appropriate configuration for observation in the high resolution electron microscope. A high resolution image taken on the JEOL 4000EX at SNL, L from

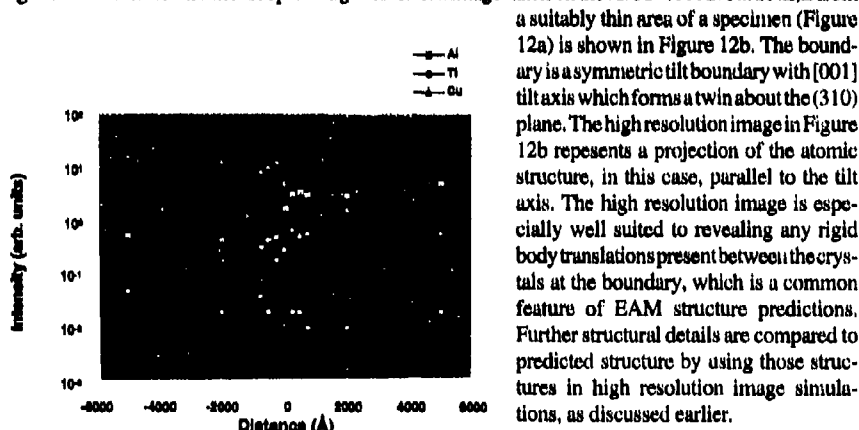


Figure 11. X-ray energy dispersive spectroscopy trace of Al, Ti, and Cu  $K\alpha$  x-rays as a function of position relative to the interface between Cu (at left in inset electron micrograph) and sapphire (at right).

a suitably thin area of a specimen (Figure 12a) is shown in Figure 12b. The boundary is a symmetric tilt boundary with [001] tilt axis which forms a twin about the (310) plane. The high resolution image in Figure 12b represents a projection of the atomic structure, in this case, parallel to the tilt axis. The high resolution image is especially well suited to revealing any rigid body translations present between the crystals at the boundary, which is a common feature of EAM structure predictions. Further structural details are compared to predicted structure by using those structures in high resolution image simulations, as discussed earlier.

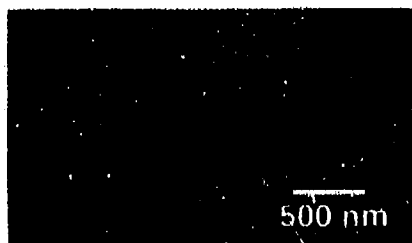


Figure 12a. Low magnification image of Mo bicrystal illustrating long flat regions of interface.

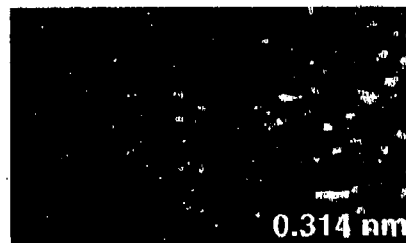


Figure 12b. HREM image from section of interface in Figure 12a.

## CONCLUSIONS

The new ultrahigh vacuum diffusion bonding machine offers a number of new opportunities in the study of interface science:

- Controlled interface crystallography can be used to carefully investigate interface atomic structure
- Controlled interface topography can be used to investigate the effect of flaws on interfacial toughness
- Controlled interface chemistry can be used to study the effect of impurities on interfacial adhesion and bonding
- Macroscopic bicrystals (as opposed to thin films) can be used to carry out mechanical tests as well as for validation of theoretical predictions of atomic structure
- Homophase boundaries (e.g. grain boundaries in metals, intermetallics, or ceramics) and heterophase boundaries (e.g. metal/ceramic interfaces, metal/semiconductor interfaces) can be produced

## ACKNOWLEDGMENTS

The authors are grateful for the great contributions of Prof. Dr. H. Fischmeister and Prof. Dr. M. Rühle at the Max Planck Institut für Metallforschung, Institut für Werkstoffwissenschaft in Stuttgart to the design of the UHBV diffusion bonding machine. We are also grateful to M. Wall for assistance with electron microscopy of Cu/alumina interfaces. This work performed under the auspices of the Division of Materials Science of the Office of Basic Energy Sciences, U. S. Department of Energy, and the Lawrence Livermore National Laboratory under contract No. W-7405-Eng-4<sup>12</sup>.

## REFERENCES

1. B. Gibbesch and G. Elsner, *Acta metall. mater.*, **40** (Suppl.), S59-S66, (1992).
2. H. F. Fischmeister, W. Mader, B. Gibbesch and G. Elsner in *Interfacial Structure, Properties, and Design*, edited by M. H. Yoo, W. A. T. Clark and C. L. Briant (Mater. Res. Soc. Symp. Proc. **122**, Pittsburgh, PA 1988) pp. 529-540.



---

## PART II

---

### **Interfacial Thermodynamics, Microstructure, and Mechanical Properties**

## TOWARDS AN UNDERSTANDING OF THE REACTION SEQUENCES IN BRAZED JOINTS: INVESTIGATION OF THE Ti-Cu-O TERNARY AT 945°C.

G. P. KELKAR\*, A. H. CARIM, and K. E. SPEAR  
Department of Materials Science and Engineering, The Pennsylvania State University,  
University Park, PA 16802.

### ABSTRACT

The joining of ceramics using active metal braze alloys is an attractive technique and has been used for a variety of material systems. The braze alloys usually contain an active element such as Ti which can reduce the ceramic and form a strong bond across the interface. Microstructural characterizations of brazed interfaces have been widely reported, though reasons for the formation of reaction products and their sequence is not clear due to the lack of thermodynamic information on the phases formed.

The Ag-Cu-Ti/Al<sub>2</sub>O<sub>3</sub> system contains an interface where Ti, the active element in the braze alloy, reduces Al<sub>2</sub>O<sub>3</sub> to form layers of reaction products which include (Ti,Cu,Al)<sub>6</sub>O, an M<sub>6</sub>X type compound. In this study we have looked at the Ti-Cu-O system as a first step towards understanding the Ag-Cu-Ti/Al<sub>2</sub>O<sub>3</sub> system. A section of the Ti-Cu-O ternary was investigated at 945°C. The system contains two M<sub>6</sub>X type compounds, Ti<sub>4</sub>Cu<sub>2</sub>O and Ti<sub>3</sub>Cu<sub>3</sub>O, which have independent single phase fields. A Ti activity diagram was generated from the available thermodynamic information and the knowledge of the ternary section. The two reaction sequences reported for such interfaces were analyzed based on the activity diagram.

### INTRODUCTION

The extreme and often contradictory demands on the materials in use today has made joining of dissimilar materials a necessity. For example, ceramics and metals can be joined to produce a component with unique properties. Brazing of metal shanks to ceramic tool bits is a typical example. Joining may also be employed to overcome processing limitations in the production of ceramic components with complex geometries. Thus the joints may either be of the ceramic-metal or ceramic-ceramic type. Joining techniques that are commonly employed include metallization, shrink fitting, diffusion bonding, and brazing with variations for particular applications.

Brazing of two components using a filler metal is a relatively simple technique which can produce a strong hermetic joint. To form a brazed joint, a metal alloy of suitable composition is sandwiched between the components to be joined; the assembly is then heated, usually in a vacuum and under a nominal load, to a temperature slightly above the melting point of the alloy, and finally cooled to room temperature. The heating and cooling cycle is designed to maximize the wetting and adhesion resulting from interfacial reactions and to minimize the thermal expansion mismatch stresses in the joint.

The alloy used as a filler is composed of a eutectic with a melting point higher than the application temperature of the joint. Since most metals do not wet ceramics, an active element is usually added to improve wetting behavior. An active element is defined as one which can reduce the ceramic and form a strong chemical bond at the interface. Although elements belonging to the IVB, VB, and VIB groups along with Ni and Pd [1-3] are possible candidates, Ti-containing braze alloys are the most extensively studied in the literature [4,5]. The commercially available braze alloys (e.g., those from Wesgo, Inc., Belmont, CA) contain a Cu-Ag or Cu-Au eutectic as the primary component along with an active element.

\* This work was supported by the Center for Advanced Materials at The Pennsylvania State University, as part of the Cooperative Program in High Temperature Engineering Materials Research, and by the Office of Naval Research Young Investigator program under grant #N00014-91-J-4051.

Other elements may be present either to enhance the activity of the active element or to improve the corrosion resistance of the alloy.

The microstructure at the Ag-Cu-Ti/Al<sub>2</sub>O<sub>3</sub> interface has been reported [6,7,8]. The formation of M<sub>6</sub>X type compounds, Ti<sub>3</sub>Cu<sub>2</sub>O and Ti<sub>4</sub>Cu<sub>2</sub>O, as reaction products is a characteristic of this interface. These compounds form as a continuous layer across the interface and hence their properties are of interest in evaluating the joint. The thermal, mechanical, and electrical characterization of these two M<sub>6</sub>X compounds in the Ti-Cu-O system have been reported elsewhere [9].

In this investigation, we have looked at the phase stability of the M<sub>6</sub>X compounds with other phases in the Ti-Cu-O system at 945°C. The phase stability data was coupled with information available on the Ti-O binary system to estimate the activities of Ti and O in the three-phase regions. A Ti activity diagram was generated based on this information, and was used to justify the reaction sequences at such interfaces.

## EXPERIMENTAL PROCEDURE

The three-phase samples were made by mixing powders of Ti, TiO<sub>2</sub>, Cu and CuO in proper proportions and pressing them into pellets. The pellets were then arc-melted in an Ar atmosphere for six seconds and then turned over and remelted to ensure homogenization. The resulting buttons were sealed in evacuated quartz tubes and annealed at 945°C for four days. The samples were air-quenched while still under encapsulation.

The samples were polished to a 0.25μm finish, mounted in bakelite molds and analyzed in an electron microprobe. The elemental compositions were determined by wavelength dispersive spectrometry. The standards used were Ti metal and TiO<sub>2</sub> for Ti, and Cu metal for Cu. NIST (National Institute of Standards and Technology) glass KA25 was used as a low oxygen standard and albite (Na-feldspar) was used as a high-oxygen standard. The compositional analysis was performed on individual phases near three-phase junctions, which represent equilibrium conditions, but far enough from the junctions to avoid any significant signal from the neighboring phases.

## RESULTS AND DISCUSSION

### Ti-Cu-O section at 945°C

The section of the Ti-Cu-O ternary as determined in this investigation is shown in Figure 1. The choice of 945°C as the temperature of interest was based on two criteria. The TiO phase observed at the Ag-Cu-Ti/Al<sub>2</sub>O<sub>3</sub> interfaces has been identified as the cubic β-TiO, and hence a temperature above 940°C had to be chosen in order to avoid the formation of the α-TiO (monoclinic) phase. Secondly, since the Ti<sub>2</sub>Cu-TiCu eutectic has a melting point of 960°C, a lower temperature was chosen to avoid the formation of a molten phase which would react with the quartz tube.

The investigation was restricted to the region of the ternary where the M<sub>6</sub>X phases were in the phase field. The nominal compositions of the samples used for analysis are shown by filled circles in the various three-phase regions marked with Roman numerals. The tie lines determined in this study are drawn solidly, whereas others are shown as dashed lines. A region in the Cu-rich corner of the section, bound by open ended dashed lines, is probably in a liquid state at the temperature of interest. The compositions of the phases determined by the microprobe had a narrow variation (<0.5 at. %) and the average values were used for plotting the ternary section.

The phase diagram determined in this investigation was based on samples annealed for four days. Further work is underway to verify the phase boundaries after extended anneals and to verify the presence of another ternary compound, Ti<sub>3</sub>CuO, which was observed inconsistently in some of the samples.

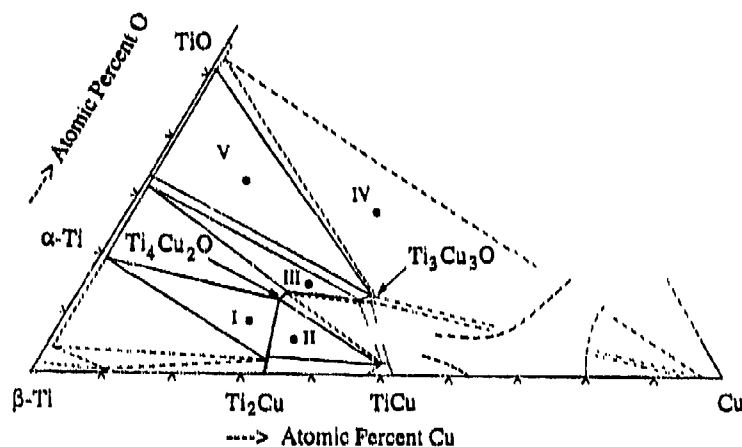


Figure 1: A section of the Ti-Cu-O ternary at 945°C. Tie lines determined in this investigation are drawn solid while others are drawn as dashed lines.

#### Analysis of the Ti-O system

The earliest version of the Ti-O system was reported by Kubaschewski and Dench [10] and was later revised by Komarek and Silver [11]. The free energy of solution of O in Ti at 945°C [11] was converted to activity values for O. The corresponding variation in the activity of Ti was calculated by the Gibbs-Duhem integration and the activity variations of the two elements as a function of atomic percent of O are plotted in Figure 2.

A  $\beta \rightarrow \alpha$  transition at low oxygen concentrations would have introduced a plateau in the activity curves, corresponding to the  $\beta$ - $\alpha$  two phase region. Such a transition is not supported by data in Figure 2 though it is reportedly present in the Ti-O system at 945°C [12]. The data from reference [11] was used here without any modification, for the Gibbs-Duhem analysis.

To draw an activity diagram for Ti, the activity values of Ti in the various three phase fields have to be known. In the absence of direct measurements, approximations based on information available on the Ti-O binary system were used by the following argument. In the three regions marked I, III, and V on Figure 1,  $\alpha$ -Ti[Cu] is one of the phases in equilibrium. The solubility of Cu in this phase is less than 1 atomic percent in all cases. Given the small amount of Cu and the weak interactions of the Cu-O and Cu-Ti pairs as compared to the Ti-O pair [13], we can assume that the effect of Cu on the activities of Ti and O in  $\alpha$ -Ti[Cu] is negligible. The data available from Figure 2 on the Ti-O binary was used to determine the activities of Ti and O in the Regions I, III, V based on the phase composition of  $\alpha$ -Ti[Cu].

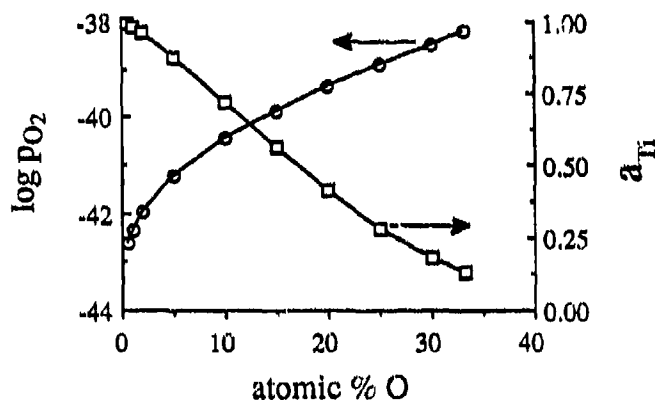


Figure 2 : Activity variation of O and Ti as a function of atomic percent O in Ti at 945°C.

#### Activity Diagram

The activity diagram for a ternary system contains information similar to the phase diagram, the difference being that one of the elements is represented by its activity rather than composition. A three-phase region on the ternary, which is constrained by Gibbs phase rule to have equal activity of an element in all three phases, is represented on an activity diagram by a horizontal line. Single phase fields are represented by finite areas.

The activity diagrams can be used to interpret reaction sequences across an interface, as has been shown for the Ti/SiC and Ti/Si<sub>3</sub>N<sub>4</sub> systems [14]. The activity of an element at the interface shows a continuous gradient, either increasing or decreasing, across the interface, unless that component is forced to diffuse uphill by the diffusion of the other elements [15]. This constraint limits the possible number of reaction sequences at the interface from amongst all possible reaction paths based purely on the phase diagram.

The activity diagram for Ti is shown in Figure 3. The three-phase regions, whose Ti activities were determined in this investigation, are marked by Roman numerals to correspond to the three-phase regions on the ternary section shown in Figure 1. Single phase regions are shown as shaded areas. Two different reaction paths are drawn as wide-dashed lines bound by filled circles and are marked A and B.

The first type of reaction sequence is the one where the Ag-Cu-Ti braze alloy is the only source of Ti for the reaction, e.g., at the Al<sub>2</sub>O<sub>3</sub>/Ag-Cu-Ti/Al<sub>2</sub>O<sub>3</sub> interfaces [6]. The reaction sequence reported at this interface is Al<sub>2</sub>O<sub>3</sub>/TiO/Ti<sub>3</sub>Cu<sub>3</sub>O/Cu. This sequence is represented on the activity diagram by a dashed line marked A. In the absence of specific information of the activity of Ti in TiO, the sequence is shown starting with an arbitrary value of Ti activity in the TiO phase field. The horizontal portions of the dashed line represent the TiO/Ti<sub>3</sub>Cu<sub>3</sub>O and Ti<sub>3</sub>Cu<sub>3</sub>O/Cu transitions. In the single phase field of Ti<sub>3</sub>Cu<sub>3</sub>O, the Ti activity can drop significantly and nearly all the way to zero and then move over to nearly pure Cu. In this process, the activity of Ti has decreased monotonically as we moved away from the Al<sub>2</sub>O<sub>3</sub> surface.

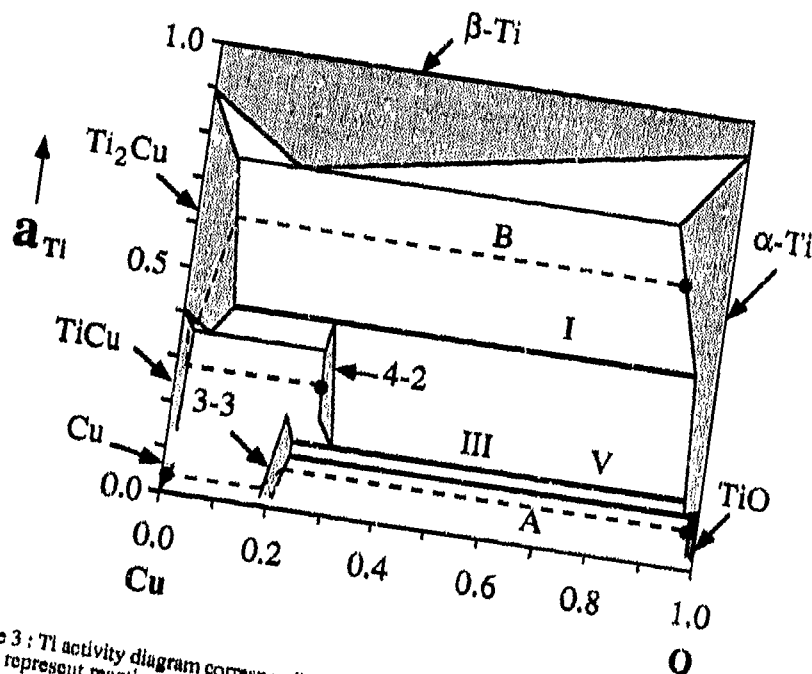


Figure 3 : Ti activity diagram corresponding to the Ti-Cu-O ternary at 945°C. Dashed lines A and B represent reaction sequences. Single phase regions are shaded, two phase regions are open spaces, and three-phase regions are depicted by horizontal lines (activity of Ti is constant in a three-phase region). The single phase fields of the two  $M_6X$  phases,  $Ti_4Cu_2O$  and  $Ti_3Cu_3O$ , are labeled as 4-2 and 3-3, respectively. The lines labeled I, III, and V in this diagram depict the three-phase regions shown in Figure 1.

The second type of reaction sequence has been observed [7] when a Ti-based superalloy such as Ti-6Al-4V (TA6V) is brazed to  $Al_2O_3$  by a Ag-Cu-Ti braze alloy. Ti from the superalloy is available for the reaction and since the superalloy contains about 90 wt.% Ti, the activity of Ti at one end of the reaction sequence will be constrained to be very high (~0.9). In this case the activity of Ti will increase as we move away from  $Al_2O_3$  towards the Ti superalloy. The reported reaction sequence is  $Al_2O_3/Ti_4Cu_2O[Al]/Ti_3Cu_3O/TiCu/Ti_2Cu/\alpha-Ti(Ti,Al)_3Cu/TA6V$ . Here again, starting from an arbitrary point in the  $Ti_4Cu_2O$  single phase region, the dashed line B traces the reaction sequence on the activity diagram with a continuous increase in the Ti activity as we move away from the  $Al_2O_3$ . The compound  $Ti_3Cu_3O$  is not stable at 945°C and hence is not shown on the Ti-Cu-O ternary or on the activity diagram. Based on the activity diagram and the presence of a third phase that the  $TiO/Ti_4Cu_2O$  interface would be unstable without the presence of a third phase between them, and hence excludes the possibility of a stable  $TiO/Ti_4Cu_2O$  interface. The good agreement between the observed reaction sequences and those permissible based on the equilibrium activity diagram suggests that the interfaces at such joints, which are formed in relatively short times (~5-10 minutes), are in equilibrium.

Ag, a constituent of the braze alloy, has been identified as a Cu-saturated phase [6,7] at the joints. Since Ag does not take part in the reactions at the interface, we assumed that the effects of Ag on the reaction sequence analysis would not be significant. In contrast, Al

based by the reduction of  $\text{Al}_2\text{O}_3$  dissolves in the ternary compounds [6,7] and in the Ti-Cu intermetallics [7] and should be accounted for in the thermodynamic analysis. It is interesting to note that even though the effect of Al was not considered in the present analysis for the lack of sufficient thermodynamic information, we were able to justify the formation of the two different types of reaction sequences reported in the literature, based purely on the Ti-Cu-O ternary system.

At the present time, the available thermodynamic information is insufficient to give us a predictive capability for reaction sequences at such joints. To predict the reaction paths and end products across the interface zone, information on the activities of all elements present and phase stabilities of the compounds in the system is required.

#### SUMMARY

Two different  $\text{M}_6\text{X}$  type compounds,  $\text{Ti}_4\text{Cu}_2\text{O}$  and  $\text{Ti}_3\text{Cu}_3\text{O}$ , were identified in the Ti-Cu-O system and their phase stability with other compounds was investigated at 945 °C. The thermodynamic information available in the literature on the Ti-O system was used in conjunction with the established ternary section to estimate the activity variation of O and Ti across the three phase regions where  $\alpha\text{-Ti(O)}$  is one of the phases. The activity of Ti was then combined with the phase stability information of the ternary to generate an activity diagram. The diagram was successfully used to explain the different reaction sequences reported in the literature.

#### REFERENCES

1. R. E. Loehman and A. P. Tomsia, "Joining of Ceramics," *Ceramic Bulletin*, 67[2], pp. 375-380, 1988.
2. W. D. Kingery, "Metal-Ceramic Interactions: I, Factors Affecting Fabrication and Properties of Ceramic Bodies," *J. Am. Ceram. Soc.*, 36[11], pp. 362-365, 1953.
3. T. Okamoto, "Interfacial structure of metal-ceramic joints," *ISIJ International*, 30[12], pp. 1033-1040, 1990.
4. H. Mizuhara and E. Heubel, "Joining of Ceramic to Metal with Ductile Active Filler Metal," *Welding J.*, 65[10], pp. 43-51, 1986.
5. A. J. Moorhead and H. Keating, "Direct Brazing of Ceramics for Advanced Heavy-Duty Diesels," *Welding J.*, 65[10], pp. 17-31, 1986.
6. M. L. Santella, J. A. Horton, and J. J. Pak, "Microstructure of Alumina Brazed with a Silver-Copper-Titanium Alloy," *J. Am. Ceram. Soc.*, 73 (6), pp. 1785-87, 1990.
7. F. Barbier, C. Peytour, and A. Revcolevschi, "Microstructural Study of the Brazed Joint between Alumina and Ti-6Al-4V Alloy," *J. Am. Ceram. Soc.* 73 (6), pp.1582-86, 1990.
8. A. H. Carim, "Convergent-Beam Electron Diffraction 'Fingerprinting' of  $\text{M}_6\text{X}$  Phases at Brazed Ceramic Joints," *Scripta Metall. et Mater.* 25, pp. 51-54 (1991).
9. G. P. Kelkar and A. H. Carim, "Synthesis, properties, and ternary phase stability of  $\text{M}_6\text{X}$  compounds in the Ti-Cu-O system," *J. Am. Ceram. Soc.* 76 (6), in press (1993).
10. O. Kubaschewski and W. A. Dench, "The free-energy diagram of the system titanium-oxygen," *J. Inst. Met.*, Vol. 82, pp.87-91, 1953-54.
11. K. L. Komarek and M. Silver, "Thermodynamic Properties of Zirconium-Oxygen, Titanium-Oxygen and Hafnium-Oxygen Alloys," *Thermodynamics of Nuclear Materials*, Proc. of Symp. on Thermodynamics of Nuclear Materials, I. A. E. A., Vienna, 21-25, May 1962.
12. J. L. Murray and H. A. Wreidt, "The O-Ti (Oxygen-Titanium) System," *Phase Diagrams of Binary Titanium Alloys*, Editor J. L. Murray, ASM, Metals Park, OH, 1987.
13. JANAF Thermochemical Tables, *J. of Phys. and Chem. Reference Data*, Vol 14, 1985.
14. Thermochemistry of ceramic-metal reactions in Ti-Si-N and Ti-Si-C systems at high temperatures and pressures, S. Sambasivan, Ph.D. thesis, Arizona State University, December 1990.
15. F. J. J. van Loo, "Multicomponent Diffusion in Binary and Ternary Solid-State Systems," *Prog. Solid St. Chem.*, Vol. 20, pp. 47-99, 1990.

## INTERFACIAL REACTIONS BETWEEN TITANIUM AND BORATE GLASS

R. K. BROW\*, S. K. SAHA\*\*, AND J. I. GOLDSTEIN\*\*

\*Sandia National Labs, Dept. 1845, Albuquerque, NM 87185

\*\*Lehigh University, Dept. of Materials Science, Bethlehem, PA 18015

### ABSTRACT

Interfacial reactions between the melts of several borate glasses and titanium have been investigated by analytical scanning electron microscopy (ASEM) and by x-ray photoelectron spectroscopy (XPS). A thin titanium boride interfacial layer is detected by XPS after short (30 minutes) thermal treatments. ASEM analyses after longer thermal treatments (8-120 hours) reveal boron-rich interfacial layers and boride precipitates in the Ti side of the interface.

### INTRODUCTION

Titanium and titanium alloys have a number of attractive properties, including outstanding strength-to-weight ratios and excellent corrosion resistance, which make them desirable materials for a variety of aerospace and biomedical applications. The use of titanium as a component alloy, however, is limited by the lack of a reliable glass/Ti sealing technology. Conventional silicate glasses readily react with Ti when sealed to form an interfacial silicide layer [1-3]. This weakly adhered layer significantly reduces the mechanical strength of silicate glass/Ti seals [3] and precludes coating titanium alloys with silicate-based bioactive glasses for prosthetic applications [4].

Borate glasses have been recently shown to form strong bonds to titanium and titanium alloys [3,5] and to improve the adhesion of bioactive glasses to titanium [4]. Borate glasses can be prepared with a wide range of thermal and chemical properties for different packaging applications. Little is known, however, about the high temperature interfacial reactions between these glasses and titanium.

### EXPERIMENTAL PROCEDURE

A variety of different borate glasses have been examined, including  $B_2O_3$  and a barium aluminoborate composition (in mole%,  $40BaO \cdot 20Al_2O_3 \cdot 40B_2O_3$ ) with a nominal thermal expansion match to titanium [for details, see refs. 3,5]. Reaction couples for analytical scanning electron microscopy were prepared from cups and lids, machined from commercially pure titanium (grade 2, 99+%), each enclosing a 6 mm diameter, 2 mm thick glass disk. Each couple was sealed in an evacuated (1 mTorr) silica ampule and heat treated for various times and temperatures, depending on glass composition. After heat treatment, the reaction couple was removed from the ampule, cross-sectioned perpendicular to the Ti/glass interface, mounted in epoxy, and polished to a one-micron diamond finish. The interfaces were observed with an optical microscope and then a scanning electron microscope (SEM). Where a reasonable amount of interface was observed, wavelength dispersive spectrometer (WDS) mapping for each of the elements in the diffusion couple was undertaken. A Pb-STE crystal was used for the light element B and O analysis. X-ray maps,  $256 \times 256$  pixels were obtained for each element with a dwell time of 0.2 sec per pixel. A beam



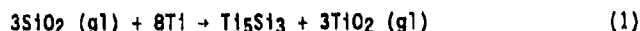
voltage of 15 kV and a beam current of ~100 nA was used. The high beam current was used to increase the x-ray count rate for B and O, although some contamination of the specimen surface occurred.

A number of axial seals were also made between 10 mm diameter aluminoborate or commercial silicate (Kimble Glass TM-9) glass rods and titanium, each joined after 30 minutes in an argon-atmosphere furnace. The aluminoborate glass seals were formed at 670°C and the silicate seals at 950°C. These seals were fractured in air at the glass/metal interface and both interfaces were examined by x-ray photoelectron spectroscopy (XPS). Binding energies have been referenced to the C1s peak at 284.8 eV for adventitious carbon.

### RESULTS AND DISCUSSION

The axial seals made between titanium and silicate glass could be easily separated by hand at the glass/metal interface, whereas the aluminoborate glasses adhered much more strongly to the titanium. These latter seals usually fractured in the glass, several millimeters from the titanium interface. These observations are in qualitative agreement with the finding that titanium pin seals made with aluminoborate glass withstand nearly twice the load before failure than do comparable seals made with silicate glass [3].

Figure 1 shows a Si2p photoelectron spectrum collected from the titanium side (upper trace) and the glass side (lower trace) of a silicate glass/titanium axial seal. The Si2p (~99 eV) and Ti2p<sub>3/2</sub> (453.6 eV, not shown) binding energies of the species on the Ti-side of this failed seal are typical of those reported for Ti-silicide thin films [6]. An interfacial silicide, most likely Ti<sub>5</sub>Si<sub>3</sub> [2], results from the reduction of the SiO<sub>2</sub> component of the glass:



TiO<sub>2</sub> (gl) represents the Ti<sup>3+</sup>/Ti<sup>4+</sup> ions that dissolve into silicate glass sealed to titanium [1-3]. The poor adherence of silicate glass to the interfacial silicide contributes to mechanically weak glass/Ti seals [2,3] and to the poor bonding of dental porcelain to Ti [7] and to the poor

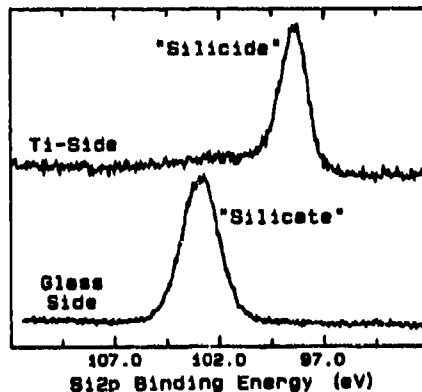


Figure 1: Si2p spectra of the two surfaces of a fractured axial seal between Ti and a silicate glass.

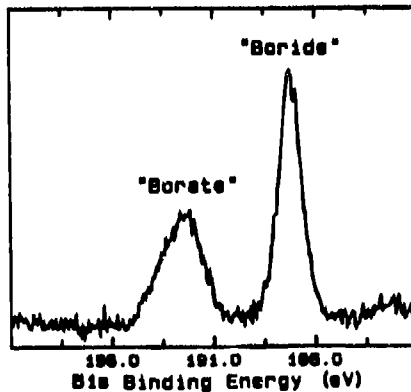


Figure 2: B1s spectrum of the Ti-side of an axial seal to an aluminoborate glass.

adherence of Ti-thin films to fused silica substrates [8].

Comparable reduction reactions occur when borate glasses are sealed to titanium. Figure 2 shows the Bis spectrum collected from the Ti side of an axial seal with a barium aluminoborate glass. These samples fractured in a much different manner than axial seals made with silicate glasses. Most of the titanium interface remains bonded to a glass layer several millimeters thick. The residual glass has a binding energy of  $\sim 192$  eV. However, a second Bis peak at  $\sim 187$  eV is associated with a reduced phase that is also adhered to the titanium. This latter binding energy is typical for metal borides [9].

The Ti-boride interfacial reaction product that forms under normal sealing conditions (e.g.,  $670^\circ\text{C}$  for 10-30 minutes) is too thin to be detected by SEM. (In comparison, the Ti-silicide interfacial layer is  $>1$   $\mu\text{m}$  thick after sealing a silicate glass for ten minutes at  $950^\circ\text{C}$  [3]). To identify the composition of this interfacial phase and to study its formation, glasses were reacted with Ti for up to 120 hours to yield sufficient reaction product for study by SEM.

Figure 3a shows a back scattered electron image of the interface between the barium aluminoborate glass and Ti after reaction for 120 hrs at  $800^\circ\text{C}$ . The glass has crystallized but remains adhered to the titanium, despite cracking. Precipitates can be seen extending up to  $10$   $\mu\text{m}$  into the titanium. The B x-ray map (fig. 3b) of this interface shows the boron-rich interfacial layer adhered to the Ti as well as the boron-rich precipitates in the Ti. Figure 4 shows the backscattered electron images of much larger precipitates extending over  $40$   $\mu\text{m}$  into the titanium from the interface of a  $1000^\circ\text{C}/16$  hr reaction couple with the barium aluminoborate glass. Similar Ti-B reaction products were noted at the interfaces of couples to  $\text{B}_2\text{O}_3$  and lanthanoborate glasses. With the possible exception of lanthanum-containing precipitates (not shown), no other glass cations are concentrated in the interfacial reaction products.

Very little is known about the thermochemical equilibria and kinetics of reactions between  $\text{B}_2\text{O}_3$  and Ti. Preliminary thermochemical calculations

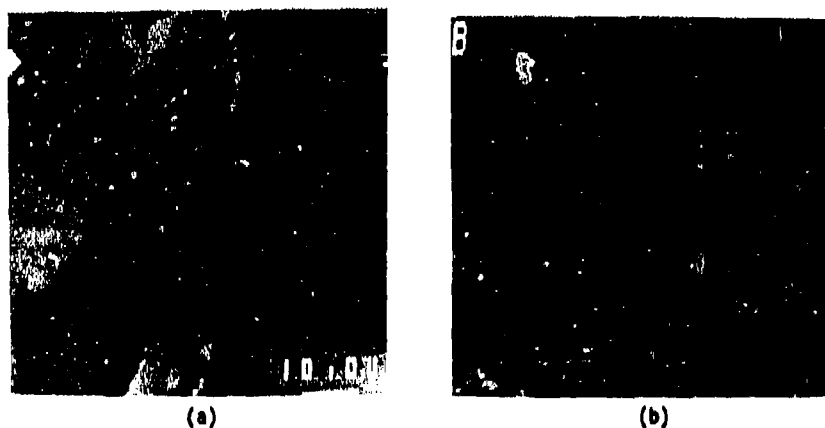


Figure 3: a) Backscattered electron image of the interface between a barium aluminoborate glass and Ti reacted at  $800^\circ\text{C}$  for 120 hours; b) the B x-ray map of the same area.

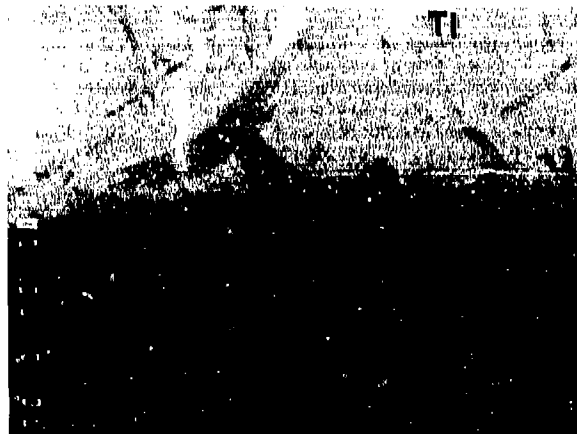


Figure 4: Backscattered electron image of the interface between a barium aluminoborate glass and Ti reacted at 1000°C for 16 hours.

of the B-O-Ti-Ar system have been done with the computer program SOLGASMIX [10] using the thermodynamic properties of potential reaction products listed in the JANAF tables [11]. At 973 K and 1 atm (conditions that simulate the environment used to prepare the aluminoborate/Ti axial seals),  $TiB_2$  is a thermodynamically stable reaction product only when the oxygen partial pressure ( $p_{O_2}$ ) is  $<10^{-33}$  atm; higher oxygen partial pressures oxidize the titanium and precludes reduction of  $B_2O_3$ . This  $p_{O_2}$  is well below that estimated for the graphite furnace ( $\sim 10^{-18}$  atm) used to prepare the axial seals that exhibit an interfacial Ti-boride. This suggests that the local environment of the glass/Ti interface is significantly more reducing than the furnace atmosphere. The dissolution of oxygen into Ti at the reaction interface may be one mechanism for lowering the local  $p_{O_2}$ .

West et al. [4] report the formation of crystalline  $TiBO_3$  as the result of the reaction between molten  $B_2O_3$  and Ti. Using this phase to represent  $Ti^{3+}$  dissolved into the glass, one possible interfacial reaction that yields  $TiB_2$  is:



$TiBO_3 (gl)$  represents the  $Ti^{3+}$  and/or  $Ti^{4+}$  ions that dissolve into the borate glass [3]. The thin borate glass layers that remain adhered to titanium when axial seals are fractured are usually discolored, suggesting that  $Ti^{3+}$  is present in the glass. The actual stoichiometry of the interfacial boride is, at present, unknown. The Ti-B phase diagram [12] suggests that  $TiB$ ,  $Ti_3B_4$ , and  $TiB_2$  are possible stoichiometries. Quantitative electron microanalysis of these reaction products are currently in progress.

The wavy interfaces of the glass/Ti reaction couples (Figs. 3 and 4) are characteristic of dissolution reactions. It thus appears that a titanium boride phase nucleates at the interface after an initial dissolution of Ti into the glass. Longer times and higher temperatures cause precipitates to grow because of the concomitant diffusion of boron from the glass into the titanium.

The development of an interfacial boride reaction product does not adversely affect the adherence of borate glass to titanium, in contrast to the well-known deleterious effect of silicide formation on the adherence of silicate glasses. This may be related to the relative kinetics of the two reactions. Considerably thicker silicide phases form when silicate glasses are reacted than the boride interfacial phases that form when borate glasses are sealed using comparable times and temperatures. As a result, the silicate seals are more susceptible to tensile stresses that would develop from possible thermal contraction and elastic moduli mismatches between the glass, the titanium, and the interfacial phases. The relative reaction kinetics and their effects on seal performance are currently under study.

#### ACKNOWLEDGEMENTS

This work was performed in part at Sandia National Laboratories and was supported by the U.S. Department of Energy under Contract No. DE-AC04-76DP00789.

#### REFERENCES

1. A. Passerone, G. Valbusa, E. Biagini, *J. Mater. Sci.* 12 (12), 2465 (1977).
2. Z. Feipeng, A.P. Tomsia, J.A. Pask, *Proc. 33rd Pacific Coast Meeting Amer. Ceram. Soc.*, San Francisco, CA, 1980 pp. 76-78.
3. R. K. Brow and R. D. Watkins, in *Technology of Glass, Ceramic, or Glass-Ceramic to Metal Sealing*, edited by W. E. Moddeman, et al. (Winter Annual Meeting, Amer. Soc. Mech. Eng., Boston, MA, 1987) pp. 25-30.
4. J.K. West, A.E. Clark, M.B. Hall, G.E. Turner, in *Handbook of Bioactive Ceramics, Vol. 1*, edited by T. Yamamuro, et al. (CRC Press, Boca Raton, FL, 1990) pp. 161-166.
5. R.K. Brow and R.D. Watkins, U.S. Patent No. 5,104,738 (14 April 1992).
6. D.R. Chopra, A.R. Chourasia, T.R. Dillinger, K.L. Peterson, B. Gnade, *J. Vac. Sci. Technol. A*, 5(4), 1984 (1987).
7. J.A. Hautaniemi, H. Hero, J.T. Juhanaja, *J. Mater. Sci. Mater. Med.*, 3, 186 (1992).
8. Y.S. Chaug, N.J. Chou, Y.H. Kim, *J. Vac. Sci. Technol. A*, 5(4) 1288 (1987).
9. G. Mavel, J. Escard, P. Costa, J. Castaing, *Surf. Sci.*, 35, 109 (1973).
10. G. Eriksson, *Chemica Scripta*, 8 100 (1975).
11. D. R. Stull, H. Propet, et al. *JANAF Thermochemical Tables*, 2nd Ed., (US Dept. of Commerce, National Bureau of Standards, Washington, DC, 1970).
12. J. L. Murray, P. K. Liao, K. E. Spear, *Bull. Alloy Phase Diagrams*, 7(6) 550 (1986).

## MICROSTRUCTURAL INVESTIGATION OF $\kappa$ -MODIFICATION LAYERS IN CVD $\alpha$ - $\text{Al}_2\text{O}_3/\kappa$ - $\text{Al}_2\text{O}_3$ MULTILAYER COATINGS

MATS HALVARSSON\*, SAKARI VUORINEN\*\* AND HANS NORDÉN\*

\* Department of Physics, Chalmers University of Technology, S-412 96 Göteborg, Sweden

\*\* Research and Development, SECO Tools AB, S-737 82 Fagersta, Sweden.

### ABSTRACT

Multi layer alumina coatings consisting of layers of either pure  $\alpha$ - $\text{Al}_2\text{O}_3$  or  $\kappa$ - $\text{Al}_2\text{O}_3$ , were deposited in a hot wall CVD reactor. In order to nucleate and grow a desired alumina polymorph ( $\alpha/\kappa$ ) in each layer, thin  $\alpha$ - and  $\kappa$ -modification layers were deposited between the alumina layers. This investigation examines the interfacial structure of the  $\kappa$ -modification and the alumina layers. The materials were examined using a combination of XRD, SEM, TEM and EDX.

The  $\kappa$ -modification layers exhibited an FCC structure and were composed of  $(\text{Ti,Al})(\text{C,O})$ . Orientation relationships were frequently found at the (i)  $\alpha$ - $\text{Al}_2\text{O}_3/\kappa$ -modification/ $\kappa$ - $\text{Al}_2\text{O}_3$  layer interfaces and (ii)  $\kappa$ - $\text{Al}_2\text{O}_3/\kappa$ -modification/ $\kappa$ - $\text{Al}_2\text{O}_3$  layer interfaces:

- (i)  $(0001)_\alpha // (\bar{1}\bar{1}\bar{1})_{\kappa\text{-mod}} // (001)_\kappa$   
 $[\bar{1}100]_\alpha // [110]_{\kappa\text{-mod}} // [010]_{\kappa 1} \text{ and } [310]_{\kappa 2}$
- (ii)  $(001)_\kappa // (\bar{1}\bar{1}\bar{1})_{\kappa\text{-mod}} // (001)_\kappa$   
 $[010]_{\kappa 1} \text{ and } [310]_{\kappa 2} // [110]_{\kappa\text{-mod}} // [010]_{\kappa 1} \text{ and } [310]_{\kappa 2}$

### INTRODUCTION

Alumina ( $\text{Al}_2\text{O}_3$ ) is one of the most frequently used CVD (Chemical Vapour Deposition) coating materials on cemented carbide cutting tools and is usually deposited on an intermediate layer of TiC, TiN or Ti(C,N) [1-3]. When alumina is produced by CVD, the most commonly occurring polymorphs are the stable alpha phase ( $\alpha$ - $\text{Al}_2\text{O}_3$ ) and the metastable kappa phase ( $\kappa$ - $\text{Al}_2\text{O}_3$ ) [1-3].

Multi  $\text{Al}_2\text{O}_3$  coatings consisting of pure  $\alpha$ - $\text{Al}_2\text{O}_3$  and  $\kappa$ - $\text{Al}_2\text{O}_3$  layers, were deposited in a hot wall CVD reactor. To nucleate and grow a desired alumina polymorph ( $\alpha/\kappa$ ) in each layer, thin intermediate layers, here referred to as  $\alpha$ - and  $\kappa$ -modification layers, were deposited between the alumina layers. To ensure good adhesion of the first  $\text{Al}_2\text{O}_3$  layer, thin layers - often referred to as *bonding layers* - were applied onto TiC before the alumina deposition. The bonding/alumina layer interfaces are described in detail elsewhere [4].

This investigation examines the interfacial structure of the  $\kappa$ -modification and the  $\text{Al}_2\text{O}_3$  layers. The composition of the  $\kappa$ -modification layers and the occurrence of orientation relationships between the  $\kappa$ -modification and the  $\text{Al}_2\text{O}_3$  layers have been examined.

### EXPERIMENTAL

#### Chemical Vapour Deposition

The coating deposition was carried out in a computer controlled hot wall CVD reactor. Commercial cemented carbide inserts (SNUN 120412) coated with TiC were used as substrates for the alumina coatings. The inserts contained 85 wt% WC and 5.5 wt% Co, the balance being cubic carbides (TiC, TaC, NbC). TiC was deposited from a  $\text{TiCl}_4$ - $\text{CH}_4$ - $\text{H}_2$  gas mixture. The  $\text{Al}_2\text{O}_3$  coatings were deposited using the gases  $\text{AlCl}_3$ ,  $\text{CO}_2$  and  $\text{H}_2$ .  $\text{AlCl}_3$  was generated within the deposition system through the chlorination of Al with HCl. The inlet gas compositions

Table I. The inlet gas composition (%).

	H <sub>2</sub>	CH <sub>4</sub>	TiCl <sub>4</sub>	CO <sub>2</sub>	HCl	AlCl <sub>3</sub>
TiC	Bal	7	4	-	1	-
Al <sub>2</sub> O <sub>3</sub>	Bal	-	-	5-7	1	2-3

which were used to grow TiC and Al<sub>2</sub>O<sub>3</sub> are given in Table I. All the experimental coatings were deposited at a pressure of 5 kPa.

In this investigation the interfaces between the  $\kappa$ -modification and the alumina layers have been examined. The  $\kappa$ -modification layers were deposited [5] both on an  $\alpha$ -Al<sub>2</sub>O<sub>3</sub> layer in order to nucleate  $\kappa$ -Al<sub>2</sub>O<sub>3</sub> on  $\alpha$ -Al<sub>2</sub>O<sub>3</sub> and on a  $\kappa$ -Al<sub>2</sub>O<sub>3</sub> layer in order to renucleate  $\kappa$ -Al<sub>2</sub>O<sub>3</sub> on  $\kappa$ -Al<sub>2</sub>O<sub>3</sub>. Hence, two different cases have been studied; (i)  $\alpha$ -Al<sub>2</sub>O<sub>3</sub>/ $\kappa$ -modification/ $\kappa$ -Al<sub>2</sub>O<sub>3</sub> layer interfaces; and (ii)  $\kappa$ -Al<sub>2</sub>O<sub>3</sub>/ $\kappa$ -modification/ $\kappa$ -Al<sub>2</sub>O<sub>3</sub> layer interfaces.

#### Analysis

The Al<sub>2</sub>O<sub>3</sub> multi coatings were examined in a JEOL 2000 FX transmission electron microscope (TEM) equipped with a LINK AN10000 energy dispersive x-ray analysis (EDX) system. In order to study the alumina/modification layer interfaces, cross section thin foils were prepared from CVD coated inserts by a method described in detail elsewhere [1,3]. Prior to the TEM investigation, the coatings were examined with scanning electron microscopy (SEM) and x-ray diffractometry (XRD).

Selected area electron diffraction (SAED) was used to determine the existence of epitaxy between the Al<sub>2</sub>O<sub>3</sub> layers and the  $\kappa$ -modification layers. Since SAED patterns can not be obtained from regions smaller than 500 nm, it was not possible to obtain SAED patterns exclusively from the  $\kappa$ -modification layer. Therefore SAED patterns from a large neighboring Al<sub>2</sub>O<sub>3</sub> grain and the  $\kappa$ -modification layer were obtained. The spots arising from the  $\kappa$ -modification layer could then be identified by dark field imaging.

In order to index a SAED pattern the symmetry elements of the analysed phases, described by their space groups, must be known [6]. There are three different types of crystal symmetry that result in the existence of reflection conditions, namely (i) centred unit cells, (ii) glide planes and (iii) screw axes.  $\alpha$ -Al<sub>2</sub>O<sub>3</sub> has a well established crystal structure and has the space group R $\bar{3}c$  [7-9], while it was only recently determined that  $\kappa$ -Al<sub>2</sub>O<sub>3</sub> is primitive orthorhombic with the space group Pna2<sub>1</sub> [10]. The reflection conditions for  $\alpha$ -Al<sub>2</sub>O<sub>3</sub> and  $\kappa$ -Al<sub>2</sub>O<sub>3</sub> are given in Table II. The indexing of  $\kappa$ -Al<sub>2</sub>O<sub>3</sub> is complicated by twinning of the orthorhombic unit cells and is further complicated by double diffraction [11].

## RESULTS AND DISCUSSION

### General microstructure

The thickness of each alumina layer was about 1  $\mu$ m. The microstructure of the  $\alpha$ -Al<sub>2</sub>O<sub>3</sub> layers consisted of equiaxed grains with a large number of dislocations and pores, while the

Table II. Reflection conditions.

$\kappa$ -Al <sub>2</sub> O <sub>3</sub>	$\alpha$ -Al <sub>2</sub> O <sub>3</sub>
Ok $\bar{l}$ : $k+l = 2n$	hk $\bar{l}$ : $-h+k+l = 3n$
h0 $\bar{l}$ : $h = 2n$	hk0: $-h+k = 3n$
h00: $h = 2n$	hh2hl: $l = 3n$
Ok0: $k = 2n$	000 $\bar{l}$ : $l = 6n$
00 $\bar{l}$ : $l = 2n$	hh00: $h = 3n$
	hh0 $\bar{l}$ : $h+l = 3n, l = 2n$

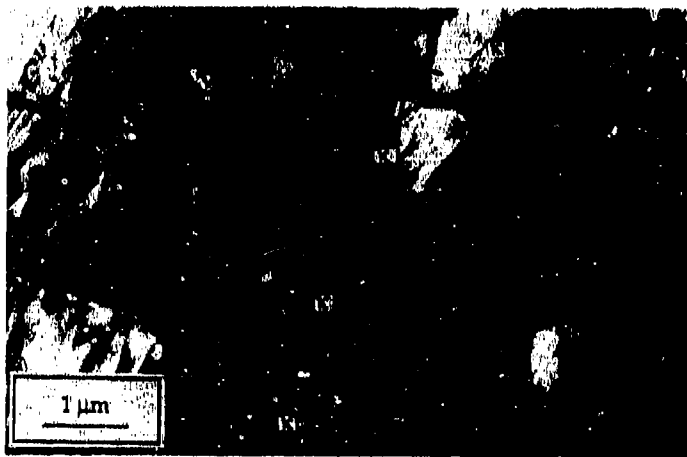


Figure 1. TEM micrograph of a multi  $\kappa$ - $\text{Al}_2\text{O}_3$  coating. The  $\kappa$ - $\text{Al}_2\text{O}_3$  layers are separated by thin  $\kappa$ -modification layers.

$\kappa$ - $\text{Al}_2\text{O}_3$  layers consisted of columnar, twinned grains which were dislocation and pore free. In all layers, the  $\alpha$ - $\text{Al}_2\text{O}_3$  grains were randomly distributed, while the preferred growth direction of  $\kappa$ - $\text{Al}_2\text{O}_3$  was along the  $c$ -axis. A multi  $\text{Al}_2\text{O}_3$  coating consisting of pure  $\kappa$ - $\text{Al}_2\text{O}_3$  layers separated by  $\kappa$ -modification layers is shown in Fig. 1.

The  $\alpha$ - $\text{Al}_2\text{O}_3$ / $\kappa$ -modification/ $\kappa$ - $\text{Al}_2\text{O}_3$  layer interfaces

Fig. 2 shows a TEM micrograph of the  $\alpha$ - $\text{Al}_2\text{O}_3$ / $\kappa$ -modification/ $\kappa$ - $\text{Al}_2\text{O}_3$  layer interfaces. EDX analyses of the  $\kappa$ -modification layer showed the presence of mainly Ti, C and O, and



Figure 2. The  $\alpha$ - $\text{Al}_2\text{O}_3$ / $\kappa$ -modification/ $\kappa$ - $\text{Al}_2\text{O}_3$  layer interfaces.



Figure 3. Diffraction patterns from a) the  $\alpha$ - $\text{Al}_2\text{O}_3$  grain and b) the  $\kappa$ -modification layer and the  $\kappa$ - $\text{Al}_2\text{O}_3$  grain at the  $\kappa$ - $\text{Al}_2\text{O}_3$ / $\kappa$ -modification/ $\kappa$ - $\text{Al}_2\text{O}_3$  layer interfaces shown in Fig. 2.

smaller amounts of Al and therefore the composition of the  $\kappa$ -modification layer can be described as  $(\text{Ti,Al})(\text{C,O})$ .

A SAED pattern from the  $\alpha$ - $\text{Al}_2\text{O}_3$  grain in Fig. 2 is shown in Fig. 3a, and a pattern from the  $\kappa$ - $\text{Al}_2\text{O}_3$  grain and the  $\kappa$ -modification layer in Fig. 2 is shown in Fig. 3b. The diffraction patterns are oriented correctly with respect to each other. The  $\alpha$ - $\text{Al}_2\text{O}_3$  pattern can be indexed as the  $[1\bar{1}20]$ -zone, while the  $\kappa$ -modification layer can be indexed as the  $[112]$ -zone for an FCC structure. The  $\kappa$ - $\text{Al}_2\text{O}_3$  pattern can be indexed as a superposition of the  $[100]$  and the  $[110]$ -zone  $[11]$ . As can be seen in Fig. 3 several plane normals are parallel:

$$(0006)_\alpha // (\bar{1}\bar{1}\bar{1})_{\kappa\text{-mod}} // (002)_\kappa \quad (1)$$

$$(\bar{3}300)_\alpha // (220)_{\kappa\text{-mod}} // (020)_{\kappa 1} \text{ and } (110)_{\kappa 2} \quad (2)$$

where  $\kappa 1$  and  $\kappa 2$  stand for two twin related  $\kappa$ - $\text{Al}_2\text{O}_3$  domains and  $\kappa$ -mod is short for  $\kappa$ -modification layer. Generally, orientation relationships between two phases a and b are given in the form

$$(h_1 k_1 l_1)_a // (u_1 v_1 w_1)_b \quad (3)$$

$$[h_2 k_2 l_2]_a // [u_2 v_2 w_2]_b \quad (4)$$

Thus in order to express the orientation relationship (1) and (2) in the form (3) and (4), parallel plane normals in (2) have to be replaced by parallel directions. Directions  $[hkl]$  are not (in general) parallel with plane normals  $(hkl)$  in non-cubic coordinate systems. For hexagonal systems the normal  $[defg]$  to the plane  $(hkl)$  will have the indices

$$[defg] = [h, k, i, \frac{3a^2}{2c^2}l] \quad (5)$$

For orthorhombic systems the normal  $[uvw]$  to the plane  $(hkl)$  is given by

$$\frac{u}{h} a^2 = \frac{v}{k} b^2 = \frac{w}{l} c^2 \quad (6)$$

Thus, the relationships (1) and (2) can be rewritten as

$$(0001)_\alpha // (\bar{1}\bar{1}\bar{1})_{\kappa\text{-mod}} // (001)_\kappa \quad (7)$$

$$[\bar{1}100]_\alpha // [110]_{\kappa\text{-mod}} // [010]_{\kappa 1} \text{ and } [310]_{\kappa 2} \quad (8)$$



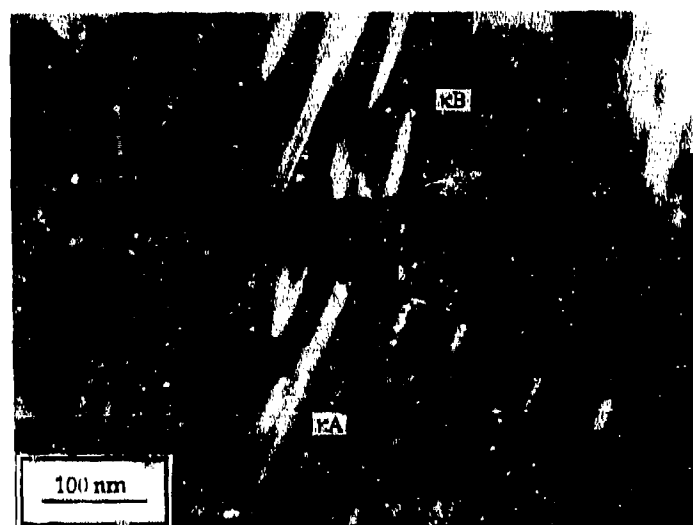


Figure 4. TEM micrograph from the  $\kappa$ -Al<sub>2</sub>O<sub>3</sub>/ $\kappa$ -modification/ $\kappa$ -Al<sub>2</sub>O<sub>3</sub> layer interfaces.

#### The $\kappa$ -Al<sub>2</sub>O<sub>3</sub>/ $\kappa$ -modification/ $\kappa$ -Al<sub>2</sub>O<sub>3</sub> layer interfaces

A TEM micrograph of the  $\kappa$ -Al<sub>2</sub>O<sub>3</sub>/ $\kappa$ -modification/ $\kappa$ -Al<sub>2</sub>O<sub>3</sub> layer interfaces is shown in Fig. 4. The EDX analyses of the  $\kappa$ -modification layer deposited on  $\kappa$ -Al<sub>2</sub>O<sub>3</sub> indicated a similar composition as for the  $\kappa$ -modification layer deposited on  $\alpha$ -Al<sub>2</sub>O<sub>3</sub>, that is (Ti,Al)(C,O), with Ti, C and O as the main constituents.

Fig. 5a shows a SAED pattern from the  $\kappa$ -Al<sub>2</sub>O<sub>3</sub> grain marked  $\kappa$ A in Fig. 4, and Fig. 5b shows a pattern from the  $\kappa$ -modification layer and the  $\kappa$ -Al<sub>2</sub>O<sub>3</sub> grain marked  $\kappa$ B in Fig. 4. The diffraction patterns are oriented correctly with respect to each other. The  $\kappa$ -modification layer can be indexed as the [112]-zone for an FCC structure. The  $\kappa$ -Al<sub>2</sub>O<sub>3</sub> pattern can be indexed as a



Figure 5. Diffraction patterns from a) the  $\kappa$ -Al<sub>2</sub>O<sub>3</sub> grain marked  $\kappa$ A and b) the  $\kappa$ -modification layer and the  $\kappa$ -Al<sub>2</sub>O<sub>3</sub> grain marked  $\kappa$ B at the  $\kappa$ -Al<sub>2</sub>O<sub>3</sub>/ $\kappa$ -modification/ $\kappa$ -Al<sub>2</sub>O<sub>3</sub> layer interfaces in Fig. 4.

superposition of the [100] and the  $\bar{1}\bar{1}0$ -zone [11]. The following orientation relationships can be determined from Fig. 5:

$$(002)_{\kappa A} // (\bar{1}\bar{1}\bar{1})_{\kappa\text{-mod}} // (002)_{\kappa B} \quad (9)$$

$$(020)_{\kappa A1} \text{ and } (110)_{\kappa A2} // (220)_{\kappa\text{-mod}} // (020)_{\kappa B1} \text{ and } (110)_{\kappa B2} \quad (10)$$

where the indices  $\kappa A$  and  $\kappa B$  refer to Fig. 4 and the indices 1 and 2 refer to two twin related  $\kappa\text{-Al}_2\text{O}_3$  domains. To obtain the orientation relationship in the form (3) and (4), relation (10) has to be transformed to parallel directions by using equation (6). Thus, (9) and (10) can be rewritten as:

$$(001)_{\kappa A} // (\bar{1}\bar{1}\bar{1})_{\kappa\text{-mod}} // (001)_{\kappa B} \quad (11)$$

$$[010]_{\kappa A1} \text{ and } [310]_{\kappa A2} // [110]_{\kappa\text{-mod}} // [010]_{\kappa B1} \text{ and } [310]_{\kappa B2} \quad (12)$$

## CONCLUSIONS

- The  $\kappa$ -modification layers exhibited an FCC structure and were composed of  $(\text{Ti,Al})(\text{C,O})$ .
- Epitaxy was frequently found at the alumina /  $\kappa$ -modification layer interfaces and can be described as:

(i)  $\alpha\text{-Al}_2\text{O}_3/\kappa\text{-modification}/\kappa\text{-Al}_2\text{O}_3$

$$(0001)_{\alpha} // (\bar{1}\bar{1}\bar{1})_{\kappa\text{-mod}} // (001)_{\kappa}$$

$$[\bar{1}100]_{\alpha} // [110]_{\kappa\text{-mod}} // [010]_{\kappa1} \text{ and } [310]_{\kappa2}$$

(ii)  $\kappa\text{-Al}_2\text{O}_3/\kappa\text{-modification}/\kappa\text{-Al}_2\text{O}_3$

$$(001)_{\kappa} // (\bar{1}\bar{1}\bar{1})_{\kappa\text{-mod}} // (001)_{\kappa}$$

$$[010]_{\kappa1} \text{ and } [310]_{\kappa2} // [110]_{\kappa\text{-mod}} // [010]_{\kappa1} \text{ and } [310]_{\kappa2}$$

## REFERENCES

- [1] S. Vuorinen and J. Skogsmo, *Thin Solid Films* **193/194**, 536 (1990).
- [2] C. Chatfield, J. N. Lindström and M. E. Sjöstrand, *J. Phys. Colloq.* **C5**, 377 (1989).
- [3] S. Vuorinen and J. Skogsmo, in *Surface Modification Technologies*, edited by T. S. Sudarshan and D. G. Bhat, (TMS, Phoenix, AZ, 1988), p. 143.
- [4] M. Halvarsson, S. Vuorinen and H. Nordén, ICMCTF 1993 San Diego, USA, to be published.
- [5] S. Ruppi, U.S. Patent No. 5 137 744 (1992).
- [6] T. Hahn and A. Vos, in *International Tables for Crystallography*, edited by T. Hahn, (D. Reidel Publishing Company, Dordrecht: Holland / Boston: USA, 1983), pp 27-30.
- [7] L. Pauling and S. B. Hendricks, *J. Am. Chem. Soc.* **47**, 781 (1925).
- [8] M. L. Kronberg, *Acta Met.* **5**, 508 (1957).
- [9] R. E. Newnham and Y. M. DeHaan, *Z. Krist.* **117**, 235 (1962).
- [10] P. Liu and J. Skogsmo, *Acta Cryst.* **B47**, 425 (1991).
- [11] M. Halvarsson, S. Vuorinen and H. Nordén, ECASIA 1993 Catania, Italy, to be published.

# LOCAL MECHANICAL STABILITY OF THE ALUMINUM / CARBON (AMORPHOUS) AND ALUMINUM / SiO<sub>2</sub> (AMORPHOUS) INTERFACE AT EXTRINSIC DISLOCATIONS

E.D. McCarty and S.A. Hackney

Dept. of Metallurgical Engineering, Michigan Technological University, Houghton, MI 49931

## ABSTRACT

Interfaces between Al and amorphous C or amorphous SiO<sub>2</sub> were prepared by sputter deposition of the ceramic phases onto the sputter cleaned surfaces of large grain Al. *In situ* TEM was used to study the behavior of the extrinsic dislocations (slip traces) at the metal/ceramic interface formed by the motion of Al lattice dislocations which intersect the interphase boundary plane. The proximity of the extrinsic lattice dislocation to the metal/ceramic interface places this interphase boundary under a highly localized stress. Relaxation behavior of extrinsic defects at the interface region is a function of the defect standoff distance from the interface, image stress and the applied stress. An experimental technique is proposed to estimate the minimum shear stress the various interfacial regions are able to withstand. Research supported by the Department of Energy.

## INTRODUCTION

The local response of bimaterial interfaces to applied loads is thought to be of great relevance to a variety of technologically important processes. The behavior of thin film epitaxial interfaces at the point of coherency breaking [1] and bimaterial interfacial fracture [2] are two cases where atomic level interfacial bonding under stress has been considered in detail from a theoretical point of view. The questions which arise about the local behavior of the interface appear to be associated with what assumptions are realistic concerning continuity of stress and displacements at the boundary between two different materials. The concepts of interface sliding, interface fracture, and interface modulus have been introduced into the literature in an attempt to treat the manner in which the local interface response will contribute to macroscopic behavior. These processes and properties are considered to be localized to the interface or the interfacial region and the introduction of such ideas suggests a conviction that the interfacial region will behave in a substantially different manner than the bulk. Experimental studies of interfacial properties must therefore be designed to extract information about the very small volume of material which constitutes the interfacial region. Macroscopic experimental measurements can be made on the work required to cause the decohesion of bimaterial interfaces under tension or shear, for example, and it may be possible to extract from these results the atomic scale interface response if the work related to the deformation of the bulk materials can be separated from the response of the interfacial region. However, it may be of interest to attempt studies which directly examine the local response of the interfacial region to applied stress. This work presents a type of dynamic transmission electron microscopy study of the local bimaterial interface response to the applied stress field of the dislocation. The approach relies heavily on previous work [3] & [4], which studied the contrast behavior of dislocation-like defects resulting from the intersection of moving dislocations with metal-oxide interfaces formed during an electropolishing process. The work presented in this paper is limited to the comparison of the interface region between sputter cleaned Al and sputter deposited, amorphous SiO<sub>2</sub> and the interface region between sputter cleaned Al and sputter deposited, amorphous C.

A moving edge dislocation with line direction perpendicular to the interface and Burgers vector in the plane of the interface will produce a shear stress at the interface due to the Al lattice displacements associated with the motion of the dislocation. If the interfacial region constrains the shear displacement a screw dislocation is formed near the interface. These line defects are referred to as extrinsic dislocations or slip traces. If the interfacial region does not constrain the shear displacements, a strain free step is produced which would not be visible in the TEM using traditional techniques. Thus, TEM imaging can be used as a tool to directly study the local response of an interface to the stress field of a dislocation.

## EXPERIMENTAL PROCEDURE

Three millimeter disks were punched from 25 micron thick, 99.9995% pure polycrystalline aluminum foil and annealed at 450 °C for 24 hours. The samples were electropolished in a 25% nitric acid, 75% methanol solution until perforation. Further thinning and cleaning of the foil was performed by ion milling both surfaces with 2 KeV accelerating voltage, 0.3 gun current, and a gun angle of 25 to 30 degrees. Five sample groups were prepared, a control group composed of undeposited samples, a group with sputter deposited carbon on both sides (C/C), a group with sputter deposited silica on both sides (S/S), a mixed deposition group with silica sputter deposited on one surface and carbon on the opposite surface (S/C), and finally, a group of samples where silica was deposited upon one surface and on the opposite surface a thin layer of carbon was sputter deposited upon the aluminum surface followed by a thicker layer of silica (SC/S). Samples were examined in a JEOL 100-CX Transmission Electron Microscope. The orientation of the sample, the Burgers vector and the slip plane of inclined dislocations were determined by  $g\cdot b$  analysis and information relating to extrinsic dislocation relaxation behavior was obtained.

## EXPERIMENTAL RESULTS

Slip traces were found to relax immediately under the influence of the transmission electron beam in the control samples which had not been coated by silica or carbon. Similar rapid extrinsic defect relaxation was observed for the C/Al interfaces in C/C samples except relaxation of the defects was also observed to occur by a slower piecewise relaxation process. The piecewise relaxation was observed to occur in three steps. Initially, catastrophic failure of a portion of the slip trace occurred followed by a gradual reduction in line length of the remaining slip traces until either total relaxation occurred or small stable extrinsic dislocation pieces remained behind. Extrinsic defects at the silica/aluminum interfaces differed in behavior from the carbon/aluminum interfaces and the undeposited surfaces where the extrinsic dislocations were found to resist relaxation. The S/C samples allowed for direct comparison of extrinsic dislocation behavior where the more complete relaxation of defects at the C/Al interface was strongly evident over the more stable extrinsic defects at the silica/Al interface, shown in Figure 1.

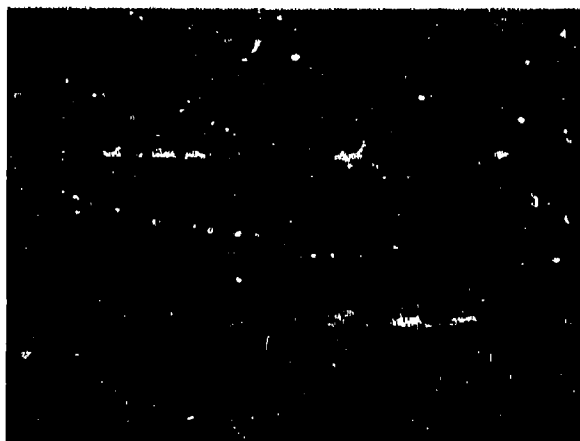


Figure 1: S/C sample with increased extrinsic defect relaxation on the Al/C interface (upper slip trace) over the silica/Al interface (lower slip trace).

Figure 2 shows the type of specimen geometry for a S/C sample where carbon is sputter deposited on one surface and silica is sputter deposited on the opposite surface. A moving dislocation, inclined at some angle to the surface of the foil, is shown to create slip traces at the intersection of the inclined dislocation with the two bimaterial interfaces. As shown in Figure 1, relaxation of the extrinsic dislocation is observed for the C/Al interface and not the silica/Al interface. The intersection of the inclined dislocation with the bimaterial interface is called a pinning point. For the TEM samples, the specimen geometry would consider a wedge shaped foil not depicted in the following figure.

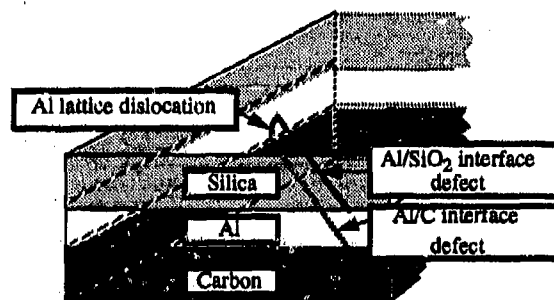


Figure 2: Specimen geometry for a S/C sample with moving dislocation and subsequent formation of slip traces at each of the bimaterial interfaces.

Shown in Figure 3, the presence of a thin interlayer of carbon between the silica and the aluminum substrate in the SC/S samples allowed for nearly complete extrinsic defect relaxation at that interface while on the opposing silica/Al interface, extrinsic defects were found to exhibit minimal relaxation.

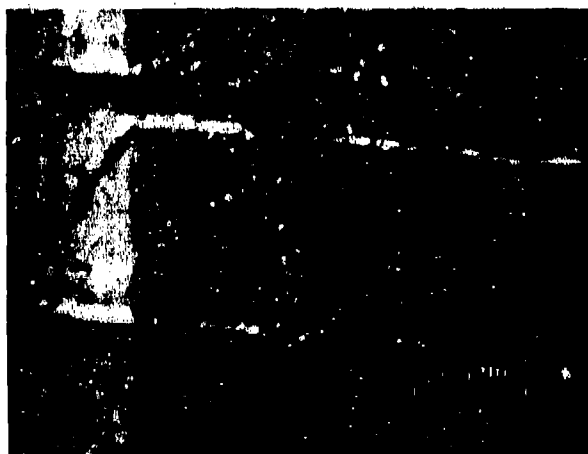


Figure 3: SC/S sample with extrinsic defect relaxation on the silica-carbon/aluminum interface (upper slip trace) and no relaxation on the silica/aluminum interface (lower slip trace).

Table I depicts the relaxation behavior and minimum times to relaxation observed for the various samples described in the experimental procedure. As shown, the relaxation behavior for the C/Al interfaces did not differ much from the control group where extrinsic defects completely relaxed in less than one minute. Extrinsic defects at the silica/Al interfaces showed substantial resistance to relaxation even after fifteen minutes but with the addition of a thin interlayer of carbon complete relaxation was observed in less than ten seconds.

Table I: Specimen groups

Group Type	Side A Behavior	Side A: Minimum Time to Relaxation	Side B Behavior	Side B: Minimum Time to Relaxation
Control group	Near Total Relaxation after 15 Minutes	10 Seconds	Near Total Relaxation after 15 Minutes	10 Seconds
C / C (2 kV)	Partial Relaxation after 15 Minutes	30 Seconds	Partial Relaxation after 15 Minutes	30 Seconds
S / S (2 kV)	Partial to Zero Relaxation	> 15 Minutes	Partial to Zero Relaxation	> 15 Minutes
S / C (2 kV)	Partial to Zero Relaxation	> 15 Minutes	Near Total Relaxation after 15 Minutes	30 Seconds
SC / S (2 kV)	Near Total Relaxation	10 Seconds	Partial to Zero Relaxation	> 30 Minutes

## ANALYSIS

Consideration is given only to the mathematically simple case where the atoms at the interface are highly resistant to the elastic displacements associated with the strain field of an extrinsic defect. The image force on an extrinsic dislocation can then be easily determined from a zero displacement boundary condition at the interface. The zero displacement boundary condition can be fulfilled by the use of an image dislocation of the same sign and equal strength. Of course, this is a limiting case which will determine the maximum possible image force. Any results which are obtained from this analysis will then be limiting values. With this disclaimer noted, the elastic displacement field along the z direction for the screw dislocation in the ductile phase is...

$$u_z = \left(\frac{b}{2\pi}\right) \times \tan\left(\frac{y}{x+\lambda}\right) + \left(\frac{b}{2\pi}\right) \times \tan\left(\frac{y}{x-\lambda}\right) \quad (1)$$

where  $\lambda$  is the stand-off distance ([6], [7]) and the geometry is shown in Figure 4. Equation (1) determines a zero displacement at the interface at  $x=0$ . The important terms which arise from this analysis are the image stress [5], the shear stress on the real dislocation from the image dislocation, and the stress on the interface from the extrinsic dislocation. The image stress is determined from linear elasticity theory as...

$$\sigma_{yz}|_{\text{image}}^{(x=-\lambda), (y=0)} = \left(\frac{-\mu b}{4\pi\lambda}\right) \quad (2)$$

which is equal in magnitude but of opposite direction to the image force from a free surface [8]. In contrast to the image force from the stress free surface, this image force pushes the dislocation away from the interface.

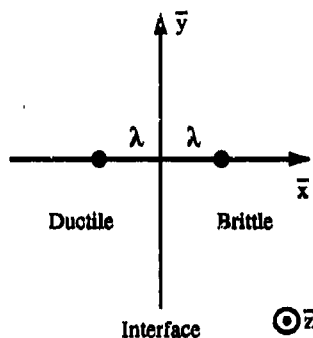


Figure 4: Image forces and dislocation relative to the beam direction  $\bar{x}$  and the direction along the interface  $\bar{y}$ .

The stress on the interface is determined from linear elasticity theory as.....

$$\sigma_{zy}|_{x=0} = 0 \quad (3)$$

$$\sigma_{zx}|_{x=0} = \left( \frac{-\mu b}{\pi} \right) \times \left( \frac{y}{\lambda^2 + y^2} \right) \quad (4)$$

with the maximum stress magnitude occurring at  $y = \pm \lambda$ .

At mechanical equilibrium,  $\sigma_{zx} = \sigma_{xz}$  and the interface will have both a normal and tangential shear strain due to the extrinsic screw dislocation. The standoff distance in equation (1-4) may be related to the applied stress on the dislocation at equilibrium when there is a balance between the applied stress and the image stress.

$$-\sigma_{yz}^{applied} = \sigma_{yz}^{image} = \frac{-\mu b}{4\pi\lambda} \quad (5)$$

With the specimen geometry used in this study, it is possible to make measurements which estimate the applied stress on the dislocation. Since the interfaces of interest are in films of wedge shaped cross section typical of electropolished TEM specimens, the dislocations will encounter increased line tension forces as the dislocation positions change from the thicker areas to the thinner areas. The applied stress may be approximated by noting the foil thickness at which the dislocations are pinned. At this point, the resolved stress on the dislocation is balanced by the line tension forces on the bowed dislocation [9]. The simplest form of this expression is.....:

$$\sigma_{yz}^{applied} \approx \frac{\mu b}{t} \quad (6)$$

where  $t$  is the experimentally measured distance between pinning points on the two foil surfaces. Thus  $\lambda$  may be determined from (5) and (6) as:

$$\lambda \approx \frac{t}{4\pi} \quad (7)$$

Of course, this is the maximum  $\lambda$  which can occur for a given applied stress due to the assumptions about the interface boundary condition used in determining equation (1). Thus, the combination of equation (4) and equation (7) determines the minimum stress on the interface due to an extrinsic dislocation for a given applied stress.

Because the resolved stress will be different on the various slip systems and even various slip planes within the same system, it is possible to study the behavior of a given interface under differing stand off distances and thus differing stresses. The experimentally observed variation of  $t$  for different dislocations may be used to determine the standoff distance (Equation 7) and thus the interfacial shear stress (Equation 4). By studying the relaxation of extrinsic screw dislocations as a function of  $t$ , it may be possible to determine limiting values of the local shear strength of the interfacial layer. By determining the Burgers vector, the slip plane and the inclined length of a dislocation, the standoff distance can be determined and thus an estimate of the minimum shear

stress the interface sees as the result of an extrinsic dislocation at standoff distance  $\lambda$  from the interface.

Using this approach it can be found that extrinsic screw dislocations at the carbon interface relaxes when  $t$  is between  $2.1 \times 10^{-5}$  cm and  $2.3 \times 10^{-5}$  cm while relaxation at the silica interface occurs when  $t$  is between  $1.4 \times 10^{-5}$  cm and  $1.8 \times 10^{-5}$  cm. Since the stress calculations are done for the maximum standoff distance, and thus the minimum interfacial stress, the experimental results may be interpreted as showing that the shear strength of the Al/carbon interface is not less than that calculated for  $t=2.3 \times 10^{-5}$  cm, which is 28 MPa and the shear strength for the Al/silica interface is not less than that calculated for  $t=1.8 \times 10^{-5}$  cm, which is 62 MPa. A more quantitative statement about the relative interface shear strength of the two interface types can be made for the case where the standoff distances are the same at applied stresses lower than that required to cause interface relaxation. In this case, the actual difference in shear strength will be closely approximated by the difference in the limiting values calculated above.

## CONCLUSION

The Al/C interfacial region showed a substantially lower shear strength than the Al/SiO<sub>2</sub> interfacial region as indicated by direct comparison of extrinsic screw dislocation relaxation behavior at the two types of interfaces on the same grain (Figure 2). One type of interface consisted of a ten second deposition of carbon between the aluminum layer and the deposited silica layer, producing a carbon layer on the order of ten angstroms thick. This thin C interlayer causes a dramatic decrease in the interfacial strength and the observed relaxation phenomenon in this case is clearly due to a process localized to an atomic scale region of the interface. The implication is that the stress from a dislocation strain field can be utilized to study the local properties of an interfacial region. Estimates of the shear strength of a specific interface can be experimentally determined by measuring the applied stress on a dislocation and the relaxation behavior as a function of this applied stress.

## REFERENCES

1. J. H. Van der Merwe, and C.A.B. Ball in Epitaxial Growth, Part b, edited by J.W. Matthews, Academic Press, New York, 1975.
2. A.B. Varias, and N.P. O'Dowd, Material Science and Engineering, 1990, A126, pp 65-93.
3. P.B. Hirsh, A. Howie, R.B. Nicholson, D.W. Pashley, and M.J. Whelan, Electron Microscopy of Thin Crystals, Butterworth Inc., Washington D.C. 1965.
4. M.J. Whelan, Journal of the Institute of Metals, 1959, Vol. 87, pp 392-405
5. A.K. Head, Phil. Mag., 1953, Vol. 44, 92-94.
6. S.V. Kamat, J.P. Hirth, and B. Camahan, Mat. Res. Soc. Symp. Proc., 1988, Vol. 103, 55-60.
7. W. Mader, and D. Knauss, "Equilibrium Position of Misfit Dislocations at Planar Interfaces," Accepted to Acta Met. Mater. 1992.
8. J.P. Hirth, and J. Lothe, Theory of Dislocations, John Wiley & Sons, New York, 1982.
9. G.E. Dieter, Mechanical Metallurgy, McGraw Hill Book Company, New York, 1986.



## MICROANALYSIS OF A COPPER-TO-GRAPHITE SOLDER BOND

JAMES B. INTRATER

Advanced Technology, Inc., 2110 Ringwood Ave., San Jose, CA 95131

### ABSTRACT

SEM, x-ray microprobe and EDS analysis was performed on a uniquely prepared joint of graphite soldered to copper with 60Sn-40Pb. The presented data shows a segregation of chromium out from the metallization paste to the graphite/solder interface. Dot maps of the other elemental species were also generated.

### BACKGROUND

Soldering and brazing to non-metals such as graphite, can be a technical challenge. One popular method for secure metallurgical bonds to carbon and general, conventional ceramics is known as the "active metal" approach [1-7]. This method relies on the addition of a column IVB metal (Ti, Zr or Hf) to conventional solder and braze compositions and firing these mixtures in an extremely inert atmosphere (e. g., Ar or vacuum) at generally 850-950° C at which point the active metal component will migrate toward the non-metal/filler interface and undergo compound formation with the various ionic species present. An alternative, patented process for thick film metallizing ceramic materials is termed the Intragene™ process [8-10]. This metallization is prepared through the application of a -325 mesh metallic powder mixture of tin with particular transition metals added to typically below 8 wt. %, in an appropriate organic vehicle. This mixture is then painted or screen printed onto the substrate of interest, dried, and the fired generally to 800-900°C for roughly 10-15 minutes at temperature. The firing atmosphere must have a presence of CO in it to facilitate the bonding/wetting reaction. It is known, however, that by firing such a paste in an N<sub>2</sub> atmosphere that sufficient CO is generated locally by the binder burnout, that successful metallization can be achieved with this atmosphere. This procedure will yield a direct metallurgical bond of the tin-rich composition to the substrate surface and, further, the formed metallization surface can be safely reflowed at 232°C (the melting point of tin) without dewetting from the surface. Through reflowing conventional solder compositions into the metallization layer, the surface can be converted into a solder layer, tenaciously adherent onto the substrate surface. It is presently believed that the metallization constituents alloy and then undergo oxycarbide formation with CO followed by solution formation with the surface of the substrate and with a substrate such as graphite, revert to a carbide structure (with oxygen outgassing). Possible advantages over active metal methods can include avoidance of excessive and unarrested diffusion reactions between the substrate and the active metal, and avoidance of oxidation/competitive reaction possibilities of the final metallization surface.

In the specific case of graphite, a composition of 5 wt. % Cr-balance Sn, is generally used as the metallization composition. The solderable layer that the above process generates allows for the soldering of graphite to OFHC copper for applications utilizing the conjunctive use of the two materials. One such application is the soldering of graphite sputtering targets to copper backing plates, where both electrical throughput and heat dissipation to and from the graphite is required, respectively.

This research focused on determining the elemental distribution analysis of a graphite to copper solder joint prepared via the described method.

## EXPERIMENTAL PROCEDURE

A piece of high purity (99.9995%)/high density (1.90 gm/cm<sup>3</sup>) graphite\* was painted with an Intragene™ composition of 5 wt. % Cr-Bal. Sn and air dried at 150°C for 8 minutes. The part was then fired in an N<sub>2</sub> atmosphere to 900°C for 20 minutes at temperature. The part was then cooled and removed. The binder had burned out from the paste and the final graphite piece was fully metallized on the surface. The graphite piece was then placed on a hot plate and heated to approx. 250°C at which point the metallization layer was then quickly thinned down in its molten state with a razor blade. Conventional solid bar 60Sn-40Pb solder was reflowed on top of the metallization surface and this part was then placed with metallization face down, against a pre-tinned, pre-solder-wetted piece of OFHC copper, also at 250°C. The resultant part was then cooled, sectioned and then subjected to SEM/x-ray fluorescence analysis. Generated were backscatter and secondary electron images of the overall joint along with elemental dot maps for C, Cr, Pb, Sn and Cu with EDS quantitative data collected for Sn and Pb in the solder region and Sn and Cu in their interdiffusion zone.

## RESULTS

Figure 1 shows a 300X backscatter image of the joint with graphite at top and copper at bottom. Scratch and pit marks reflect haste in our sectioning work though this did not seem to interfere with data collection. Five zones appear distinctly present. From the top down they are:

- 1-A pitch black (i. e. low atomic #) layer (graphite)
- 2-A approx. 10µm. thick semi-dark region
- 3-The bulk of the intermediate phase (approx. 100µm. thick)
- 4-A region between zone 3 and the bottom phase (approx. 45µm. thick)
- 5-Bottom phase (copper)

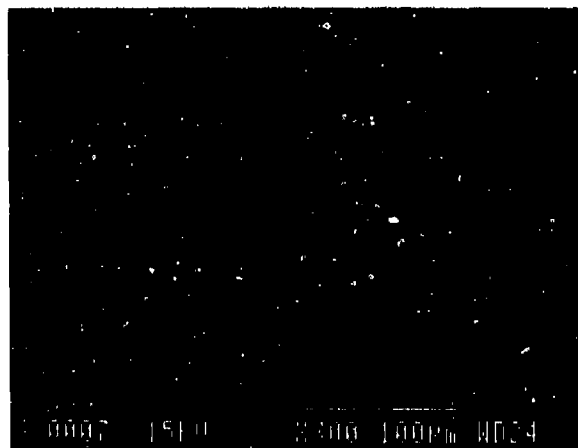


Figure 1. 300X backscatter electron image of bond cross-section showing 5 distinct phases present in bond.

\* Grade 1G510U, Toyo Tanso USA, Troutdale, OR

Figure 2. is a 500X secondary electron image of the joint. Figures 3-7 are the elemental dot maps for this same region for C, Cr, Pb, Sn and Cu, respectively. Ignoring possible stray signals and dots due to debris effects, the same 5 regions appearing in Figure 1 can be described as follows:

- 1- Pure carbon
- 2-Almost pure Cr
- 3-Sn-Pb solder region
- 4-Zone of interdiffusion of Sn with Cu
- 5-Pure Cu

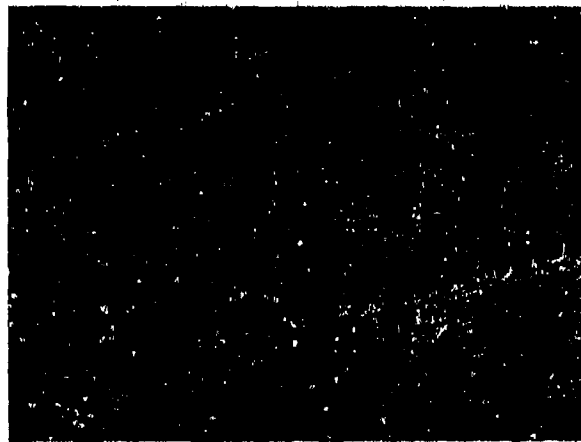


Figure 2. 500X Secondary electron image of solder bond.

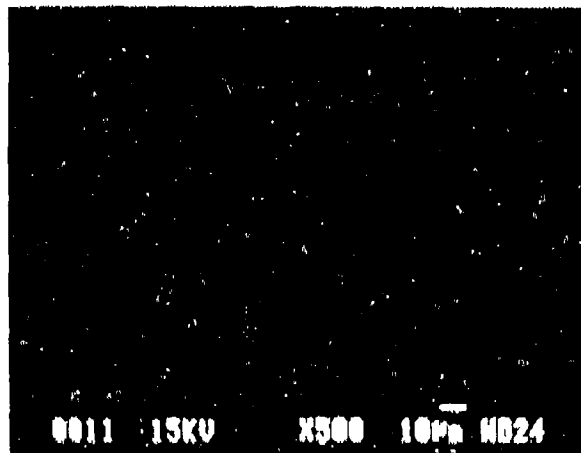


Figure 3. Elemental dot map for C showing graphite where expected.

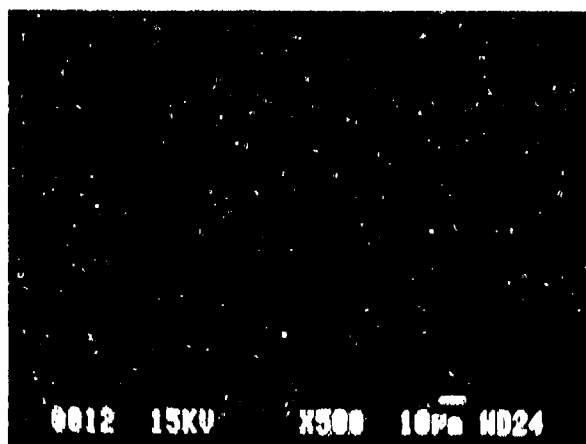


Figure 4. Elemental dot map for Cr showing enrichment at the solder/graphite interface. Spectrum for this region is shown in Figure 8. Zone is essentially pure Cr.

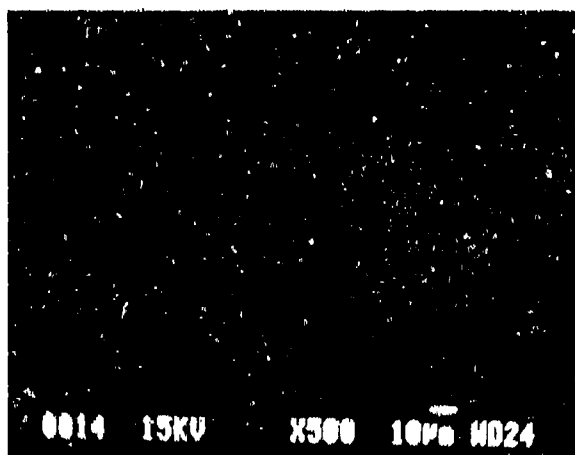


Figure 5. Elemental dot map for Pb showing uniform distribution throughout the solder layer. EDS analysis showed this region to have roughly 37.5 wt. % Pb which approximates the starting composition.

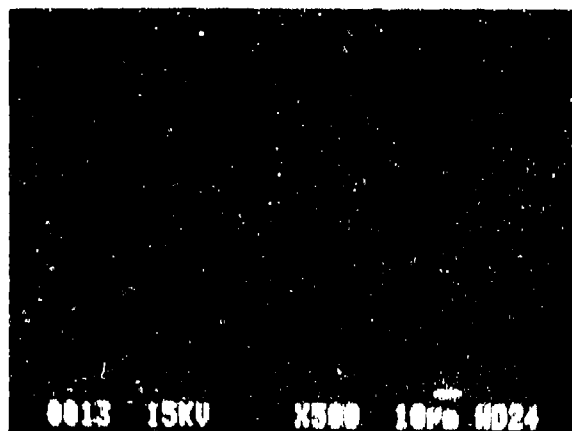


Figure 6. Elemental dot map for Sn showing uniform presence throughout the solder layer but also some diffusion with Cu.

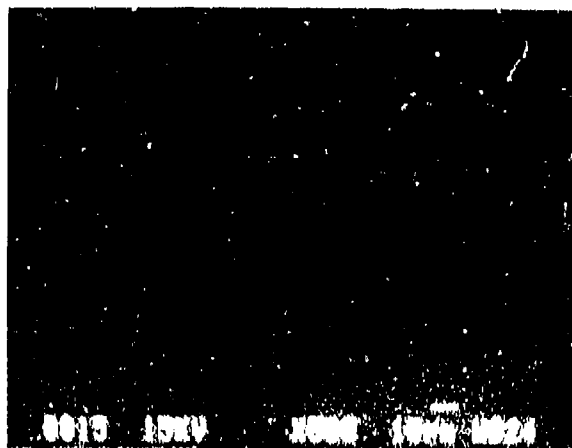


Figure 7. Elemental dot map for Cu showing some diffusion with Sn.

Closer examination of zone 2 (spectrum shown in Fig. 8) could not find more than trace amounts of C, Sn and Pb and their presence could not be ruled out as being due to signal bleed-over from the adjacent zones. It appears that in order to detect the region of actual transition from the Cr to the C, much high resolution microscopy would be required. It should be further stated that there is some possibility that the Cr presence at the interface may not be entirely due to chemical bonding potential but that some small amount of Cr may segregate to that location due to solidification effects of the bulk solder layer.

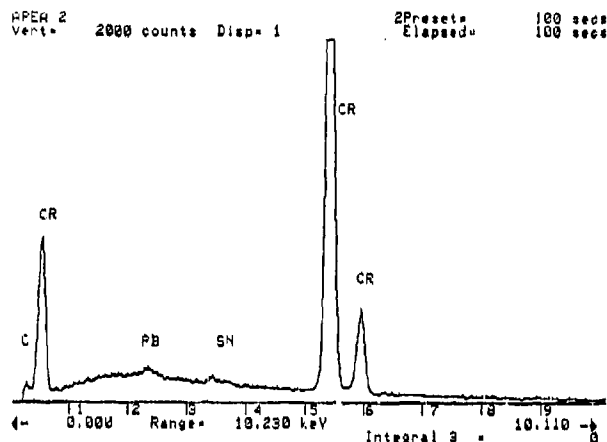


Figure 8. Spectrum for Cr region highlighted in figure 4.

Energy dispersive spectroscopic (EDS) analysis of Zone 3 showed 62.43 wt. % Sn- 37.57 wt. % Pb. EDS is never expected to give highly precise numbers and these values are clearly representative of the starting solder composition. It is, nevertheless, possible that since these values are so close to the eutectic composition that there is some greater fluorescence being detected from the eutectic structure. It is necessary to consider a possibility along these lines especially compensate for the additional fact that some Sn is lost to diffusion into the Cu and thus less than 60 wt. % Sn should be remnant in the solder layer. This was not a crucial point in this work.

The spectrum for this Sn-Cu diffusion zone is shown in Figure 9. EDS analysis of this region gave compositional values of 80.35 wt. % (88.42 at. %) Cu and 19.65 wt. % (11.58 at. %) Sn in this zone. If accurate, this would correspond to a two phase mixture of almost pure Cu and  $\epsilon$ -bronze seen in the Cu-Sn phase diagram [11] shown in Figure 10.

## SUMMARY AND CONCLUSIONS

A solder bond between graphite and copper was prepared through metallization of the graphite with a Sn-Cr mixture followed by reflow soldering with 60Sn-40Pb. SEM, x-ray microprobe and EDS analysis showed that Cr is enriched at the solder/graphite interface and that a diffusion zone of Sn (but no Pb) with copper occurs at the solder/copper interface. The latter finding is not at all unexpected as a natural solder joint interface. The preferential reaction of Sn with Cu over Pb with Cu could be due to the physical and chemical aggression of the pre-tinning of the copper.

Meticulous reexamination of the Cr region could not verify sufficient C presence to suggest definite carbide formation throughout. To detect the exact nature of the Cr-C interaction, it is clear that much higher magnification microscopy work would have to be performed. However, 5 distinct zones were identified and show a general macroscopic, chemical transition from the graphite to the copper.

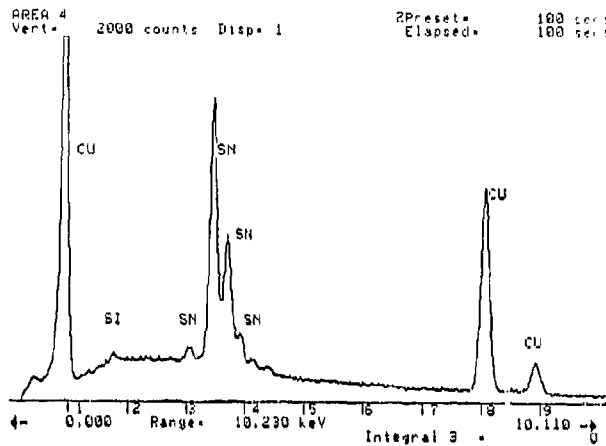


Figure 9. Spectrum of Cu-Sn reaction zone. EDS analysis showed this zone to have an approx. composition of 80.35 wt. % Cu- balance Sn.

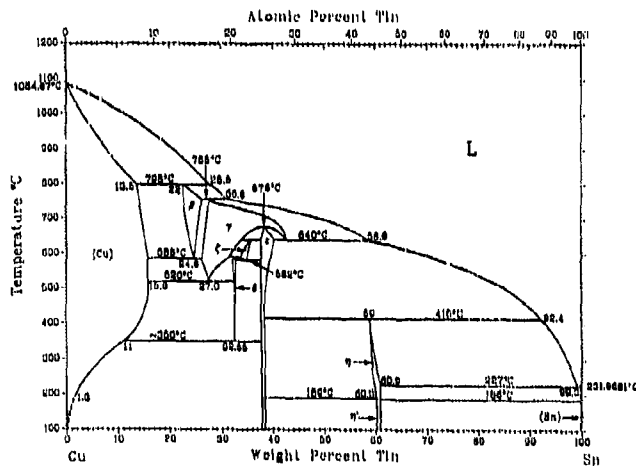


Figure 10. Binary alloy phase diagram for Cu-Sn. At approx. 80.35 wt. % Cu the equilibrium phase is a 2-phase mixture or extremely copper rich solid solution and a bronze phase.

## REFERENCES

1. Donnelly, R. G., G. M. Slaughter, "The Brazing of Graphite", Weld. Jnl., 41 (5), (1962), reprinted in Source Book on Brazing and Brazing Technology (ASM International, Metals Park, OH, 1980), pp. 308-314.
2. A. G., Pincus, S. Chang, Amer. Cer. Soc. Bull., 56 (4), 433-436, (1977).
3. J. P. Hammond, S. A. David, M. L. Santella, Weld. Jnl., 67 (10), 227-232 (1988).
4. H. Mizuhara, Amer. Cer. Soc. Bull., 68 (9), 1591-1599 (1989).
5. C. W. Fox, G. M. Slaughter, Welding Jnl., 43 (7), (1964), reprinted in Source Book on Brazing and Brazing Technology (ASM International, Materials Park, OH, 1980), pp. 308-314.
6. R. E. Lochman, Amer. Cer. Soc. Bull., 68 (4), 891-896, (1989).
7. Nicholas, M. G., "Active Metal Brazing", Brit. Cer. Trans. Jnl, (85), 144-146 (1986).
8. Jos. Intrater, G. Bertoldo, U. S. Patent No. [4,358,506] (9 November 1982).
9. J. Intrater, Cer. Ind., 134 (2), 34-37, (1991).
10. J. Intrater, Machine Design, 61 (24), 95-100, (1989).
11. N. Saunders, A. P. Miodownik in ASM Handbook Vol. 3-Alloy Phase Diagrams, edited by H. Baker, H. Okamoto (ASM International, Materials Park, OH, 1992) p. 2:178.



## EVALUATION OF ADHESION STRENGTH IN A Ti/Al<sub>2</sub>O<sub>3</sub> COMPOSITE

HSIN-FU WANG\*, JOHN C. NELSON\*, CHIEN-LI LIN\*, WILLIAM W. GERBERICH\*, CHARLES J. SKOWRONEK\*\* AND HERVE E. DEVE\*\*

\*University of Minnesota, Minneapolis, MN 55455.

\*\*Metal Matrix Composites Program, 3M Company, MN 55144.

### ABSTRACT

The mechanical properties of interfaces in Ti/Al<sub>2</sub>O<sub>3</sub> composites were characterized by four point bending and fiber pushout tests. To determine the bi-material fracture toughness with four point bending tests, planar interfaces were evaluated as sandwich composites. By changing the processing temperature from 700°C to 1000°C, the interfacial fracture energy was found to increase up to 950°C. It then decreases when the processing temperature is further increased to 1000°C. This is because of the formation of the intermetallic compound (Ti<sub>3</sub>Al). Interfacial shear strength and interfacial frictional stress of 323 MPa and 312 MPa were obtained, respectively, by performing pushout tests of the Al<sub>2</sub>O<sub>3</sub> fiber reinforced Ti matrix composites. These values are smaller than the shear yielding strength of the Ti matrix which is 525 MPa.

### INTRODUCTION

Continuous fiber reinforced Ti matrix composites have received attention in the aerospace industry as advanced structural materials because of their high specific strength, excellent corrosion resistance and good high temperature thermal stability[1-3]. The macroscopic mechanical properties of these composites are controlled not only by the mechanical properties of the constituents but also by the adhesion strength of the fiber/matrix interfaces. Usually, bonding and adhesion between the metal and the ceramic are critical to the mechanical properties of the composites. When a metal/ceramic interface in the composite is subjected to excessive external or residual stress, failure will occur along the interface or within one of the two constituents[4][5]. Interfacial debonding and sliding play an important role in determining the overall fracture toughness of the composites under tensile loading. It is recognized that the interfacial debonding and sliding process in the fiber composites are dominated by the interfacial fracture energy and interfacial frictional stress respectively[6]. The main purpose of this paper is to report on the interfacial fracture energy and interfacial frictional stress in Ti/Al<sub>2</sub>O<sub>3</sub> composites as measured by four point bending and fiber pushout tests. The relationship between the mechanical properties and microstructure is also discussed.

### EXPERIMENTAL PROCEDURE

#### Four point bending tests

The test specimen which served as a model system to evaluate the interfacial fracture energy consists of a bimaterial beam with symmetric precracks, as shown in Fig.1. To make sandwich specimens for the four point bending tests, they were prepared as follows: thin foils of Ti (99.8% pure) and Al<sub>2</sub>O<sub>3</sub> plates were immersed in isopropyl alcohol for 10 min and then cleaned in an ultrasonic cleaner for 20 min. They were sandwiched with a 3mm gap between the two foils to form a precrack, wrapped with Ta foils and encapsulated in glass containers evacuated to 10<sup>-6</sup> torr. They were then Hot

Isostatic Press (HIP) bonded in an Ar gas atmosphere. Specimens were first heated to the softening point of the glass under a pressure of 1.75 MPa for 30 min and then pressure and temperature were simultaneously raised to 7 MPa and a fixed temperature which ranged from 700°C to 1000°C. The bonding time was fixed at 1 hr. After HIPing, a notch was cut in the sandwich specimen from the  $\text{Al}_2\text{O}_3$  side with a low speed diamond saw. Because of the gap between the foils, this forms a well defined precrack.

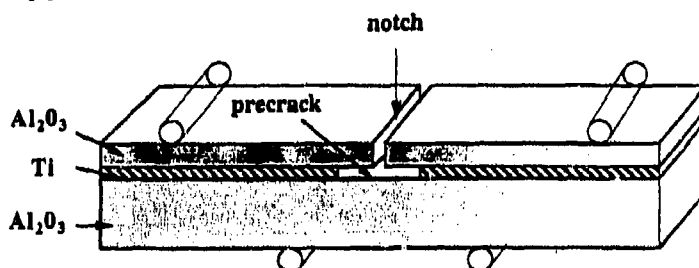


Fig. 1. Specimen geometry for four point bending tests with symmetric precracks

The specimens were placed in a four point bending fixture mounted on an MTS machine. The crosshead speed was 0.06 mm/min with load and displacement being recorded during the test. A critical load drop marks the propagation of a crack along the interface between Ti and  $\text{Al}_2\text{O}_3$ . This critical load was used to calculate the interfacial fracture toughness. The details of the calculation are described elsewhere[7]. After the four point bending tests were completed, the specimens were cut perpendicular to the bonding interface with a low speed diamond saw. The exposed cross section was then polished. Following this, microstructural observations and chemical analyses were conducted by Scanning Electron Microscopy (SEM) and Energy Dispersive X-ray Analysis (EDAX).

#### Fiber pushout tests

The  $\text{Al}_2\text{O}_3$  fiber reinforced  $\beta$ -21S Ti alloy composites used in this test were provided by 3M company. The diameter of the  $\text{Al}_2\text{O}_3$  fibers was 10  $\mu\text{m}$ . To reduce the chemical reaction between the fiber and the matrix, the fibers were coated with a refractory metal and  $\text{Y}_2\text{O}_3$  duplex coating, the nature of which is proprietary. A sample with a thickness of around 0.3 mm was cut perpendicular to the  $\text{Al}_2\text{O}_3$  fibers by using a diamond saw. This was thinned down to 100  $\mu\text{m}$  by sanding followed by polishing with 1.0  $\mu\text{m}$  diamond paste. By utilizing a dimpler to provide the final thinning and polishing, a thickness of 30  $\mu\text{m}$  could be achieved for the fiber pushout test.

A schematic diagram of the setup for the fiber pushout tests is shown in Fig. 2. The fiber pushout tests were performed by driving the indenter into the fiber at a constant rate of 0.3  $\mu\text{m/s}$ . During the test, the load-displacement curve was recorded continuously by using an IBM personal computer and a chart recorder. When the displacement of the fiber was about 3  $\mu\text{m}$ , the

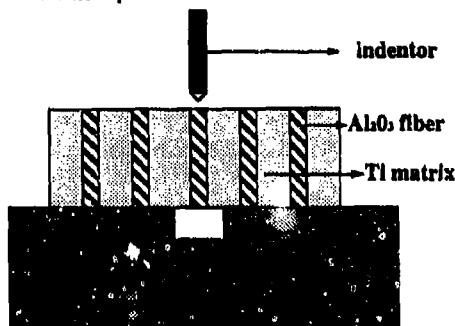


Fig. 2. Setup for pushout tests

indenter was unloaded. The load-displacement data was used to calculate the interfacial shear strength and interfacial frictional stress. Scanning electron microscopy was performed to observe the fracture surface after the pushout test.

## RESULTS AND DISCUSSION

### Four point bending tests

The interfacial fracture toughness was measured at different applied bonding temperatures for a 25  $\mu\text{m}$  thickness Ti interlayer. The relationship between interfacial fracture toughness (or interfacial fracture energy) and bonding temperature is shown in Fig.3. The interfacial fracture toughness (or interfacial fracture energy) increases to 2.66  $\text{MPa}\cdot\text{m}^{1/2}$  (or 34.1  $\text{J}/\text{m}^2$ ) as the bonding temperature increases to 950°C. Then the interfacial fracture toughness drops to 1.9  $\text{MPa}\cdot\text{m}^{1/2}$  (or 16.9  $\text{J}/\text{m}^2$ ) when the bonding temperature is further raised to 1000°C. A reaction layer exists between Ti and  $\text{Al}_2\text{O}_3$  when the bonding temperature is 1000°C. The composition of the reaction product at the interface was analyzed by using EDAX with the semi-quantitative data being shown in Fig.4. From the measured atomic % of Ti and Al, the reaction layer between Ti and  $\text{Al}_2\text{O}_3$  is identified as  $\text{Ti}_3\text{Al}$ . Because the  $\text{Ti}_3\text{Al}$  intermetallic alloy is very brittle[8,9], it will reduce the fracture toughness of the interface. It is expected that when the bonding temperature is 1000°C, a great deal of  $\text{Ti}_3\text{Al}$  is produced which will decrease the interfacial fracture toughness of Ti/ $\text{Al}_2\text{O}_3$  composites. This is consistent with Tressler and Moore's[10,11] results on the deterioration of Ti/ $\text{Al}_2\text{O}_3$  composite tensile strength caused by the presence of  $\text{Ti}_3\text{Al}$  produced during processing.

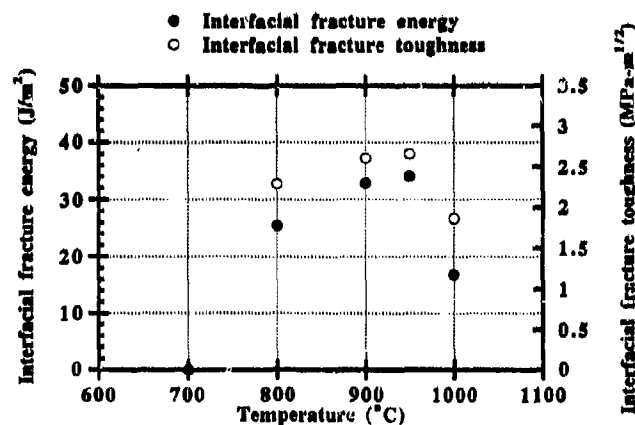


Fig. 3. The relationship between the interfacial fracture toughness (or interfacial fracture energy) and applied bonding temperature.

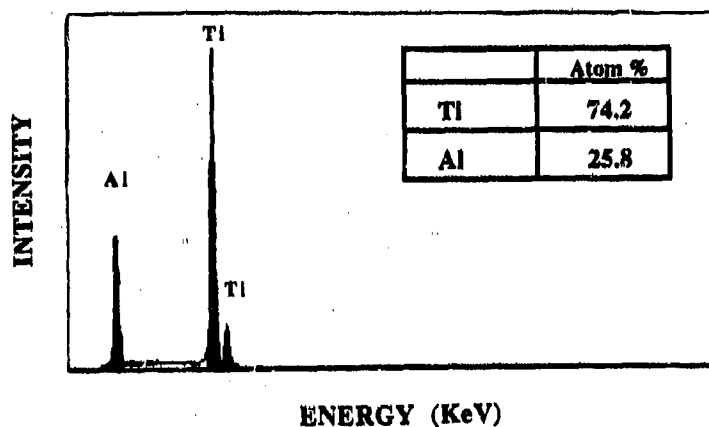


Fig. 4. EDAX analysis of the reaction product at the interface.

#### Fiber pushout tests

The load-displacement curve of a fiber pushout test is shown as Fig. 5. At first, the load increased with increasing displacement. This corresponds to the initial elastic loading. There is a critical load drop ( $P_{cr}$ ) at 0.3 N which means that the initial debonding between the fiber and the matrix occurred. Then continuing debonding and fiber sliding happened concurrently to a fiber sliding distance of 1  $\mu\text{m}$  which marked the end of debonding. After the fiber had slid another 1.5  $\mu\text{m}$ , the unloading stage was initiated. The observation of the fiber after the pushout test is shown in Fig. 6.

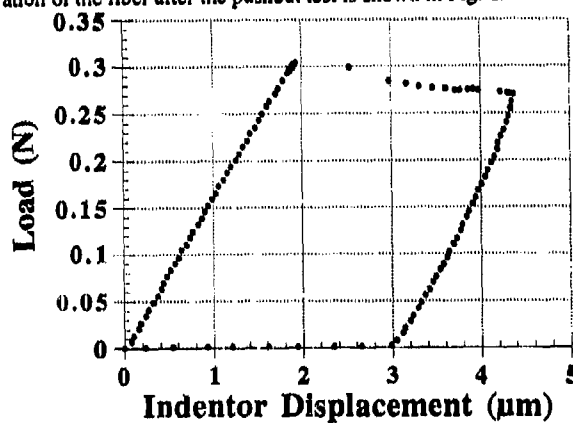


Fig. 5. The load-displacement curve for the pushout tests.

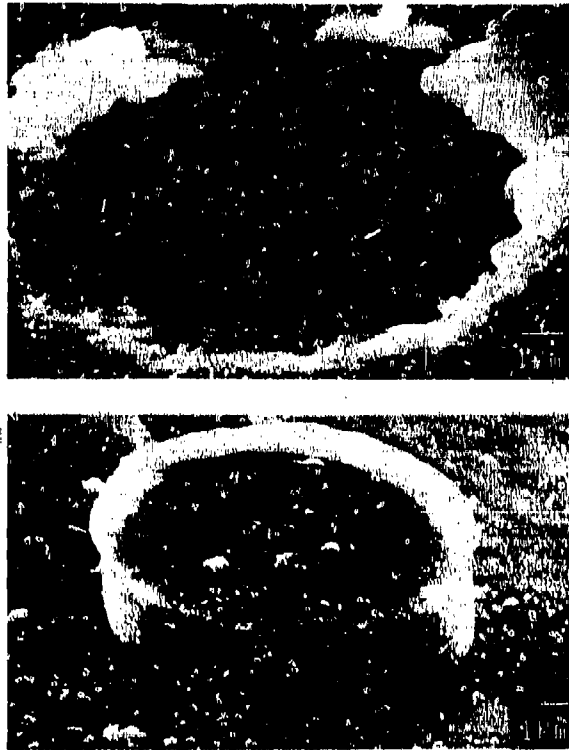


Fig. 6. SEM micrograph of the pushed-out fiber. (a) Indented side. (b) Pushed-out side.

The interfacial shear strength ( $\tau_i$ ) and interfacial frictional stress ( $\tau$ ) were calculated as follows:

$$\tau_i = \frac{P}{2\pi Rl}$$

$$\tau = \frac{P}{2\pi R(t-d)}$$

where  $P$  is the load measured during the pushout test,  $R$  is the radius of the fiber,  $t$  is the thickness of the composite and  $d$  is the pushout length of the fiber. The relationship between the interfacial frictional stress and fiber displacement is shown in Fig. 7. The calculated interfacial shear strength and interfacial frictional stress are 323 MPa and 312 MPa respectively. The calculated interfacial shear strength is a little higher than that of a Boron fiber reinforced Ti-6-4 alloy composite[3]. These values are also smaller than the shear yielding stress of the  $\beta$ -21S alloy which is 525 MPa[12]. From the X-ray mapping, it was found that the interfacial fracture process occurred between the refractory metal and  $Y_2O_3$  interface.

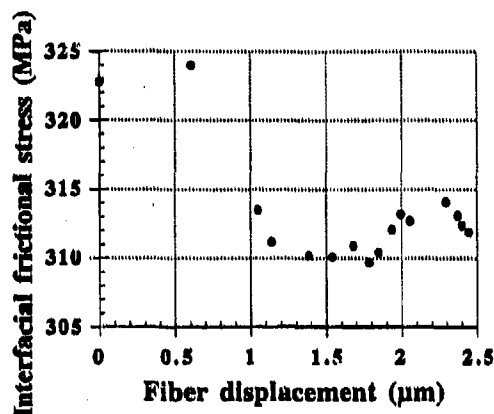


Fig. 7. The relationship between the interfacial frictional stress and fiber displacement.

## CONCLUSIONS

The interfacial fracture toughness (or interfacial fracture energy) reaches a maximum value of  $2.66 \text{ MPa}\cdot\text{m}^{1/2}$  (or  $34.1 \text{ J/m}^2$ ) with a bonding temperature of  $950^\circ\text{C}$  for the  $\text{Ti}/\text{Al}_2\text{O}_3$  composites. Because the intermetallic compound  $\text{Ti}_3\text{Al}$  was produced during bonding at  $1000^\circ\text{C}$ , it deteriorates the composites. The interfacial shear strength and interfacial frictional stress in  $\text{Al}_2\text{O}_3$  fiber reinforced Ti matrix composite are 323 MPa and 312 MPa respectively. These stresses are smaller than the shear yielding stress of the  $\beta$ -21S alloy which is 525 MPa. It was seen that the crack propagates at the interface between the refractory metal and  $\text{Y}_2\text{O}_3$ .

## ACKNOWLEDGMENT

This research was supported by 3M/DARPA/ONR Metal Matrix Composite Model Factory Program under subcontract No. GS 01080 - KAS and ONR N/N00014-92-J-1962.

## REFERENCES

1. Y.M. Yang, S.M. Jeng and C.J. Yang, *Mater. Sci. Eng.*, A138, 155 (1991).
2. J. Wadsworth and F.H. Froes, *J. Met.*, 41, 12 (1989).
3. J.M. Yang and S.M. Jeng, *J. Met.*, 44, 52 (1992).
4. A.G. Evans, M. Ruhle, B.J. Dalgleish and P.G. Charalambides, *Mater. Sci. Eng.*, A126, 53 (1990).
5. M.Y. He and J.W. Hutchinson, *J. Appl. Mech.*, 56, 278 (1989).
6. A.G. Evans, *9th Riso Int. Sympos. Met. Mater. Sci.*, 13, (1988).
7. H.F. Wang, C.J. Skowronek and W.W. Gerberich, accepted for publication in *Acta. Met.*
8. H.A. Lipsitt, D. Shechtman and R.E. Schafrik, *Metall. Trans.*, 11A, 1370 (1980).
9. H.T. Kestner-Weykamp, C.H. Ward, T.F. Broderick and M.J. Kaufman, *Scripta Met.*, 23, 1697 (1989).
10. R.E. Tressler and T.L. Moore, *Met. Eng. Quarterly*, 2, 16 (1971).
11. R.E. Tressler and T.L. Moore and R.L. Crane, *J. Mater. Sci.*, 8, 151 (1973).
12. H.E. Deve, unpublished research.

## STRESS-CORROSION CRACKING AT CERAMIC-METAL INTERFACES

J. C. CARD, R. M. CANNON, R. H. DAUSKARDT and R. O. RITCHIE

Center for Advanced Materials, Materials Sciences Division, Lawrence Berkeley Laboratory,  
and Department of Materials Science and Mineral Engineering, University of California,  
Berkeley, CA 94720.

### ABSTRACT

It is known that the fracture resistance of glass-copper interfaces depends strongly on the water content in ambient gaseous environments. In the present study, subcritical crack growth stimulated by water and other environmental species is investigated for such interfaces. Tests were conducted in various liquids, namely water, N-methylformamide, and n-butanol. All were found to accelerate fracture with the greatest effects from liquid water. Results are considered in the context of current models for stress-corrosion crack growth.

### INTRODUCTION

Understanding the mechanical behavior of ceramic-metal interfaces is vital to predicting the performance and reliability of numerous components for advanced technologies. Composite materials, microelectronic devices, wear and corrosion resistant coated components all have mechanical properties that critically depend on the ceramic-metal interfaces contained within them.

The integrity of such bimaterial interfaces is often characterized in terms of their resistance to fracture, as defined by a critical fracture energy  $G_c$ , or fracture toughness  $K_{Ic}$  [1]. However, since components often fail at stresses far below those required for such catastrophic failure, it is necessary to consider additionally subcritical crack growth [2] and cyclically induced fracture [3] at or near these interfaces when predicting *in service* life.

It has previously been observed that glass-copper interfaces exhibit environmentally-assisted subcritical crack growth at rates that vary by orders of magnitude depending on the water content of the gaseous environment [2]. Accordingly, the purpose of the present ongoing study is to determine the accelerating effects of various liquid environments on such stress-corrosion crack growth relative to that in water. Results are being compared with those for bulk glass, rather than copper which is immune to stress corrosion in these environments [4], with the objective of providing some insight into the micro-mechanisms of stress-corrosion cracking along glass-copper interfaces.

### BACKGROUND

A schematic crack velocity-driving force ( $v$ - $G$ ) curve for stress-corrosion cracking along a glass-copper interface (Fig. 1a) displays *four* distinct regimes of behavior which should be anticipated based on reported behavior [2,5]. Three of the regions, labeled I, II, and III, are analogous to the three regions readily observed for stress corrosion in bulk glass [6,7] (Fig. 1b). Models for these regions, developed largely for glass, are described briefly. However, it is recognized that for interface cracks, a stress field rotation is introduced by elastic discontinuities [8] which makes the relationships among strain energy release rate,  $G$ , stress intensity factor  $K$ , and crack-tip geometry more complex. Even so, the approximate models now available for stress corrosion crack growth should provide useful guidance especially for nominally symmetrical far-field loading wherein shear effects are minimal.

#### Threshold Regime

The threshold region, displayed in Fig. 1a, is somewhat ambiguous for bulk glass. Although there have been studies in which a threshold has been indicated for glass [9], its existence is hard to confirm since it occurs at such low crack growth velocities that measurements are difficult. However, the observations for fracture of glass-Cu interfaces reveal pronounced threshold-like behavior becoming apparent at higher velocities than for glass [2,5] that must be considered and further characterized.

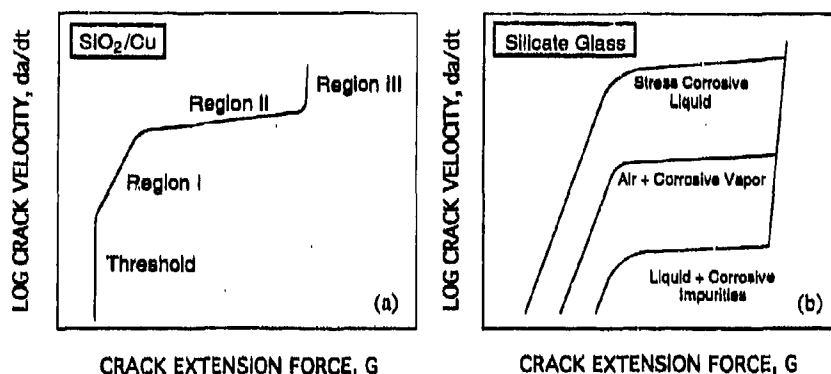


Fig. 1: Schematic diagrams showing (a) regimes of stress corrosion crack growth anticipated for a typical ceramic-metal interface, and (b) behavior typically observed for glass.

### Region I

In Region I, the crack velocity is highly dependent on applied stress intensity and is thought to be controlled by the rate of a stress-dependent chemical reaction occurring virtually at the crack tip, where adsorbing species expedite bond rupture giving [10,11,12]:

$$v = v_0 \exp[(-\Delta H + AG)/kT] \quad (1)$$

where  $v_0$  is approximately proportional to the activity of reactive species;  $\Delta H$  is an activation enthalpy;  $A$ , the activation area;  $k$ , Boltzmann's constant and  $T$ , the absolute temperature.

### Region II

Two distinct situations have been identified for stress corrosion in bulk glass wherein crack growth rates are limited by transport of water, or other reactive species, to the crack tip [6,13]. In a gaseous environment, the transport is limited by the rate of diffusion of the reacting species through a stagnant region which extends a distance  $\delta$  behind the crack tip. The crack velocity in this plateau region is given by [6,12]:

$$v_{\text{plateau}} = \frac{bDC_0}{\delta} \quad (2)$$

where  $b$  is a constant dependent on bond length and number of bonds broken per unit area of fracture surface,  $C_0$  is the bulk concentration of the diffusing species,  $D$  is the diffusivity of the diffusing species, which may be inversely proportional to  $\eta$  the viscosity of the solution. Similar behavior obtains for specimens immersed in inert liquids in which impurities of an active species control crack extension, e.g. for toluene containing trace amounts of H<sub>2</sub>O [7].

Tests conducted on glass in liquid water also display a plateau region; this case cannot be described by diffusion limitations but instead derives from viscous drag effects [13]. As the crack extends and the crack surfaces are pulled further apart, a negative pressure develops in the liquid immediately behind the crack tip. The negative pressure causes closing tractions on the crack flanks thereby opposing the applied stress intensity. Calculations suggest that the crack-tip stress intensity,  $K_I$ , is reduced from the far field value by the amount [12]:

$$\Delta K = -8.76 \nu \eta [E'/2K_I]^2 (\pi c)^{1/2} \quad (3)$$



where  $c$  is the crack length. The dependence in terms of  $G$  can alternatively be seen by using the approximation for a homogeneous material:  $K=(GE')^{1/2}$ . For plane-strain conditions,  $E'=E/(1-\nu^2)$ , where  $E$  is Young's modulus and  $\nu$  is Poisson's ratio. This equation predicts a gradual downturn in the  $v$ - $G$  curve at higher crack growth velocities, which is often less sharp than the transition observed between Region I and the plateau region [12].

Further models for this regime yield differences based upon the assumed profile of the crack flank and upon whether or not the fluid is supposed to be retained clear to the tip of the moving crack [14,15]. However, cavitation was found to cause an abrupt transition from the plateau region into Region III by Michalske and Frechette for bulk glass [16]. Apparently there is a critical crack growth velocity at which the pressure gradient created is not sufficient to drive the fluid fast enough to keep up with the rapidly moving crack tip. Once cavitation bubbles nucleate, they rapidly spread and largely eliminate the viscous drag. A simple model for the critical velocity at which cavitation first occurs is [16]:

$$v_{\text{crit}} = [(2\gamma/r) + p] / [2\eta\alpha^2(X_2^{-1} - X_1^{-1})] \quad (4)$$

where  $\gamma$  is the surface tension of the liquid,  $r$  is the radius of the cavitation bubble,  $p$  is the atmospheric pressure,  $\alpha$  is the half-angle crack opening, and  $X_2$  and  $X_1$  represent the positions of the center of the cavitation bubble and the open end of the crack, respectively.

### Region III

Crack growth in Region III is dictated by thermally activated processes in which inherent barriers associated with bond rupture at the crack tip must be overcome for brittle ceramics. Although crack growth seems relatively independent of environment, weak environmental dependencies have been studied for bulk glass [12]. The further complexities associated with plasticity for ceramic-metal interfaces remain to be understood.

### Reactive Species

Studies conducted in various liquid environments for bulk glass [17] showed that species other than water promoted stress corrosion crack growth provided that they have a similar structure as water (proton donor on one side of molecule and lone pair of electrons on the other) and, equally important, that they can reach the crack tip free of steric hindrances. Fig. 1b shows the difference between a liquid environment that enhances stress corrosion and one where the residual impurities are responsible for any subcritical crack growth. The large differences in the velocity for Region II have been used to judge whether or not a specific liquid is active toward glass. In the following, several liquids are compared in terms of their behavior at glass/Cu interfaces versus that with bulk glass.

### EXPERIMENTAL PROCEDURES

Studies were conducted using double-cantilever-beam (DCB) specimens, consisting of a 1.5  $\mu\text{m}$  thick copper film bonded between two glass substrates (Fig. 2). Samples were prepared by evaporating copper films onto each of two fused silica substrates (of size 75 by 25 by 2 mm). A 10-20 nm layer of chromium was evaporated onto one substrate prior to the copper in order to confine crack propagation to one interface. The substrates were then diffusion bonded at 470°C for 2 hours under a pressure of 9 MPa. These conditions lead to interface impurities such that fracture is always exactly at the interface [2,3,5]. To permit loading of the sample, aluminum arms were attached using epoxy.

Testing in liquid environments was achieved by immersing the bottom grip and specimen in the liquid contained in a 500 ml dish and surrounding the whole loading apparatus with an environmental control chamber. The chamber was purged with dry nitrogen gas (passed through Drierite™) for at least one half hour prior to the addition of each test liquid. A constant flow of ~1 liter/min was used to minimize the water absorbed by the liquids from the surrounding environment during testing.

Both constant displacement and constant crosshead-speed loading conditions were used. In constant displacement tests, the samples were loaded to a pre-determined value and the crosshead position was fixed. The load was then allowed to relax during crack advance. The

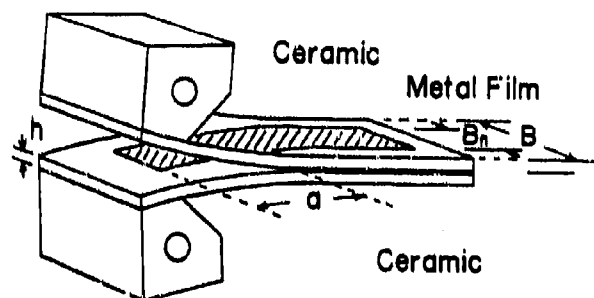


Fig. 2: DCB specimen used to evaluate subcritical fracture.

load versus time data were converted into a crack velocity versus strain energy release rate plot using compliance relations and a computer curve fitting routine. A similar, although more complex, analysis was used for the constant crosshead-speed tests, which are more accurate for higher velocities. The results presented are consistent with those from direct optical measurements of crack position (used earlier [2]), which means the technique is applicable for opaque ceramic-metal couples with single interface cracks.

## RESULTS

Due to differences in bonding and chemistry introduced during fabrication, each interface is expected to have somewhat different fracture resistance and crack growth behavior. Thus, it is necessary to synthesize results from several samples in a way that recognizes such variations, as well as the geometry dependencies for different crack growth regimes.

### Vapor Environments

Data for several tests conducted in ambient air (~50% relative humidity) shown in Fig. 3a exhibit marked acceleration of fracture in the moist atmosphere. Note that there is significant sample-to-sample variation in the threshold and Region I regimes. However, these data are consistent with prior results [2] indicating that the plateau (Region II) regime remains relatively unaffected. At lower velocities, the log  $v$ - $G$  curves become very steep, again consistent with earlier data for glass-Cu interfaces [2,5] that show distinctly threshold-like behavior obtains over a much wider range of crack velocities ( $< 1 \times 10^{-7}$  m/s) than for glass; for glass any indication of threshold behavior only appears at very low crack velocities ( $< 4 \times 10^{-10}$  m/s) [9]. The position of the threshold shifts to higher or lower  $G$  values depending on the chemistry of the interface. Although further evidence is needed, the threshold is thought to be associated with crack-tip bridging [2] or blocking processes, resulting from formation of corrosion debris in the near-tip region.

A few data for tests in dry  $N_2$  in Fig. 3b suggest that some thermal activation, i.e. velocity dependence, occurs in Region III. The magnitude of  $G$  is similar to that for a few other high velocity data in Fig. 3a. Although some sample to sample variation exists, these provide an estimate of the inherent  $v$ - $G$  behavior to be compared with fracture in active environments.

### Liquid Environments

Three of the liquid environments used to conduct tests on glass-Cu interfaces were: water, N-methylformamide, and n-butanol. These were chosen as some amides and alcohols cause stress corrosion in glass, but n-butanol, which possesses the necessary reactive groups, is not aggressive to glass since it has too large a molecular size to penetrate through the small crack opening to reach the tip [12,17].

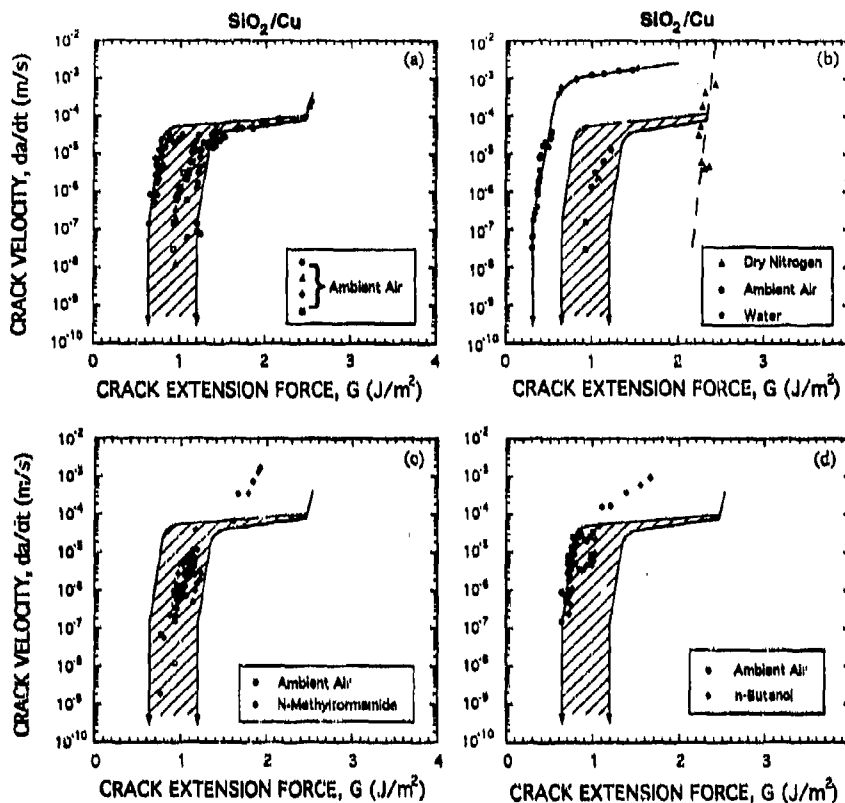


Fig. 3: Subcritical crack growth rates versus driving force for  $\text{SiO}_2/\text{Cu}$  interfaces. (a) exhibits data for tests in ambient air (50% R.H.) from four samples, including those shown in (b)-(d). In each of (b)-(d) the data are from only a single specimen; for each, part of the test was in ambient air and part was in a different liquid, respectively water, N-methylformamide, and n-butanol. Also note that in (b) some of the data were taken in dry  $\text{N}_2$ .

**Water:** A comparison of the water test results with those for ambient air and dry nitrogen are shown in Fig. 3b, where the air curve is extrapolated by overlaying the cross-hatched region (the bound of all air data) shown in Fig. 3a. The plot shows that water greatly enhances crack growth relative to that in moist air, a much greater increase than is seen for glass [6]. This increase may be due to the deterioration of the corrosion product film at the crack tip by the water.

The plateau region for the water test appears at a much higher crack velocity than observed for moist air. In this case, the plateau is not caused by transport limitations due to the diffusion of the reacting species to the crack tip as for gaseous species but rather to viscous drag effects as discussed previously.

**N-Methylformamide:** Tests conducted in an N-methylformamide environment show that it also actively causes stress corrosion cracking for glass-copper interfaces (Fig. 3c). Comparing the results to those for moist air shows that the accelerating effects are comparable except at

high crack velocities where the formamide is more aggressive. The details of the curve are unfortunately hidden in the scatter of the data, but there seems to be a lack of a plateau region within the range of measured crack growth velocities.

**Butanol:** It was found that an n-butanol environment also causes stress corrosion crack growth at glass-Cu interfaces (Fig. 3d). Again the rates in Region I are more like those induced within H<sub>2</sub>O vapor than liquid. There is a suggestion of a high velocity plateau regime, but it is much less pronounced than that seen with liquid water.

## DISCUSSION

Results presented in Fig. 3 are consistent with the situation hypothesized in Fig. 1. Although not studied in detail here, the behavior in all environments suggests threshold-like behavior obtains at relatively high crack velocities compared with fracture of bulk glass, and at 0.1 to 0.5 of  $G_c$ , depending upon the environment. The transition from threshold to Region I may be determined by a mutual competition between the rate of chemical reaction, which promotes crack extension, and the rate of corrosion product formation, which hinders it.

For both the vapor and liquid H<sub>2</sub>O environments, the crack growth curves clearly exhibit Region I type behavior, within which crack growth is controlled by the kinetics of a stress-dependent chemical reaction. Using Eqn. (1), the activation area for the reaction can be determined from the slope of the log  $v$ - $G$  curves; this yields  $A = 0.15 \text{ nm}^2$  and  $0.12 \text{ nm}^2$  for the glass-Cu interfaces tested in moist air and in liquid water, respectively. For fracture within the two organic liquids, the activation areas are similar. By comparison,  $A = 0.01$ - $0.02 \text{ nm}^2$  for typical data for glass in H<sub>2</sub>O containing environments, e.g., from refs. [6,7]. The latter values imply an activation step involving rupture of a single atomic bond. The former values remain to be explained, but are still plausible for a local chemical reaction. Complete explanation must address the role of the residual interface impurities as well as that of the atmospheric species.

For tests in liquid water, a well defined plateau is evident at much higher velocities than for the vapor case. For the liquid case, the plateau, at velocities of  $\sim 1.3 \times 10^{-3} \text{ m/s}$ , reflects viscous drag control. However, the plateau velocities reported for bulk glass in water are about 10 times higher [16], consistent with the extent of other Region I data for glass [6,9]. The discrepancy likely results because the glass tests were performed on samples with a thickness of a few millimeters whereas these interface samples are 25 mm thick. Thus, the plateau in many other tests may be controlled by fluid flow from the sample sides, (parallel to the crack front) and so occurs at higher velocity than here.

For the n-butanol and especially the N-methylformamide, no plateau behavior was clearly evident. The lack of a plateau at low velocities and the accelerated cracking in the velocity range studied combine to confirm that both species promote corrosive cracking. However, both liquids are more viscous than water, as shown in Table I [18,19]. Thus, Region II type behavior similar to that seen so clearly in liquid water is expected, but at velocities reduced by the viscosity ratio, i.e., factors of 2-3. Although the absence of well defined plateaus could merely reflect scatter in the data, it may instead represent a rapid onset of cavitation near the crack tip. From Eqn. (4), the critical velocity is proportional to the ratio of surface tension to

TABLE I

LIQUID	SURFACE TENSION $\gamma$ (mN/m)	VISCOSITY $\eta$ (Pa·s)	RATIO $\frac{\gamma}{\eta}$ (m/s)
Water	73	$1.0 \times 10^{-3}$	73
N-Methylformamide	38	$1.7 \times 10^{-3}$	23
n-Butanol	25	$2.9 \times 10^{-3}$	8.3

viscosity for the liquid, i.e.,  $v_{cav} \propto \gamma/\eta$ . It also depends on details of the crack-tip geometry, which should be similar among the present tests. The values of  $\gamma/\eta$ , listed in Table I, indicate that near-tip cavitation should occur at as much as an order of magnitude lower velocity for these organic fluids than for liquid  $H_2O$ . Thus, although confirming experiments are needed, it is considered likely that the absence of a well defined plateau for crack growth within these two liquids results because near-tip cavitation occurs at velocities just above those for which viscous drag becomes appreciable.

Steric hindrances are considered to play a major role in determining which environments cause stress corrosion for glass [17]. Thus, N-methylformamide and n-butanol were studied here because they are, respectively, amongst the largest molecules that are active and the smallest that are inactive in promoting stress corrosion cracking in glass [12,17]. As both are active for glass-Cu interfaces, it is suggested that the limited plastic deformation at the crack tip is sufficient to expose the critical atomic bond at the interface to a larger reacting molecule during crack extension. The issue is shown schematically in Fig. 4 where crack profiles are compared for the maximum sustainable loads, i.e., at  $G_c$  and at apparent threshold conditions,  $G_{TH}$ . These are based upon continuum calculations using purely elastic behavior for the glass, and supposing crack blunting leads to a crack-tip opening displacement given by  $CTOD = 2\gamma/\sigma_y$  (where  $\sigma_y$  is the yield stress) for the Cu side of an interface crack [20]. Clearly, only angstrom sized molecules can access the tips of cracks in glass at threshold conditions, whereas molecules several times bigger may possibly be aggressive for the glass-Cu interfaces. However, it should be recalled that these profiles reflect the dimensions of the load bearing material; some adsorbate or other reaction products may reduce the access relative to that in the schematic.

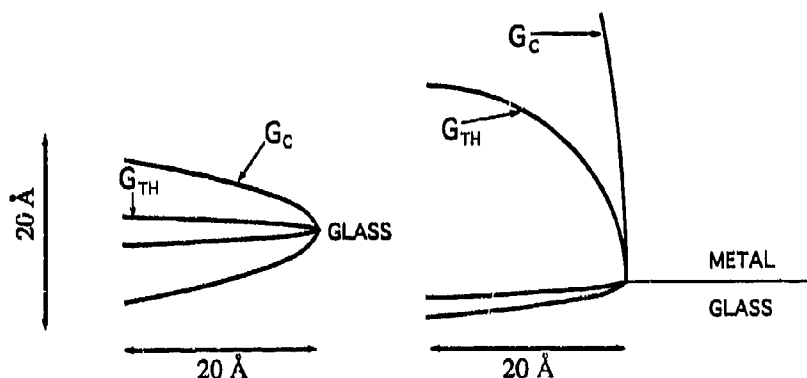


Fig. 4: Calculated crack profiles for loading at  $G_c$ , the maximum possible force, and at  $G_{TH}$ , the threshold force for glass (assuming purely elastic continuum behavior) and for glass/Cu (assuming continuum plastic and elastic behavior in the Cu and glass, respectively).

The enhanced crack-growth rates in aqueous and organic liquids has adverse implications for devices. The high residual stresses typically near most ceramic-metal interfaces could drive appreciable crack growth upon even brief exposure of unloaded pieces to aggressive environments. The resultant damage could critically depend upon the level of the high velocity plateau. Clearly, owing to the geometry dependence indicated for Region II, further analysis of this issue for small cracks that would typify devices is needed.

## CONCLUSIONS

Subcritical crack growth along glass-copper interfaces is markedly accelerated by water, alcohol and amides. Relative to glass, the presence of the metal alters the type of corrosion products formed and introduces plasticity that increases the CTODs.

Crack growth is strongly enhanced in moist air, and in the presence of liquid water is even more rapid. This greater enhancement in liquid is contrary to experience with cracking in bulk glass. It may be due to the deterioration of the corrosion product film at the crack tip by the water, either by making it more permeable or by carrying away some of the corrosion products and increasing access to the crack front.

Both N-methylformamide and n-butanol can cause stress corrosion cracking along glass-copper interfaces. Although n-butanol has too large a molecular size to reach the crack tip in bulk glass, the larger CTOD due to plasticity in the metal apparently allows it to be reactive for glass-copper interfaces. Thus, it is anticipated that many alcohols and amides should promote stress corrosion cracking of such glass-metal interfaces.

Mechanistic studies, still in progress, suggest that fracture is controlled by mechanisms similar to those that govern the stress corrosion in glass. Four distinct regions of behavior in glass-copper interfaces appear to occur for both liquid and vapor environments to varying degrees. Region I is controlled by as yet unidentified, highly stress-dependent chemical reactions at the crack tip. Region II is only mildly dependent on the applied stress intensity. Where it is controlled by diffusive transport of reacting species to the crack tip for gaseous environments, it is very pronounced in extent. In contrast, it may result from viscous drag in stress corrosive liquids, but then seems often to be limited in extent by cavitation near the crack-tip. The environmentally insensitive Region III appears to be thermally activated. The threshold region, which is rarely observed for glass, is very apparent for glass-copper interfaces and occurs at much higher crack velocities; it likely involves the more extensive corrosion products formed from the metal.

#### **Acknowledgments**

This work was supported by the Director, Office of Energy Research, Office of Basic Energy Sciences, Materials Sciences Division of the U.S. Dept. of Energy under Contract No. DE-AC03-76SF00098. Additional support for RMC and JCC was provided by IBM Corp.

#### **References**

1. R.M. Cannon, V. Jayaram, B.J. Dalgleish and R.M. Fisher, in Ceramic Microstructures '86: Role of Interfaces, ed. J.A. Pask and A.G. Evans (Plenum, NY, 1987), p. 959.
2. T.S. Oh, R.M. Cannon and R.O. Ritchie, *J. Am. Ceram. Soc.* **70**, c-352 (1987).
3. R.M. Cannon, B.J. Dalgleish, R.H. Dauskardt, T.S. Oh and R.O. Ritchie, *Acta Metall. Mater.* **39**, 2145 (1991).
4. K. Sieradzki and J.S. Kim, *Acta Metall. Mater.* **40**, 625 (1992).
5. T.S. Oh, R.M. Cannon, J. Rödel, A.M. Glaeser and R.O. Ritchie, in Interfaces in Polymer, Ceramic, and Metal Matrix Composites, ed. H. Ishida (Elsevier, 1988), p. 567.
6. S.M. Wiederhorn, *J. Am. Ceram. Soc.* **50**, 407 (1967).
7. T.A. Michalske and S.W. Freiman, *J. Am. Ceram. Soc.* **66**, 284 (1983).
8. J.R. Rice and G.C. Sih, *J. Appl. Mech.* **32**, 418 (1965).
9. A.G. Evans, *J. Mater. Sci.* **7**, 1137 (1972).
10. R.J. Charles and W.B. Hillig, in Symp. on Mechanical Strength of Glass and Ways of Improving It (Union Scientifique Continentale du Verre, Belgium, 1972), p. 682.
11. W.B. Hillig and R.J. Charles, in High Strength Materials, ed. V.F. Zackay (Wiley, NY, 1965), p. 682.
12. S.M. Wiederhorn, S.W. Freiman, E.R. Fuller and C.J. Simmons, *J. Mat. Sci.* **17**, 3460 (1982).
13. S.M. Wiederhorn, in Fracture Mechanics of Ceramics, Vol. 4, ed. R.C. Bradt *et al.* (Plenum Press, NY, 1978), p. 549.
14. J.L. Tzou, C.H. Hauch, A.G. Evans and R.O. Ritchie, *Acta Metall.* **33**, 117 (1985).
15. A. Turnbull and R.C. Newman, in Small Fatigue Cracks, edited by R.O. Ritchie and J. Lankford (The Metallurgical Society, Warrendale, PA, 1986), p. 269.
16. T.A. Michalske and V.D. Frechette, *J. Am. Ceram. Soc.* **63**, 603 (1980).
17. T.A. Michalske and B.C. Bunker, *J. Am. Ceram. Soc.* **70**, 780 (1987).
18. Handbook of Chemistry and Physics, 72nd ed., ed. D.R. Lide (CRC Press, Boca Raton, FL, 1991).
19. Lange's Handbook of Chemistry, 13th ed., ed. J.A. Dean (McGraw-Hill Book Company, New York, 1970).
20. C.F. Shih, *J. Mech. Phys. Solids* **29**, 305 (1981).

---

### **PART III**

---

## **Microwave, Laser, and Infrared Joining**

## JOINING CERAMICS USING MICROWAVE ENERGY

IFTIKHAR AHMAD and RICHARD SILBERGLITT

Technology Assessment & Transfer, Inc., 133 Defense Highway, Suite 212,  
Annapolis, MD 21401.

### ABSTRACT

In the past several years there has been an explosive growth in the use of microwave energy for the processing of a host of materials. Microwave energy provides rapid internal heating which results in an overall reduction in the processing time. The important features of microwave processing are described, as well as several applications.

Microwave energy has been used by a few groups for the joining of alumina, mullite, silicon nitride and silicon carbide. The work performed by these groups will be reviewed. Typically, a single mode microwave applicator has been used to join ceramics at temperatures ranging between 1250°C - 1800°C. Microwave joining of ceramics was achieved in a matter of minutes, in contrast to hours reported by conventional methods. The strength of the joints was equal to or greater than the as-received materials. Joining of specimens of sintered silicon carbide (Hexoloy™) using interlayers, and direct joining of reaction bonded silicon carbide (RBSC) to itself and Hexoloy™ has been accomplished recently. Both single mode and multimode microwave applicators were used and larger specimens of RBSC having complex shapes were joined using hybrid heating. The paper describes microwave joining apparatus, techniques and results.

### INTRODUCTION

The use of microwave energy for industrial applications is not new. In the past microwave applications have been mainly confined to communications. Other uses of microwave power include medical and biological applications, as well as heating. Heating applications exist in the consumer, commercial, industrial and scientific areas. The most common application is heating food in consumer microwave ovens.

A comprehensive historical review of microwave heating is given by Osepchuk [1]. There is little evidence of RF heating, and even less of microwave heating, before the Second World War. However, the patent literature includes some references to using microwave energy to affect materials properties for industrial purposes. In particular, Kassner (having patents on a spark-gap microwave generator) believed that it is possible to achieve useful changes in molecular state, and hence the chemistry of materials, without heating [1].

During the Second World War, there were efforts to measure dielectric properties of various materials. This work was done as a necessary task in the development of the radar, telephone and communication systems. The work begun under Von Hippel at the MIT Laboratory for Insulation Research and the relevant lectures given by experts in this area appeared as a book "Dielectric Materials and Applications" [2]. This work provides the foundation for all future efforts in radio frequency and microwave heating.

### Industrial Microwave Heating Applications

Microwave processing, which until recently dealt principally with food processing [3], is now expanding drastically to include almost all materials. The interest in this



emerging technology has given rise to a number of symposia on the use of microwave energy as applied to materials processing. The symposia are organized on alternate years by the Materials Research Society and the American Ceramic Society, with the first one held by MRS only recently in 1988. Numerous interesting applications of microwave energy have been presented at these meetings [4-7]. Applications of microwave energy currently being explored are growing substantially to encounter almost all materials. Some of them are briefly described below.

In the food industry microwave energy is utilized for numerous processes including tempering of frozen foods, pasta drying, poultry processing, potato processing, baking, cocoa bean roasting and sterilization of food [3].

In the polymer industry microwave energy is used for curing rubber tires and bonding of composites, thermosets and thermoplastics. A recent overview of the microwave processing of polymers appears in the MRS Proceedings Vol. 269 [8].

Medical applications include both treatment and diagnostic techniques. Medical treatment deals with hyperthermia (deliberate elevation of body temperature) to produce beneficial effects such as killing cancerous tumors. The medical diagnostics area includes measuring the changes in lung water content, blood flow measurements and microwave imaging [9].

In another application, an apparatus and process has been developed which facilitates the exposure of all external surfaces to microwave radiation and accomplishes sterilization in as little as 30 seconds to 8 minutes. The standard 2.45 GHz microwave irradiation achieved sterilization of dental instruments, artificial dentures, anesthesia nasal hoods and hydrophilic contact lenses contaminated with a variety of bacteria, fungal and viral pathogens [10].

In the electronic industry Superwave Technology (Santa Clara, CA) is pioneering microwave heating in the electronics industry. The Supertherm line of automated ovens is designed for a variety of thermal processes which include curing wafer coatings, drying and reflowing solder, and fusing laminated printed circuits [11].

For mineral processing the U.S. Bureau of Mines is looking into means to reduce energy for grinding (50 to 70% of the total energy used) of minerals. The Bureau has demonstrated that many minerals absorb microwaves and are rapidly heated, thereby inducing thermal stress cracking and improving the grindability [12].

Waste treatment and disposal of radioactive as well as municipal waste has been investigated using microwave energy. The Living Environmental Systems Research Laboratory, Matsushita Company of Japan, has developed a burning processor in which the waste material is dried and decomposed into gas by means of microwave energy. The gas generated is burned in a sanitary way, leaving only a small amount of ash [13]. Similar processes are under investigation for the treatment and disposal of radioactive waste [14, 15].

Ceramic processing technology is still in an early stage of development. Microwave energy is being explored to process a wide variety of ceramics. An excellent summary of almost all the applications in the area of microwave processing of ceramics is presented by Sutton [16]. These include, but are not limited to ceramic drying--particularly effective in removing water from thick ceramic bodies; binder burnout--removal of polymers used in the ceramic forming process; sintering of numerous ceramics and composites--including ferrites, boron carbide, titanium boride, partially stabilized zirconia, and composites such as  $\text{Al}_2\text{O}_3/\text{SiC}$ ,  $\text{Al}_2\text{O}_3/\text{TiC}$ ,  $\text{ZrO}_2/\text{SiC}$ ,  $\text{ZrO}_2/\text{Si}_3\text{N}_4$  and  $\text{Al}_2\text{O}_3/\text{Si}_3\text{N}_4$ ; processing and sintering of PZT and PLZT--with high density, small grain size and improved piezoelectric properties; processing of superconducting ceramics--microwave processed samples exhibiting more diamagnetism than conventionally

processed samples; *combustion synthesis of ceramics and composites*--internal ignition of combustible mixtures and controlled combustion wave propagation; *surface modification of glasses*--to strengthen the surface by ion exchange; and *joining of ceramics*.

#### Important features of microwave processing of ceramics

Researchers have recognized in various applications that microwave heating, because of the rapid processing cycle, provides a powerful new tool and energy source. Besides the savings in energy and cost, a major reason for this substantial interest is the importance of processing-microstructure-properties relationships. One of the principal advantages is the novel rapid internal heating pattern, which results in a unique microstructure that can provide superior product quality [17,18].

The use of microwave energy in the ceramic industry provides a fundamental change in the basic heating process. The penetrating action of the microwave energy into the material results in the internal and uniform heating of large masses in relatively short periods of time. Generally the internal heating results in an inverse temperature gradient, which significantly reduces the thermal stresses that may cause cracking during the processing of large volumes. In contrast, conventional heating starts from the surface of the body and is completely dependent on the heat transfer characteristics of the material.

Another important aspect is that different constituents (as well as phases) absorb microwaves at different rates. The possibility of controlled selective heating has promising implications for improving the properties of ceramics, especially in the area of composites. Generally, dielectric materials become more receptive to microwave energy with increasing temperature, and as a consequence absorb greater amounts of energy as the temperature increases. A typical example of this type of response is given in Figure 1. The critical temperature  $T_c$  gives an approximate indication of the point at which the loss tangent increases significantly.

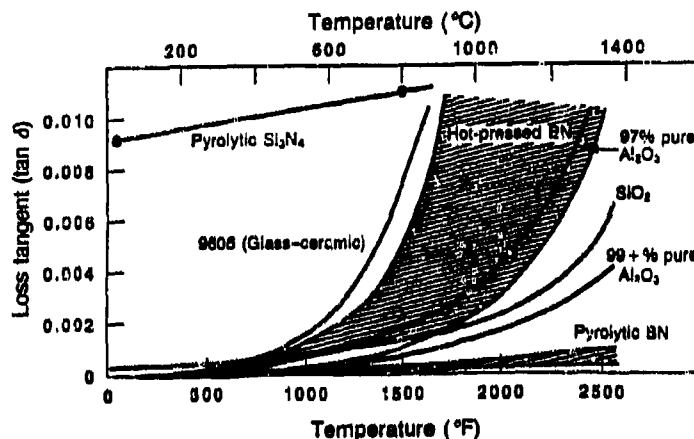


Figure 1. Qualitative representation of the loss tangent (8 to 10 GHz) as a function of temperature [19].

(Reprinted by permission of the American Ceramic Society)

Coupling agents can be added to materials that cannot be efficiently heated with microwave energy. The coupling agent preheats the entire sample, which at higher temperature starts to couple with microwave radiation. A common example is that of the SiC whiskers in a low loss alumina matrix. SiC is an excellent absorber of microwave energy, which can heat the entire composite sample, making sintering of the composite possible.

Alternatively, the sample may be preheated to temperatures where it efficiently couples with microwave energy. This can be conveniently achieved by placing the sample inside a susceptor (low loss insulation lined on the inside with high loss material such as silicon carbide). The heat generated in the silicon carbide is retained within the insulation, which preheats the sample to above its critical temperature where microwave losses become substantial. This is referred to as "Microwave Hybrid Heating." Usually with microwave heating alone there is an inverse temperature gradient, with higher temperatures in the interior of the sample and lower temperature on the surface because of the energy radiated from the surface. Microwave hybrid heating, in addition to preheating the low loss materials, provides an external heat source and compensates for radiation losses from the surface. Microwave heating is generally much faster than conventional heating. However, for low loss materials, heating rapidly with microwave energy alone (without a susceptor) may be difficult. This problem can be overcome with hybrid heating. Heating rates of 750°C per minute have been reported by microwave hybrid heating. The sintering of alumina with this method resulted in fine and uniform microstructures [17,18].

#### MICROWAVE JOINING OF CERAMICS

One of the important aspects of microwave processing is the joining of ceramics, which is imperative to the widespread commercial use of these advanced materials. The high-temperature, corrosion- and wear-resistant ceramics need to be joined to metals to allow their use in severe environments. Ceramics can also be joined to ceramics to form complex shapes required in industrial applications, which will eliminate the costly machining of these hard materials.

The novel use of microwave energy for joining of ceramics allows rapid and preferential heating throughout the joint interface, which makes it a viable and efficient method of joining ceramics. Microwaves can penetrate the material to rapidly provide the heat necessary to join ceramics. Conventional processes, on the other hand, heat the surface of the specimen and rely on thermal conduction to join ceramics. Sealing of ceramics using microwave energy was first accomplished by Meek and Blake [20]. Alumina substrates were sealed using glass as the interlayer material. Direct microwave joining of ceramics was reported by two groups. One of the groups was at Toyota Central R&D Laboratories in Japan, where a 6 GHz klystron power amplifier was used as the power source. A directional coupler was used to sample the power reflected from the cavity. The outputs from a pyrometer monitoring the surface temperature and the directional coupler were directed to a control system that automatically changed the iris dimension and tuned the cavity by adjusting the plunger. The feedback system was designed specifically to control the thermal runaway that may result from the rapid increase of dielectric loss with increasing temperature, which can cause local melting in the specimen. The sample was mounted transverse to the electric field and was slowly rotated to allow uniformity in heating. The system was equipped with a compressor and had the provision for flowing a gas during the joining process [21].

The other group was originally at QuesTech Inc. in McLean, VA. The apparatus (now with Technology Assessment & Transfer/George Mason University) has a 2.45 GHz magnetron as the power source. Microwaves are directed through standard waveguides to a microwave reflection bridge composed of a ferrite circulator, which sends any power reflected from the cavity to a voltage sampling probe and power head for measurement. An identical combination of voltage sampling probe and power head samples the power incident on the cavity. The difference of these two power measurements allows determination of the power available for ceramic joining. The surface temperature of the sample is monitored by a pyrometer and a hydraulic compressor applies pressure on the ceramic specimens to be joined. Figure 2 shows the block diagram of this single mode microwave joining apparatus. Provision was made to alter the environment of the sample either by evacuating the cavity or by filling the cavity with an appropriate gas. An important feature of this system is the acoustic probe which allows in-situ non-destructive evaluation (NDE) of the joint. This system consists of an acoustic transducer embedded in a stainless steel acoustic lens that forms the bottom anvil of the compressor. The transducer is connected to a transceiver that transmits acoustic pulses and receives acoustic echoes. The echoes are displayed on an oscilloscope, and the echo from the joint interface is identified from a knowledge of the speed of sound in the material. The oscilloscope display is then adjusted to enhance this echo, which is monitored continuously throughout the joining process. When a joint is formed, the echo from the joint interface disappears, and a new echo from the far end of the sample appears on the right of the oscilloscope [22].

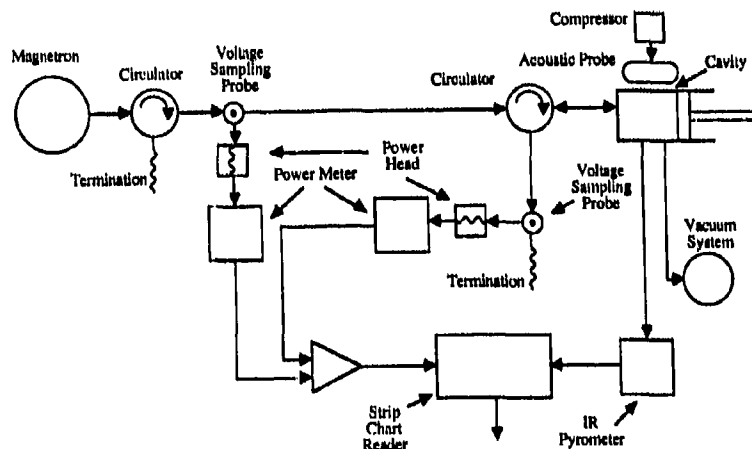


Figure 2. Block diagram of the single mode microwave joining apparatus.

(Reprinted by permission of the American Ceramic Society)

The ceramic materials joined by these two groups include alumina, mullite and silicon nitride. Typical microwave joining times were in minutes as opposed to hours by conventional joining. The joints exhibited greater strength than the as-received materials and did not fail at or near the joint. The joints were not detectable in microscopic observations and the microscopic homogeneity in the vicinity of the joints was retained. There was little difference in the microstructure before and after joining. These results clearly indicate that engineering quality joints of both oxide and non-oxide ceramics can be made in very short times using modest microwave power and compression with very little surface preparation. The increased hardness and fracture toughness implies increased densification at the interface which suggests the diffusion-bonding mechanism as observed in conventional heating of ceramics.

Joining of alumina substrates using AlOOH gel as the interlayer was reported by Al-Assafi and coworkers [23]. AlOOH gel was brushed on both surfaces before joining. The specimens that had gel as the interlayer, and were microwave heated at 1520°C for a soak time of 10 minutes under a pressure of 0.6 MPa, exhibited good joining. The specimens without any gel did not join under identical conditions. However, joining was achieved in both cases, with and without gel, when the samples were heated to temperatures of 1600°C and 1650°C.

Yu et al. reported simultaneous sintering and joining of alumina specimens [24]. The specimens joined were pellets of alumina dry pressed at 2800 MPa. A slip interlayer of the same material was used to conform to the asperities under isostatic pressure of 150 MPa. The whole body was pre-fired at 600°C for two hours before microwave heating/joining at 1400°C for 14 minutes at 0.283 MPa pressure. Some defects were identified at the joining interface, but the dimensions of these defects were similar to those in the sintered bulk material. With conventional heating at the same temperature and pressure for 2 hours, the low density interface was clearly visible.

#### Sintered silicon carbide (SiC) and reaction bonded silicon carbide (RBSC)

The combination of high thermal conductivity, excellent thermal shock resistance and corrosion resistance makes silicon carbide (SiC) an excellent candidate material for a number of applications. These include structural materials for advanced heat engines, heat exchanger tubing, radiant burner tubes and pump components. The use of this material has been limited by the difficulty and cost of manufacturing components of complex shapes.

Sintering and joining of a SiC body is a difficult process. So far, it has not been possible to sinter SiC to high densities without additives and/or external pressure. Small additions of boron and carbon have been shown [25] to result in high densities without the application of external pressure. This development has allowed the fabrication of some components of SiC.

These difficulties in forming and sintering complex shapes of an excellent ceramic material necessitate development of inexpensive and reliable methods to join ceramics, so that complex components could be fabricated from smaller and simpler shapes, which would be easier to reliably manufacture. One of the novel methods involves infiltration of a SiC preform (having excess carbon) by molten silicon at high temperatures. The resultant material, "reaction bonded silicon carbide," (RBSC) is a nearly fully dense ceramic with up to 15 volume percent of free silicon. The residual silicon is distributed at the boundaries between the SiC grains.

### Joining of reaction bonded silicon carbide (RBSC)

Joining of reaction bonded silicon carbide by a conventional heating method was reported by Iseki [26], with aluminum metal as the interlayer. No reaction layer was detected in the micrograph of the region near the reaction bonded SiC-Al interface. Aluminum and silicon in the reaction bonded SiC formed a continuous liquid phase at high temperature; therefore aluminum penetrated into the reaction bonded silicon carbide. However, some cracks were found at the front of the aluminum-penetrated region. These cracks are believed to be formed because of the difference in thermal expansion of aluminum, SiC and silicon.

Microwave joining of reaction bonded silicon carbide with aluminum as the interlayer was reported by Ylin et al. [27]. A single mode resonant cavity was used to heat and join reaction bonded silicon carbide. The joined specimen was reported to be stronger than the as-received material, similar to the earlier microwave joints in oxides and nitrides. A similar penetration of aluminum into Si regions between the SiC grains as noted above was reported.

### **EXPERIMENTAL RESULTS**

Experiments have been carried out for joining of SSiC and RBSC, both in a single mode resonant cavity (as indicated in Figure 2), as well as in a multimode microwave oven with hybrid heating. Microwave joining of SiC (Carborundum Hexoloy™), was performed on specimens 0.9 cm in diameter and 0.6 cm height, as cut with a wafering saw with no polishing. Since direct joining of SSiC is difficult, two different avenues using interlayer materials were followed [28]. The first is essentially a metallic braze joint using Si as the interlayer material. The second attempts to form a SiC or SiC/TiC composite through combustion synthesis using blended powders of Si, C and Ti. The SiC specimens and the interlayer material were held in place in the single mode applicator described above by two alumina rods under a pressure of 2-5 MPa provided by a hydraulic press. The microwave power was turned on and the movable plunger adjusted to minimize the reflected power.

A series of joints was made using Si (powder or slurry) as the interlayer material. Typically, the joining temperature was close to 1450°C for 5-10 minutes with applied power around 250 watts. Figure 3 shows the SEM micrograph of the sectioned joined specimen, with a homogeneous but fairly thick Si interlayer (almost 50 microns when used as powder). Joining was also achieved using the combustion synthesis of SiC/TiC as the interlayer. This technique resulted in a thick interlayer (around 300 microns) with significant porosity (inherent in these reactions). The best results were obtained by plasma spraying a Si layer on one of the specimens to be joined. This joint was made using a 6 Kw power supply and a 61x61 cm square multimode cavity. The specimen was placed inside zirconia insulation and no external pressure was applied. The interlayer region was less than 5 microns in width and no variation in Knoop hardness across the joint was observed.

As described above [26,27] RBSC could be joined using aluminum as the interlayer both by microwave as well as conventional joining. Our experiments demonstrated microwave joining of sintered SiC using silicon as the interlayer material. Furthermore microwave heating has been observed to result in enhanced diffusion and reaction rates. In light of these results it is evident that microwave heating should, in principle, eliminate the need of using any interlayer material to join RBSC. The presence of silicon at the grain boundaries of silicon carbide grains, and the enhanced

mass transport of silicon across the interface (the preferential heating area in microwave heating) would result in a diffusion bonding of the pieces to be joined. This would avoid problems caused by the mismatch of thermal expansion coefficient. With this rationale, experiments were carried out for microwave joining of RBSC specimens. Joining of these specimens without an interlayer was indeed successful using both the single mode cavity and microwave hybrid heating.

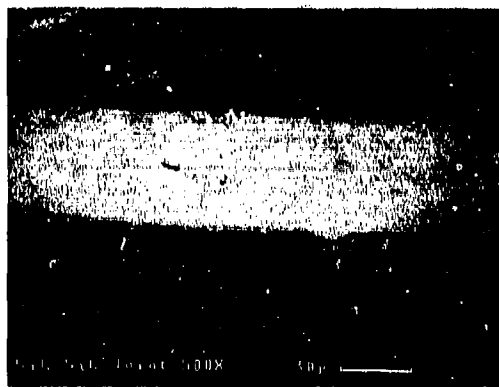


Figure 3. SEM micrograph of a sectioned joint showing a fairly thick interlayer of Si. (Reprinted by permission of the American Ceramic Society)

Direct joining of RBSC specimens of 0.9 cm diameter and 0.5 cm height were performed in the single mode applicator described earlier. The specimens were enclosed in alumina insulation (with a viewing hole to monitor temperature) and placed at the maximum electric field position in the cavity. Microwave power was coupled to the specimen by adjusting a plunger and an adjustable iris such that the reflected power was minimized. In a few minutes the specimens turned red hot and the surface temperature was monitored with an optical pyrometer. The specimens were held in the 1450 - 1500°C temperature range for 10 - 15 minutes and then cooled by turning off the microwave power. Figure 4 shows an example of the micrograph of RBSC specimens joined in a single mode cavity.

The interfacial region is similar to the bulk of the specimens. A silicon rich band of about 5 micron width is observed at the interfacial region. Since similar patches of silicon are seen throughout the RBSC material, the presence of this band does not negatively impact the mechanical properties of the joint. This argument is supported by the essentially identical appearance of micrographs of sectioned joints that had greater strength than as received RBSC [27].

Joining of ceramics is possible with the single mode apparatus, but there is a limitation on the size of the specimens that can be joined. Therefore, designing of special applicators is essential for specific applications. Microwave hybrid heating, on the other hand, is more flexible for industrial applications. Specimens of varying shape

or size can be placed inside the insulation lined with a susceptor. The radiative losses from the surface of the specimen are compensated by the radiant heating from the susceptor, which provides for uniformity in heating the specimen. The soak temperature can be maintained by pulsing the microwave power. Pulsing the microwave power helps to level off the temperature profile within the sample. With microwave power continuously on, although the power level may be lowered, the area in the specimen that is at higher temperature will absorb more microwave energy, which may result in nonuniform heating and even thermal runaway. The combination of microwave hybrid heating and maintaining the temperature by pulsing the power (as opposed to lowering the power level) provides much better uniformity.

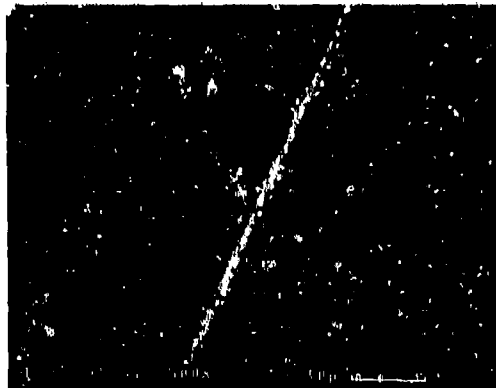


Figure 4. SEM of RBSC-RBSC joint.

Short lengths (2.5 cm) of small scale (5 cm diameter) RBSC tubes intended for radiant burner tube applications were supplied by Coors Ceramics. These tube sections were joined directly with and without any polishing, using the multimode oven with hybrid heating [29]. The bleeding of silicon filled the void space, making the joint leak-tight. The joined tube was installed on a vacuum line which held the vacuum ( $12 \times 10^{-3}$  torr) as well as a single tube. Similar joining experiments were performed with surfaces polished (by LANL) to a 5 micron finish. Figure 5 is a picture of these joined RBSC tubes. Joining is apparent all around the circumference with substantial bleeding of silicon. The tubes were cut into test bend bars (by Coors) for mechanical testing. The specimens resulted in flexural strengths ranging up to 250 MPa with an average of 190 MPa [30]. Microwave joining of small specimens in a single mode applicator has resulted in higher flexural strengths than the as-received specimens, in contrast to the present results. These experiments on fairly large specimens were performed in a multimode applicator with only 900 watts, some of which is absorbed by the susceptor used for hybrid heating. It is anticipated that if more power per unit mass were available, the joint strengths observed in microwave joining using single mode applicators (having very high power densities) would be attained with multimode applicators.



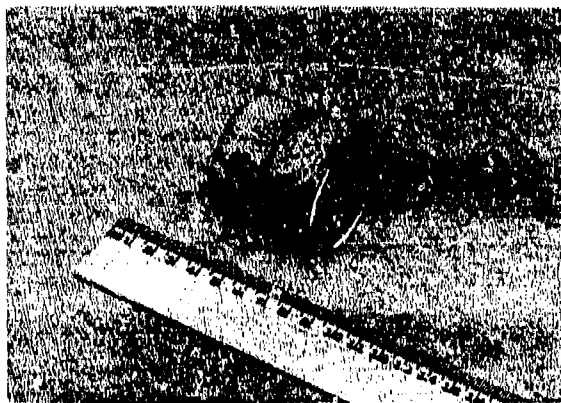


Figure 5. Photograph of Coors RBSC tube sections joined in a multimode oven.

Joining of RBSC to Hexoloy™ (SiC) specimens (0.9cm dia) was first carried out in a single mode cavity. The joined specimens were sectioned and polished for electron microscopy. Figure 6 shows a low magnification micrograph of a joint between RBSC and Hexoloy™. The joint is not visible in the interior of the sample (region A) but is identified close to the edge of the sample (region B) because of the poor matching of the two surfaces. A crack in the RBSC (region C) where the joint is good indicates that the joint is stronger than RBSC. Figure 7 shows a higher magnification of region A which is similar in appearance to that of the RBSC-RBSC joint shown in Figure 4.



Figure 6. SEM micrograph of RBSC to SiC joining. Note a crack in RBSC where joining appears to be good.

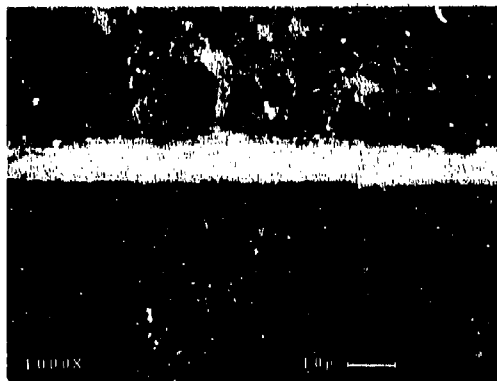


Figure 7. RBSC to SSiC using a single mode applicator.

Larger diameter (2.5 cm) tubes of SSiC were joined to RBSC tubes in a multimode applicator with hybrid heating. Micrographs of joined sections were identical to that of Figure 7, indicating that a similar joint can be made with either a single mode or a multimode applicator. This work has demonstrated the feasibility of joining RBSC to itself and to SSiC, an important step for the fabrication of tube assemblies for high temperature heat exchangers and radiant burners.

#### SUMMARY AND CONCLUSIONS

It has been demonstrated that joining of oxide, nitride and carbide ceramics can be accomplished using microwave energy. Strong joints can be produced much more rapidly than with conventional methods. Single mode applicators are presently restricted to small specimens of simple configurations. However, joining of larger specimens having more complex shapes is possible using a multimode applicator with hybrid heating. Current efforts are underway to scale-up the microwave applicator design to allow joining of larger components for industrial applications.

## REFERENCES

1. J.M. Osepchuk, A History of Microwave Heating Applications, IEEE Transactions on Microwave Theory and Techniques, MTT-32, (9), (1984).
2. A.R. Von Hippel, Dielectric Materials and Applications, MIT Press and John Wiley & Sons, New York (1954).
3. R.V. Decarreau and R.A. Peterson, Microwave Processing and Engineering, Ellis Horwood Ltd., Chichester, U.K., (1986).
4. W.H. Sutton, M.H. Brooks and I.J. Chabinsky, Microwave Processing of Materials I, Mater. Res. Soc. Proc. 124, Pittsburgh, PA, (1988).
5. W.B. Snyder, W.H. Sutton, M.F. Iskander and D.L. Johnson, Microwave Processing of Materials II, Mater. Res. Soc. Proc. 189, Pittsburgh, PA, (1991).
6. D.E. Clark, F.D. Gac and W.H. Sutton, Microwaves: Theory and Application in Materials Processing, Ceram. Trans. 21, Westerville, OH, (1991).
7. R.L. Boutty, W.H. Sutton and M.F. Iskander, Microwave Processing of Materials III, Mater. Res. Soc. Proc. 269, Pittsburgh, PA, (1992).
8. D.A. Lewis, Microwave Processing of Polymers - An Overview, p. 21, Ref. 7.
9. M.F. Iskander, Medical and Biological Applications of Electromagnetic Techniques -- A relevant Experience to the Microwave Processing of Materials Research, p. 69, Ref. 4.
10. M.D. Rohrer and R.A. Bulard, Microwave Sterilization of Dental Instruments and Hydrophilic Contact Lenses, Presented at the Microwave Processing of Materials Symposium, Spring Meeting of Materials Research Society, San Francisco, CA (1990).
11. J. Zygmunt, Industry warms up to microwave ovens, High Technology, p. 62, March (1987).
12. J.W. Walkiewicz, S.L. McGill and L.A. Moyer, Improved Grindability of Iron Ores using Microwave Energy, p. 297, Ref. 4.
13. J. Suzuki, M. Hosaka, Y. Kawasaki, A. Nishino and K. Sogon, A Microwave Burning Processor for Waste Disposal, The Journal of Microwave Power & Electromagnetic Energy, 25, (3), 168 (1990).
14. C. Shibata and H. Tamai, An Improved Microwave Melting Furnace for Radioactive Wastes, The Journal of Microwave Power & Electromagnetic Energy, 25, (2), 81 (1990).
15. R. Varma, S.P. Nandi and J.D. Katz, Detoxification of Hazardous Waste Streams Using Microwave-assisted Fluid-bed Oxidation, p. 67, Ref. 5.
16. W.H. Sutton, Microwave Processing of Ceramics - An Overview, p. 3, Ref. 7.
17. A.S. Dé, I. Ahmad, E.D. Whitney and D.E. Clark, Effect of Green Microstructure and Processing Variables on the Microwave Sintering of Alumina, p. 283, Ref. 5.
18. A.S. Dé, I. Ahmad, E.D. Whitney and D.E. Clark, Microwave (Hybrid) Heating of Alumina at 2.45 GHz: I. Microstructural Uniformity and Homogeneity, p. 319, Ref. 6.
19. W.H. Sutton, Microwave processing of Ceramic Materials. Ceram. Bull. 68, No. 2, p. 376, (1989).
20. T.T. Meek and R.D. Blake, Ceramic-glass-ceramic seal by microwave heating, U.S. Patent No. 4,529,857. Ceramic-glass-metal seals by Microwave heating, U.S. Patent No. 4,529,856, (1985).
21. H. Fukushima, T. Yamanaka and M. Matsui, Microwave Heating of Ceramics and its Application to Joining, p. 267, Ref. 4.
22. D. Palath and R. Silbergliit, Microwave Joining of Ceramics, Ceram. Bull. 68, (9), p. 1601, (1989).
23. S. Al-Assafi, I. Ahmad, Z. Fathi and D.E. Clark, Microwave Joining of Ceramics, p. 515, Ref. 6.
24. X.D. Yu, V.V. Varadan and V.K. Varadan, Application of Microwave Processing to Simultaneous Sintering and Joining of ceramics, p. 497 Ref. 6.
25. S. Prochazka, Sintering of Silicon Carbide, p. 239 in Proc. Conf. Ceramics for High-Performance Applications, Eds. J.J. Burke, A.E. Gorum and R.M. Katz, Brook Hill, (1975).
26. T. Isaki, T. Kumeda and T. Maruyama, Interfacial Reactions between SiC and Aluminum during Joining, Journal of Materials Science, 19, p. 1692, (1984).
27. T-Y Ylin, V.V. Varadan and V.K. Varadan, Microwave Joining of Si-SiC, p. 507, Ref. 6.
28. R. Silbergliit, D. Palath, W.M. Black, H.S. Sa'adaldin, J.D. Katz and R.D. Blake, Investigation of Interlayer Materials for the Microwave Joining of SiC, p. 487, Ref. 6.
29. I. Ahmad, R. Silbergliit, W.M. Black, H.S. Sa'adaldin and J.D. Katz, Microwave Joining of Silicon Carbide using Several Different Approaches, p. 271, Ref. 7.
30. J. Sibold, Measurements made by Coors Ceramics Company, Golden, CO (Unpublished, private communication).

# TEM INVESTIGATION OF MICROWAVE JOINED Si-SiC/Al/Si-SiC AND $\alpha$ -SiC/Al/ $\alpha$ -SiC.

S. ARUNAJATESAN and A. H. CARIM, Department of Materials Science and Engineering, and T. Y. YILIN and V. K. VARADAN, Department of Engineering Science and Mechanics, The Pennsylvania State University, University Park, PA 16802.

## ABSTRACT

Electron probe microanalysis (EPMA) and transmission electron microscopy (TEM) have been used to examine the SiC/Al interfaces in microwave joined Si-SiC/Al/Si-SiC and  $\alpha$ -SiC/Al/ $\alpha$ -SiC. Both the SiC/Al interfaces display intimate contact between the ceramic and metal and are free of porosity. EPMA of the  $\alpha$ -SiC/Al/ $\alpha$ -SiC joints reveals that no Al has diffused into the bulk  $\alpha$ -SiC, unlike the reported diffusion of Al in Si-SiC/Al/Si-SiC. The TEM investigations show that while the Si-SiC/Al/Si-SiC interface is reaction-free, the  $\alpha$ -SiC/Al/ $\alpha$ -SiC joint contains Si at the interface. The TEM findings are correlated to the strength data available on these joints and the possible reasons for the presence of Si in the absence of  $Al_4C_3$  in the  $\alpha$ -SiC/Al/ $\alpha$ -SiC joint are discussed.

## INTRODUCTION

Silicon carbide is an excellent candidate for advanced high-temperature structural applications in automobile and aerospace industries, due to its toughness, high strength to weight ratio, and good strength retention at high temperatures. The applications involve the fabrication of complex SiC components; hence, the joining of SiC becomes important. One technique employed is to join SiC blocks using foils of Al or Ti as an intervening layer. Al has been widely investigated due to the good wetting, fewer reaction products, and lower fabrication temperatures associated with it. In the conventional joining of SiC in a furnace, the Al foil, due to a much higher thermal conductivity, heats faster than the SiC bulk material, setting up sharp temperature gradients in the ceramic. Complex heating cycles, which can prove to be costly, are therefore required to ensure uniform heating and subsequent joining. One alternative route, which offers features like uniform and rapid heating and consequently very short joining times, is microwave heating.

Since microwave heating is based on the "in-situ" conversion of electromagnetic energy to thermal energy within a material, it provides the possibility of uniform heating of the bulk material. The feasibility of utilizing microwave energy as a joining technique has been explored extensively and the resulting joints have been reported to have strengths equal to and sometimes exceeding those of the starting materials [1-3].

In this preliminary investigation, transmission electron microscopy (TEM) combined with energy dispersive spectroscopy (EDS) has been used to examine the microstructure at the SiC/Al interface formed in the microwave joining of SiC with an intervening layer of Al. To the best of our knowledge, this is the first reported TEM investigation of microwave joints. A TEM study of this kind uncovers important microstructural information about the metal-ceramic interface such as the wetting and porosity at the interface and characteristics such as the morphology, grain size, and distribution of the phases present at the interface. This information, along with the measured properties of the joints, can lead to a better understanding and subsequently better control of joint properties.

Two cases have been examined in this study using TEM: siliconized silicon carbide (Si-SiC) joined to itself using an Al foil (Si-SiC/Al/Si-SiC) and single-phase alpha silicon carbide ( $\alpha$ -SiC) joined to itself using an Al foil ( $\alpha$ -SiC/Al/ $\alpha$ -SiC). EPMA has been performed at the  $\alpha$ -SiC/Al/ $\alpha$ -SiC interface to examine the diffusion of Al into bulk  $\alpha$ -SiC. Fracture strength values and Weibull moduli of both types of SiC measured before and after joining have been reported earlier [1]. For reference, the fracture strength values are listed in Table I.

Table I. Fracture Strength data.

Material	Average Fracture Strength (MPa)
Original Si-SiC	215.4
Si-SiC/Al/Si-SiC	219.4
Original $\alpha$ -SiC	~388
$\alpha$ -SiC/Al/ $\alpha$ -SiC	194.4

Table II. Compositions and Dimensions of materials used.

Material	Composition	Dimensions
Si-SiC	8 at% Si, balance SiC	30x20x6 mm <sup>3</sup>
$\alpha$ -SiC	0.1-5.0 wt%B 0.5-2.0 wt%C balance SiC	35x25x6 mm <sup>3</sup>
Al foil	1.5 at% Fe 0.9 at% Si, balance Al	16 $\mu$ m thick

## EXPERIMENTAL PROCEDURE

The compositions and dimensions of the Si-SiC,  $\alpha$ -SiC, and Al foil used as the interlayer are as given in Table II. The joining surfaces were polished and were cleaned in an ultrasonic cleaner just before joining.

The Al foil was sandwiched between a pair of SiC blocks and the specimen was then placed inside the center of a multi-mode Cu cavity. 500 W of microwave power was supplied to the cavity through a variable iris which was tuned to resonate at 2.45 GHz by an adjustable short. Quartz through-tubes were placed above and below the SiC Al-SiC assembly to exert pressure of 1.2 MPa on the system. The entire process was carried out in air and the system was heated until the surface temperature (measured by a pyrometer) reached 1250°C. The temperature was maintained at 1250°C for one minute and the system was then turned off to let the assembly cool to room temperature. After joining, cross-sectional samples were cut and polished and EPMA was performed using a Camebax SX30. Sections of the sample containing the interface were used to make TEM samples by standard techniques - mechanical polishing and dimpling followed by ion-beam thinning [4]. The TEM and EDS were done on a Philips 420T instrument at 120 kV. Both the EPMA and microscopy were done at the Materials Characterization Laboratory of the Pennsylvania State University.

## RESULTS AND DISCUSSION

### (i) Diffusion of Al

While the presence of Al at the SiC/SiC joint limits the high-temperature applicability of the joint itself, the joined component could still be subjected to higher temperatures at regions away from the SiC/Al interface. However, a significant in-diffusion of Al would seriously restrict the high-temperature capability of the entire SiC component. Electron probe microanalysis (EPMA) was done on the  $\alpha$ -SiC/Al/ $\alpha$ -SiC sample to examine the diffusion of Al into bulk  $\alpha$ -SiC and Fig. 1 shows a line scan of the Al K $\alpha$  signal at the interface. It is evident from the scan profile that the concentration of Al falls off rapidly away from the interface. Point analyses of the Al concentration were performed at varying distances from the interface and it was found that, at distances of more than 3.6  $\mu$ m from the interface, the amount of Al present was less than the detection limit of the instrument (500ppm).

EPMA of microwave joined Si-SiC/Al/Si-SiC, reported earlier [2], showed extensive diffusion of Al into the free Si present in the bulk Si-SiC. Since Al-Si is a eutectic system [5], it is possible that above the eutectic temperature of 577°C, Al diffuses through the free Si (in the Si-SiC) through liquid phase transport. This hypothesis is supported by the absence of detectable amounts of Al in the (Si free) bulk  $\alpha$ -SiC.



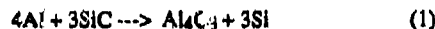
Fig. 1. EPMA scan of the Al  $K_{\alpha}$  line superimposed on the backscattered image of the  $\alpha$ -SiC/Al interface.

### (ii) Interface morphology

Figs. 2 and 3 are TEM micrographs of the SiC/Al interface in Si-SiC/Al/Si-SiC and  $\alpha$ -SiC/Al/ $\alpha$ -SiC respectively. The boundary between SiC and Al, in both cases, is completely continuous and pore-free. It was seen that the Al accurately follows the contours of the SiC along the entire length of the interface observed in the TEM. In some regions of the interface examined in the TEM, it was found that crevices on the SiC surface, up to a few microns in depth, were completely filled with Al. This can be seen to a lesser extent in Fig. 2, in which the Al has fully penetrated a dent, about 0.25  $\mu\text{m}$  deep, on the SiC surface. The presence of strain contrast along the interface in Fig. 2 further emphasizes the intimate contact between the interlayer and the SiC substrate. The difference in the extent of polishing of the two samples is seen in the different surface roughness at the interfaces. The Al interlayer has an unusually large grain size, with the grains being much larger in the direction along the interface than that perpendicular to it. This would suggest that the Al foil melted during the joining process, which is consistent with the surface temperature of 1450°C recorded by the pyrometer. The thickness of the Al interlayer, from Figs. 2 and 3, is about 1  $\mu\text{m}$  in the Si-SiC/Al/Si-SiC and 2  $\mu\text{m}$  in the  $\alpha$ -SiC/Al/ $\alpha$ -SiC, while the original foil used in both cases was 15  $\mu\text{m}$  thick. The observations of beads of Al at the edges of the sample after microwave joining and the diffusion of Al into the bulk Si-SiC are consistent with this large reduction in the thickness of the Al interlayer.

### (iii) $\text{Al}_4\text{C}_3$ formation

The microstructure of the SiC/Al interface that results from conventional joining techniques has been widely investigated [6-8] and the relevant reaction at this interface has been shown to be [6]



This reaction is generally not desired at the interface, since the presence of aluminum carbide, a brittle product, adversely affects the mechanical properties and the corrosion resistance of the joint [9]. As is evident from reaction (1), the formation of the carbide can be suppressed by the presence of free Si with a sufficiently high chemical activity. Since there is almost no solubility of Si in Al at temperatures below 300°C, and Si in SiC below 2000°C [5], even a small amount of Si present in either Al or SiC would be associated with a significant chemical activity.

In the Si-SiC/Al/Si-SiC interface, the free Si in the Si-SiC retards the formation of  $\text{Al}_4\text{C}_3$  by reaction (1) and hence the interface is expected to be free of reaction products. This is consistent with the fracture strength values of the Si-SiC/Al/Si-SiC joints [1], which are similar to those of the original Si-SiC before joining. In the presence of  $\text{Al}_4\text{C}_3$ , a brittle phase, the joint

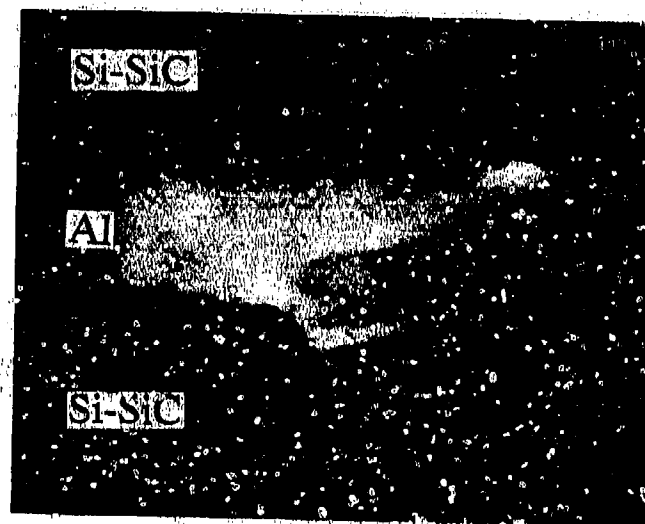


Fig. 2. TEM micrograph of Si-SiC/Al/Si-SiC interface.

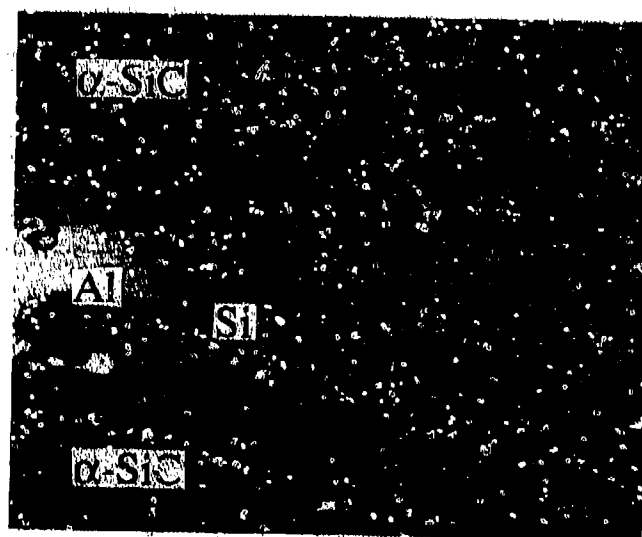


Fig. 3. TEM micrograph of  $\alpha$ -SiC/Al/ $\alpha$ -SiC interface.

strength would be expected to show a deterioration. No interfacial reaction products were detected at the Si-SiC/Al/Si-SiC interface.

The  $\alpha$ -SiC/Al/ $\alpha$ -SiC interface, with no free Si, might be expected to contain the products of reaction (1):  $\text{Al}_4\text{C}_3$  and Si. Here, although the strength values of the  $\alpha$ -SiC/Al/ $\alpha$ -SiC joints have been found to be only 50% of those of the original  $\alpha$ -SiC before joining [1], it must be noted that the average strength values of the SiC/Al interface itself in both the Si-SiC/Al/Si-SiC and the  $\alpha$ -SiC/Al/ $\alpha$ -SiC are within 10% of each other. This would be consistent with the absence of the brittle  $\text{Al}_4\text{C}_3$  at both interfaces. TEM micrographs of the  $\alpha$ -SiC/Al/ $\alpha$ -SiC interface showed the presence of free Si at the  $\alpha$ -SiC/Al/ $\alpha$ -SiC interface; however,  $\text{Al}_4\text{C}_3$  was not detected. Fig. 4 is a TEM image of the Si particles. The presence of these Si particles was confirmed both by the corresponding electron diffraction pattern and EDS. All the Si detected was in contact with the SiC surface, i.e., there were no isolated Si particles within the Al interlayer. This presence of free Si and the absence of  $\text{Al}_4\text{C}_3$  at the interface could be due to one of several reasons as described below.

One possibility is that reaction (1) did occur at the interface and Si and  $\text{Al}_4\text{C}_3$  were formed as reaction products. The Si has been detected in the TEM, but the carbide has not. This would be the case if Si forms as isolated particles, while  $\text{Al}_4\text{C}_3$  is present as a very thin film – a few nanometers thick – along the  $\alpha$ -SiC/Al boundary. A simplistic calculation using reaction (1) and the densities of  $\text{Al}_4\text{C}_3$  and Si shows that the amount of free Si detected in the  $\alpha$ -SiC/Al/ $\alpha$ -SiC system could be consistent with the presence of such a thin layer of  $\text{Al}_4\text{C}_3$  at the interface. Further investigation using high-resolution TEM would be necessary to examine this possibility. It is also possible that isolated particles of  $\text{Al}_4\text{C}_3$  are present, but were not seen in the electron transparent areas of the samples examined. This is also conceivable, since the electron transparent area in a TEM sample is only a small fraction of the total interfacial area in the sample; which in turn is a small fraction of the interface formed. On the other hand, the  $\text{Al}_4\text{C}_3$  formed as a reaction product would be expected to exist in contact with the Al, SiC, and the Si; however, no  $\text{Al}_4\text{C}_3$  was detected in the vicinity of the Si particles. The formation of  $\text{Al}_4\text{C}_3$  and its subsequent diffusion into the bulk  $\alpha$ -SiC does not appear to occur, since results of the EPMA confirm the absence of any Al in the bulk  $\alpha$ -SiC.

Another explanation arises from the 0.85 wt% Si present as an impurity in the Al

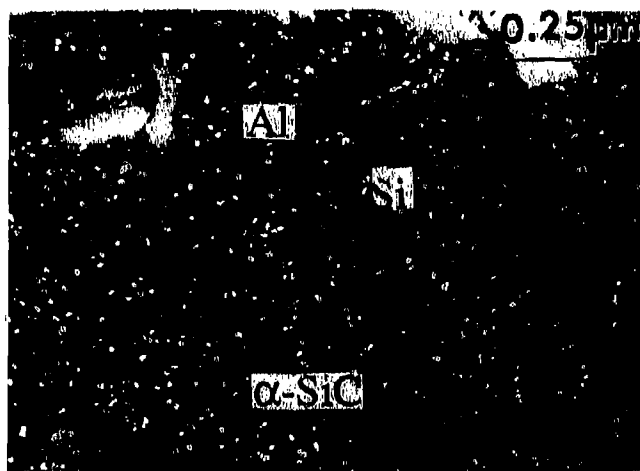


Fig. 4. TEM micrograph showing Si particles at  $\alpha$ -SiC/Al interface. Inset shows selected area diffraction pattern from a Si particle and corresponds to [011] zone axis of Si.



interlayer. Since Si has practically no solubility in Al below 300°C [5], even a small amount of Si present in the Al would have a high activity, increasing the surface energy of the system. On cooling, this Si could tend to segregate to the interface with  $\alpha$ -SiC to lower the energy, resulting in a sharp increase in the concentration of Si at the interface. This in turn would suppress the formation of  $\text{Al}_4\text{C}_3$ , and eventually, the free Si would precipitate at the SiC/Al interface. While the amount of Si seen in Fig. 2 does not appear to be consistent with the 0.85 wt% Si present in the Al, it must be noted that for the most part, the interface was barren and contained no Si; the free Si was present only in small isolated pockets. This argument, however, would imply the precipitation of free Si in the Si-SiC/Al/Si-SiC system also; as mentioned earlier, the interface in the Si-SiC/Al/Si-SiC system appears to be free of any additional phases (including Si).

### SUMMARY AND CONCLUSIONS

SiC/Al interfaces in microwave joined Si-SiC/Al/Si-SiC and  $\alpha$ -SiC/Al/ $\alpha$ -SiC have been investigated using EPMA and TEM. EPMA of the  $\alpha$ -SiC/Al/ $\alpha$ -SiC joints reveals that no Al has diffused into the bulk  $\alpha$ -SiC, as opposed to Si-SiC/Al/Si-SiC joints in which diffusion of Al into the bulk Si-SiC has been previously reported. This would support the contention that the Si in the Si-SiC provides a diffusion path for the Al due to liquid phase transport.

TEM investigation of the SiC/Al interfaces in Si-SiC/Al/Si-SiC and  $\alpha$ -SiC/Al/ $\alpha$ -SiC shows that both interfaces are free of porosity and display intimate contact between the Al and SiC. Large grains of Al are seen, indicating that the Al has melted during joining. As expected, TEM images show no reaction products at the Si-SiC/Al/Si-SiC interface. While the  $\alpha$ -SiC/Al/ $\alpha$ -SiC interface might be expected to contain both  $\text{Al}_4\text{C}_3$  and Si (formed as products of the reaction between SiC and Al), there was no clear degradation of the fracture strength of the joint, as would be expected in the presence of significant amounts of a brittle phase like  $\text{Al}_4\text{C}_3$ . Si was detected by the TEM, but no  $\text{Al}_4\text{C}_3$  was imaged. One explanation would be that the  $\text{Al}_4\text{C}_3$  is present at the interface but has not been imaged in the TEM due to the limited field of view in the TEM samples. It is also possible that  $\text{Al}_4\text{C}_3$  is present as a thin layer – a few nanometers thick – along the  $\alpha$ -SiC/Al interface. The presence of such a thin film of  $\text{Al}_4\text{C}_3$  would be expected to have little effect on the strength of the joint, which is consistent with the observations. It would be difficult to confirm the presence of such a thin layer in a conventional TEM investigation of this kind; further work using HREM would be necessary to examine this possibility. Another explanation, the precipitation of supersaturated Si from the Al interlayer, would satisfactorily explain the presence of Si but not  $\text{Al}_4\text{C}_3$  at the joint, and is also consistent with the absence of any clear change in interfacial strength. This would, however, suggest the precipitation of Si in the Si-SiC/Al/Si-SiC system also, which was not observed.

### ACKNOWLEDGEMENTS

The authors would like to thank Girish Kelkar for useful discussions and Mark Angelone for help with EPMA. This work was supported by the Department of the Navy, Office of the Chief of Naval Research, Young Investigator program under grant #N00014-91-J-4051.

### REFERENCES

1. T. Y. Ylin, Ph. D. thesis, The Pennsylvania State University, 1992.
2. T. Y. Ylin, V. V. Varadan, V. K. Varadan, and J. C. Conway in *Microwaves: Theory and Applications in Materials Processing*, edited by David E. Clark, Frank D. Gac, and Willard H. Sutton (Ceramic Transactions 21, 1991).
3. H. Fukushima, T. Yamanaka, and M. Matsui, *J. Mater. Res.* 5 (2), 397 (1990).
4. J. C. Bravman and R. Sinclair, *J. Electron Microsc. Tech.* 1, 53 (1984).
5. W. G. Moffatt, *Handbook of Binary Phase Diagrams*, Vol. 1 (Genium Publishing Corp., New York, 1984).
6. T. Isaki, T. Kameda, and T. Maruyama, *J. Mater. Sci.* 19, 1692 (1984).
7. J. C. Viala, P. Fortier, and J. Rouix, *J. Mater. Sci.* 25, 1842 (1990).
8. S. D. Peteves, P. Tambuyser, P. Helbach, M. Audier, V. Laurent, and D. Chatain, *J. Mater. Sci.* 25, 3765 (1990).
9. D. J. Lloyd, H. Lagace, A. Moleod, and P. L. Morris, *Mat. Sci. Eng. A107*, 73 (1989).

## HIGH SPEED JOINING OF ALUMINUM METAL MATRIX COMPOSITES USING CONTINUOUS WAVE AND PULSED LASERS

PARWAIZ A. A. KHAN AND ANAND J. PAUL

Concurrent Technologies Corporation, 1450 Scalp Avenue, Johnstown, PA 15904

### ABSTRACT

Due to their superior mechanical properties and high strength to weight ratio, metal matrix composite materials are increasingly being used in aerospace, automotive and defense industries. The use of a fusion related conventional joining technique, such as arc welding, leads to the formation of undesirable non-equilibrium phases in the weld zone, where as diffusion and adhesive joining techniques are rather slow. Non contact multi-kilowatt laser joining, though fully developed for high speed autogenous joining of different alloys, is not yet adequate for joining of metal matrix composites. Efforts have been made by several researchers to control the composition and microstructure of laser joined aluminum metal matrix composites by controlling the energy input and by the use of filler wires. In view of the current industry trend to use more light weight structural composite materials, and greater use of high energy density beams for a variety of metalworking applications, the authors have reviewed the current status of high speed laser joining of metal matrix composites. Emphasis is placed on problems and various techniques which can be used to achieve a better control on composition and microstructure during high energy laser joining of aluminum metal matrix composites.

### INTRODUCTION

The ever growing demand for new high performance materials to be used in highly specialized applications spurred the development of new engineering materials. Composite materials were developed because no single, homogeneous structural material could be found that had all of the desired properties for a given application [1,2]. Various stiffer and stronger reinforcements such as particulates, continuous and discontinuous fibers or laminates when added to a relatively weak matrix form a composite material whose properties are superior to that of the matrix. Depending upon the type of the matrix, composites are divided into polymer and metal matrix. Metal matrix composites consist of a metal base that is reinforced with one or more constituents, such as continuous graphite, alumina, silicon carbide, or boron fibers and discontinuous graphite or ceramic materials in particulate or whisker form. When compared with polymer composites, metal matrix composites offer certain advantages, such as, high tensile and shear moduli (which are compatible with those of the fibers), high melting point, small thermal expansion coefficient, resistance to moisture, dimensional stability, joinability, high ductility and toughness.

Some of the important applications of metal matrix composites include, mid fuselage, landing gear drag link of space shuttle, neutron shielding, aircraft, missiles, engines, bridging, pressure vessels, projectile fins, drive shafts, tubes, reinforced pistons and missile wings [3]. The structures made of composites are often trimmed or joined to net size and/or shape and attached to the final assembly. The use of a low density fusion related joining technique, such as, arc welding leads to the formation of undesirable non-equilibrium phases in the weld zone, where as diffusion and adhesive joining techniques are rather slow. Several researchers have conducted different studies to control the composition and microstructure of laser joined metal matrix composites. The current status of high speed high energy laser joining of metal matrix composites is discussed in this review paper.

Electron beam (EB) and laser beam (LB) are two important high power density joining processes that have gained world wide acceptance in many industries. Electron beam welding of composites has not been very successful due to vacuum requirements. Recent advances in

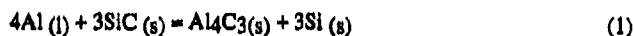
laser systems, especially in laser beam and workpiece positioning and process control, have significantly enhanced materials processing applications of lasers. Although, lasers have been used for joining many important engineering materials, its applications to joining of metal matrix composites is not yet fully developed. A survey of the recent composite and laser literature clearly demonstrates that in the last thirteen years, Japanese, European and Russian investigators have published more articles on laser processing of composites than their US counterparts. Furthermore, most of the work has been on laser machining of epoxy based composites, such as, Kevlar, Graphite or Glass epoxy composites [4-6]. The earlier work on laser processing was performed on continuous fiber metal matrix carbon/1100 aluminum matrix composite, carbon/6061 aluminum composite, graphite/aluminum composite, and SCS-6/Ti-15-3 composites [7,8].

More recent work (Table I) has been primarily on cutting and welding of SiC and Alumina reinforced aluminum matrix composites which are increasingly being used in aerospace applications due to their high strength and light weight [9-15]. Dahotri et al. have performed several studies in which the cutting and welding behavior of A356-Al composite reinforced with 10-12% SiC was investigated [9-12]. A 3.7 Kilowatt, RF excited, carbon dioxide laser operating in continuous and pulsed mode was used. Cola et al. also investigated high speed laser welding behavior of A356-Al composite reinforced with 15% SiC particulates by using a 1.5 Kilowatt continuous wave, carbon dioxide laser, and a 300 watt pulsed Nd:Yag laser [13]. More recently Kawali et al. and Meinert et al. performed cutting and welding studies on 6061-Al matrix composite reinforced with 20% Al<sub>2</sub>O<sub>3</sub> using continuous wave 5 and 1.5 Kilowatt carbon dioxide lasers respectively [14,15]. These recent studies have greatly emphasized the advantages of lasers which make it possible to achieve a better control of composition and microstructure during laser welding of metal matrix composites.

Table I  
Summary of Recent Studies on Laser Joining of Metal Matrix Composites [9-15]

Dahotri et al. (1989-91)	Cola et al. (1990)	Kawali et al. (1991)	Meinert et al. (1992)
A356 + 10% SiC	A356 + 15% SiC	6061 Al +20%Al <sub>2</sub> O <sub>3</sub>	6061 Al + Al <sub>2</sub> O <sub>3</sub> , 20%SiC
3.7 Kilowatt CO <sub>2</sub> (RF Excited)	1.5 Kilowatt CO <sub>2</sub> and 300 watt Pulsed Nd:Yag	5 Kilowatt CO <sub>2</sub> (Continuous wave)	1.5 Kilowatt CO <sub>2</sub> (Continuous wave)
Microstructure Composition Control	Microstructure	Weld Chemical Analysis	Composition Control

In their earlier study, Dahotri et al. used a continuous laser power of 2, 3 and 4 Kilowatt, a traverse speed of 25 cm/s and Ar flow rate of 4 liters per minute to weld A356-Al matrix reinforced with 10% SiC [9]. The microstructural analysis showed, that the fusion zone consisted of platelike and blocky precipitates distributed in a fine dendritic matrix, whereas, the HAZ consisted of platelike precipitates along with SiC particulates and small blocks of Si. X-ray analysis of the laser melted region (Figure 1) showed the presence of Al<sub>4</sub>C<sub>3</sub> carbide and other phases. It is believed by many researchers that the formation of Al<sub>4</sub>C<sub>3</sub> carbide takes place due to the following chemical reaction between aluminum and SiC.



The intense heat developed in the laser melted region melts SiC to provide C for the formation of Al<sub>4</sub>C<sub>3</sub> (Figure 2). It can be seen from Figure 2a, that the amount of Al<sub>4</sub>C<sub>3</sub> formed in the fusion zone is a function of specific energy. This can be verified from Figure 2b, where the effect of

specific energy on the volume of SiC is plotted along with the volume of  $\text{Al}_4\text{C}_3$ . A drop in the volume of SiC associated with an increase in the volume of  $\text{Al}_4\text{C}_3$  can be seen. A high heat input destroys SiC particulates completely and forms large carbide plates in the fusion zone. The excess amount of carbide is detrimental and can be controlled to some extent by controlling the heat input [9-12].

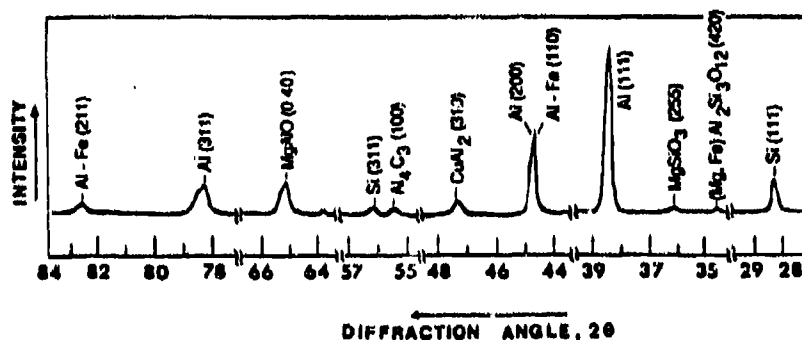


Figure 1. The X-ray analysis of laser melted A356-Al+10% SiC composite [9].

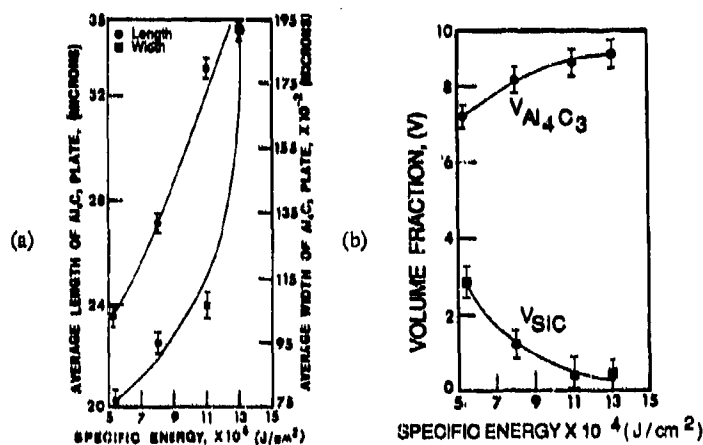


Figure 2. (a) The length and width of  $\text{Al}_4\text{C}_3$  plates and (b) volume fraction of SiC and  $\text{Al}_4\text{C}_3$  as a function of specific energy [9].

In another study, Dahotri et al. investigated the effect of laser power on the extent of energy transfer for three different materials, namely, A356-Al, A356 reinforced with 10 and 20% SiC [11]. It was found that the heat transfer to the composite is actually energy dependent (see Table II). At low laser powers, the surface emissivity plays an important role, hence the 20% SiC reinforced composite had the highest absorption and melting (Figure 3). At medium laser power, the extent of energy transfer is controlled by fluid flow, hence the ratio of Dispersive Power to Incident Power (EDP/IP) which is similar to absorptivity, increases more rapidly for A356-Al than for any of the composites tested. It actually decreases for A356-20%SiC composite, indicating that other heat transfer effects were influencing the fusion zone.

The presence of reinforcement diminishes the role of convection. At high laser power, due to onset of the keyhole, the absorptivities (Table II) and hence the extent of melting (Figure 3) was same for all the materials.

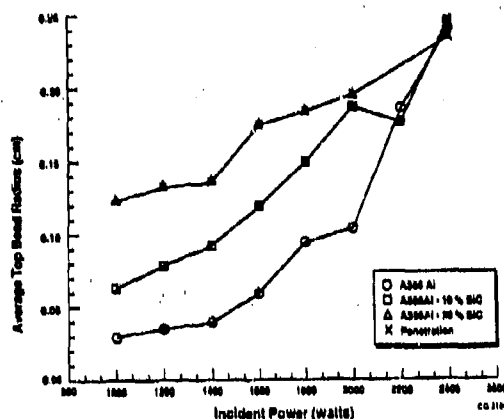


Figure 3. Weld bead radius versus incident power [12].

Table II\*  
Ratio of Dispersive Power to Incident Power (EDP/IP)

Incident Power (Watts)	A356-Al	EDP/IP 10% SiC	20% SiC
1000	0.04	.11	.24
1200	0.04	.10	.20
1400	0.04	.10	.17
1600	0.07	.13	.17
1800	0.09	.13	.16
2000	0.09	.14	.15
2200	0.12	.12	.13
2400	0.12	.15	.15

\*Reference 12

It is important to mention that these observations are similar to those reported by Meinert et al. (Figure 4) on absorptivities and depth of penetration for 6061-Al and 6061-Al reinforced with SiC and Al<sub>2</sub>O<sub>3</sub> [15]. It can be seen that 6061-Al has the lowest penetration, whereas, the presence of SiC and Al<sub>2</sub>O<sub>3</sub> increased the absorptivity. 6061-Al reinforced with Al<sub>2</sub>O<sub>3</sub> showed highest absorptivity and depth of penetration. The presence of Al<sub>2</sub>O<sub>3</sub> changes the electrical resistivity and surface properties of 6061-Al matrix, hence due to a better coupling, more efficient transfer of energy takes place. The formation of carbide was still a problem, however, it was proposed that by adding a suitable filler alloy its formation could be suppressed to a large extent. Free energy data shows that due to their low energy of formation (Figure 5) titanium and zirconium form carbides in preference to aluminium carbide. The laser welds made with titanium filler wire showed that formation of aluminium carbide was indeed suppressed. Instead of large plates of aluminium carbide, a very fine dendritic structure was found in the fusion zone of 6061-Al composite [15].

Kawali et al. provided some very interesting results on the role of shielding gas flow and direction on the suppression of plasma, weld quality and surface appearance [14]. Welds were made on 6061-Al and Duralcan composites using a 5 Kilowatt laser and nozzles of different

orientation and shapes. All orientations of nozzles, except when the nozzle was placed in such a way that the gas flow and weld directions were same, failed to produce good welds in Duralcan. A theory to explain plasma breakage and formation of crescent shape ridges for laser welding of Duralcan was proposed. When the gas flow is in the direction of welding, the gas pushes the ridge out of the plasma plume region and hence the explosive plasma- $\text{Al}_2\text{O}_3$  interaction does not take place. Any other nozzle orientation would result in plasma-alumina reaction for laser welding of Duralcan. It was suggested that to make good welds, the gas flow should be laminar and free of any turbulence in the weld area [14].

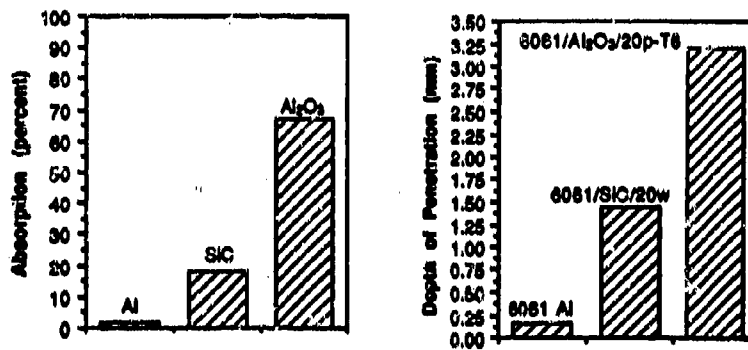


Figure 4. Absorptivities and depth of penetration for Al, Al+SiC and Al+  $\text{Al}_2\text{O}_3$  [15].

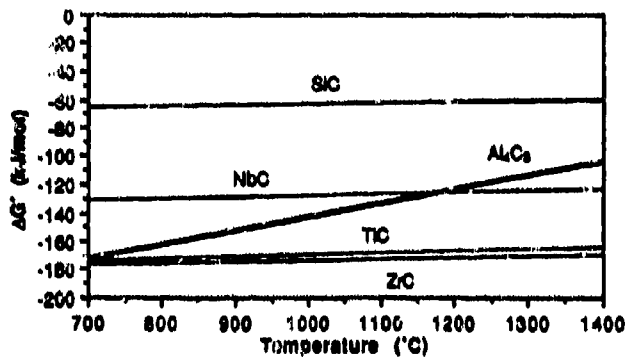


Figure 5. Free energy of formation of several metallic carbides [15].

## CONCLUSION

Several researchers have performed high speed joining of metal matrix composites using both continuous wave and pulsed lasers. It was found that the formation of non-equilibrium phases, which is very common for fusion welding, and loss of reinforcement particles, which leads to excessive porosity, can be reduced significantly by (a) controlling the heat input, and (b) using a suitable filler alloy, such as titanium wire during laser welding.

## REFERENCES

1. F. A. A. Khan, and A. J. Paul, Proceedings of the 1992 ICALEO Conference on Applications of Lasers, (Laser Institute of America, Orlando, FL, 1992).
2. T. R. Reinhart, Engineered Materials Handbook, Vol. 1. Composites, (ASM, Metals Park, OH, 1987), p.28.
3. K. Tempo, Proceedings of Seventh Metal Matrix Composites Technology Conference, (816 State Street, PO Drawer QQ, Santa Barbara, CA, 1987).
4. K. Mukherjee, F. A. A. Khan and M. Tayal, Laser Materials Processing III, (TMS, Warrendale, PA, 1988), pp. 217-232.
5. K. Mukherjee, and P. A. A. Khan in Proceedings of the American Society for Composites, Fifth Technical Conference, (Technomic Publishing Company Inc., Lancaster, PA, 1990), pp. 91-104.
6. K. Mukherjee, P. A. A. Khan, and C. Mondher, Proceedings of International Symposium on Manufacturing and Materials Processing, (Hemisphere Publishing, Washington, D.C, 1990).
7. S. Utsunomiya, Y. Kagawa and Y. Kogo, In Composites, 86: Recent Advances in Japan and the United States, edited by Kagawa et al. (Japan Society for Composite Materials, Japan, 1986), pp. 589-595.
8. J. J. Lee, in Boeing Aerospace Company, Internal Report, (Boeing, Seattle, WA, 1987).
9. N. B. Dahotri, T. D. McCay and M. H. McCay, Journal of Applied Physics, 65 (12), 5072-5077, (1989).
10. N. B. Dahotri, M. H. McCay, T. D. McCay, and S. Gopinathan, Journal of Materials Research, 6 (3), 514-529, (1991).
11. N. B. Dahotri, S. Gopinathan, M. H. McCay, T. D. McCay, and C. M. Sharp, Light Weight Alloys for Aerospace Applications II, edited by E. W. Lee and N. I. Kiri, (TMS, Warrendale, PA, 1991), pp. 313-326.
12. M. C. McCay, T. D. McCay, N. B. Dahotri, and C. M. Sharp, Journal of Laser Applications, 3 (3), 35-39, (1991).
13. M. J. Cola, T. J. Lienert, J. E. Gould, J. P. Hurley, Weldability of Materials, edited by R. A. Patterson and K. W. Mahin, (ASM Metals Park, OH, 1987), pp. 297-303.
14. S. M. Kawaii, and G. L. Viegelaahn, Proceedings of the 1991 ICALEO Conference on Laser Materials Processing-Vol 74, (Laser Institute of America, Orlando, FL, 1991), pp.156-166.
15. K. C. Meinert, Jr., R. P. Martukanitz, and R. B. Bhagat, Proceedings of the American Society for Composites, Seventh Technical Conference, (Technomic Publishing Company Inc., Lancaster, PA, 1992), pp.168-177.

## RAPID INFRARED JOINING OF TITANIUM ALLOYS AND TITANIUM MATRIX COMPOSITES

CRAIG A. BLUE\* AND RAY Y. LIN\*

\*Department of Materials Science and Engineering, M.L. #12 University of Cincinnati,  
Cincinnati, Ohio 45221-0012

### ABSTRACT

A rapid infrared joining (RIJ) technique has been developed at the University of Cincinnati for high temperature materials. This technique takes only a few seconds to a few minutes to join parts up to 1.8 cm in thickness. The advantages of the RIJ technique are quick, simple, inexpensive, no vacuum or pressure needed, no effect on the microstructure of the base material, flexible and feasible for portable operation. For titanium joining, both Ti-6Al-4V and  $\beta$ 21S/SCS-6 composite have been successfully joined with infrared at about 1000 °C for 30 seconds in argon with a TiNiCu brazing alloy. The maximum joint shear strength is up to 554 MPa, which is higher than that of any bond joined with conventional brazing techniques. Our study has shown that the longer the joining time, the wider the joining affected zone. Prolonged joining cycles allow for attack of the titanium alloy by the molten brazing alloy. Results from the titanium matrix composite (TMC) joining show that the joining strength for the infrared bonded parts is superior to those processed with the conventional techniques.

### INTRODUCTION

With increasing complexity of engineering components to fulfill ever increasing needs in machine performance, new demands for joining advanced high temperature materials are warranted. Bonding of honeycomb structures, small parts, composites, and devices where the materials are relatively thin and intricate, requires a fast, controllable method of heating in order to limit the diffusion, chemical reaction, and alloying between the base material and brazing alloy. A rapid infrared joining process being developed at the University of Cincinnati has met the stringent requirements of such new demands in materials joining[1]. This process has been demonstrated to provide a rapid, simple, and instant starting and stopping technique for materials bonding.

In joining of titanium alloys and titanium matrix composites, issues of concern include (1) the joining temperature, (2) the development of the Widmanstätten structure in the joint, and (3) solid-state diffusion of brazing alloy into the substrate, which results in requiring excess amounts of filler material to provide perfect wetting and bonding. Joining above the  $\alpha/\beta$  transition temperature, 955-982 °C, for an extensive period has been reported to cause the mechanical properties of the base metal, such as ductility and toughness, to be impaired because of the phase transformation and coarsening of grains of the base metal[2,3]. Conventionally, joining of titanium alloys is accomplished by fusion welding, resistance welding, diffusion bonding, or brazing[2-6]. Among them, brazing and diffusion brazing are preferred for joining complicated and precise components. Joint strengths of Ti-6Al-4V reported in the literature vary with different joining methods. When joined with laminated brazing filler metals, Ti-14Cu-14Ni wt%, with an overlap length equal to the thickness of the base material, designated as 1T, a room temperature tensile shear strength of 310 MPa was obtained[2]. Diffusion brazed Ti-6Al-4V joints using Cu filler metals with 1T overlap showed room temperature tensile shear strengths of up to 496 MPa[4]. In the case of induction brazing, room temperature tensile shear strengths for Ti-6Al-4V 1T overlap joints of 427 MPa have been reported with an amorphous Cu-30Ti wt% filler metal[6].

The rapid infrared joining technique that we developed can produce heating rates exceeding 100 °C/sec up to the brazing temperature and cooling to below 500 °C in a few seconds which decreases or eliminates the adverse effects of prolong heating above the  $\alpha/\beta$  transformation temperature. Precise heating with infrared further minimizes the formation of the Widmanstätten structure in the joint, which was believed to cause deterioration of joint



ductility[3]. With infrared joining, the amount of filler material necessary to form a good joint can be minimized due to the fast heating rate which limits the solid-state diffusion of the filler material, thereby leaving most brazing alloy available for forming liquid to wet the base material. Blue and Lin have reported shear strengths of Inconel on the order of 483 MPa with total processing times of 120 seconds under inert atmosphere[1]. This value is on the order of that obtained by conventional vacuum brazing of the same material.

## EXPERIMENTAL

The Ti-6Al-4V alloy used in this study was obtained from Air Force Wright Laboratory. The titanium matrix composite,  $\beta$ 21S/SCS-6, was obtained from NASA Lewis Research Center. Ti-6Al-4V was sectioned into 50mm x 15mm x 3.5mm specimens by electron discharge machining, EDM.  $\beta$ 21S/SCS-6 specimens were sliced with diamond wheels on a Buehler low speed saw into 31 mm x 3.5 mm x 1.2 mm specimens. All Ti-6Al-4V samples were chemically cleaned with a chemical etchant consisting of 10ml HF, 45ml HNO<sub>3</sub> and 45ml water. The TMC samples were ground to a 16  $\mu$ m finish. The etched samples had a surface roughness of less than 14 microns when measured with a profilometer. Such surface roughness was similar to that polished to a 600 grit finish. Before joining, samples and filler material were degreased in an ultrasonic cleaner and rinsed in acetone. The filler material was a 17 micron thick foil, MBF 5003 Ti-15Cu-15Ni wt% supplied by METGLAS. The specimens with the filler metal were then placed in the infrared furnace in a single lap joint configuration according to ASTM standard D0012-72[7]. No external pressure was applied to the parts being joined. The specimens were argon purged for approximately 60 seconds prior to the heating cycle. During the entire joining process, argon was purged through the heating chamber at 250 ml/min in order to prevent oxidation. The processing temperature was monitored with a chromel-alumel K type thermocouple spot welded on the specimen near the joining area. Typically, the temperature of the specimen was brought to the preset joining temperature in 10-20 seconds and then, held at that temperature for various lengths of time before the power is terminated. After joining, the sample cooled naturally in an argon atmosphere. The cooling rate was rapid due to the cold wall process of infrared joining, in which only the sample was heated to the desired joining temperature. The samples normally cooled to below 500 °C in less than 10 seconds.

## RESULTS AND DISCUSSION

### Joining of Ti-6Al-4V

With Ti-15Cu-15Ni alloy as the filler material, Ti-6Al-4V specimens were joined at various temperatures for 30, 60 and 120 seconds. Figures 1a, b, and c show plots of joint shear strength as a function of joining temperature for holding times of 30, 60, and 120 seconds respectively. It can be seen that the bond shear strength increases with increasing temperature and time to a maximum value of 554 MPa. It is clear that at the joining time of 30 seconds, the higher the temperature, the higher the shear strength. At 60 seconds, the bond shear strength shows a maximum at 1100 °C; and at 120 seconds, the bond strength shows a maximum at 1250 °C. It appears that the 60 second bonds are stronger than both the 30 second and 120 second bonds, except those joined at 1250 °C. Joining at 1250 °C, however, is not desirable due to the large reaction zone.

The quality of joining was inspected from cross sections of a different set of joints made at 1120 °C with infrared as shown in Figure 2. The joint cross section inspections from optical microstructural photos reveal that: (1) all infrared bonds exhibit excellent wetting between the filler alloy and the base Ti-6Al-4V alloy; (2) no voids were observed in the joint; (3) the Widmanstätten structures has developed in all joints; (4) the width of the joint area increase with increasing joining time and temperature; and (5) a bright zone observed in the middle of the joint at low joining temperature and short joining time diminished as the joining temperature and time increased.

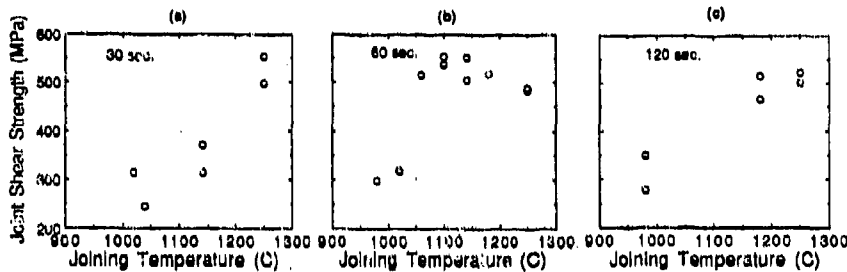


Figure 1. Joint Shear Strength of IR Bonded Ti-6Al-4V Specimens.

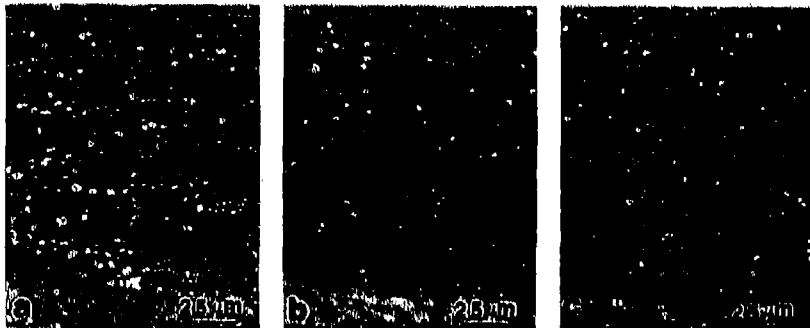


Figure 2. Optical Micrograph of Joint Cross Sections, 1120 °C a. 30 sec, b. 60, and c. 120.

From Figure 1, it can be concluded that the optimum infrared joining condition for Ti-6Al-4V is at 1100 °C for 60 seconds. Joints made under this condition have a joint shear strength of 554 MPa. The best joint strength reported is 496 MPa for joints made by Freedman[4] with a diffusion brazing technique using Cu as the filler material. Due to the prolong heating of Freedman's joining procedure, it was reported that the mechanical strength of Ti-6Al-4V has been deteriorated significantly. With Freedman's joining process, the tensile strength of the base alloy can be reduced by 6% and, the yield strength by 9%. Not only providing stronger joints, the infrared joining process is superior also in that there is little effect on the base material properties.

Figure 3 shows the measured width of the joint area as a function of the joining time at respective temperatures. Data from this diagram indicated that the joint width varies linearly with the processing time. Such a trend suggested that the bond width is controlled by the dissolution of the base material by the molten filler alloy during joining. Comparing the bond strength with the width of joints, it can be seen that there is no definite correlation between these two joint properties. However, examinations of the debonded fracture surface of the joints with SEM reveal a possible linkage between the bond strength and the bond morphology.

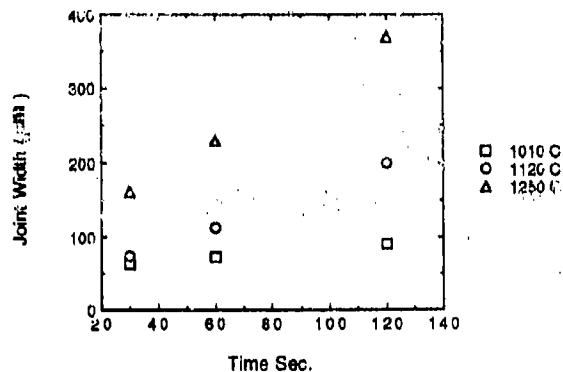


Figure 3. Joint Zone Width as a Function of Joining Temperature and Time.

#### Dissolution of Ti-6Al-4V During Joining

Careful inspection of the joint cross section microstructures suggest that during rapid infrared joining, dissolution of the base metal begins as soon as the braze alloy melts. The addition of Ti-6Al-4V into Ti-15Ni-15Cu shifts the brazing alloy composition and changes both liquidus and solidus temperature of the molten phase. As time goes on, more Ti-6Al-4V is dissolved. Eventually, the composition of the molten phase will shift to a composition in equilibrium with the Ti-6Al-4V phase. From then on, no more dissolution of Ti-6Al-4V will occur. However, since both Ni and Cu are present in the molten phase, these two elements will diffuse into the Ti-6Al-4V phase. Concentration gradients of Cu and Ni will be established. The depth of diffusion depends on the temperature, time, and the diffusion coefficients of Cu or Ni in the Ti-6Al-4V structure. Meanwhile, as a result of the diffusion, the Cu and Ni concentrations in the molten phase will be reduced. Such a shift in composition will cause precipitation of the Ti-6Al-4V phase back on to the dissolution front. It is likely that the growth of the Widmanstatten structure is the result of such Ti-6Al-4V phase precipitates which contain both Ni and Cu.

Although the infrared joining time is short, our experiments have shown that the dissolution has largely widened the joint area. Meanwhile, at 1250 °C and long processing time, regions of diffusion affected zone beyond the joint zone can be identified, Figure 2. At the completion of joining, the power was terminated and cooling occurred rapidly. Typically, it takes only less than 10 seconds for the specimen to cool down to 500 °C. With such rapid cooling, solidification would occur most likely following a non-equilibrium path. During solidification, even if the composition in the molten portion of the joint could be treated as homogeneous due to rapid diffusion in liquid, the solidified portion would have significant composition variation since the solid state diffusion is several orders of magnitude smaller than that in the liquid.

There is no phase diagram of the Ti-Al-V-Ni-Cu system available for us to verify the joining path mentioned above. However, it is most likely that the final drop of the liquid would be the composition approaching the eutectic composition of this five component system. It is to be noted, also, that depending on the amount of the Ti-6Al-4V dissolution and the temperature of joining, the solidification path will be slightly differed and, the final liquid composition will be shifted.

The existence of the Widmanstatten structure has been reported in the joint of Ti-6Al-4V with conventional vacuum brazing techniques. The development of this structure was believed to have jeopardized the joint properties. In this study, although the joining time is only up to 120 seconds, the Widmanstatten structure was still developed even in the joint prepared at the least severe condition of this study. Since even the least severe processing condition has evolved the Widmanstatten structure, it is unlikely that there is an optimum joining procedure in which the Widmanstatten structure can be eliminated in the as joined

specimen. However, due to the fact that this structure is the result of the micro-segregation during the solidification stage of joining, it can be removed via a post heat treatment practice should this structure be not tolerable in the final product.

#### Effect of Infrared Joining on Ti-6Al-4V Base Materials

Long heating times above 955 °C have been reported to cause excess grain growth and  $\beta$ -phase embrittlement of Ti-6Al-4V[3]. In this study, although joining was performed up to 1250 °C, since the joining time was extremely short, i.e. 2 minutes at most, there was little grain growth observed. Figure 4 shows the microstructure of the as received and infrared heat treated (1250 °C for 120 seconds) Ti-6Al-4V specimens etched with a 2 ml HF in 100 ml water etching solution for 10-20 seconds. Both the grain size and the  $\alpha/\beta$  phase ratio remain unchanged from the heat treatment. In order to determine the effect of the infrared joining cycle on the tensile property of the Ti-6Al-4V alloy, six dog-bone tensile specimens were prepared with EDM to a dimension of 10 x 1.5 x 0.3 cm with a gage area being 3.5 x 0.65 cm. Four of the specimens were infrared heated to 1100 °C for 60 seconds. All specimens were mechanical tested at a strain rate of 0.127 cm/min. Results show that no weakening of the test specimens was detected. This constitutes another advantage of infrared joining over other joining techniques for Ti-6Al-4V reported in the literature.

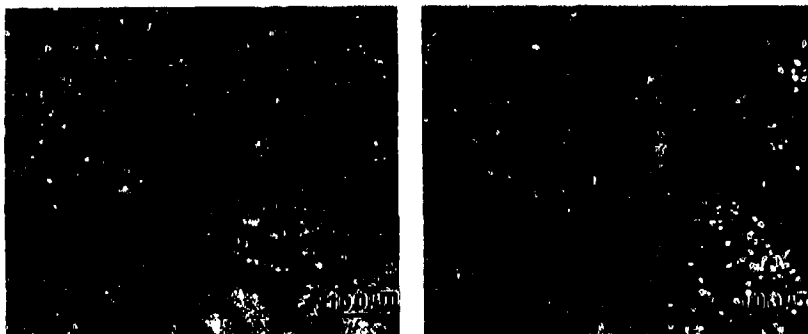


Figure 4. Base Material Microstructural Comparison of Ti-6Al-4V Before & After IR Joining

#### Joining of Titanium Matrix Composites

The joined TMC,  $\beta$ 21S/SCS-6, samples were tested by the shear method used above in order to obtain shear strengths for the joined lap specimens[8]. The strain rate used was .254 mm/min for all cases. In order to determine the effects of the heating cycle during joining on the degradation of composite fibers and the properties of the TiMC, a separate experiment was carried out by exposing the TMC specimens to the IR brazing conditions. Three point bend tests were conducted on the as received and thermal cycled TMC in order to establish the strength and modulus of the TMC. SEM examinations were performed on the as-received and IR cycled TMC in order to establish if any expansion of the reaction zone around the fiber had occurred. Optical examinations of the cross sections of the debonded TMC joint were also conducted to reveal the plane of failure.

#### Effects of Infrared Joining on the Titanium Matrix Composite $\beta$ 21S/SCS-6

Joint shear strengths of 285.6 MPa were obtained for the IR joined  $\beta$ 21S/SCS-6 TMC [8]. Optical examinations of cross sections of the TMC/TMC joints show no void content. The three point bend tests on the TMC samples revealed that there is little change in flexural strength, approximately 3%, due to the IR temperature cycling. This suggests that there is no

detrimental effects occurring to the TMC during joining of shear samples. Also, a 2.5 % total strain was observed in the thermal cycled samples which further suggests that no detrimental effects occurred in the base TMC as a result of the infrared joining. Scanning electron microscopic examinations of the reaction zone between the fiber and matrix reveal no change in the reaction zone size. This indicates that the rapid infrared joining technique is so rapid that essentially no microstructural modification is made to the base TMC.

The plane of failure of the TMC/TMC was in the joint area for the RIJ samples. There was delamination effects observed in conventional joining of TMC[8]. Such delamination phenomenon of the TMC in the conventional processing is believed to be due to the brazing affected zone. The RIJ processed TMC etched cross sections in and outside the joint areas further depict that there is little to no braze affected zone.

A comparison of conventional vacuum brazing of  $\beta 21\text{-S}/\text{SCS-6}$  TMC and RIJ joining of  $\beta 21\text{S}/\text{SCS-6}$  TMC reveals that the shear strengths of the RIJ joined material are 12.5% larger. Also, the conventional process shows a 38% degradation in the room temperature strength of the TMC due to processing, assuming a three point bend test was used to obtain strength values. On the other hand, a 3% degrade in the base TMC was observed when three point bend tests were performed on the RIJ thermal cycled TMC which is within experimental error. Furthermore, the conventionally processed TMC showed a 8.9 % total strain while the RIJ process TMC showed a 2.5-2.6 % total strain at room temperature[8].

## CONCLUSIONS

Joining of Ti-6Al-4V and  $\beta 21\text{S}/\text{SCS-6}$  has been studied applying a rapid infrared joining technique being developed at the University of Cincinnati. The joining was performed at temperatures between 1000 and 1250 °C and times between 10 and 120 seconds. Excellent joints were obtained using Ti-15Ni-15Cu wt% as the joining filler material. A maximum joint shear strength of 544 MPa was obtained for Ti-6Al-4V when processed at 1100 °C for 60 seconds. It was observed that the width of the joint increases linearly with time at a constant temperature. However, there is no definite correlation between the joint strength and the joint zone width. IR joining of  $\beta 21\text{S}/\text{SCS-6}$  revealed void free joints with shear strengths of 285.6 MPa at a processing temperature of 1000 °C and time of 10 seconds. The TMC maintained 97% of its original flexural strength after infrared processing while producing the largest joint shear strength available in the literature.

## ACKNOWLEDGMENTS

Financial supports from NASA Space Engineering Research Center, Edison Materials Technology Center, and NASA Lewis Research Center are very much appreciated. Thanks are also due to Dr. Theodore Nicholas of Wright-Patterson Air Force Base for the supply of Ti-6Al-4V alloy and Tom Edwards of Allied Signal for the supply of the METGLAS foil. Technical assistance from John Whitaker and Douglas Bowling and valuable discussions from Chris Eppich, Sunil Warrier, and C.C. Chen of the University of Cincinnati are appreciated.

## References

1. C. A. Blue, S. G. Warrier, M. T. Robson and R. Y. Lin, to be published in the *Welding Journal*, (1993).
2. S. W. Lau, *Welding Journal* 61(10), 23-38 (1982).
3. T. Onzanawi, et al. *Welding Research Supplement Dec.*, 462-s to 467-s (1990).
4. A. H. Freedman, *Welding Journal* 50(8), 343-s to 356-s (1971).
5. I. H. Staffens, *Welding and Cutting* 5, 217-220 (1990).
6. O. Kubaschewski and C. B. Alcock, *Metallurgical Thermochemistry*, 5th Ed., Pergamon Press, N.Y., (1979).
7. ASTM Standard D 1002-72, Annual Book of ASTM Standards *Adhesives* 15.06.(15), 45-49 (1986).
8. C. A. Blue, R. Y. Lin, J.-F. Lei, and W. D. Williams, *NASP Technology* NASP Contractor Report 1153 April (1993).

---

## **PART IV**

---

### **Advanced and Novel Joining Techniques I: Capacitor Discharge Welding and SHS**

## CAPACITOR DISCHARGE WELD MODELLING USING ULTRA HIGH SPEED PHOTOGRAPHY

R. D. WILSON<sup>1</sup>, J. A. HAWK<sup>1</sup> AND J. H. DEVLETIAN<sup>2</sup>

<sup>1</sup> U.S. Bureau of Mines, Albany Research Center, Albany, Oregon 97321-2198

<sup>2</sup> Oregon Graduate Institute of Science and Technology, Beaverton, Oregon 97006-1999

### ABSTRACT

Capacitor discharge welding (CDW) is a rapid solidification joining process where high cooling rates ( $10^6$  K/s) are obtained as a result of the large weld surface area to small weld volume. The objective of this study, directed by the U.S. Bureau of Mines and the Oregon Graduate Institute of Science and Technology, was to use ultra-high speed photography to quantify transient arc behavior during the CDW cycle. The simple cylindrical geometries of the CD welds have been used to formulate analytical models which are compared to the high speed photographs of the welding process. The high speed photographs were analyzed with respect to welding time and process weld variables and compared to predicted values from the analytical model. The detailed photographic analyses revealed that material is continuously ejected as a plasma from the weld area due to induced magnetic forces, rather than having the liquid metal squeezed out of the weld upon contact. It was found that welding time was controlled by tip length and drop height. Results from high speed photographs found the arc travel speed around tube welds to be 109m/s. Finally, the high speed photographs revealed that the velocity of arc propagation during ignition was fast enough to allow the CDW process to be modelled as one-dimensional heat flow.

### INTRODUCTION

The capacitor discharge (CD) welding unit consists of a capacitor bank, a power supply for charging the capacitors, and the electrodes to be welded. This unit, in operation, is shown in Fig. 1. The actual welding process takes from 1 to 3 ms, using a current of about  $10^4$  A (DC). Initial contact starts at the welding tip with tip length controlling the welding time. Recent studies have shown that cooling rates during CDW approach  $10^6$  K/s, making CDW a rapid solidification process.<sup>1-3</sup>

The purpose of the CDW investigation was to determine the characteristics of arc initiation and propagation, the interaction of the metal plasma with the induced magnetic field, and the flow behavior of the metal plasma/molten metal upon joint closure. Ultra-high speed photography was used to develop a mathematical model, capable of predicting arc behavior and welding time. In another study, the results from the high speed photography coupled with a one-dimensional finite element heat transfer model, were used to predict the weld thickness, amount of expelled metal, cooling rate, and the solidification parameter as a function of time and distance from the weld centerline.<sup>4</sup>

The important factors controlling the CDW process are welding tip length, capacitance, voltage, and electrode separation, i.e., drop height. Figure 2 is a schematic representation of the CDW cycle. Figure 2a shows the initial position of the cathode with welding tip and the anode. At this point the capacitor bank is fully charged and the resistance of the circuit is infinite. Figure 2b shows the tip of the cathode striking the anode, thus discharging the capacitor bank and initiating the arc. The arc quickly spreads across the electrode face and metal plasma streams away from the joint (Fig. 2c). At this

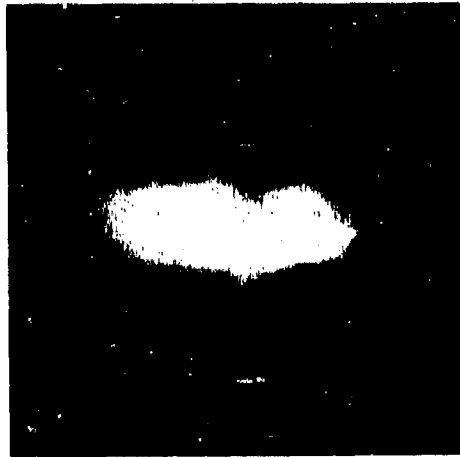


Fig. 1. Capacitor discharge welding process used to join metal cylinders.

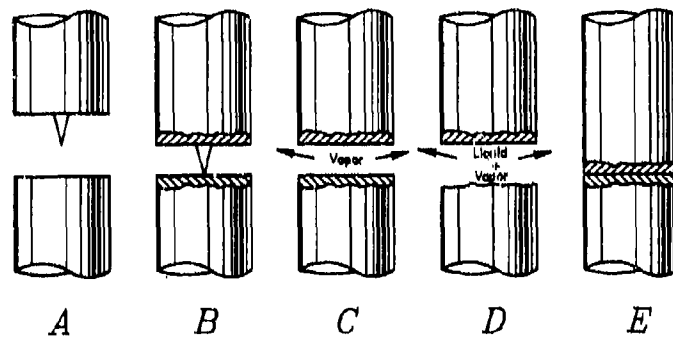


Fig. 2. Time process of CDW process: (a) cathode positioned above anode; (b) arc ignition at the welding tip; (c) plasma expulsion; (d) ejection and condensation of plasma into small metal particles; and (e) CD joint after electrode contact.



instant, the resistance of the circuit is  $2 \times 10^{-2}$  ohms. As the plasma moves away from the joint, the superheated vapor cools and condenses into spherical metal particles. The plasma and solid particles continue to move away from the weld joint in trajectories defined by the magnetic field. Figure 2e shows full electrode contact. The resistance of the circuit at contact decreases to zero as the arc is extinguished and the layer of liquid metal at the electrode interface solidifies to form the joint. Figure 3 shows the microstructure of CDW 304 stainless steel. Planar solidification occurs at the base metal-weld interface, but changes to columnar solidification with narrow cell spacings as the weld centerline is approached. Near the weld centerline, the cell spacing is wider, a direct result of the slower solidification rate.

Since CDW is a rapid solidification process, it has several commercial benefits in terms of metallurgy and manufacturing. The CDW process leads to increased solute solubility and stability of metastable phases. In dissimilar CD welds, deleterious equilibrium intermetallic phase formation is suppressed and only small discontinuous islands of intermetallics form in the weld zone. The fusion zone (FZ) in CD welds is very thin, approximately 100  $\mu\text{m}$  thick, and the heat affected zone (HAZ) is also very narrow. The CDW process is fast and cost effective; moreover, the process can be automated to produce high production rates. CD welds do not penetrate through base metals, so parts can be welded onto sealed containers.

Some of the practical problems associated with the CDW process include limitations on weld size due to the finite amount of energy stored in the capacitor banks. The process also requires a precision arc ignition tip to initiate the welding process. Finally, although dissimilar metals, composites or ceramics can be welded, they must be electrically conductive.

## EXPERIMENTAL PROCEDURES AND MATERIALS

Various electrodes were used in the CDW experiments. The  $\text{Fe}_3\text{Al}$  intermetallic alloy was vacuum induction cast. Electrodes for the dissimilar metal welds were made from commercially available 304 stainless steel and 6061-T6 aluminum rods. Each CDW experiment used a pair of 6.35 mm diameter by 16.5 mm long electrodes. Each cathode had an ignition tip machined at the center of the cylinder base. Tip lengths were varied from 0.63 mm to 1.65 mm, while the tip diameter remained 0.5 mm. Tube weld specimens were made from 6.35 mm diameter 304 stainless steel, with a wall thickness of 1.01 mm. A 60° beveled edge was machined on the end of the tubular specimen to act as the ignition tip.

The welding equipment consisted of a Eric Jones (Model PSWW-100)\* capacitor discharge, production welding system. The welding unit uses gravity to drop the cathode onto the anode while discharging the capacitor bank. Table 1 lists the welding conditions used in these experiments. Four primary welding parameters were selected for evaluation in this investigation: drop height, tip length, voltage and capacitance.

High speed photography was used to capture the CDW process events. A Hycam 16 mm high speed camera equipped with a 1/4 frame rotating prism allowed a top speed of 44,000 frames/second. Kodak Ektachrome 2253 high speed daylight film (450 foot rolls) was used to record each weld experiment. The film had an ASA of 400 and was commercially processed. To ensure that the camera was at full speed, a one-second delay was used before the welding process was started. On several CDW experiments, an intense 1000 watt spotlight was used to illuminate the weld area prior to arc initiation.

---

\*Reference to specific products does not imply U.S. Bureau of Mines endorsement.

TABLE I

Welding Conditions	
Voltage	90-100 V
Capacitance	80,000 $\mu$ F
Drop Height	50 mm
Tip Length	0.63-1.4 mm
Film Speed	44,000 frames/s

## RESULTS AND DISCUSSION

Ultra high speed photography was used to record the CDW of similar metals with different tip lengths, dissimilar metal joining, and the joining of stainless steel with various electrode geometries. Figure 4 is a high speed photograph of a typical arc strike observed at the onset of the CDW process. The cathode, with its 1.1 mm long, 0.5 mm diameter tip, can be seen above the anode. An inverted cone shape is often seen in the first frame of arc initiation, indicating the ignition tip has contacted the anode. If the arc had jumped the gap between the cathode and anode, the shape of the ignited arc would have been cone shaped, but with its base on the anode. At 44,000 frames/second, the elapsed time between frames is 22.7  $\mu$ s. Within 44  $\mu$ s, the arc has spread across the surface of the anode. Compared to the total arc time of 1.5 ms, 97% of the arc process is between the electrodes as determined by the one-dimensional heat transfer model.<sup>1</sup>

After arc initiation, metal plasma is expelled from the CDW joint. Figure 5 (Frame P-2-14) illustrates the process of plasma expulsion due to arc magnetic forces. The magnitude of the arc force ( $F_{ARC}$ ) is defined by Eq.(1)<sup>5</sup>

$$F = \frac{\mu_0 I^2}{8\pi} \quad (1)$$

where  $\mu_0$  is the permeability of free space and  $I$  is the current. When the current is 132 kA, for example, an arc force of 877 N is calculated from Eq.(1). Thus, the plasma is expelled from the joint at a velocity of 35 m/sec, as measured from high speed photography.

The shape of the plasma cloud (Fig. 5, Frame P-2-14) is a torus and is due to the interaction of the positively charged, metallic plasma with the current induced magnetic field. A schematic representation of this process is shown in Fig. 6. (Conventional electric current is upward in the opposite direction of electron flow from the cathode to the anode. The magnetic field vector on the right side of Fig. 6 is into the page while the magnetic field vector on the left side is out of the page, consistent with the right hand rule from electro-magnetic theory.) The plasma is expelled with an initial velocity perpendicular to the axis of the electrodes. The plasma experiences a Lorentz force perpendicular to the velocity vector and changes direction as it moves through the magnetic field. The plasma moves in a circle with its radius equal to 3.17 mm, as measured from the photograph in Fig. 5 (Frame P-2-14). A radius,  $R$ , for the expelled plasma can be calculated, assuming singly charged iron ions moving at a velocity observed in the high speed photographs, using Eq.(2)



Fig. 3. 304 stainless steel weld deposited by CDW using short (0.63 mm) ignitor tip. The cell spacing is  $1.0 \mu\text{m}$ , corresponding to a cooling rate of  $5 \times 10^5 \text{ K/s}$ . 500X.



Fig. 4. High speed photograph of the CD welding tip, as the cathode contacts the anode.

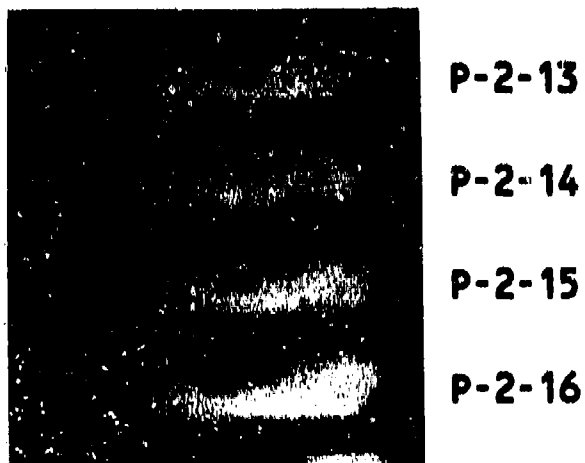


Fig. 5. CD weld of  $\text{He}_2\text{Al}$  at 100 V, 50 mm drop height, and 0.88 mm ignition tip length. The plasma "curl" has a radius of 3.17 mm.

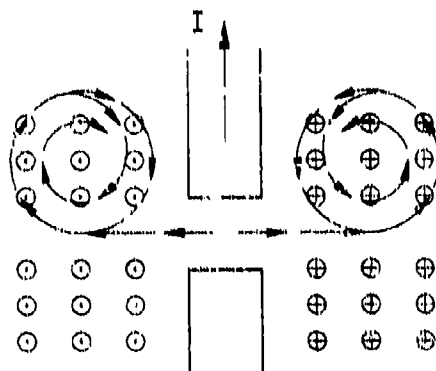


Fig. 6. Illustration of the electric current and induced magnetic field lines generated during CDW. Magnetic field lines out through the paper as indicated--the path of the metal plasma ions is circular with a radius equal to  $R$ .

$$R = \frac{2\pi m v^2 t}{q_0 \mu_0 I} \quad (2)$$

Where  $m$  is the mass of the moving ion,  $v$  is the magnitude of the initial velocity,  $t$  is the elapsed time from arc initiation,  $q_0$  is the charge on the metal ion,  $\mu_0$  is the permeability of free space and  $I$  is the current at the elapsed time after arc initiation. Eq.(2) predicts the plasma radius (Fig. 5, Frame P-2-14) to be  $2.1 \text{ mm} \pm 0.8$ . The correlation between the observed metal plasma behavior and the predicted values from Equation 2 strongly suggest: (1) the plasma consists of metal ions with a single charge, or greater; (2) the magnetic field is the primary force controlling the plasma behavior; (3) the radius is inversely related to ionic charge and current; (4) the plasma radius is directly related to the ion mass and welding time; and (5) the plasma radius is related to the square of the initial velocity. Equation 2 through 4 were derived from the conservation of mass and energy by the author.

As the electrodes close, several important observations can be made from the high speed photographs. After arc initiation, metal plasma is seen to continuously stream from the CDW joint. At joint closure (Fig. 7), metal plasma ceases to be expelled from the joint. As the plasma cools, it condenses into hot metal particles and continues to move away from the joint. Contrary to popular belief, liquid metal is not extruded from the CDW joint after electrode contact due to hydrodynamic pressure. Instead, a thin film of metal remaining on the electrodes at the time of closure rapidly solidifies due to the good heat transfer between molten metal and electrode.

The elapsed time from arc initiation to joint closure was measured for several CD welds, with various tip lengths and drop heights. Figure 8 illustrates these results. Two CD welding trends can be related to ignition tip length and drop height. Increasing the ignition tip length increases the CD welding time. Conversely, if the drop height is increased, the welding time is decreased.

The current in the CDW circuit increases after arc initiation and then decreases as a function of the resistor-capacitor (RC) time constants. As the electrodes make contact, the circuit resistance decreases, resulting in a current spike, as illustrated in Fig. 9. The welding time is measured from the start of current flow to the current spike at electrode closure. An equation was developed to predict the welding time with the results illustrated as dashed lines in Fig. 8. The welding time,  $T_w$ , is calculated from:

$$T_w = \frac{L + b}{\sqrt{2gH}} \quad (3)$$

Where  $L$  is the welding tip length,  $b$  is the distance the electrodes melt back,  $g$  is the acceleration of gravity, and  $H$  is the drop height. Control of the welding time is very important in CDW, because  $T_w$  is directly related to certain metallurgical characteristics, such as weld strength and weld porosity. For example, too short of a welding time results in poor electrode fusion, because the capacitors cannot discharge into the weld completely before electrode contact. However, the molten metal of the electrode surfaces can solidify before joint closure if the welding time is longer than the RC time constant. Eq.(3) suggests the most important factor controlling welding time is tip length. The melt back distance is linearly related to welding time, but melt back distances are very short in the CDW process compared to welding tip length. At high heat input, however, melt back distance can be an important variable, increasing the overall welding time. The square root of drop height is inversely related to the welding time; this means it has a lesser effect

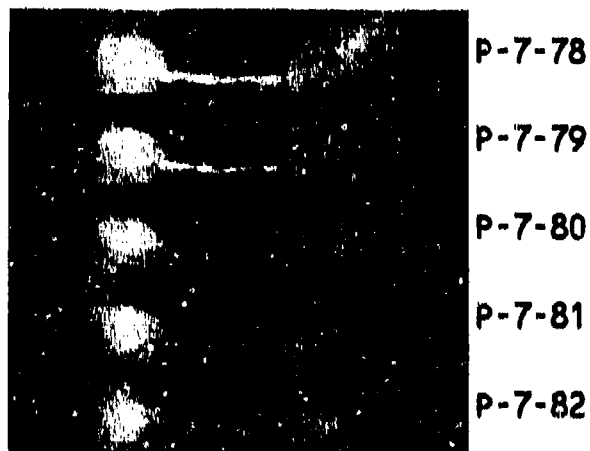


Fig. 7. High speed photograph of joint closure during CDW. Plasma and metal particles continue to move away from joint in trajectories described in Fig. 6.

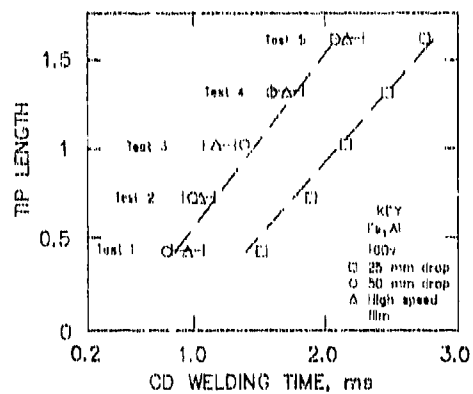


Fig. 8. Tip length vs a function of welding time for 50 mm and 25 mm drop heights.

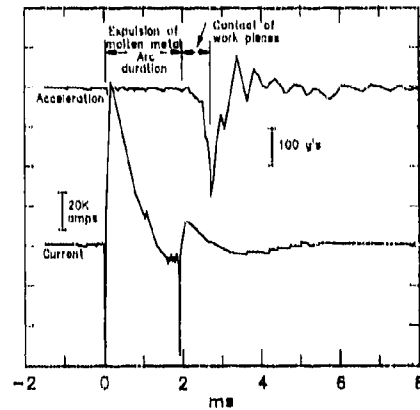


Fig. 9. Electrical current and acceleration of the capacitor as a function of discharge time. The current increase at 2.5 ms is due to a reduction in circuit resistance on electrode contact.



Fig. 10. SEM micrograph of a CD welded 304 stainless steel (cathode)-6061 aluminum (anode) couple. Note the partially mixed zone of steel and aluminum along the weld centerline.

on the weld time compared to tip length. It is interesting to note that drop weight is not a factor in Eq.(3). Furthermore, Danks<sup>6</sup> and Venkataraman et al.<sup>3</sup> have shown that variations in drop weight have an insignificant effect on welding time.

### Dissimilar Metal Welds

Due to the rapid solidification characteristics of the CDW process, joints in dissimilar metals have only small amounts of deleterious intermetallic phases. Dissimilar metal couples have been recently examined by Dogan et al.<sup>7</sup> Figure 10 illustrates a joint between a 304 stainless steel (cathode) and Al-6061-T6 (anode). A partially mixed zone of the primary base metal constituents is observed in the weld zone. However, in dissimilar welds where aluminum was used as the cathode and 304 stainless steel was used as the anode, significant microstructural differences resulted. For example, a thinner weld is obtained using stainless steel as the cathode. In addition, the partially mixed zone (PMZ) in the CD weld (Al cathode) is wider than the PMZ in the weld which uses the stainless steel cathode.

High speed photography was used to examine the CDW of dissimilar metals. Aluminum/steel cathodes were welded to steel/aluminum anodes. No observable differences in arc initiation and plasma expulsion could be determined from the high speed photographs. Further experimentation is needed to clarify the source of the metallurgical differences in the dissimilar metal welds.

### Capacitor Discharge Tube Welding

Typically, CDW has been used to weld fasteners to plate or sheet. Recently, methods for welding tubular products have been developed, e.g., the welding of 304 stainless steel tube to stainless steel plate or tube. Some of the important factors to consider when tube welding include: (1) welding time and (2) the velocity of the arc travelling around the circumference of the tube arc initiation. As with the CDW of cylinders, the welding time must be controlled, or cold welds (i.e., poor fusion of surfaces) with little strength will result. If the welding time is too long, then solidification of the weld pool occurs before the electrodes make contact.

Control of arc velocity is important in tube welding, because the arc must move around the tube fast enough to ensure that both anode and cathode are still liquid upon contact. Figure 11 shows the steady-state CD tube welding process. Imagine that a tubular cathode is cut along the longitudinal axis and then flattened. Assuming the cathode is perpendicular to the anode, the arc will move along the shortest distance from the anode to the cathode. The factors controlling the melt back distance include the geometry of the cathode, the energy input, and the heat of fusion of the material. The relationship between arc velocity,  $dx/dt$ , and the CDW variables in CGS units, is given in Eq.(4):

$$\frac{dx}{dt} = \frac{2V^2}{R\rho\Delta H_f w b} \exp\left(-\frac{t}{RC}\right) \quad (4)$$

where  $V$  is the capacitor charge voltage,  $R$  is the resistance of the arc,  $\rho$  is the density of the material,  $\Delta H_f$  is the heat of fusion of the material,  $w$  is the tubing wall thickness,  $b$  is the melt back distance,  $t$  is time, and  $C$  is the capacitance. Eq. 4 suggests several interesting variables for controlling the arc velocity in CD tube welds. The arc velocity is directly related to the discharge rate of the capacitors. Therefore, at the beginning of the discharge cycle, the velocity is fast, but it slows at a rate equal to the RC time constant



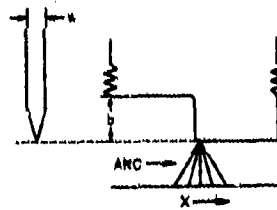


Fig. 11. Illustration of the CD tube welding process.  $W$  is the wall thickness and  $b$  is the melt back distance.



Fig. 12. Sequence of high speed photographs of an arc moving (from right to left) around the periphery of a 6.35 mm diameter tube. The arc velocity is 109 m/s.

until it reaches zero at complete discharge. The arc velocity is also directly related to the square of the voltage; that is, slight increases in voltage will produce significant quadratic, nonlinear increases in arc velocity. As would be expected, electrical resistance and the thermo-chemical melting factors  $w$ ,  $b$ ,  $\rho$  and  $\Delta H_f$  are inversely related to arc velocity. This simply means that materials with high melting temperatures, or tubes with thick walls, will have slower arc velocities.

Figure 12 shows a high speed photograph of the CD tube welding process. A 304 stainless steel cathode, 6.35 mm in diameter with a 1.0 mm wall thickness and a 60° beveled edge, was welded to a similar stainless steel tube anode. Initial welding conditions were 90 V and 80,000  $\mu$ F. The first frame shows the arc strike at the right edge of the tube which moves to the left at 109 m/s. After four frames, the arc has moved completely around the tube. A predicted arc velocity from Eq.(4) of  $108 \pm 10$  m/s was calculated, assuming the melt back distance is 1 mm, the arc resistance is  $10^{-2}$  ohms, and the energy needed to melt iron is 1925 J/g. Research continues in the area of CD tube welding in order to determine the maximum tube weld size and the viability of joining dissimilar metal tubes.

## CONCLUSIONS

Ultra high speed photography is an effective means of examining the transient behavior of the capacitor discharge process. High speed photography has shown that welding time is primarily controlled by welding tip length. Metal plasma is continuously expelled as a consequence of the induced magnetic force generated during CDW and hydrodynamic extrusion of weld metal after joint closure is an insignificant effect. Finally, CDW tube welding is possible if arc velocity and welding time can be controlled.

## ACKNOWLEDGMENTS

The authors would like to thank Steve Anderson of the U.S. Bureau of Mines Technical Communications Department for his assistance in taking the ultra high speed movies.

## REFERENCES

1. R. D. Wilson, J. R. Woodyard and J. H. Devletian, *Weld. J. (suppl.)* 72, 101s (1993).
2. S. Venkataraman and J. H. Devletian, *Weld. J. (suppl.)* 67, 111s (1988).
3. C. J. Elinson, D. E. Clark and J. H. Devletian, in *Proc. of the 1987 ASME/ISME Thermal Engineering Joint Conf., Volume Three*, edited by P. J. Marto and I. Tanasawa(ASME, New York, 1987), p. 217.
4. R. D. Wilson, PhD thesis, Oregon Graduate Institute of Science and Technology, 1991.
5. T. D. Eurligh and T. W. Eagar, *Metall. Trans A* 14, 1223 (1983).
6. D. Danks, MS thesis, Oregon Graduate Institute of Science and Technology, 1987.
7. C. P. Dogan, R. D. Wilson and J. A. Hawk in *Joining of and Adhesion of Advanced Inorganic Materials*, edited by A. H. Carim, D. S. Schwartz, R. S. Silbergliitt and R. E. Lochman (Mater. Res. Soc. Proc., Pittsburgh, PA, 1993).

## CAPACITOR DISCHARGE AND FLASH WELDING OF SiC-REINFORCED HIGH TEMPERATURE Al ALLOYS

D. S. SCHWARTZ\*, J. H. DEVLETIAN†, S. J. CHEN†, AND J. GOULD‡

\*McDonnell Douglas Corporation, m/c 111-1041, PO Box 516, St. Louis, MO 63166-0516

†Oregon Graduate Inst., Dept. of Materials Sci. and Engineering, Beaverton, OR 97006-1999

‡Edison Welding Inst., 1100 Kinnear Rd., Columbus, OH 43212

### Abstract

Discontinuously reinforced Al alloys (DRAs) are difficult to join using conventional fusion welding techniques due to inhomogeneous redistribution of the reinforcements and reaction between molten Al and SiC. Two specialized welding techniques, capacitor discharge welding and flash welding, were assessed as possible ways to avoid these problems. Using these techniques, welds were made with two DRAs: 8009/SiC/11p and 2009/SiC/15w. Capacitor discharge welding resulted in the formation of Al-carbides in the weld zones, but flash welding produced satisfactory joints in both DRAs.

### Introduction

The aerospace industry is seeking Al alloys with increased elevated temperature strength and increased modulus in order to lower aircraft weight and improve performance. Discontinuously reinforced Al alloys (DRAs), reinforced with SiC whiskers or particles, are currently receiving considerable attention. Joining DRAs by fusion techniques such as metal/inert gas or laser welding is problematical, however. The high temperatures experienced in the weld zone (WZ) can cause molten Al to react with the SiC reinforcements, forming undesirable Al-carbide precipitates. In addition, the reinforcements can redistribute themselves in the molten weld pool, resulting in an inhomogeneous distribution of the reinforcements in the WZ and degraded mechanical properties.

Two joining methods which show promise for overcoming these problems were given a preliminary assessment at McDonnell Douglas Aerospace. The first, capacitor discharge welding (CDW), forms joints at rapid solidification rates with very narrow WZs [1,2]. Most of the molten material produced during this joining technique is rapidly squeezed out of the WZ before solidification, so the SiC reinforcements do not have time for significant redistribution. The second joining technique, flash welding (FW), also forms joints with exceedingly narrow WZs [3]. FW joints experience relatively low, localized heating, and little or no melted material remains in the WZ. CDW and FW were used to make weld specimens from 8009/SiC/11p and 2009/SiC/15w. The former alloy is a hybrid material, consisting of a rapid solidification processed, dispersion strengthened (RSP) matrix, reinforced with 11 vol. % SiC particles. The composition of the 8009 matrix is nominally Al-8.5Fe-1.3V-1.7Si (wt. %). The latter alloy is a conventional Al matrix composite, reinforced with 15 vol. % SiC whiskers. The composition of the 2009 matrix is nominally Al-3.8Cu-1.3Mg-0.25Si-0.1Zn-0.05Fe (wt. %). Both CDW and FW have been shown to be suitable for joining RSP Al alloys [4,5], which are difficult to join by conventional techniques even when free of SiC reinforcements. The welds were mechanically and metallographically assessed, and the results will be discussed in this paper.

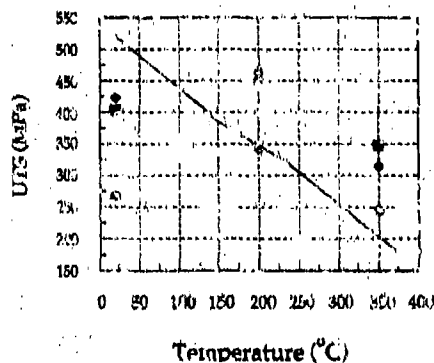


Figure 1. Ultimate tensile strength vs. temperature for CDW 8009/SiC/11p (● 225J, ■ 324J, ◆ 486J, — baseline).

FW was performed on 2.5cm x 1.0cm x 0.2cm plate shaped coupons. FW is an upset process, and the key process variable is the upset rate. An upset rate of 15-25cm/sec was found to be suitable for the DRAs studied in this program. FW was performed using DC power, which produces fine, even flashing [3]. Ar shielding gas was used to avoid trapped oxide defects in the joint. The FW specimens were examined metallographically, machined into mechanical test specimens with a 0.3cm gauge width, and tensile tested.

## Results

### CDW 8009/SiC/11p

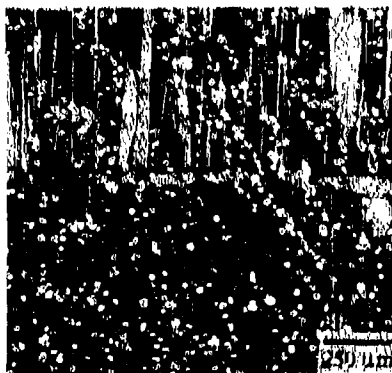


Figure 2. CDW 8009/SiC/11p, showing inhomogeneous redistribution of reinforcements and cracking.

### Experimental details

CDW was performed on 0.6cm diam x 2.5cm long cylindrical studs. The CDW voltage and capacitance were systematically altered to optimize the weld strengths and to learn how the parameters affect the welds. For the CDW process voltage (V) and capacitance (C) are to a large degree dependent variables, the significant variable being the weld energy, given approximately by  $\frac{1}{2}CV^2$ . Therefore, weld energy will be the quantity reported. The welds were examined metallographically, and specimens were machined into 0.3cm diam cylindrical mechanical test specimens and tensile tested.

CDW was used to join 8009 reinforced with 11 vol.% particulate SiC at three different weld energy inputs, 225J, 324J, and 486J. The weld tensile strengths are plotted as a function of temperature in Figure 1. Due to lack of material for baseline tensile testing, the baseline strength plotted in Figure 1 is taken from [6], and is for sub-optimal sheet material, which has lower strength than the extruded rod used for CDW. The weld strengths significantly exceed the strength of this sub-optimal sheet at elevated temperatures, and it is likely that the welds are fully as strong as the base material. However, at room temperature and 200°C, the specimens failed before yielding, and even at 350°C the ductility was low. The specimens welded using 225J input energy were

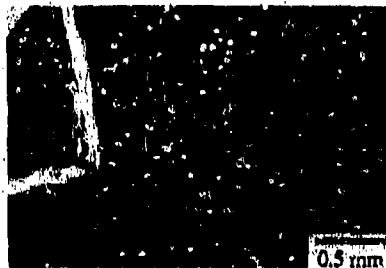


Figure 3. Fracture surface of weld failure in CDWed 8009/SiC/11p.

substantially weaker at all temperatures, but the difference between the 324J and 486J specimens was not significant. Failure of the CDW specimens generally occurred in the WZ. Examination of the WZ (Figure 2) shows that the weld microstructure is inhomogeneous, and a crack can be seen initiating in the WZ. Figure 3 shows a typical fracture surface, displaying brittle transgranular fracture, as well as large-scale cracking through the WZ. This fracture mode was generally observed, and did not change with the weld energy input. TEM of the WZ (Figure 4) shows the formation of acicular precipitates. These have been studied in detail

using electron diffraction, and were identified as  $Al_4C_3$  precipitates formed by reaction of Al with the SiC reinforcements. During CDW when the studs come into contact and the capacitor discharges, extreme temperatures are reached locally, producing superheated liquid Al which reacts with the SiC. At lower temperatures, the reaction between molten Al and SiC is comparatively insignificant. Due to the likelihood of reaction also occurring during CDW of 2009/SiC/15w, CDW welds were not performed on that alloy. The matrix surrounding the  $Al_4C_3$  precipitates in Figure 4 has a cellular structure, typically observed in the WZ of CDWed Al alloys like 8009 [4] and 8019 [5]. This structure results from the very rapid solidification of the weld zone, which freezes a nonequilibrium level of solute into the matrix. Welds with this cellular structure show high tensile strengths [4], so if the reaction between Al and SiC during CDW of 8009/SiC/11p could be eliminated, it is likely strong joints could be produced.



Figure 4. Center of WZ in CDWed 8009/SiC/11p showing  $Al_4C_3$  precipitates formed by reaction of superheated Al and SiC.

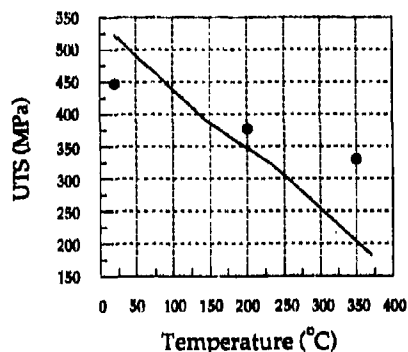


Figure 5. Ultimate tensile strength vs. temperature for FWed 8009/SiC/11p (● FW, — baseline).

normally observed in FWed Al alloys (typically  $<10\mu\text{m}$ ). It is probable that the increased viscosity of the SiC reinforced material prevents a portion of the molten material from flowing out of the WZ during flashing. At higher magnification (Figure 7), the distribution of SiC reinforcements appears fairly uniform in the WZ, and no obvious Al-carbides or other large-scale precipitates are present.

#### FW 8009/SiC/11p

The tensile strength of FWed 8009/SiC/11p is shown in Figure 5. The weld strengths are comparable to the base metal at room and elevated temperatures. The FW upset process strongly deforms the specimens in the WZ, as seen in Figure 6. The deformed material extends  $\sim 200\mu\text{m}$  from the weld center. Striations, which are a characteristic microstructural feature of the 8009 matrix and are normally approximately straight, can be seen to bend  $>90^\circ$  in the heat affected zone (HAZ). The width of the WZ is about  $40\mu\text{m}$ , which is significantly wider than WZ widths



Figure 6. FWed 8009/SiC/11p showing large deformation in the HAZ.



Figure 7. WZ of FWed 8009/SiC/11p showing uniform reinforcement distribution.

#### FW 2009/SiC/15w

The tensile strength of 2009/SiC/15w as a function of temperature is plotted in Figure 8. At room temperature and  $200^\circ\text{C}$ , the welds are comparable in strength to the base material. No data was readily available for the baseline strength of 2009/SiC/15w above  $200^\circ\text{C}$ . Figure 9 shows the weld region, and it can be seen that the upset process alters the texture of the SiC reinforcements in the HAZ. The HAZ is wide, about 2mm, and the striations which typically run in the extrusion direction in this alloy bend  $\sim 90^\circ$  from this direction. In addition, the

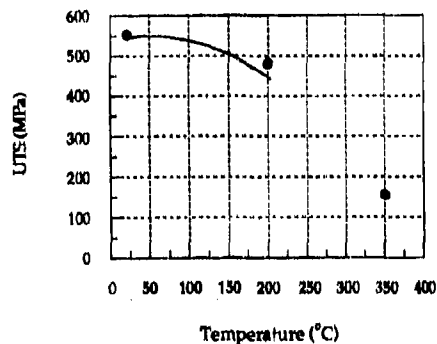


Figure 8. Ultimate tensile strength vs. temperature for FWed 2009/SiC/15w (● FW, — baseline).

striations appear to be closer together in the HAZ than in the base metal. Figure 10a shows the base microstructure in the material at higher magnification, to compare to Figure 10b, the weld microstructure. The weld, which runs vertically through the center of Figure 9, is very narrow (<20µm) and nearly invisible. The SiC whiskers, which are randomly oriented in the base microstructure, are oriented parallel to the weld plane in the WZ. The parallel orientation of the whiskers is consistent with the direction of deformation flow occurring during FW. The orientation change does not appear to have a strong effect on longitudinal tensile properties.

## Conclusions

CDW appears to be unsuitable for joining SiC DRAs. The SiC reinforcements are typically not uniformly distributed throughout the WZ in CDWed SiC reinforced Al alloys, and reaction can take place between Al and SiC to form embrittling  $Al_4C_3$  precipitates in the WZ. These factors result in low ductility joints for CDWed DRAs. FW appears promising for both of the DRAs examined in this study. The WZ was typically wider for these DRAs than is normally observed in non-reinforced Al alloys, but the WZ is nevertheless much more narrow than those produced using conventional welding techniques. The material that remains in the WZ is never heated enough to cause any reaction between Al and SiC, and the WZ is free of embrittling precipitates. The FW upset process heavily deforms the specimens up to ~200µm from the weld center. The SiC reinforcements change their orientation significantly in the WZ, but the longitudinal tensile properties are not significantly impacted by this orientation change.

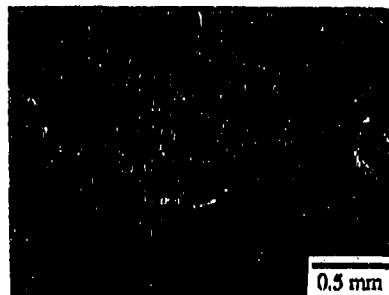


Figure 9. Microstructure of FWed 2009/SiC/15w.

## Acknowledgments

The authors would like to thank Mike Zedalis of Allied Signal for supplying the 8009/SiC/11p material used in this study. This work was supported by McDonnell Douglas Independent Research and Development program.

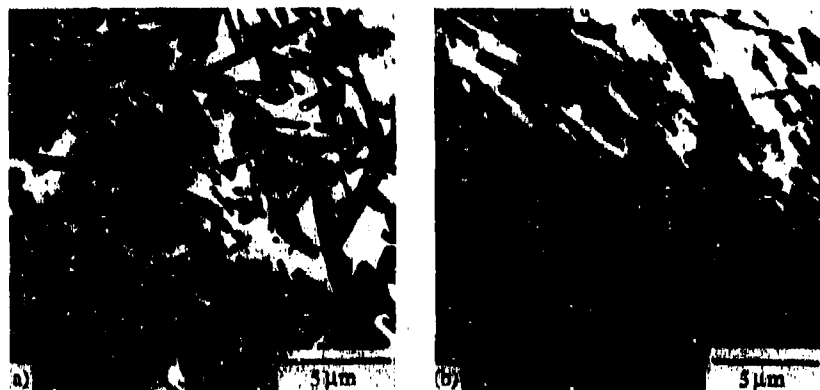


Figure 10. TEM micrograph of (a) base microstructure of 2009/SiC/15w, and (b) HAZ in FWed 2009/SiC/15w showing alignment of whisker reinforcements.

#### References

1. J. H. Devletian, *Welding J.* **66**, pp. 33-39 (1987).
2. W. H. Kearns (ed.), *Welding Handbook*, American Welding Soc., pp. 282-294 (1978).
3. J. E. Gould, T. Z. Stottler, *J. Eng. for Gas Turbines and Power*, **115**, pp. 177-183 (1993).
4. D. S. Schwartz, S.-J. Chen, and J. H. Devletian, submitted to *Scripta Metall.*
5. W. A. Baeslack III, K. H. Hou, and J. H. Devletian, *J. Mater. Sci. Let.*, pp. 944-948 (1988).
6. "Results of 8009/SiC/11p Sheet Qualification Testing, High Strength Discontinuously Reinforced Al", Evaluator Team Report vol. 1, Air Force contract no. F33733-89-C-1015.



## CD WELD INTERFACIAL STRUCTURE FOR Al-Fe BASED COUPLES

C. P. DOGAN, R. D. WILSON AND J. A. HAWK

U. S. Bureau of Mines, Albany Research Center, Albany, Oregon 97321-2198

### ABSTRACT

The U.S. Bureau of Mines has studied the capacitive discharge weld interface between Al and Fe using optical and transmission electron microscopy (TEM). Capacitive discharge welding (CDW) is a rapid solidification process in which the amount of molten metal at the interface is small compared to the sample size. As a result, high cooling rates ( $10^6$  K/s) can be achieved, providing a weldment made up of small grains. Large magnetic fields produced by the process tend to mix the molten metals at the interface to form a complex alloy, the nature of which depends upon the starting electrode materials. This effect is characterized by a marblecake pattern in optical micrographs. The amount of mixing is related to the melting temperature of the cathode with respect to the anode. Increased mixing occurs when the melting temperature of the cathode is higher than the melting temperature of the anode. TEM has revealed that when aluminum is the anode material, the iron grains of the cathode are surrounded by a layer of aluminum. When the iron is the anode, a thin layer of iron surrounds the aluminum grains.

### INTRODUCTION

One possible method of joining dissimilar materials is capacitor discharge welding (CDW), a rapid solidification technique<sup>1</sup> that has evolved into an efficient method for stud welding.<sup>2</sup> In CDW, energy is applied for very short times to create a shallow layer of molten metal, which cools very rapidly ( $10^6$  K/s) when in contact with a large thermal heat sink. As a result, the fusion zone (FZ) is narrow, and the heat affected zone (HAZ) is virtually nonexistent.

The CDW process involves the gravity assisted, axial impact of cylindrical specimens with subsequent arcing and melting (and thus joining) of the materials by the discharge of a capacitor bank. During impact the arc is extinguished, and any excess molten metal is expelled prior to electrode contact. Attractive features of CDW include the suppression of FZ porosity due to hydrogen uptake and a minimal HAZ.<sup>3</sup> In addition, the welds tend not to hot crack because of the compressive forces developed during the welding cycle. Thus the microstructure close to the weld is characteristic of the base metal and is affected little by the joining process. The width of the fusion zone can be controlled by varying the welding parameters, and thus the cooling rate.<sup>4-6</sup> For example, a slow cooling rate ( $10^5$  K/s) leads to a larger FZ. Faster cooling rates ( $> 10^6$  K/s) result in much narrower FZs.

### EXPERIMENTAL PROCEDURE

Electrodes were prepared from 6061-T6 aluminum and commercial purity iron rod. (For details of CDW specimen preparation see Ref. 7.) The 6061 aluminum contained the following: Al (bal)-1.0 Mg-0.6 Si-0.6 Fe-0.2 Cu-0.2 Mn-0.2 Cr (all values in weight

percent). The iron contained a number of minor impurities. The drop height for these tests was 51 mm and the drop weight was 1.9 kg. The welding operation was performed at 90 V and 0.08 F.

Optical microscopy and transmission electron microscopy (TEM) of the FZ and HAZ were performed on samples sectioned transverse to the weld centerline. In addition, x-ray chemical analyses of these regions were performed using a microprobe. Knoop microhardness measurements (300 g load) were made from the base metal on one side of the weld centerline through the FZ and into the base metal on the other side of the weld centerline. Each indent covered a lateral distance of around 50  $\mu\text{m}$ , dependent upon the material being tested.

Samples were prepared for TEM examination by grinding and polishing the transverse sections to a thickness of approximately 100  $\mu\text{m}$ ; cutting 3 mm discs from the sections, insuring that the weld line was near the center of each disc; and dimpling grinding the weldment to a thickness of approximately 10  $\mu\text{m}$ . Samples were then ion milled to electron transparency using Ar ions with a 5 kV potential. Samples of the base metal Al and Fe were similarly prepared, except that they were electropolished to electron transparency using a 1:4 solution of nitric acid in methanol and a 1:9 solution of perchloric acid in acetic acid, respectively. All TEM analyses were performed at 100 kV. Phase identification was through a combination of X-ray Energy Dispersive Spectroscopy (XEDS) and electron diffraction analysis.

## RESULTS AND DISCUSSION

### CDW Microstructures

Figures 1 and 2 are optical micrographs of the Al-Fe CD weld and the interfacial region for the Al-Fe CDW couples. At low magnifications (Figs. 1a and 2a), the CD welds look quite similar regardless of whether Al or Fe is used as the cathode material. The weld is thin, with no evidence of cracking. At higher magnifications, however, the variations in microstructure with cathode material become apparent. When aluminum is used as the cathode, the amount of "mixing" of the base metals and intermetallic phases is less than that observed when iron is the cathode. The marblecake structure, or partially mixed zone, created when Al is the cathode, forms adjacent to the iron interface of the welded region, as seen in Fig. 1b. The marblecake structure forms when Al and Fe are not intimately mixed in the liquid weld pool because of the rapid solidification process.<sup>8</sup> Note that the marblecake region accounts for only about one-half the thickness of this weld. When iron is used as the cathode, on the other hand, the marblecake structure in many places accounts for the entire weld thickness (Fig. 2b). In both cases, weld FZ thickness, determined from optical micrographs, ranges from 50 to 100  $\mu\text{m}$ .

X-ray microprobe traces were performed on the marblecake regions of the weld interface, and an example of one such region, in which Al is the cathode, is illustrated in Fig. 3. Each line on the micrograph indicates one set of microprobe traces. At position 1, the composition is approximately 100% Fe (all values are in atomic percent). Between points 1 and 2, the material has a near stoichiometric composition of FeAl, and at point 2, the composition is 90% Al. At point 3, the composition of the weld is 95% Al and 5% Fe. As the trace is made into this region, the atomic percent of Al decreases to a low of 43% (marked on the trace in Fig. 3) and then increases again to 72% at 4. These data suggest that there are pockets of near 100% base metal intermixed with Fe-Al intermetallics within the weld, and correlates well with TEM observations to be presented shortly.

Knoop microhardness measurements were made on each set of welded Al-Fe samples, i.e., for the separate cases when Al and then Fe served as the cathode. The

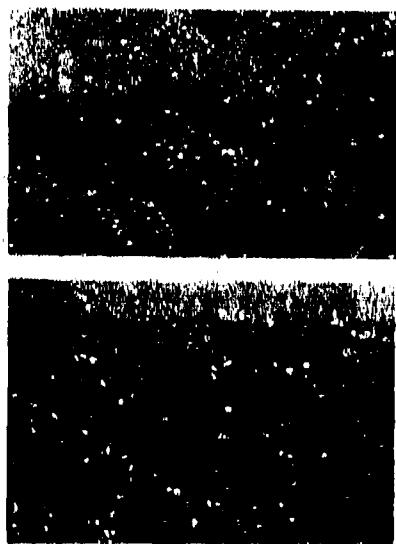


Fig. 1. Optical micrograph of CD weld in which Al is the cathode and Fe is the anode. (a) Low magnification and (b) higher magnification of the same weld showing the partially mixed weld zone.

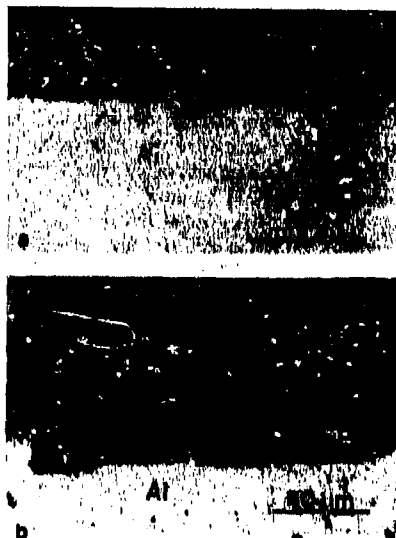


Fig. 2. Optical micrograph of CD weld in which Fe is the cathode and Al is the anode. (a) Low magnification and (b) higher magnification of the same weld showing the partially mixed weld zone.

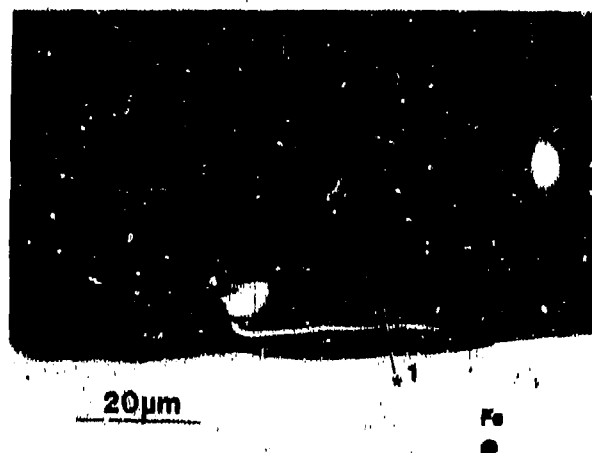


Fig. 3. SEM image of the FZ of an Al-cathode Fe-anode weld. The numbered points and lines indicate positions of microchemical analyses, as described in the text.

microhardness of the Al, well away from the FZ, averages  $119.3 (\pm 4.2)$  kg/mm<sup>2</sup>, regardless of whether the measurements are made on the anode or the cathode. The microhardness of the bulk Fe is  $165.1 (\pm 8.5)$  kg/mm<sup>2</sup>. When Fe is used as the cathode, the hardness begins to decrease some 200 to 300  $\mu$ m from the interface, falling to a low of 77 kg/mm<sup>2</sup> within the FZ. The Al anode counterpart maintains a relatively constant microhardness from the bulk up to approximately 100  $\mu$ m from the weld centerline, at which point the hardness begins to decrease. On the Al-anode side of the FZ, the microhardness is 71 kg/mm<sup>2</sup>.

When Al is used as the cathode material, the microhardness values of the near-weld regions on both the cathode and anode sides are substantially affected. Some 2 mm from the weld centerline, the microhardness of the Al is about 104 kg/mm<sup>2</sup>, and the hardness continues to drop to less than 80 kg/mm<sup>2</sup> at about 1.3 mm from the weld centerline. The microhardness then increases as the weld centerline is approached, reaching a maximum of 104 kg/mm<sup>2</sup> 130  $\mu$ m from the weld centerline. The corresponding Fe anode shows a significant decrease in its bulk microhardness in this weld couple. At 110  $\mu$ m from the weld centerline, the hardness of the Fe is only 83 kg/mm<sup>2</sup>, roughly half the microhardness of the bulk. The microhardness of the Fe then begins to increase as the distance from the FZ increases, rising to 125 kg/mm<sup>2</sup> 400  $\mu$ m from the FZ. The average Fe hardness is  $120.9 (\pm 2.6)$  kg/mm<sup>2</sup> over the next 3 mm, and only approaches its average bulk value 3.5 mm from the weld centerline. From this data, it is clear that while the HAZ in CDW Al-Fe is narrow when Fe is used as the cathode, it can become quite substantial if Al is the cathode material.

#### Base Metals

TEM examination of the base metals, several centimeters from the weldment, indicates no change in microstructure as a result of the welding process. The microstructure of the Al is typical of that of a 6061 alloy, and includes a number of intra- and trans-granular  $\alpha$ -AlFeSi and Mg<sub>2</sub>Si precipitates (Fig. 4a). The base-metal iron is primarily ferritic, with an occasional small, transgranular Fe-Cr precipitate (Fig. 4b).

#### Weldments

As is apparent in the optical micrographs (Figs. 1 and 2), the microstructure of the weldment does not change in an orderly manner from base metal to base metal. Rather it is a marbled mix of regions of metals and intermetallics that gradually changes in composition across the weld from iron to aluminum. Although specific features vary, dependent upon which material is the anode and which is the cathode, the general microstructural characteristics of the fusion zone of CD-welded aluminum-iron are as follows. Some 50 to 100  $\mu$ m from the FZ, the grain size of the base metals decreases, and the size of the  $\alpha$ -AlFeSi precipitates within the Al alloy increases, although this is strictly a qualitative observation and has not yet been quantified. Outside of this region, however, there is no obvious change in microstructure with change in cathode material that explains the large variations in microhardness described previously. At the Iron-FZ interface (Fig. 5), there is a narrow region of equiaxed Fe<sub>3</sub>Al grains, followed by an area of mixed FeAl and Fe<sub>3</sub>Al. The Fe<sub>3</sub>Al grains at the interface frequently contain fine, transgranular precipitates that are tentatively identified as FeAl<sub>2</sub>O<sub>4</sub>; these precipitates also form in the base metal adjacent to the interface, in rows perpendicular to the FZ. When iron is the cathode material, the intermetallic grains are frequently bounded by an Al-rich, amorphous phase, and larger  $\alpha$ -Fe grains are also present within the FZ.

On the aluminum-side of the FZ, columnar Al grains, bounded by an Fe-Al intermetallic phase, form with their long axes at an angle to the Al-FZ interface, as

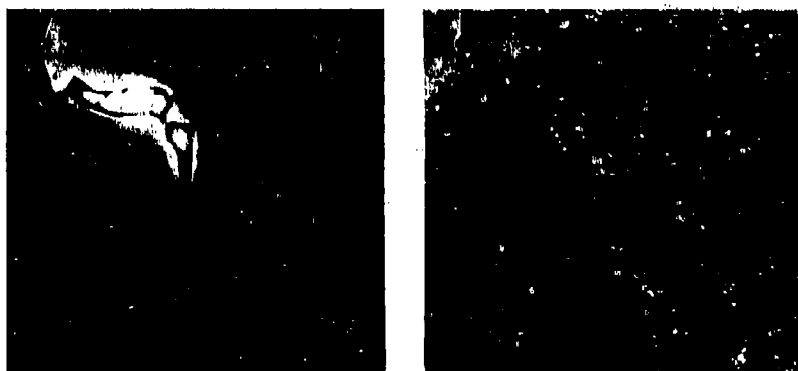


Fig. 4. TEM images of the base metals several centimeters from the FZ, (a) Al and (b) Fe.



Fig. 5. The Fe-FZ interface. In this case, Fe is the cathode.



BASE METAL Al

Fig. 6. The Al-FZ interface. Here Al is the cathode material.

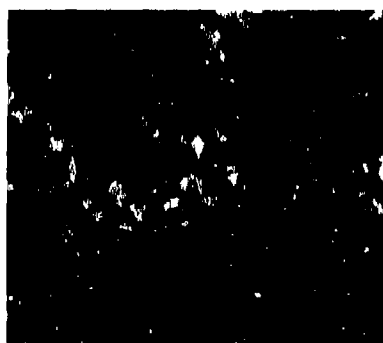


Fig. 7. Region of cellular Al within the FZ of the CD weld in which Fe is the Cathode material. The cellular phase is Fe-rich.

illustrated in Fig. 6. When iron is the cathode material, the columnar Al grains tend to be coarser than when aluminum is the cathode. And in fact, the overall scale of the microstructure within the FZ tends to be coarser when iron is the cathode. In the welds in which Al is the cathode, a narrow zone of  $\text{Al}_3\text{Fe}$  grains may also form at the interface between the base-metal Al and the columnar Al grains, as illustrated in Fig. 6. These  $\text{Al}_3\text{Fe}$  grains are oriented with their {001} planes perpendicular to the interface. This {001} grain orientation is a preferred growth direction in many cubic materials. During solidification, grains with their "easy growth direction parallel to the direction of the maximum temperature gradient" grow at the expense of grains which are not so favorably oriented.<sup>9</sup>

The central regions of the FZ generally consist of mixed areas of metals and intermetallics. If Al is the cathode, the combination is of equiaxed  $\text{FeAl}$  and  $\text{Fe}_3\text{Al}$  grains and columnar, faulted  $\text{Al}_3\text{Fe}$ . (Diffraction analysis suggests that these faults are stacking faults on {001} planes, with a displacement vector in the [010] direction.) "Pipes" of an amorphous, Al-rich phase form boundaries between these different regions. When Fe is the cathode, the microstructure is similar, with mixed regions of  $\text{Fe}_3\text{Al}$ ,  $\text{FeAl}$ ,  $\text{Al}_3\text{Fe}$ , and faulted  $\text{Al}_3\text{Fe}$ . In addition, on the Al-side of the FZ, there are pockets of cellular, and cellular-dendritic Al grains (fig. 7), with an Al-Fe intercellular phase and occasional intermetallic primary particles. The cellular spacing varies from pocket to pocket in this region.

## CONCLUSIONS

Capacitor discharge welding is an effective technique to join dissimilar metals, producing narrow welds with little or no cracking. The joining of iron to aluminum results in a FZ, consisting of a mix of base metals and intermetallic phases, that possesses a marblecake appearance. The overall effect of the welding process on the microstructure can be localized to a region of several hundred micrometers on either side of the centerline of the weld, and depends upon the choice of anode and cathode materials. For Al-Fe couples, the use of Fe as the cathode limits the size of the FZ and HAZ to a total width of about 400  $\mu\text{m}$ . However, if Al is used as the cathode, the FZ remains small, but the HAZ encompasses about 5 mm, with the major effect occurring in the Fe anode.

## ACKNOWLEDGMENT

The authors would like to thank Dr. Roger L. Nielsen, Oregon State University, for performing the microprobe analyses on the CDW samples. The authors are grateful for the help and discussions provided by Dr. John W. Simmons during the course of this study.

## REFERENCES

1. H. Jones, *Mater. Sci. Eng.*, **5**, 1 (1969).
2. T. E. Shoup, C. C. Pease and M. Tamliusu, in *Metals Handbook*, Vol. 6, 9th ed. (ASM, Metals Park, OH 1983), p. 729.
3. J. H. Devletian, *Weld. J.*, **66**, 33 (1987).
4. S. Venkataraman, and J. H. Devletian, *Weld. J.*, (suppl.), **67**, 111s (1988).
5. S. Venkataraman, and J. H. Devletian, in *Principles of Solidification and Materials Processing*, Vol. 2, edited by R. Trivedi, J. A. Sekhar, and J. Mazumdar (Trans Tech Publications, New York, 1988), p. 859.

6. C. J. Einerson, D. E. Clark and J. H. Devletian, in Proc. of the 1987 ASME/JSME Thermal Engineering Joint Conf., Volume Three, edited by P. J. Marto and I. Tanasawa (ASME, New York, 1987), p. 217.
7. R. D. Wilson, J. A. Hawk, and J. H. Devletian, in Joining and Adhesion of Advanced Inorganic Materials, edited by A. H. Carim, D. S. Schwartz, R. S. Silbergliitt, and R. E. Loehman (to be publ. Mater. Res. Soc. Proc., Pittsburgh, PA).
8. S. Kuo, Welding Metallurgy (John Wiley and Sons, New York, 1987), p. 202.
9. ibid., p. 146.

## FUNDAMENTALS OF THE SHS JOINING PROCESS

ROBERT W. MESSLER, JR.\* AND TIMOTHY T. ORLING\*\*

\*/\*\*Rensselaer Polytechnic Institute, Department of Materials Engineering, Troy, NY 12180

### ABSTRACT

The process of self-propagating high-temperature synthesis offers potential for joining similar or dissimilar combinations of heat-resisting or refractory metals and refractory or corrosion resistant oxide or nonoxide ceramics or intermetallics by using the exothermy inherent in the synthesis reaction. The process offers unique capability for producing functionally gradient material joints between dissimilar materials to overcome mismatches in chemical, mechanical and physical properties, facility for incorporating reinforcing phases in the filler, and exceptional efficiency given that the energy for joining is largely internally generated. A systematic study of the fundamentals of the process critical for joining in either a primary or a secondary mode is being undertaken. Specialized fixture is being employed to study the role of substrate temperature in bond formation and strength, and the role of precompaction density and applied pressure on joint density. A Gleeble thermomechanical simulator is being used to study the role of reactant composition, reactant particle size, heating rate and reaction mode, precompaction and applied pressure, and atmosphere. Ultimately, a model of the SHS process for joining will be developed to facilitate joint design, predict joint properties, and enable intelligent control.

### BACKGROUND

Designers are increasingly looking to oxide and nonoxide ceramics and intermetallic compounds, in both monolithic and reinforced forms, to achieve enhanced performance in severe corrosion, wear or temperature environments. Frequently, these materials must be combined with corrosion- or heat-resisting metals to provide needed structural integrity, particularly to accommodate load-induced strain or shock, or to keep the resulting optimized, hybrid structure affordable. Joining of ceramics, intermetallics or their composites, in similar and dissimilar combinations with one another or with metals, poses numerous challenges arising from inherent characteristics of one or more of the materials or from incompatibilities between materials. Chemical decomposition, sublimation without melting, loss of long-range order, brittleness, and sensitivity to thermal shock limit inherent weldability, while incompatibility between chemical, mechanical or physical properties complicate production of hybrid joints.<sup>1-2</sup> Clearly, new joining processes are needed.

Self-propagating high-temperature synthesis (SHS) or combustion synthesis offers great promise as a joining process for advanced materials and hybrid structures therefrom.<sup>3</sup> By taking advantage of the energy generated internal to the synthesis reaction, simultaneous consolidation by reactive sintering has already been demonstrated and employed,<sup>4-5</sup> while joining has been shown feasible but remains to be developed.<sup>6-7</sup> Advantages inherent to the SHS process for joining include: (1) energy efficiency (given that energy for joining is generated internally); (2) capability for joining in a primary mode, while one or more of the joint materials are being synthesized, or in a secondary mode, in which two or more preexisting substrates or joint elements are joined; (3) suitability to the production of functionally gradient material (FGM) joints that bridge chemical, mechanical and physical property mismatches by grading composition from one joint element to the other; (4) potential for incorporating reinforcing phases within joint filler to produce a composite; and (5) similarity to the process that was or could have been used to produce the substrate material(s).

Despite the need for an advanced process for joining advanced materials, and the numerous potential advantages of SHS as a joining process, little is known about how the process can or should be practiced to advantage for joining.



## RESEARCH OBJECTIVES

The objective of on-going research at Rensselaer is to systematically investigate and develop SHS or pressurized combustion synthesis for joining monolithic or reinforced ceramics and intermetallics to themselves, to one another, or to metals. The goal is to thoroughly understand the mechanism of bond formation, to characterize the role of key processing parameters, to optimize the process, and, ultimately, to develop a model to enable bonding predictions, process and property optimization, and intelligent process control.

## TECHNICAL APPROACH

### Cooperative and Multidisciplinary Approach

Until now, SHS joining R&D has not been the focus of joining specialists, but, rather, of ceramists as a variant of the basic synthesis process to some other end. Joining specialists tend to approach the challenge of joining from a broader perspective, considering the challenges of secondary joining of preexisting, fully dense substrates as much or more than primary joining of green parts during material synthesis. In this effort, joining specialists are working in cooperation with specialists in ceramic and intermetallic materials, powder processing, and material characterization in an essential multidisciplinary approach.

### Key Process Variables

There are several problems related to successfully employing SHS for joining. The first is achieving wetting and bonding to a preexisting substrate, as opposed to producing a joint in situ during fabrication of the joint end elements and filler. For successful bonding to preexisting substrates, sufficient heat must be developed by the reaction at the interface to either cause melting and wetting or solid-state reaction or interdiffusion. Substrate temperature, reaction mode (i.e., self-propagating or simultaneous combustion), and substrate surface condition (including reaction atmosphere) are key variables that need to be evaluated and understood. A second problem is producing a dense, porosity-free joint. Several factors lead to poor density during SHS including residual packing porosity, reaction product expansion, or entrapment of previously dissolved gases or gaseous reaction by-products. The key variables that need to be evaluated are precompaction density of the reactant, reactant particle size and size ratios, and applied pressure-time profile during reaction. The third problem is avoiding cracking of substrates, filler, or, especially, substrate/filler interfaces due to mismatch of thermal coefficients of expansion. Here, appropriate selection of process heating rates, cooling rates, and reactant composition are important variables. The use of functional gradient materials offers particular promise.

### Innovative Use of Specialized Fixtures

To simplify study of key parameters in SHS joining, these parameters are being decoupled wherever possible. As a means of expeditiously investigating and characterizing the role of substrate temperature on bond formation and precompaction and applied pressure on joint density, three special fixtures are being employed. In a Substrate Temperature Gradient Fixture (Figure 1), a rectangular groove machined along the centerline of a plate of the desired substrate material is filled with reactant powder precompacted to the desired density. The plate is fixtured between two large thermal masses, one held at a high temperature near the reaction triggering temperature ( $T_i$ ) and the other near room temperature (using cooling). Temperature is monitored at several points along the plate to provide data on the prevailing gradient during reaction. Gas inlets and outlets provide protection by argon throughout processing. The reaction is triggered from the cool end using a resistance heated element. Following reaction, the plate is sectioned to permit examination of the degree and mechanism of bonding as a function of substrate temperature (i.e., solid-state reaction, interdiffusion, or fusion and wetting). Initial studies are being conducted with Inconel 600 substrates and  $\text{Ni}_3\text{Al}$  filler.

Subsequent studies are planned for SiC fillers to SiC or Ni superalloy substrates and TiC to graphite or titanium alloy substrates, using appropriate inserts in the Inconel 600 fixture.

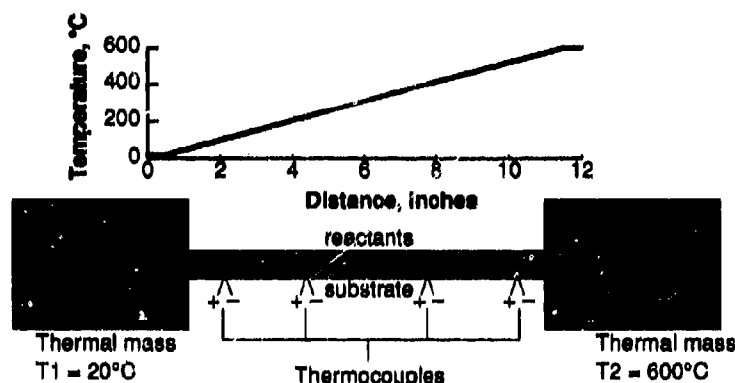


Figure 1: Substrate Temperature Gradient Fixture

In other fixtures, called Compaction Density Gradient and Applied Pressure Gradient Fixtures, various schemes for applying either graded compaction pressure prior to reaction or graded or stepped applied pressure during reaction are being considered. In one design (Figure 2), a tapered cover plate will be forced into powdered reactant in a machined rectangular slot in a plate to produce high compaction at one end and low compaction at the other. Other schemes are planned for stepping applied pressure along the groove. The entire fixture will be at a uniform temperature, just below the reaction triggering temperature ( $T_i$ ) for the self-propagating mode or just above  $T_i$  for the simultaneous combustion reaction mode. The rate of reaction-front propagation, the degree of reaction, the peak temperature reached following reaction, the degree of bonding to the substrate, and final density will all be assessed by monitoring temperature and by conducting metallographic analysis.

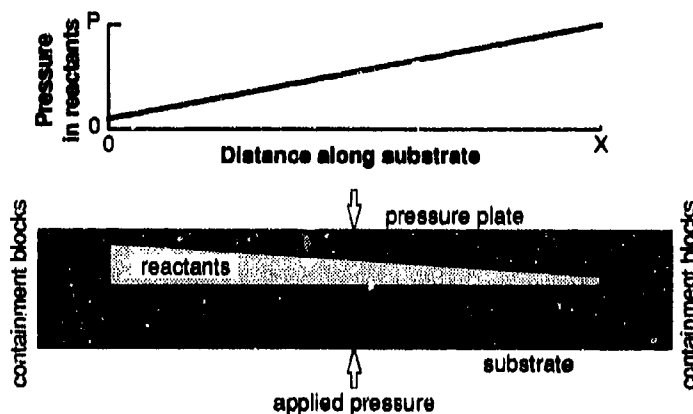


Figure 2: Compaction Density Gradient Fixture

### Gleeble-Based Studies

There are some process parameters and conditions that are not amenable to study using the specialized fixtures described above, so a Duffer's Gleeble 1500™ thermomechanical simulator and test apparatus is being employed. Using a test set-up (Figure 3) consisting of a graphite support tube, sandwiched end-elements and reactant fillers, and graphite load-application plungers, various key parameters are being systematically studied, functionally gradient material joints are being fabricated, and finished joints will, eventually, be tested. Parameters to be studied include: reactant powder particle size and size ratio (as these affect reaction kinetics and product homogeneity); reactant composition (as this affects peak temperature, liquid phase formation, bonding, and, for graded compositions, property mismatch); processing pressure-time profile; reaction mode (propagating versus simultaneous combustion); heating rate (as this affects reaction kinetics and mode); and atmosphere (vacuum versus inert versus active gas). Figure 4 shows Ni<sub>3</sub>Al joints formed between Inconel 600 end elements using various temperatures, hold times, and applied pressures. Bond integrity is always excellent, while porosity is reduced, but not eliminated, by reacting at higher temperatures (i.e., 1000 versus 650 °C), for longer hold times (i.e., 15 versus 2 minutes), and for increasing applied pressures (e.g., from 17.9 MPa or 1250 psi to 85.7 MPa or 6000 psi). Figure 5 shows the effects of these parameters on degree of reaction. The reaction is more complete, with more homogeneous product, as the reaction temperature and/or hold time is increased. Axially-gradient joints are also being produced between various metal, ceramic and intermetallic end elements. Such FGM joints have been already been attempted between Ni-base superalloys and silicon carbide and between Ti-6Al-4V and graphite.

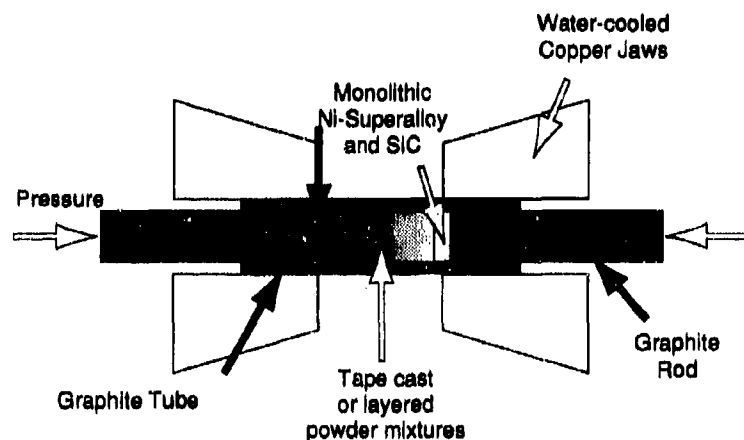


Figure 3: Functionally Gradient Material (FGM) Joint Gleeble Fixture

### FGM Joint Design Model

In joints between dissimilar materials, mismatch of coefficients of thermal expansion give rise to stresses due to temperature excursions and/or gradients. If too high, these stresses can preclude sound joint fabrication or lead to joint failure in service. FGM joints offer an attractive means of overcoming such property mismatch and associated stresses. As part of this research, an analytical model based on a thin plate assumption that allows simplification of the generalized heat flow equation to one dimension has been developed to permit the ready calculation of temperature distribution and associated thermally-induced stresses, accounting for critically important material properties as functions of temperature. The model facilitates FGM joint design for successful processing.

## SUMMARY

SHS represents an exciting possibility for joining similar and dissimilar combinations of refractory ceramics, intermetallics and metals, but only if process fundamentals are fully understood. An on-going program of research at RPI is systematically studying the role of SHS joining process fundamentals using a multidisciplinary approach, innovation specialized fixtures, and the Gleeble thermomechanical simulation and test apparatus.

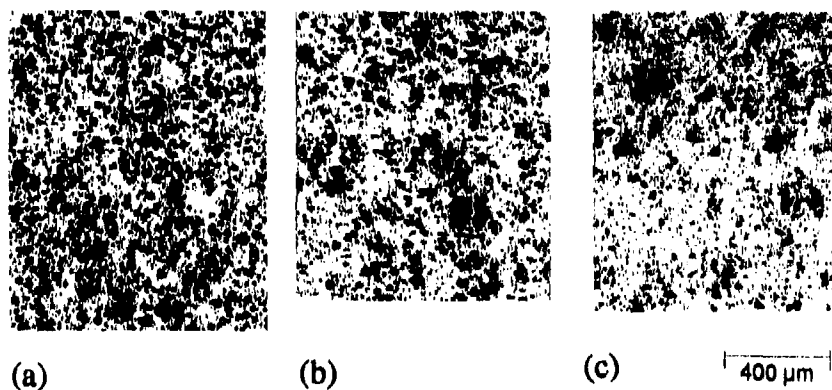


Figure 4: SHS joints of IN600/Ni<sub>3</sub>Al/IN600 show excellent bond integrity and decreasing levels of porosity with increasing reaction temperature, hold time, and applied pressure: (a) 650 °C/15 minutes/1250 psi (17.9 MPa); (b) 650 °C/2 minutes/6000 psi (85.7 MPa); and (c) 1000 °C/15 minutes/2500 psi (35.8 MPa). As-polished.

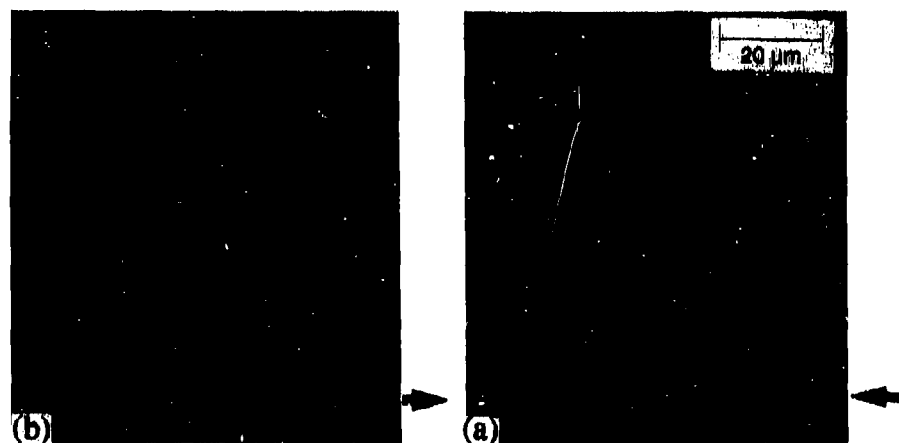


Figure 5: The degree of reaction in joints of IN600/Ni<sub>3</sub>Al/IN600 is more complete when reaction occurred at (a) 1000 versus (b) 650 °C for 15 minute versus 2 minute hold times, respectively. Nonuniformity of composition is indicated by discoloration around pores. As-polished. Arrows indicate interface.

## REFERENCES

1. M. Schwartz, Ceramic Joining (ASM Int'l., Metals Park, OH, 1990), pp. 6-11.
2. R.W. Rice, Advances in Joining Technology, edited by J.J. Burke (Brook Hill Publishing Co., Chestnut Hill, MA, 1976), pp. 69-111.
3. H. Lai, Powder Metall. Technol. 10(3), 223-227 (1992).
4. B.H. Rabin, A. Bose and R.M. German, "Processing Effects on Densification in Reactive Sintering of Ni-Al Materials" in Modern Development in Powder Metallurgy, vol. 20, edited by P.U. Gummerson and D.A. Gustafson (MPIF, Princeton, NJ, 1988).
5. W.Z. Misiulek, N.D. Sopchak and R.M. German, "Pressure-Assisted Reactive Sintering of NiAl/TiB<sub>2</sub>" in Processing and Fabrication of Advanced Materials for High Temperature Applications, edited by V.A. Ravi and T.S. Sviversen (Proceedings of the Annual TMS Meeting, 1992).
6. M. Ohyanagi, Y. Taketani, Y. Nakamura, E. Kamiyo and M. Kuzumi, J. Self-Prop. High-Temp. Synth. 1(1) (1992).
7. V. Hlavacek, Amer. Cer. Soc. Bulletin 70, 240-43 (1991).

## SELF-PROPAGATING, HIGH TEMPERATURE SYNTHESIS AS A TECHNIQUE TO JOIN METALS

J. A. HAWK, A. V. PETTY, C. P. DOGAN and J. C. RAWERS  
U. S. Bureau of Mines, Albany Research Center, Albany, Oregon 97321-2198.

### ABSTRACT

Self-propagating, high temperature synthesis (SHS) can be used to bond both similar and dissimilar metals. A unique feature of this technique is the ability to stack either metal foils or metal foils and powder, and to process them to form two-dimensional, layered composites with a "graded" intermetallic interface between layers. This process can also be used to modify a surface for corrosion or wear resistance. To date Bureau of Mines research has focused on making iron-, titanium-, and nickel-aluminum composites. The elemental metal foils are stacked and placed in a hot press, and the temperature is raised until the composite sandwich undergoes the SHS reaction. At approximately 660°C (i.e., the melting point of aluminum), the aluminum reacts with the transition metal to form intermetallic phases. The SHS process is mass and energy limited; i.e., mass transport controls the chemical reaction rates, while the energy liberated by the chemical reaction is distributed to the surroundings by heat conduction, convection and radiation.

### INTRODUCTION

In self-propagating, high temperature synthesis (SHS), the initial reactants (often in the form of elemental powders) are ignited, initiating a self-sustaining, heat-generating chemical reaction that results in their transformation into compounds or intermetallic phases.<sup>1,2</sup> For example, if a stoichiometric one-to-one mixture of elemental Ti and Al powder is compacted into a rod and one end is heated, the Ti and Al at that end will react, producing primarily titanium aluminide (TiAl). (During the SHS processing of elemental powders, a wide range of phases will form. For example, the 50/50 atom % mixture of Ti and Al will form not only TiAl, but also TiAl<sub>3</sub> and Ti<sub>3</sub>Al.) Because of the large amount of exothermic heat liberated during the formation of TiAl, the powder immediately adjacent to the reaction will also be heated and will react. This reaction continues, increasing in magnitude, until a self-sustaining front forms. This reaction front then propagates through the rest of the powder compact, converting it to TiAl. No additional external heat is required for the reaction to go to completion. SHS processing has been successfully used to form metal-aluminides, -borides, -carbides, -nitrides, and -silicides.

Advantages of the SHS process include the following: (1) The ability to preform green powder compacts into the shape desired for the final product. Thus, SHS allows for *near net shape* production of hard-to-fabricate and hard-to-machine materials. (2) SHS can lead to economic savings because the reaction is heat-generating and self-sustaining. Additionally, the starting materials need only be heated to the temperature of the reaction, which can be hundreds of degrees less than the melting temperature of the product. SHS can thus reduce the cost of material processing, leading to an environmentally-cleaner process. (3) SHS results in a purified final product. Because the SHS reaction is exothermic, the process volatilizes contaminants ahead of the reaction front and removes them, thereby purifying the end product. (4) The SHS process allows several different reactions to occur concurrently. Thus, it is possible to produce difficult-to-form intermetallic-ceramic

composites *in-situ*. (5) SHS processing offers high productivity as it has the highest reaction rates.<sup>2</sup> This is especially attractive when compared to the usual high energy processes used to obtain some refractory compounds (e.g., cubic tantalum nitride), which require long hours of reaction at high temperatures in furnaces or plasma reactors. The usual problems associated with the scale-up of a process are not encountered since the SHS reaction approaches complete conversion with larger quantities. This results in better product yields.

Because the starting density of the powder compact is significantly less than that desired in the final solid compact, U. S. Bureau of Mines scientists have developed a technique leading to full density compaction during SHS processing.<sup>3-5</sup> Powder compacts, or metal foils, are placed into graphite dies and furnace heated under pressure until the SHS reaction begins. As a consequence of the entire compact being at the reaction temperature, a *thermal explosion* occurs throughout the sample; i.e., the SHS reaction is initiated at many points in the sample simultaneously. Porosity is greatly reduced because pressure is applied when the reactant material is molten and the process is carried out in a vacuum furnace.

U. S. Bureau of Mines scientists have also successfully fabricated a number of products with commercial potential, including TiAl diesel engine valve lifters. However, in addition to being a technique that allows the formation of near-net-shape products, SHS can also be utilized as a unique method of joining metals and alloys. The principle of the technique is quite simple. In SHS joining, the exothermic heat generated is used both for the SHS combustion reaction and the SHS reaction at the joint interface. The result in many instances is a layered metal-aluminide composite, where the metallic phase is separated by SHS intermetallic product phases. This technique has been successfully used to join sheets of Al with sheets of Ti, Ni, Fe, and stainless steel (SS), and to make layered metal sheet and powder composites. Consequently, SHS layers with unique wear, corrosion, or heat resistant properties can be synthesized, or joined, to inexpensive metal substrates.

## SHS PROCESSING PRINCIPLES

Two variations of the SHS process are generally recognized: the process in which layer-wise combustion occurs, and the process in which volumetric combustion occurs. Layer-wise combustion occurs when the SHS reaction is initiated at some point on the compact (usually at an outer surface), with the combustion wave then propagating with a definite velocity throughout the rest of the compact. Most Bureau of Mines current powder SHS research utilizes the second approach, that is, the volumetric combustion, or thermal explosion, method. In this thermal explosion method, a volumetric reaction takes place as a consequence of the entire reactant compact being heated uniformly in a furnace. Once the reaction temperature is reached, a number of small SHS reactions occur simultaneously throughout the entire volume of the compact. Most SHS research at the Bureau of Mines focuses on two physicochemical classifications:<sup>6</sup> (1) both components are in the liquid state, and (2) one component remains solid while the other component is a liquid.

In SHS, if the adiabatic temperature exceeds the melting point of the reactants but is lower than their boiling points, then the combustion reactions will occur in the liquid state. In general, adiabatic temperatures for aluminides are low compared to silicides, carbides, borides, etc., and it is usually necessary to heat the reactants to elevated temperatures in order to initiate the SHS reaction.<sup>2</sup> As a consequence of the additional heat input, the reactants are, in most instances, in the liquid state during combustion. An example of this type of reaction is the formation of NiAl from Ni and Al. The adiabatic temperature for the formation of NiAl is 1637°C, while the melting temperatures of Ni and Al are 1453°C and 660°C, respectively. (It should be noted that powder particle size and heating rate are important process conditions.<sup>7</sup> With a small powder size for both the Ni and Al, a liquid-liquid reaction can take place. However, if the Ni powder size is large in comparison to the

Al powder, only partial melting occurs, so a solid-liquid reaction occurs. Higher heating rates decrease the tendency for the formation of precombustion, or diffusional, phases. This also increases the amount of liquid formed during the reaction, thus creating a product with lower porosity.)

When the adiabatic temperature lies between the melting points of the two starting components, the liquid formed from the lower melting component spreads rapidly throughout the compact, resulting in the highest velocity combustion reaction. Solid-liquid combustion reactions are common in the SHS of silicides, carbides and borides, as for example, in the formation of TiC from Ti and C.<sup>8</sup> It is established that the melting of Ti precedes the combustion reaction in the conversion of Ti and C to TiC. However, as with aluminide formation, processing parameters such as powder size are important. The extent of melting, and the details of the Ti-C interactions which result in TiC formation are imprecisely known. Larger particle sizes tend to slow the combustion reaction, leading to incomplete carbide conversion.<sup>9</sup>

It is clear that many processing parameters affect the formation of SHS materials. In this study, no attempt has yet been made to "optimize" the processing parameters for the SHS of layered sheet and powder-sheet composites. Rather, the focus of this research has been to explore the limits of possibility in making and joining advanced materials.

## MATERIALS AND PROCESSING PROCEDURE

### Materials and Processing

The intermetallics selected for study by the Bureau of Mines were based on metals that would react with Al to form a metal-aluminide. The material systems studied include: Ni-Al, Ti-Al, Fe-Al and stainless steel (SS)-Al, with the starting materials consisting of either sheet or powder. Figure 1 diagrams the lay-up sequence typically used to make the composites. Several composites were made by layering thin sheets of Al with thin sheets of either Ni, Ti, Fe or SS. The powder and powder-sheet composites studied to date were based on the Fe-Al (i.e., either a stoichiometric Fe<sub>3</sub>Al or FeAl composition for the powder components) and the Ti-Al (i.e., a stoichiometric TiAl composition for the powder components) systems. The sheet material used to form the powder-sheet composite was either Fe, SS, or Ti, depending upon the metal-aluminide desired. In the case of the powder-sheet composites, the powder was sandwiched between metal sheets and vacuum hot-pressed to initiate the SHS reaction. TiAl powder-Ti sheet composites prepared using this technique have been studied extensively.<sup>3-5,10,11</sup> In addition to layered composites of Ti and TiAl, intermetallic-ceramic particulate composites have also been formed, with TiAl as the matrix. Ternary additions of C, B, and Si have been made with mole fractions of up to 60%, yielding high volume fractions of TiC, TiB<sub>2</sub> and Ti<sub>3</sub>Si<sub>2</sub> strengthening dispersoids.<sup>12</sup>

As previously mentioned, composite formation was accomplished in a vacuum hot-press. The general processing sequence was as follows: the material was placed in a graphite die and transferred to the hot-press; a slight pressure was applied to the sample as the temperature was ramped to the SHS initiation temperature; at the point where the SHS reaction began, the applied pressure was increased to between 10 and 20 MPa, and the sample was either held at the reaction temperature, or given a post-reaction heat-treatment at an elevated temperature; and finally, the sample was furnace cooled to room temperature under pressure. The application of pressure to the composite during the SHS reaction, and any post-SHS heat treatment, reduced composite porosity and improved bonding at the interface. A number of processing times, temperatures and pressures have been investigated by Bureau scientists. For example, the layered sheet samples were placed in a graphite die and vacuum hot-pressed at 650°C for one hour under a pressure of 10 MPa. The samples were furnace cooled under vacuum. To create layered sheet-powder composites, the



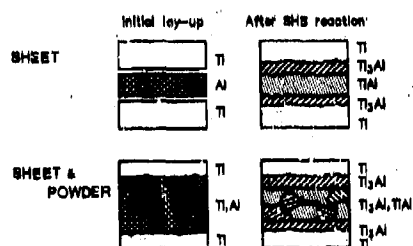


Fig. 1. Schematic representation of initial lay-ups for metal sheet and sheet-powder composites.

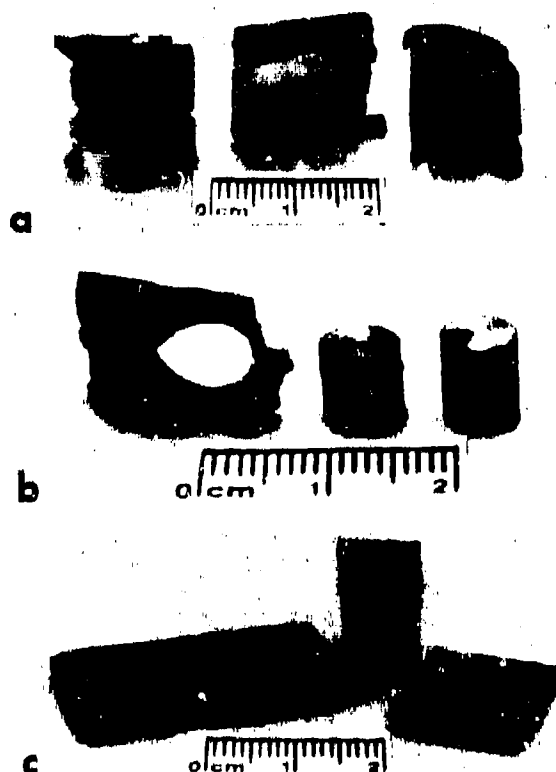


Fig. 2. SHS layered composites: (a) Ni-Al metal sheet composite; (b) Fe-Al metal sheet composite with EDM'd cylinders; and (c) SS-Al metal sheet composite.

elemental powders or powder mixtures were placed between metal disks in a graphite die and then hot-pressed. To obtain maximum density and optimum strength, the layered metal-powder composites were hot-pressed for times equal to or greater than one hour at temperatures equal to or greater than 1000°C. The usual pressure applied to the compact during this procedure was 20 MPa. These composite samples were also furnace cooled.

#### TEM Specimen Preparation

Transmission electron microscopy (TEM) was used to investigate the microstructure of the interfaces of the SHS-joined metal foils. Samples were prepared for TEM analyses by sectioning the material transverse to the foil interfaces and grinding to a thickness of approximately 100  $\mu\text{m}$ ; cutting 3 mm diameter discs from the samples, insuring that at least one interface was near the disc center; and dimple-grinding the interface region to a thickness of approximately 10  $\mu\text{m}$ . Samples were ion milled to electron transparency using argon ions at a potential of 7 kV. All microstructural analyses were performed at 100 kV.

### STATUS OF SHS JOINING TECHNOLOGY

#### Layered Sheet Composites

Anselmi-Tamburini and Munir<sup>13,14</sup> were the first to investigate the possibility of using the SHS process to form intermetallics from thin metal foils. Their initial goal was to model the characteristics of the SHS reaction front and to understand the nature of the interfacial reactions, all of which are less complicated when the geometry is planar. Subsequent to the Bureau's metal-intermetallic composite studies, Wright et. al.<sup>15</sup> and Rabin<sup>16</sup> have also used SHS process technology, both pressureless and pressure-assisted, to join iron aluminide ( $\text{Fe}_3\text{Al}$  and  $\text{FeAl}$ ) and SiC.

Bureau of Mines researchers have modified the SHS composite process developed by Anselmi-Tamburini and Munir to successfully produce large, layered metal-intermetallic composites. Figure 2 illustrates several examples of layered composites formed using the Bureau-modified SHS technique. Table I shows the thicknesses of the starting metal sheet used to form the composites in Figure 2. In Fig. 2a, Al sheets are used to join Ni sheets. During SHS processing, some molten Al was squeezed from the compact as pressure was applied; nonetheless, a good bond between the Ni sheets was obtained, as is apparent in the figure. Interface integrity is further illustrated by the fact that although thin sections of this composite curl during sectioning, the composite remains intact.

TABLE I. Thickness of the disks used to form layered composites.

Composite	Metal Disk Thickness (mm)	Aluminum Disk Thickness (mm)
Fe-Al	0.75	0.10
Ni-Al	1.40	0.10
Ti-Al	0.40	0.10
SS-Al	0.25	0.10

A look at the Ni-Al interfacial regions of these SHS composites in the TEM indicates that they consist of a residual layer of Al, in this case some 0.05 to 0.15  $\mu\text{m}$  thick, surrounded on either side by small grains of Ni containing intragranular  $\gamma$  Ni<sub>3</sub>Al precipitates. This microstructure is revealed in the dark field image of Fig. 3. The intermetallic region



Fig. 3. Dark field micrograph of interface in SHS Ni-Al sheet composite showing the  $\text{Ni}_3\text{Al}$  precipitation adjacent to the SHS joint.



Fig. 4. SEM micrograph of SS-Al layered composite.

stretches approximately 20  $\mu\text{m}$  on either side of the residual Al foil, with Ni grain size increasing with distance from the interface. Within the intermetallic region there are also small, intragranular Al- and Al+Mg-rich precipitates which are as yet unidentified.

An example of Fe foil joined to Al can be found in Fig. 2b. Cylindrical samples of this composite were electro-discharged machined (EDM) from the compact to make pin-on-drum abrasive wear specimens and it is the EDM'd samples and a remaining portion of the original compact that are shown. Wear tests, performed on the layered compact both perpendicular and parallel to the joints, indicate that in this composite as well, joint integrity is good: the SHS-joined material did not separate at the interfaces upon abrasive wear testing in either orientation.

TEM examination of the interfacial regions of the Fe-Al composites has met with limited success to date. Because the residual Al foil ion mills much more rapidly than the adjacent Fe, sample preparation has been difficult. Nonetheless, it appears as though the microstructure of these composites must be similar to that described for the Ni-Al materials. That is, it probably consists of a thin, residual layer of Al surrounded by a narrow zone of  $\text{Fe}_3\text{Al}$  and/or  $\alpha\text{-Fe}$  with Al in solution.

A first attempt to join thin sheets of stainless steel with Al is illustrated in Fig. 2c. To date, a square composite, 50 mm x 50 mm x 3 mm, has been fabricated that can be sectioned without gross layer separation. Thin sectioning this composite into slices  $\sim 300$   $\mu\text{m}$  thick is not possible, however, as the stresses generated cause the material to separate at the steel-Al interfaces. As a result, TEM examination of this material has not yet been possible.

Increasing the ratio of the thickness of the Al sheet to that of the stainless steel sheet results in a composite in which the aluminide interface forms a significant portion of the whole. An example of such a multilayer composite can be found in the scanning electron microscope image of Fig. 4. A closer look at the intermetallic regions of a thick Al-Ti composite using TEM indicates that it consists primarily of grains of  $\text{Al}_3\text{Ti}$  wet by an Al boundary phase. Aluminum is present at all of the three- and four-grain junctions within this region, and likely wets most, if not all, of the two-grain boundaries as well. An occasional grain of TiAl is also observed, and is also wet by the Al boundary phase. In addition, there are also  $\text{Al}_2\text{O}_3$  particles at the boundaries which were probably present on the starting Al sheet, but which did not dissolve during the SHS reaction.

Joining thin Al sheets to thicker metal (Ni, Fe, and Ti) sheets results in a layered composite which appears quite different from those in which the Al sheet is thick compared to the metal. Several examples of thin Al/thick metal composites are given in Fig. 5. Note that all of the composites develop porosity in the join region, as is apparent in greater detail at the Ni-Al interface in Fig. 5b.

The results of microprobe analyses and microhardness measurements across the interface regions for the Ni-Al, Ti-Al, and Fe-Al layered sheet material are given in Fig. 6. Microprobe data across the interface seem to suggest that a number of stoichiometric intermetallic phases form as a result of the SHS reaction between the Al and the metal. However, TEM analyses have indicated that this conclusion is not entirely correct.

#### Layered Powder and Sheet Composites

An alternative to layering metal sheets to form composites is to use either only powders, or a combination of powder and sheet, to make a composite. The advantages of using powders are many, among them the ability to make complicated (i.e., not purely rectangular) shapes, to use low-cost starting components, and to design the properties of the layered composite through judicious selection of layer composition, thickness and location.

A number of TiAl matrix composites with strengthening dispersoids have been produced at the Bureau of Mines using the powder-sheet method. Figure 7 shows a

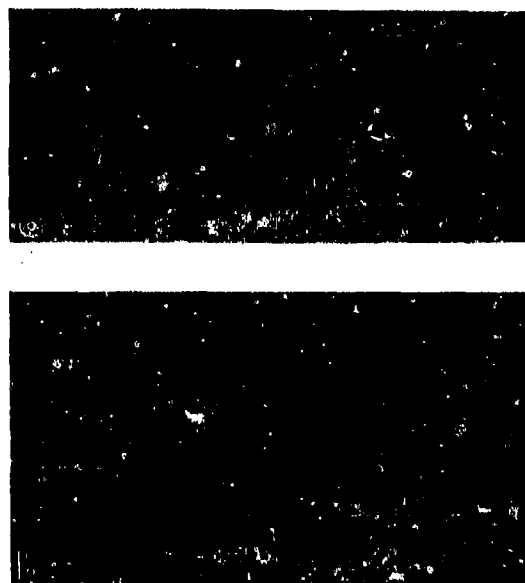


Fig. 5. SHS Ni-Al layered composite showing porosity (a) low magnification and (b) high magnification.

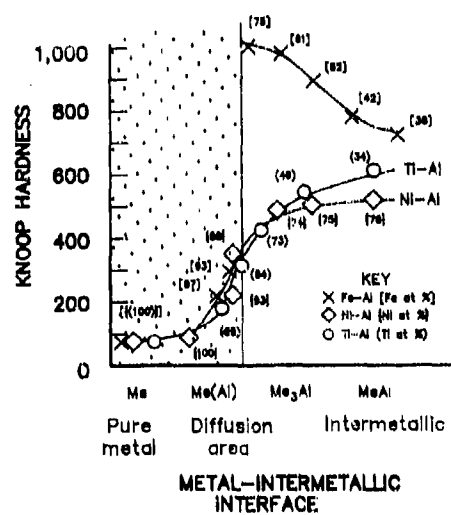


Fig. 6. Microhardness and microprobe data from traverses across metal-Al interfaces.

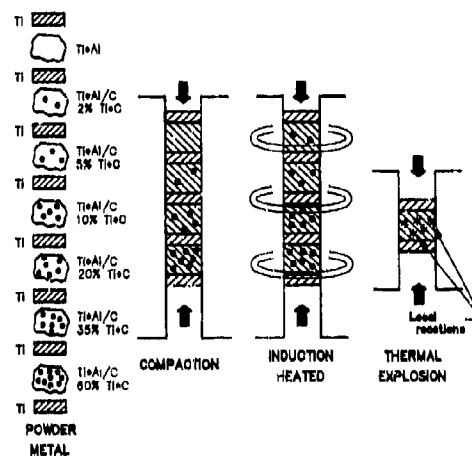


Fig. 7. Schematic representation of powder-sheet layered composites.



Fig. 8. SEM of typical powder (TiAl)-metal (Ti) interface.

schematic representation of the composite design. These experiments have been initiated with several goals in mind: First is to determine the feasibility of creating intermetallic-ceramic composites with differing ceramic volume fraction. The second goal is to determine which ceramic dispersoid is most effective in strengthening the TiAl matrix. The third goal of this study is to assess the microstructural features of the powder-sheet interface and then to find ways to optimize them.

Figure 8 shows a typical interface that develops between SHS-processed powder and sheet. In almost all instances, good bonding occurs between the TiAl powder mixture (both Ti and Al powders < 325 mesh) and the Ti sheet. Some porosity forms, but it is felt that this is more a result of the SHS reaction in the powder, than the SHS interaction between powder and sheet, and can probably be eliminated with the appropriate processing steps. When the material is given a significant post-SHS heat treatment, the interface shows evidence of interdiffusion and directional phase growth (Fig. 9).

#### UTILIZATION OF TECHNOLOGY--APPLICATIONS

The SHS joining process has many exciting potential applications, a few of which are listed below:

- (1) Inexpensive means of producing engineered outer surfaces of varying thicknesses, with designable mechanical, physical, or chemical properties, on low-cost base metals.
- (2) Efficient way of applying thin, well-bonded, multi-phase, i.e., metallic, intermetallic, or ceramic, layers to the surface of a homogeneous material.
- (3) Process technique which can produce bulk, non-isotropic properties in materials.
- (4) Technique for developing functionally-gradient interfaces between dissimilar materials.
- (5) Means of joining similar or dissimilar materials.
- (6) Low cost method of providing a variety of engineered, protective surfaces (e.g., corrosion or oxidation resistant) to a single substrate.

#### POTENTIAL AVENUES OF RESEARCH

Several innovative research possibilities may make use of SHS process technology, and warrant further investigation. For example, vacuum rolling technology might be used to densify layered structures following SHS (thermal explosion) reactions. Laminated structures, i.e., foils/sheets or foils/sheets plus powders (with or without cladding), can be heated in a vacuum furnace until thermal explosion is initiated. The layered composite can then be quickly transferred to rolls for bonding/densification. Ideally, cladding will not be necessary and a relatively good vacuum ( $10^{-3}$  to  $10^{-4}$  Pa) will prevent gas entrapment during densification. This technique has potential to internally-bond complex layered structures such as lightweight structural components made of, for example, honeycomb material sandwiched between continuous metal sheets.

A second avenue of research might be into the feasibility of using SHS to join metals to ceramics. In this technique, the design of the metal-ceramic interface will be critical in order to avoid the creation of large thermal expansion mismatch stresses. A continuous compositional gradient from metal to ceramic would seemingly offer the greatest potential for success. SHS might also provide a means of joining metals to "conductive" ceramics for electrical applications at elevated temperatures.

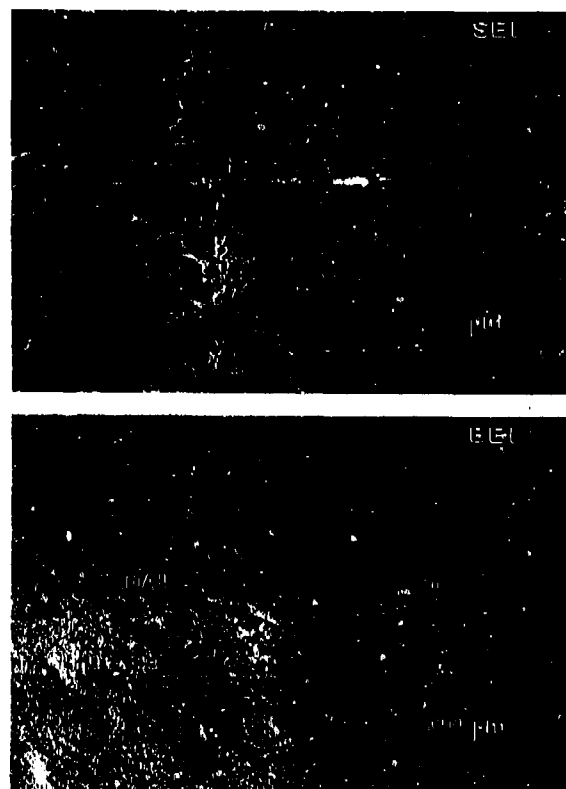


Fig. 9. SEM of powder interface region showing directional solidification and growth from the grain boundary due to post-SHS heat treatment.

Still another potential use for SHS processing is in the incorporation of continuous fibers, both metal and ceramic, into layered structures. Similarly, two- or three-dimensional woven fabrics might also be used to form composites through SHS. A key goal in such a study will be to obtain fully-dense composites without significant fiber degradation.

#### SUMMARY

Research at the Bureau of Mines has concentrated on using SHS technology to make many different types of layered and dispersed phase composites. In the course of the research, techniques have been developed which allow the SHS technique to be applied to joining and coating of materials. The Bureau will continue to explore potential research avenues as described above, in an effort to develop low-cost process and joining technology.



## REFERENCES

1. Z. A. Munir, Ceram. Bull. **67**, 342 (1988).
2. J. Subrahmanyam and M. Vijayakumar, J. Mater. Sci. **27**, 6249 (1992).
3. J. C. Rawers, W. R. Wrzesinski, E. K. Roub and R. R. Brown, Mater. Sci. Technol. **6**, 187 (1990).
4. J. C. Rawers and W. R. Wrzesinski, Scripta Metall. Mater. **24**, 1985 (1990).
5. J. C. Rawers and W. R. Wrzesinski, J. Mater. Sci. **24**, 2877 (1992).
6. A. G. Merzhanov, Fizik. Khim. Soverem. Problem, **6** (1983).
7. Y. S. Naiberdenko and V. I. Itin, Combust. Explos. Shock Waves USSR **11**, 293 (1975).
8. A. R. Serkisyan, S. K. Dolukhanyan, I. P. Borovinskaya and A. G. Merzhanov, Combust. Explos. Shock Waves USSR **14**, 310 (1978).
9. A. S. Rogachev, A. S. Mukasyan and A. G. Merzhanov, Dokl. Phys. Chem. **297**, 1240 (1987).
10. W. R. Wrzesinski and J. C. Rawers, J. Mater. Sci. Lett. **9**, 432 (1990).
11. H. E. Maupin and J. C. Rawers, J. Mater. Sci. Lett. **12**, 165 (1993).
12. H. E. Maupin, J. C. Rawers and J. A. Hawk, in International Conference on Advanced Synthesis of Engineered Structural Materials (ASM, Materials Park, OH, 1993), p. 9.
13. U. Anselmi-Tamburini and Z. A. Munir, J. Appl. Phys. **66**, 5039 (1989).
14. U. Anselmi-Tamburini and Z. A. Munir, in Combustion and Plasma Synthesis of High-Temperature Materials (VCH Publishers, New York, 1990) p. 100.
15. J. K. Wright, R. N. Wright and G. A. Moore, Scripta Metall. Mater. **28**, 501 (1993).
16. B. H. Rabin, J. Am. Ceram. Soc. **75**, 131 (1992).

---

## PART V

---

### **Advanced and Novel Joining Techniques II: Other Approaches**

## REACTION PROCESSING AND PROPERTIES OF SiC-TO-SiC JOINTS

B. H. RABIN AND G. A. MOORE

Idaho National Engineering Laboratory, P.O. Box 1625, Idaho Falls, ID 83415-2218

### ABSTRACT

Reaction processing methods have been developed for fabricating SiC-to-SiC joints that can be used in elevated temperature applications. Processing steps include tape casting thin sheet SiC+C interlayer precursors, clamping the tape between the ceramic parts, providing a source of Si adjacent to the joint, and heating above the melting point of Si in argon. Molten Si infiltrates the tape via capillary action forming a reaction bonded silicon carbide (RBSC) interlayer and simultaneously joining the ceramic parts. Four-point bending strength and fracture toughness of joined pressureless sintered  $\alpha$ -SiC test specimens have been evaluated at room and elevated temperatures. At low temperatures the joint mechanical properties were comparable to those reported for bulk SiC, while at elevated temperatures the joint properties were characteristic of the RBSC interlayer.

### INTRODUCTION

SiC ceramics and SiC-matrix composites have considerable potential as elevated temperature structural materials in fossil energy applications. It is widely recognized that joining methods are needed for these materials to allow the fabrication of large or complex shaped parts, and the integration of structural components into existing systems. Although considerable efforts have been devoted to understanding the processing, microstructures and properties of SiC-based materials, joining remains largely an unresolved issue. Ideally, joined components should exhibit mechanical properties and environmental resistance comparable to the base material, and the joining methods should be practical, reliable, and cost effective.

Reported techniques for joining SiC including direct diffusion bonding [1,2]; co-densification of interlayer and green bodies [3]; diffusion welding or brazing with boride, carbide and silicide interlayers [1]; hot pressing of sinterable SiC powder [4]; bonding with polymeric precursors [5]; brazing with oxide [6] or oxynitride materials [7]; solid state reactive metal bonding [8]; active [9] or traditional [10] metal brazing; and pressurized combustion reactions [11]. Unfortunately, none of these methods completely satisfy the criteria mentioned above. Direct diffusion bonding and hot pressing with ceramic powder or reactive metal interlayers can yield suitable properties; however, the need for high processing temperatures (e.g.  $>1650^\circ\text{C}$ ) and/or high pressure equipment makes them somewhat impractical. Polymeric precursor or vitreous interlayers provide inadequate material properties. Metallic brazing has received considerable recent attention since processing is attractive and high joint strengths can be achieved. Unfortunately, such joints are limited to low service temperatures by the metal constituent, thus eliminating one of the key advantages of utilizing ceramic materials.

The formation of joints by reaction processing is attractive since the thermoelastic properties of the interlayer are very close to those of SiC and excellent mechanical properties can be achieved. Furthermore, as with brazing, external pressure is not required, thus making the process inexpensive and practical compared to other joining methods. Reaction bonded interlayers have previously been used to join bulk RBSC [12]. More recently, investigations demonstrated the success of this approach for joining dense SiC and SiC/SiC composites [13-15]. This paper briefly describes the reaction processing method as applied to the joining of a commercial pressureless sintered  $\alpha$ -SiC. A typical joint microstructure is shown, and the results of mechanical property assessments are presented.

### EXPERIMENTAL

Joining experiments were carried out using a commercial pressureless sintered  $\alpha$ -SiC (Hexalloy SA, The Carborundum Company, Niagara Falls, NY) in the form of rectangular bars  $12 \times 12 \times 25$  mm. Prior to joining, the specimen surfaces were prepared by hand lapping with  $6 \mu\text{m}$  diamond, followed by ultrasonic cleaning in acetone and rinsing in alcohol.

Precursor interlayer materials were prepared by tape casting mixtures of SiC and graphite powders. The materials and amounts used in the tape casting formulation are listed in Table 1. The ratio of SiC:C was 2:1. A polysorbate surfactant was found to be effective for

stabilizing the slurry, allowing a stable homogeneous mixture of SiC+C to be produced using a relatively simple ultrasonic dispersion treatment rather than extensive ball milling as is common in slurry preparation. De-airing was carried out by continuous stirring under a partial vacuum to avoid the formation of dried agglomerates, prevent migration and segregation of the C, and achieve the desired slurry viscosity prior to tape casting. To increase the powder packing within the as-cast tapes, a mixture of two different SiC particle sizes was used.

Tape casting using an adjustable doctor blade allowed green sheets to be produced with thicknesses typically in the range of 0.05 to 0.20 mm. Pieces of tape were then cut to the desired size and shape, placed between two pieces of SiC, and held firmly in place using a simple threaded graphite jig. A small lump of silicon was placed near the joint, the assembly was heated at  $\sim 20^\circ\text{C min}^{-1}$  under flowing argon to  $\sim 1450^\circ\text{C}$ , and the temperature was held for 30 min to allow infiltration and reaction bonding to occur. The completely assembled joining jig just prior to furnace heating is shown in Figure 1.

Table I. Tape Casting Formulation

material	type/vendor	amount, wt%
SiC	-325 mesh, 99%, Cerac Inc., Milwaukee, WI	14.3
SiC	3.0 $\mu\text{m}$ , Grade A1, Hermann C. Starck, Goslar, Germany	14.3
graphite	1.0 $\mu\text{m}$ , type 7X99, Cummings-Moore, Inc., Detroit, MI	11.9
solvent	ethanol, Quantum Chemical Corp., Tuscola, IL	36.8
solvent	toluene, Fisher Scientific, Fair Lawn, NJ	17.1
binder	Ethocel "Standard", Dow Chemical Co., Midland, MI	2.6
plasticizer	glycerin, Fisher Scientific, Fair Lawn, NJ	0.2
surfactant	Tween 40, ICI Americas, Inc., Wilmington, DE	2.8

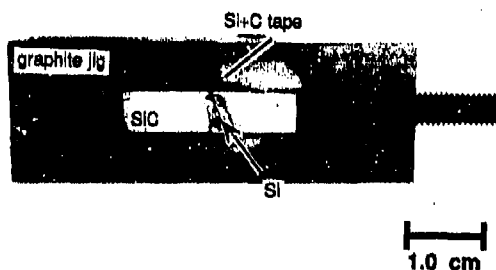


Figure 1. Macrophotograph showing the experimental arrangement used to produce SiC-to-SiC joints by reaction processing.

After joining, specimens were sectioned and polished for microscopic examination. Standard bend bars having dimensions of 3 x 4 x 50 mm were prepared by surface grinding. The edges were beveled, and the surfaces were polished to a 12  $\mu\text{m}$  finish. Strength and fracture toughness were measured in four-point bending with spans of 20 and 40 mm using a crosshead speed of 0.13 mm  $\text{min}^{-1}$ . Fracture toughness was determined using the single-edge notched beam (SENB) method in which a 0.16 mm wide x 1.0 mm deep notch was cut as close as possible to the center of the joint using a high speed saw. The notch tip radius was estimated to be  $\sim 75 \mu\text{m}$  by microscopic examination. Fracture toughness,  $K_{Ic}$ , was calculated according to the formula

$$K_{Ic} = \sigma \pi a^{1/2} Y(a/h) \quad (1)$$

where  $\sigma$  is the maximum stress,  $a$  is the notch depth,  $h$  is the specimen height, and  $Y(a/h)$  is a known geometry function [16]. Elevated temperature tests were performed in air. Specimens were heated to the desired temperature at a rate of  $\sim 20^\circ\text{C min}^{-1}$ , and held for 10 min prior to testing. A minimum of 8 specimens were tested for each condition, and the average values and standard deviations were determined.

## RESULTS AND DISCUSSION

Bulk commercial RBSC is produced by capillary infiltration of molten silicon into compacts containing SiC and C. The processing, microstructures, and properties of these materials have been studied extensively [17-23]. Typical commercial RBSC ceramics are near full density composites consisting of 85 to 90 vol% of SiC and 5 to 15 vol% of free Si. The joint interlayers fabricated in this work exhibited similar microstructures, as shown in Figure 2. The joint interlayer thickness was approximately the same as the thickness of the original tape, about 150  $\mu\text{m}$  in the case of Figure 2a. Complete infiltration of the interlayer usually occurred, and in most cases the interlayer material exhibited fewer and smaller defects than what was typically observed in the SiC. Occasionally, large porosity defects were observed in the joints; these were believed to originate from defects within the as-cast tapes. Figure 2b shows a higher magnification view of the interface between the interlayer material and the SiC. Note the continuous SiC grain structure that has apparently formed across much of the interface.



(a)



(b)

Figure 2. Typical microstructure of a SiC-to-SiC joint bonded with a RBSC interlayer fabricated by Si infiltration of SiC+C tape cast precursors. Optical micrograph in (a) and higher magnification view of the SiC/RBSC interface in (b).

Tape casting offers several advantages for fabricating joining precursor materials from powder mixtures. This approach allows the production of high quality, uniform and controlled thickness tapes, thus providing a simple means for adjusting joint interlayer thickness. Once formed, the tapes can be stored indefinitely and are easy to handle. Furthermore, because the

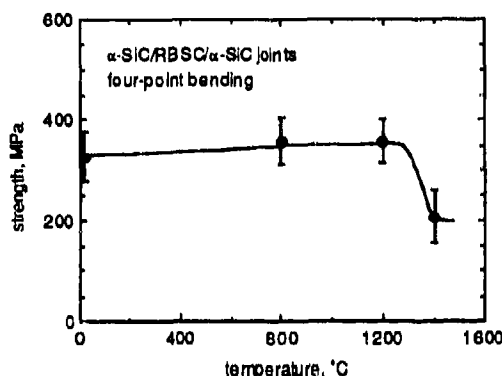


Figure 3. Four-point bending strength of SiC-to-SiC joints bonded with RBSC as a function of test temperature.

tapes are flexible, they can be cut into various shapes and molded to allow the joining of curved surfaces and complex-shaped parts.

The results of four-point bend strength testing are shown in Figure 3. The average room temperature strength was 327 MPa, comparable to the strength reported in the literature for bulk pressureless sintered  $\alpha$ -SiC [24-28]. The strength increased very slightly with increasing test temperature up to 1200°C. At 1400°C the strength decreased significantly to an average of 208 MPa. The reduction in joint strength at this temperature is characteristic of RBSC wherein the Si phase softens appreciably as it approaches its melting point (i.e. 1412°C) [19-21]. Above the melting point of Si the RBSC materials still retain some strength as a result of the continuous network of SiC grains within the microstructure.

The failure probabilities were calculated for sets of specimens tested at room temperature and 1200°C; the resulting Weibull distribution plots are shown in Figure 4. The Weibull modulus,  $m$ , was calculated for each data set giving  $m=5$  and  $m=7$  for room temperature and 1200°C tests, respectively. An increase in Weibull modulus with testing temperature has previously been observed for SiC, although the values obtained for the joined specimens were slightly lower than the values reported in the literature for bulk pressureless sintered  $\alpha$ -SiC [28]. In almost all cases, fracture occurred either within the joint interlayer or within the  $\alpha$ -SiC adjacent to the joint; few interface failures were ever observed.

The results of fracture toughness measurements using SENB specimens tested in four-point bending are summarized in Figure 5. In all cases the load-deflection curves were linear up to the point of failure. At room temperature  $K_{I0}$  was calculated to be 2.8 MPa·m<sup>1/2</sup>. This value is similar to the toughness values reported in the literature for bulk SiC [26,29-31]. The joint toughness remained constant at 600°C, but increased significantly at higher testing temperatures. The effective  $K_{I0}$  values calculated for the 1200 and 1400°C tests were ~7 MPa·m<sup>1/2</sup>. This behavior can be explained based on the presence of free Si in the joints. The compressive flow stress of Si is known to decrease markedly above ~800°C, allowing for increased plasticity and crack-tip blunting at higher testing temperatures [32]. Such an effect has previously been observed in studies on the elevated temperature fracture behavior of bulk Si/SiC materials [19,20]. Evidence of plasticity can be readily observed on the fracture surface, as illustrated in Figure 6, which compares the fracture morphology observed at room temperature with that typically seen at 1200°C. As in the strength tests, most failures were observed to take place by crack propagation within the joint interlayer. In some specimens, the notch was not centered exactly on the joint region and occasional failures within the base

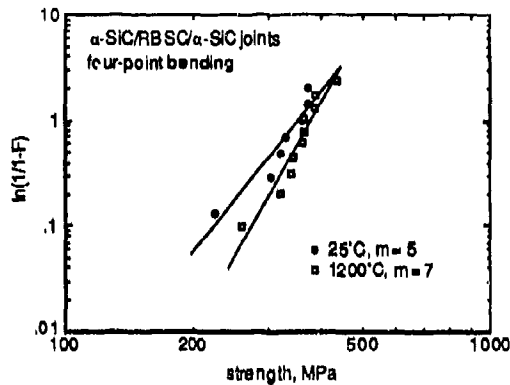


Figure 4. Weibull plots showing the strength distributions for the sets of specimens tested at room temperature and at 1200°C.

ceramic occurred. It was also observed in most cases when cracks initiated at the SiC/RBSC interface they were diverted away from the interface and into either the interlayer or base ceramic. In a few specimens, crack initiation occurred either in the interlayer or base ceramic and traversed the interface, entering the other material. These observations all indicate the formation of a very strong interface during joining. Under such circumstances, the failure mode was determined solely by the local toughness values of the interlayer and SiC materials, as determined by the flaw distribution within the region of the joint.

In both strength and fracture toughness tests, failures were occasionally observed to occur entirely within the base ceramic adjacent to the joint. Nevertheless, the overall results indicate that the strength and toughness of joined specimens are controlled primarily by the properties of the RBSC interlayer, particularly at elevated temperatures. The potential therefore exists to improve the elevated temperature joint properties by altering the RBSC

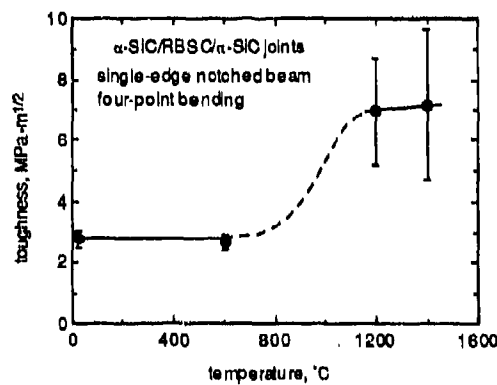
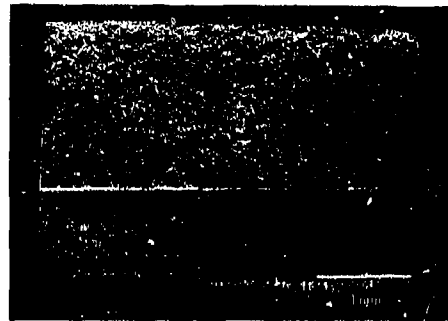


Figure 5. SENB fracture toughness for SiC-to-SiC joints bonded with RBSC as a function of test temperature.

microstructure. For example, it has been shown that by infiltrating with alloyed Si-Mo melts, it is possible to produce reaction bonded SiC-MoSi<sub>2</sub> composites, containing little or no free Si, that exhibit superior elevated temperature capabilities [33,34]. Such an approach has been used to produce SiC-MoSi<sub>2</sub> joint interlayers, although property measurements have not yet been carried out [15].



(a)



(b)

Figure 6. Scanning electron micrographs showing the morphology of joint fracture surfaces for specimens tested at (a) room temperature, and (b) 1200°C.

In order to further illustrate the utility of this joining method, several additional experiments have been carried out. For example, it has been successfully demonstrated that the method can be applied to join SiC (Nicalon®) fiber-reinforced SiC matrix composites produced by a chemical vapor infiltration (CVI) [13,15]. Joint microstructures were essentially identical to that shown in Figure 2, however, since the CVI composites typically contained about 15 vol% porosity, infiltration of free Si into the pores of the composite occurred within the joint region. Other than requiring the use of a larger than usual lump of Si to ensure complete filling of the joint, the presence of Si in the composite is believed not to be detrimental.

Another series of experiments were intended to illustrate that joining can be accomplished using localized external heating rather than furnace heating. This is important for the ability to join very large components and for providing a means to conduct joining or repair work in the field. Although several methods are available for localized external heating (e.g. microwave, laser, etc.), the initial experiments were conducted using RF induction heating. The assembled graphite jig (Figure 1) was placed inside an induction coil such that only the joint was heated to the maximum (joining) temperature. The joint microstructure was again similar to that shown in Figure 2. Using this heating method it would be possible to join, for example, long SiC heat exchanger tubes. The only requirement is that intimate contact be maintained between the joining surfaces. Although a graphite jig was used in this case, it would be possible to use a simple mechanical clamping device, since only the joint region is heated.



## SUMMARY

Reaction processing methods have been developed and applied to the fabrication of SiC-to-SiC joints for potential use at elevated temperatures. The microstructure and properties of joined ceramics have been characterized using a commercial sintered  $\alpha$ -SiC as a model system. The strength and fracture toughness of joined specimens were found to be controlled primarily by the properties of the RBSC interlayer, and were comparable to or higher than those reported for bulk SiC for testing temperatures approaching 1400°C. The joining technique was shown to be applicable to other SiC-based ceramics and provides a practical means for joining large or complex-shaped parts.

## ACKNOWLEDGMENTS

This work was supported by the U. S. Department of Energy, Assistant Secretary for Fossil energy, under DOE Idaho Field Office Contract DE-AC07-76ID01570. The authors are grateful for the assistance provided by V. L. Smith-Wackerle.

## REFERENCES

1. T. J. Moore, J. Amer. Ceram. Soc. **68** (6), C151 (1985).
2. D. DeLeeuw, J. Amer. Ceram. Soc. **75** (3), 725 (1992).
3. C. H. Bates, et al., Amer. Ceram. Soc. Bull. **69** (3), 350 (1990).
4. T. Iseki, K. Arakawa and H. Suzuki, J. Mater. Sci. Letters **15** 1049 (1980).
5. S. Yajima, et al., Amer. Ceram. Soc. Bull. **60** (2), 253 (1981).
6. A. P. Gehris Jr., M.S., New Mexico Institute of Mining and Technology, 1989.
7. N. Tamari, et al., Yogyo-Kyokai-Shi **94** (10), 1087 (1986).
8. S. Morozumi, et al., 20 3976 (1985).
9. J. K. Boadi, T. Yano and T. Iseki, J. Mater. Sci. **22** 2431 (1987).
10. J. R. McDermid and R. A. L. Drew, J. Amer. Ceram. Soc. **74** (8), 1855 (1991).
11. B. H. Rabin, J. Amer. Ceram. Soc. **75** (1), 131 (1992).
12. T. Iseki, M. Imal and H. Suzuki, Yogyo-Kyokai-Shi **91** (6), 239 (1983).
13. B. H. Rabin, Mater. Sci. Eng. **A130** L1 (1990).
14. B. H. Rabin and G. A. Moore, ORNL/FMP-92/i (Oak Ridge National Laboratory), 1992.
15. B. H. Rabin and G. A. Moore, J. Mater. Synthesis and Proc. **1** (4), in press (1993).
16. J. E. Srawley and B. Gross, in ASTM STP601, edited by J. L. Swedlow and M. L. Williams (ASTM, Philadelphia, 1976), p. 559.
17. P. Popper, in Special Ceramics, edited by (Heywood & Company, London, 1960), p. 209.
18. C. W. Forrest, P. Kennedy and J. V. Shennan, in Special Ceramics 5, edited by P. Popper (British Ceramic Research Association, Stoke-on-Trent, 1972), p. 99.
19. W. B. Hillig, et al., Amer. Ceram. Soc. Bull. **54** (12), 1054 (1975).
20. J. R. McLaren, G. Tappin and R. W. Davidge, Proc. British Ceramic Soc. **20** 259 (1972).
21. G. C. Trantina and R. L. Mehan, J. Amer. Ceram. Soc. **60** (3-4), 177 (1977).
22. G. R. Sawyer and T. F. Page, J. Mater. Sci. **13** 885 (1978).
23. J. N. Ness and T. F. Page, J. Mater. Sci. **21** (4), 1377 (1986).
24. S. Dutta, J. Mater. Sci. **19** 1307 (1984).
25. R. K. Govila, J. Mater. Sci. **19** 2111 (1984).
26. A. K. Ghosh, et al., J. Amer. Ceram. Soc. **72** (2), 242 (1989).
27. S. G. Seshadri, M. Srinivasan and K. Y. Chia, in Ceramic Transactions, Vol. 2: Silicon Carbide '87, edited by J. D. Cawley and C. E. Semler (The American Ceramic Society, Westerville, OH, 1989), p. 215.
28. A. Charif and F. Osterstock, Mater. Sci. Eng. **B11** 299 (1992).
29. A. G. Evans and F. F. Lange, J. Mater. Sci. **10** 1659 (1975).
30. K. D. McHenry and R. E. Tressler, J. Amer. Ceram. Soc. **63** (3-4), 152 (1980).
31. I. Merkel and U. Messerschmidt, Mater. Sci. Eng. **A151** 131 (1992).
32. M. Brede, Acta Metall. Mater. **41** (1), 211 (1993).
33. R. P. Messner and Y.-M. Chang, J. Amer. Ceram. Soc. **73** (5), 1193 (1990).
34. Y.-M. Chang, R. P. Messner and C. D. Terwilliger, Mater. Sci. Eng. **A144** 63 (1991).

## JOINING OF METAL FILMS TO CARBON-CARBON COMPOSITE MATERIAL BY METAL PLASMA IMMERSION ION IMPLANTATION

ANDRÉ ANDERS<sup>1</sup>\*, SIMONE ANDERS<sup>1</sup>\*, IAN G. BROWN<sup>1</sup>, AND PETER CHOW<sup>2</sup>

<sup>1</sup>Lawrence Berkeley Laboratory, University of California, Berkeley, CA 94720

<sup>2</sup>Superior Vacuum Technology, Eden Prairie, MN 55344.

\*On leave from Max-Planck-Institut für Plasmaphysik, Bereich Berlin, Mohrenstr. 40/41,  
10117 Berlin, Germany

### ABSTRACT

Adhesion of metal films to carbon-carbon composite materials is a problem when using conventional techniques such as sputter deposition. Metal plasma immersion ion implantation is a novel technique which in combination with metal plasma deposition can produce metal-to-composite bonding with very good adhesion characteristics. The substrate is immersed in a metal plasma which is produced by a pulsed vacuum arc. When the substrate is biased to high negative voltage the metal ions are accelerated toward and implanted into the substrate. A repetitively pulsed bias ( $\mu$ s pulses) is used to avoid arcing and other deleterious effects. Between high voltage pulses, metal plasma is deposited onto the surface with an energy typical of vacuum arcs, about 50-100 eV. The underlying idea of this mixed implantation-deposition technique is the formation of an extended substrate-film intermixed layer. We have demonstrated the technique for nickel films on carbon-carbon composite materials.

### INTRODUCTION

Carbon-carbon materials are composites which can be made in a variety of forms such as sheets, tows, tapes or woven cloth. Because of their diversity they can be easily tailored to meet the requirements of specific applications. Carbon-carbon composites are used for structural application since they exhibit high strength and high thermal and chemical stability in an inert environment, and they maintain their strength at high temperatures up to 3000 K [1]. Application of carbon-carbon materials has been restricted by the low oxidation resistance at high temperatures in an oxidizing environment. The protection of these materials from oxidation or penetration by moisture has been a major problem because the formation of reliable protective coatings which can resist the high temperatures is difficult. Different techniques including sputtering, chemical vapor deposition, painting or spraying have been used to apply protective coatings which usually consist of several layers since the primary oxidation protection film (e.g. SiC) develops cracks due to the mismatch in thermal expansion between substrate and film [2]. For example, SiC is used as an oxidation barrier with silicon or boron doped glass sealants on top to fill the cracks caused by the mechanical mismatch of the SiC film and the carbon-carbon substrate. Another structure consisting of pyrolytic carbon for mechanical compatibility, SiC for carbon diffusion protection and  $\Delta_2\text{O}_3$  as an oxidation barrier, has been tested as a protective coating for carbon-carbon [3].

The application of carbon-carbon materials for aircraft requires furthermore a high electrical conductivity to reduce damage caused by lightning impact. Metallic overcoats are one possible solution, but the standard coating techniques such as sputtering are plagued by the problem of poor film adhesion. Metallic coatings could also prevent the carbon-carbon material from oxidation and moisture if the films were continuous and sufficiently thick.

In the present paper we describe a technique of combined plasma immersion implantation and deposition, using vacuum arc plasma sources, to form metal films with superior adhesion to carbon-carbon composite materials. This method has been applied successfully to form films with good adhesion to various substrates, such as metal on metal and ceramics on metal [4]. Here we describe our first results for metal bonding to carbon-carbon substrates.

## EXPERIMENTAL

The carbon-carbon composite material used as a substrate in this investigation was made from carbon fibers impregnated in an epoxy resin matrix to form a two-dimensional mat. The material had a mass density of  $1.8 \text{ g/cm}^3$ . The samples were cleaned prior to deposition by ethanol.

The metal plasma for the deposition was produced by small plasma sources based on vacuum arc discharges [5]. The plasma formed at the cathode of a vacuum arc discharge expanded through the hollow anode and was focused by an axial magnetic field around the electrode arrangement [6].

The deposition was carried out in two phases. The aim of the first phase was to produce a well intermixed layer between the carbon-carbon substrate and the metal film, so providing very good adhesion of the film to the substrate. For this purpose, one of the plasma sources was combined with a magnetic filter to prevent contamination of the first part of the film by macroparticles (droplets of micrometer size which are produced at the cathode along with the plasma). The substrate was exposed to the metal plasma and pulse biased to a negative voltage of  $-2 \text{ kV}$  to accelerate the ions to the substrate and implant them with an energy that is given by the accelerating voltage and the ion charge state. For vacuum arc plasmas, the mean ion charge state is between 1 and 3 depending on the cathode material. We have chosen Ni for our first tests which has a mean ion charge state of 1.8 [7]. A film of about several hundred angstroms was produced that showed a broad intermixing between the Ni film and the carbon-carbon substrate.

In the second phase, a  $1 \mu\text{m}$  thick metal film was deposited on top of that intermixed layer using a second plasma source, without magnetic filter to obtain a high deposition rate. In this phase the substrate was not biased and the ions were deposited upon the substrate with an energy of about  $50 \text{ eV}$ , which is typical for vacuum arc plasmas [8]. A schematic of the arrangement is shown in Fig. 1.

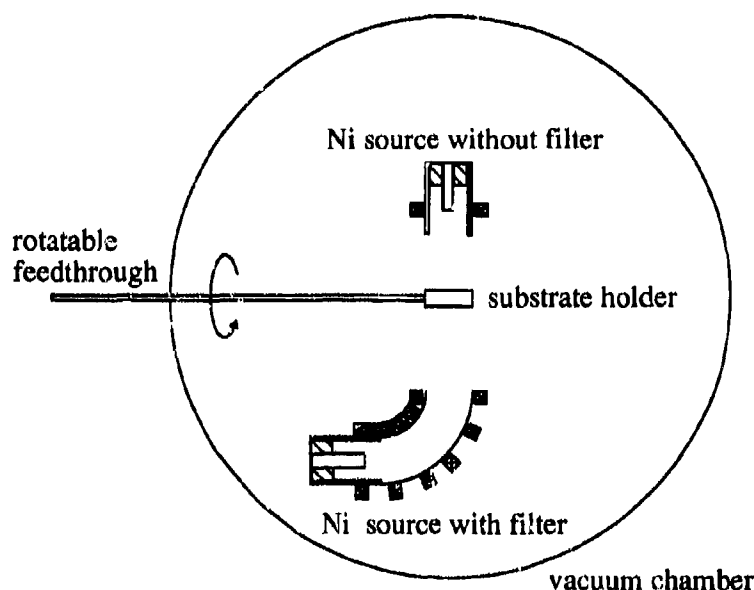


Fig. 1: Schematic of the implantation/deposition arrangement.

## RESULTS

The films were investigated by Auger Electron Spectroscopy (AES), and the broad intermixing between the substrate and the film of thickness several hundred angstroms was confirmed. Fig. 2 shows the AES spectrum of a film after the first phase of the process (metal plasma immersion ion implantation).

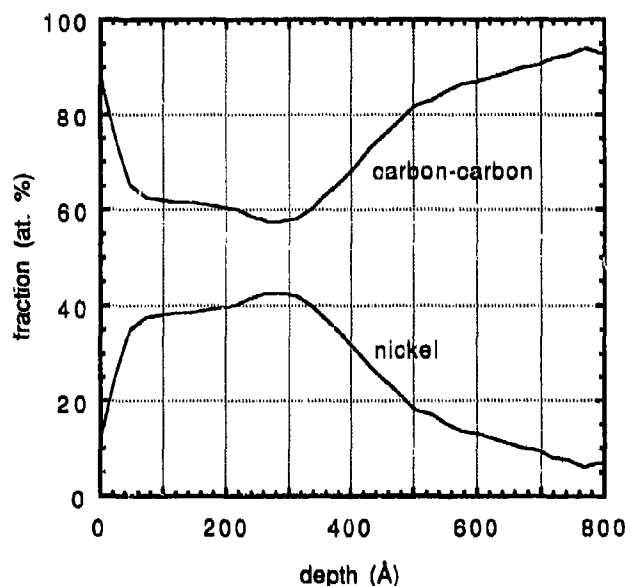


Fig. 2: AES spectrum of a Ni film intermixed into the carbon-carbon substrate after the first phase of the deposition process (metal plasma immersion ion implantation).

The adhesion was first qualitatively tested by the usual tape test using "Scotch Magic Tape No. 810". It was found to be very good; the film could not be removed. In a pull test it was found that the adhesion exceeded 9800 psi ( $6.8 \times 10^7$  N/m<sup>2</sup>). The pull test was done in a Sebastian Pull Tester where the sample is mounted on a test platter and a stud is bonded to the coating surface at one end. The other end of the stud is then inserted into the tester. The test measures the strength required to lift the coating off the substrate. Further tests were performed to analyze the moisture protection of the carbon-carbon material by the Ni films. For this purpose the samples were placed in an environmental chamber where the temperature was varied between room temperature and 100 °C and the humidity between 50 and 100 %, respectively. No peeling of the coating or cracks in the coating were observed.

The high ion energy elevates the temperature of the sample during deposition. This leads to outgassing of the substrate. When depositing on *all* sides of a carbon-carbon material, blistering of the film can occur. Interestingly, the film did not simply peel off from the substrate in this case but the substrate structure itself was destroyed. Possible ways to solve this problem are preheating of the substrate in vacuum prior to deposition or strong cooling of the sample during deposition, or both.

## CONCLUSIONS

Plasma immersion implantation is a novel technique for coating and bonding of carbon-carbon composite materials, providing films with excellent adhesion to the substrate by forming a broad intermixed layer between the carbon-carbon substrate and the film. Any solid metal can be implanted and deposited by the vacuum arc deposition technique described, and chemical compounds such as nitrides or oxides can also be formed by adding gas to the deposition process [4]. Structures of several layers can be formed also by grouping several plasma sources with different cathode materials [9]. By varying the biasing of the substrate the intermixed layers can be tailored over a broad range of parameters. The superior adhesion of the films and the great variety of possible coatings makes this method a promising tool for protection of carbon-carbon against oxidation and moisture penetration as well as for the formation of conductive or base films on carbon-carbon composite material for further coatings.

## ACKNOWLEDGMENTS

Two of the authors (S. A. and A. A.) acknowledge the support by the Deutsche Forschungsgemeinschaft. This work was supported by the Electric Power Research Institute under RP2426-27 and the U.S. Department of Energy, Advanced Energy Projects, under contract No. DE-AC03-76SF00098.

## REFERENCES

- [1] J. D. Buckley, *Ceramic Bulletin* **67**, 364 (1988).
- [2] H. Dietrich, *Materials Engineering*, August 1991, 34.
- [3] D. P. Stinton, T. M. Beshmann and R. A. Lowden, *Ceramic Bulletin* **67**, 350 (1988).
- [4] I. G. Brown, A. Anders, S. Anders, M. R. Dickinson, I. C. Ivanov, R. A. MacGill, X. Y. Yao and K. M. Yu, *Nucl. Instr. and Meth. B*, in press (1993).
- [5] X. Godechot, M. B. Salmeron, D. F. Ogletree, J. E. Galvin, R. A. MacGill, M. R. Dickinson, K. M. Yu and I. G. Brown, *Mat. Res. Soc. Symp. Proc.* **190**, 95 (1991).
- [6] S. Anders, A. Anders, K. M. Yu, X. Y. Yao and I. G. Brown, *Proc. XVth Int. Symp. Discharges and Electr. Insul. in Vacuum*, Darmstadt 1992 (VDE-Verlag GmbH, Berlin, 1992), pp. 416-420.
- [7] I. G. Brown and X. Godechot, *IEEE Trans. Plasma Sci.* **19**, 713 (1991).
- [8] J. Kutzner and H. C. Miller, *IEEE Trans. Plasma Sci.* **17**, 688 (1989).
- [9] S. Anders, A. Anders, J. B. Kortright, K. M. Yu, I. G. Brown and I. C. Ivanov, *Proc. Int. Conf. Metal. Coat. Thin Films*, San Diego, April 19-23 1993, also to be published in *Surf. Coat. Technol.*

## DIRECT BONDING METHOD OF ALUMINUM TO STAINLESS STEEL BY PRESSURE CASTING OF ALUMINUM

KATSUAKI SUGANUMA

National Defense Academy, Department of Materials Science and Engineering,  
Hashirimizu 1-10-20, Yokosuka 239, Japan.

### ABSTRACT

A new process for joining Al to stainless steel has been established by using pressure casting of Al in air. Blocks of AISI type 304 austenitic stainless steel to be joined were placed in a mold and were preheated at 450 °C - 600 °C in air. Molten Al was poured into the mold and a pressure of 50 MPa was applied immediately. Stainless steel was tightly bonded to Al by the present process. At the optimum preheating condition, the interface strength was higher than that of Al and fracture did not occur at the interface. At the interface, an intermetallic compound layer was formed, and it was analyzed by TEM. Because this process can be carried out in air by casting of Al, the process has a potential for the mass-production of Al/stainless steel joints or clads.

### INTRODUCTION

Al alloys have been expanding their uses in industrial fields primarily because of their light weight character. In many applications, Al alloys are combined with other materials and then joining technology becomes one of the major concerns. Joining Al alloys to dissimilar materials primarily has two difficulties. One is the presence of a stable oxide film on Al alloys. The Al oxide film prevents obtaining good wetting between Al alloys and brazing fillers or materials to be joined. A certain activation treatment of the Al alloy surface is required before joining. The other problem is high reactivity of Al alloys. Once the stable oxide is removed from the interface, Al alloys severely react with most metallic materials at elevated temperature and form brittle intermetallic compounds at interfaces.

As the mating metals with Al alloys, low alloy steels and stainless steels are two of the most important materials because they have been used for most structural components in commercial fields. Joining Al alloys to steels/stainless steels is not so easy because of the same reason mentioned above. By brazing or by solid-state bonding, the formation of a thick intermetallic compound layer prevents getting a sound joint. Friction welding and explosive welding are two of the successful methods but they have critical limitations such as limited dimension or as specific joining skill. Then the present work shows the new joining technique to bond Al and stainless steels by a simple method. The method utilizes squeeze casting of Al alloys, a method that is widely used as the mass-production of metallic components in industries. In the present method, liquid Al is cast and joined with mating materials.

### EXPERIMENTAL PROCEDURE

#### Materials

The stainless steel used was a commercial AISI type 304 austenitic stainless steel (Fe-18wt%Cr-8wt%Ni). Hereafter, this alloy is simply called 304 steel. The rod of 20 mm diameter x 15 mm high was prepared and one end became the face to be bonded. This face was finished with 400 mesh abrasive paper. The rod was washed ultrasoni-

cally in acetone and then the surface not to be bonded was coated with BN powder. The Al used was commercial JIS1050 (99.5 wt% pure). Blocks of 304 steel and  $\text{Si}_3\text{N}_4$  of 15 mm x 20 mm x 20 mm were also used for joining trials.

### Cast bonding

The set-up for the cast bonding is schematically illustrated in Fig.1. The 304 steel rod and the mold were preheated at 450 °C - 600 °C. Two types of joining constructions were examined, which are shown in the figure as Type A and Type B. The 304 steel rod was put in the mold and, immediately, Al melt was poured into the mold. Then a pressure of 50 MPa was applied. The whole process was carried out in air. By the present method, the surface stable oxide of Al liquid is broken under pressure and, furthermore, the reaction between Al and the steel finishes within a very short period because Al liquid solidifies within one minute under pressure. Thus, if the casting condition is appropriately selected, good interface bonding can be achieved even in oxidizing atmosphere. Because the squeeze cast process itself is widely applicable for the mass-production of structural components, the present joining method can be an economic joining method.

Several trial joints such as the 304 steel/6061 alloy, the 304 steel/6061 matrix composite and the 304 steel/Al/ $\text{Si}_3\text{N}_4$  were also made by the present method.

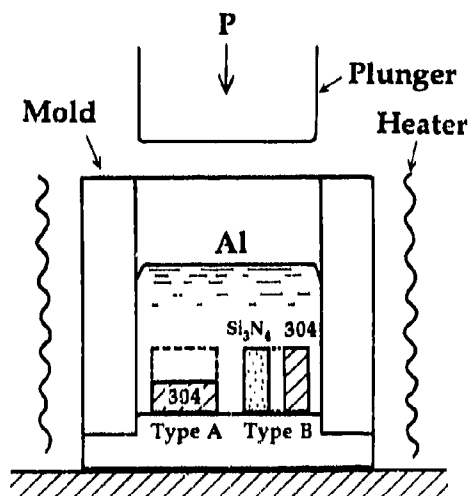


Fig.1 Schematic illustration of cast bonding.

### Evaluation

Joints were cut from cast joined ingots. Tensile specimens had a cross section of 1 mm thick x 4 mm wide. Bending bars having 3 mm x 3 mm square cross-section were also prepared. The crosshead speed was 0.5 mm/min for both tests and the tests were carried out at room temperature.

The microstructure was observed by SEM, EPMA and TEM. The TEM specimen was made by mechanical thinning followed by Ar ion thinning. The TEM used was a JEM200CX operated at 200 kV.

## **RESULTS AND DISCUSSION**

### Strength of interface

Table 1 summarizes the tensile strength of the 304 steel/Al joints (type A) varying the preheating temperature and the appearances of the joint fracture. All joint had a strength higher than the yield stress of pure Al and showed some plastic deformation before fracture. When the preheating temperature of the mold was low, e.g., 450 °C,

the joint strength became high and fracture occurred not at the interface but in Al. The effect of the preheating temperature on strength is ascribed to the resulting thickness of the intermetallic reaction layer mentioned in the next subsection. Table 1 also summarized the measured thickness of the reaction layer. As the thickness of the reaction layer increased, the strength of the joint decreased. It can be said that the interface strength is higher than 70 MPa in the optimized joining condition. On the other hand, when the preheating temperature was high, the strength decreased and fracture occurred at the interface after a little plastic deformation in Al because of the formation of a thick reaction layer.

Table 1. Strength of joints and fracture positions.

	MT : 450 °C ST : 550 °C	MT : 450 °C ST : 600 °C	MT : 550 °C ST : 500 °C
Tensile strength (MPa)	> 70	56	40
Fracture position	in Al	304/Al interface	304/Al interface
Reaction layer thickness (μm)	4	10	20

MT: Mold temperature, ST: 304 steel temperature

#### Interface microstructure

In every case a reaction layer was found at the interface. The total thickness of the reaction layer is also listed in Table 1. When fracture occurred near the interface, cracking proceeded near the 304 steel/reaction layer interface, not in the central region of the reaction layer.

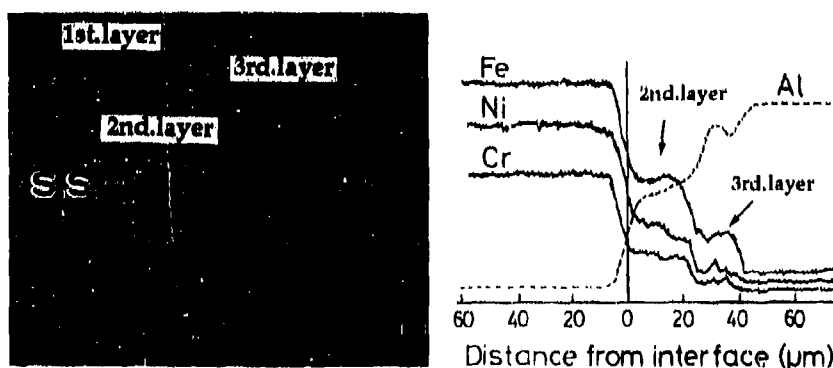


Fig.2 SEM photograph and EPMA line analysis of 304 steel/Al interface. Temperatures of the mold and 304 steel were 550°C and 500°C, respectively.



Fig.2 shows a SEM photograph and EPMA line analysis across the interface. The interface reaction layer consists of three distinct layers. The first layer, which is facing the 304 steel is quite thin and was not distinguished by the line analysis. The second layer was richer in Fe, Cr and Ni than the third layer, which is on the Al side.

Since the first layer is quite thin, EDX quantitative analysis also does not have any meaning on the layer. Then, reaction promoted by dipping the 304 steel rod in Al liquid heated at 800 °C for 30 min. The reaction layers grew to be more than 80 µm thick as the total thickness. The third layer was not the monolithic compound but Al with a fine particle dispersion. The particles had similar compositions as the second layer. Quantitative analysis by EDX on the first and the second reaction layers is summarized in Table 2. The composition of the first layer is expressed approximately as  $(\text{Fe,Cr,Ni})\text{Al}_{2.3.3}$ . Similar expression of the second layer is  $(\text{Fe,Cr,Ni})\text{Al}_{8.13}$ . No macroscopic diffusion layer is observed either in the steel or in the Al.

Table 2. Typical composition of reaction layers determined by EDX (at%).

Elements	Fe	Cr	Ni	Al
1st. layer	23.0	5.2	3.1	68.7
2nd. layer	3.5	1.5	1.7	93.3

Fig.3 shows a TEM photograph of the 304 steel/Al interface. The thickness of the first reaction is approximately 0.1 µm. From electron diffraction, this layer has an  $\text{FeAl}_3$  (orthorhombic) crystal structure. Thus, combined with the quantitative analysis, the first layer is determined as  $\text{FeAl}_3$  compound containing Cr and Ni. The identification of the second layer is now under examination.

The joint with a thinner reaction layer had higher strength. It was reported that the strength of the pure iron/Al joint decreased with increasing thickness of the reaction layer<sup>1</sup>. Also in the present case, the higher strength was achieved for the thinner reaction layer. Then it is required to choose the appropriate casting conditions to control the thickness of the reaction layer.

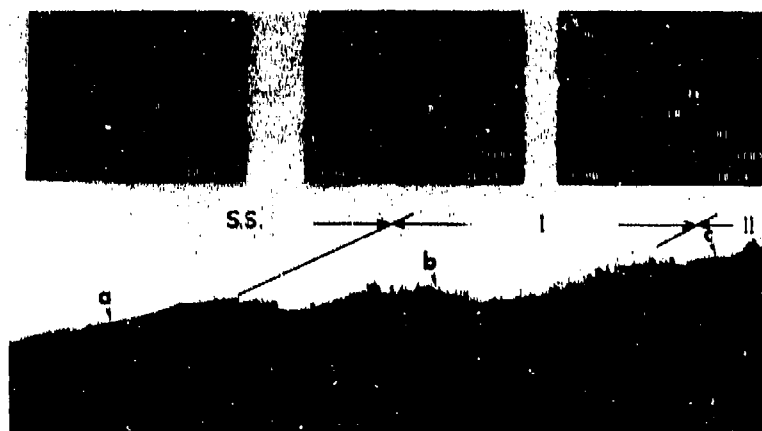


Fig.3 TEM photograph of 304 steel/Al interface. Temperatures of 304 steel and mold were 550 °C and 450 °C, respectively.

### Joining 304 steel to 6061 alloy and to 6061 matrix composite

6061 alloy and 6061 matrix composite reinforced with 20 vol%  $K_2Ti_6O_{13}$  whisker were also joined to 304 steel successfully by the cast bonding method. The joining structure was the sandwich structure (type B) of 304 steel/6061 or its composite/304 steel. The thickness of the center layer was 2 mm. Table 3 summarizes the strength data of the joints. Both joints have excellent strengths. T8-treated 6061 alloy had a strength of 280 MPa and then the joint achieved approximately 71 % of the parent materials' strength. The strength of 6061 matrix composite is 350 MPa and this joint strength reached 88 % strength of the parent materials.

Table 3. Joint strength of 304 steel/6061 alloy and 304 steel/6061 composite with 20 vol%  $K_2Ti_6O_{13}$  whisker. Both were heat-treated under T8 condition.

Joints	304 steel/ 6061 alloy	304 steel/ 6061 composite
Tensile strength (MPa)	197	310
Fracture position	Interface	Interface

Fig.4 shows one of the trial joints of 304 steel and 6061 alloy, where the bond face had some curvature. One of the benefits of the present joining method is to make a tight interface even if the bond face is not flat. Any kind of joining shapes can become possible. Furthermore, the size limitation is less serious compared with explosive welding and with friction welding. It only depends on the size of the squeeze casting mold and, to the authors knowledge, squeeze casting of Al has produced components larger than 100 cm in diameter.

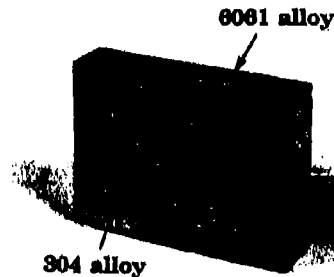


Fig.4 304 steel/6061 alloy joint having a curved bond face.

### Joining 304 steel to $Si_3N_4$ with Al interlayer

Joining ceramics to metals requires a certain kind of an interlayer to accommodate thermal expansion mismatch between the two constituents.  $Si_3N_4$  is one of the most difficult ceramics to be joined with metals because of its extremely low thermal expansion coefficient. Several types of interlayer structure have been developed for such joining system. A soft metal layer, which can reduce thermal stress by elastic-plastic deformation, is one of the effective methods to reduce thermal stress near the interface. Al has been frequently used as the soft metal interlayer and successful results were obtained for many joining systems<sup>2,3,4</sup>. Then, in the present work,  $Si_3N_4$ /Al/304 steel joining was performed by the cast joining method of type B. Al is infiltrated into the gap between  $Si_3N_4$  and the steel and becomes the soft metal interlayer. The distance between the two constituents was set to be 1 mm, a thickness which is thought to be effective to compensate thermal expansion mismatch between

ceramics and metals. The preheating temperature of the specimen was 800 °C. This temperature was determined by two reasons. When  $\text{Si}_3\text{N}_4$  contacts with Al liquid at 800 °C,  $\text{Si}_3\text{N}_4$  will suffer from thermal shock. The temperature difference between  $\text{Si}_3\text{N}_4$  and Al must be within the heat shock resistance. On the other hand, the excess increase of the preheating temperature decreases the strength of the interface of 304 steel/Al as shown in

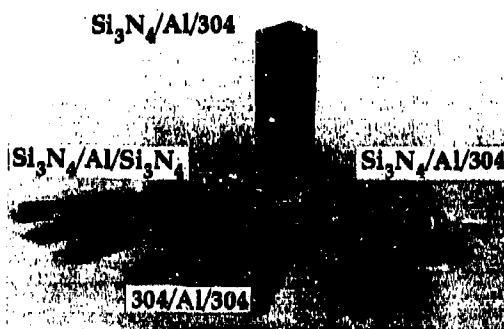


Fig.5  $\text{Si}_3\text{N}_4$ /Al/304 joint and various bending bars.

Table 2. The other joining conditions were the same as for the 304 steel/Al system. Fig.5 shows the  $\text{Si}_3\text{N}_4$ /Al/304 steel joint and the bending bars of  $\text{Si}_3\text{N}_4$ /Al/Al/ $\text{Si}_3\text{N}_4$ , 304 steel/Al/304 steel and  $\text{Si}_3\text{N}_4$ /Al/304 steel.

Table 4 summarizes the four point bending strength of these joints. All joints fractured after plastic deformation in the Al layer. Then it can be said that the strengths of the interfaces are higher than the yield stress of Al. However, the preheating condition of the steel was too high for the 304 steel/Al joining. The intermetallic compound layer grew thicker than 10  $\mu\text{m}$ . To prevent the growth of the reaction layer in such a joining system, a certain kind of surface treatment of the steel may be needed.

Table 4. Four point bending results of various joints.

	$\text{Si}_3\text{N}_4$ /Al/ $\text{Si}_3\text{N}_4$	304/Al/304	$\text{Si}_3\text{N}_4$ /Al/304
Strength (MPa)	> 125	> 94	> 103
Fracture position	$\text{Si}_3\text{N}_4$ /Al interface	304/Al interface	304/Al interface

## CONCLUSION

The present work concentrated on a new joining technique of Al alloys to stainless steels utilizing squeeze casting of Al alloys. Several trials were successfully performed. In the optimized case, the interface reaction layer became thin, resulting in an interface strength beyond the parent body strength. In such a case, the interface did not fracture by tensile testing. Because the squeeze casting method has been widely used for mass-production of Al products, this process has great potential for joining Al alloys to stainless steels in commercial fields.

## REFERENCES

1. M. Kikuchi, H. Takoda and S. Morozumi, *J. Japan Inst. Light Metals* **34**, 185 (1984).
2. M.G. Nicholas and R.M. Crispin, *J. Mater. Sci.* **17**, 3347 (1982).
3. A. Kohno, T. Yamada and K. Yokoi, *J. Japan Inst. Metals* **49**, 876 (1985).
4. K.Suganuma, T. Okamoto, M. Koizumi and M. Shimada, *J. Mater. Sci. Letters* **22**, 1359 (1987).

## A NOVEL BRAZING TECHNIQUE FOR ALUMINUM AND OTHER METALS

ROLAND S. TIMSIT\* AND B.J. JANEWAY\*

\*Alcan International Ltd., Kingston R&D Centre, Kingston, ON, Canada K7L 5L9

### ABSTRACT

In the novel brazing technique, the aluminum components in the joint assembly are coated with a powder mix consisting of elemental Si and a potassium fluoroaluminate flux. During brazing at  $\sim 600^\circ\text{C}$  in nitrogen gas, the flux melts and removes the native  $\text{Al}_2\text{O}_3$  surface film from the coated aluminum components. This action allows the silicon to diffuse into the aluminum to generate *in-situ* a layer of Al-Si filler metal of eutectic composition. The liquid metal then flows into the joint and yields a metallurgical bond on cooling.

This brazing technique may be exploited with aluminum using intermediary elements other than Si. The technique may also be used for joining other metals.

### INTRODUCTION

Recent years have witnessed an increased reliance on nitrogen-furnace brazing for the joining of aluminum heat-exchangers and air-conditioning condensers [1,2]. This brazing technique requires that one of the aluminum components in a joint be clad with filler material consisting of an Al-Si alloy of near-eutectic composition such as AA4045 or AA4343 [3]. These alloys are characterized by a melting temperature ( $\sim 577^\circ\text{C}$ ) [4] considerably lower than that of the core alloy ( $\sim 660^\circ\text{C}$ ). Joining is carried out at approximately  $600^\circ\text{C}$  in the presence of a non-corrosive flux, such as potassium fluoroaluminate [1], to remove native oxide films from the aluminum surfaces. At that temperature, the filler metal melts and flows into the joint to yield a metallurgical bond on cooling.

The present work was motivated by the need to develop a brazing technique that obviates the use of clad aluminum sheet. The novel technique reported in this paper fulfills this requirement and has been used for brazing aluminum/Cu, Cu/Cu and Cu/brass in addition to aluminum/aluminum joints.

### THE BRAZING PROCESS

In the novel brazing technique, at least one of the aluminum surfaces is coated with a layer of a powder-mix consisting of Si and a flux capable of dissolving surface oxide films [5], as illustrated in Fig. 1(a). A non-corrosive flux compatible with aluminum [1,3] consists of a mixture of  $\text{KAlF}_6$  and  $\text{K}_2\text{AlF}_6 \cdot \text{H}_2\text{O}$  powders in a molar ratio of approximately 13:1 with a particle dimension of the order of  $1\text{ }\mu\text{m}$ . Typical surface coverages by Si powder range from a few to several grams per square metre, depending on the joining application. Considerably larger Si surface coverages may be used. The weight ratio of Si to flux-powder varies typically from  $\sim 1:1$  to  $1:3$ , also depending on the application. The Si powder-particle dimensions may range from  $\sim 1$  to  $100\text{ }\mu\text{m}$ . Brazing is carried out by heating the joint at approximately  $600^\circ\text{C}$  in nitrogen gas at near-atmospheric pressure for a time interval of the order of one minute. During temperature ramp-up, the flux melts at  $\sim 562^\circ\text{C}$  and dissolves the surface oxide layers on aluminum [6] as illustrated in Fig. 1(b). Oxide removal allows the silicon particles to come into intimate contact with the bare metal and diffuse into it (Fig. 1(c)). At temperatures exceeding  $577^\circ\text{C}$ , the silicon diffuses rapidly into the aluminum to generate *in-situ* a layer of Al-Si liquid alloy of eutectic composition (Fig. 1(d)). The filler metal penetrates the joint of interest by capillarity action and forms a fillet, thus producing a metallurgical bond on cooling. Some unused filler metal may remain on the aluminum surface to form a thin layer of Al-Si alloy of near-eutectic composition (Fig. 1(e)).

In industrial applications of the new brazing technique the entire joint assembly is coated with the Si/flux mix, generally by exposure to a slurry, in order to keep the application technique simple. Filler metal is thus formed from all the contacting surfaces. However, excellent joints are also obtained if only one surface in a joint is coated with the brazing mix. This is because the molten flux spreads rapidly across the joint to remove oxide films from the mating surfaces, and sufficient filler metal can be formed from only one surface to yield a good metallurgical bond. Because joints are formed through capillarity flow of the filler metal, brazing requires only minimal contact force at the joint interface.

### PROCEDURES AND RESULTS

The successful use of the novel brazing technique requires a uniform coating of Si/flux powder on the metal surfaces prior to brazing. Uniform coatings could be deposited by dipping into a water- or alcohol-based slurry after cleaning the surfaces chemically [7]. The Si/flux weight ratio in the slurry was varied between 1:2 and 1:3. Depending on the concentration of solids in suspension, total surface coverages by the brazing mix ranging from 1 to  $80\text{ g m}^{-2}$  could easily be obtained on aluminum. After deposition, the coating

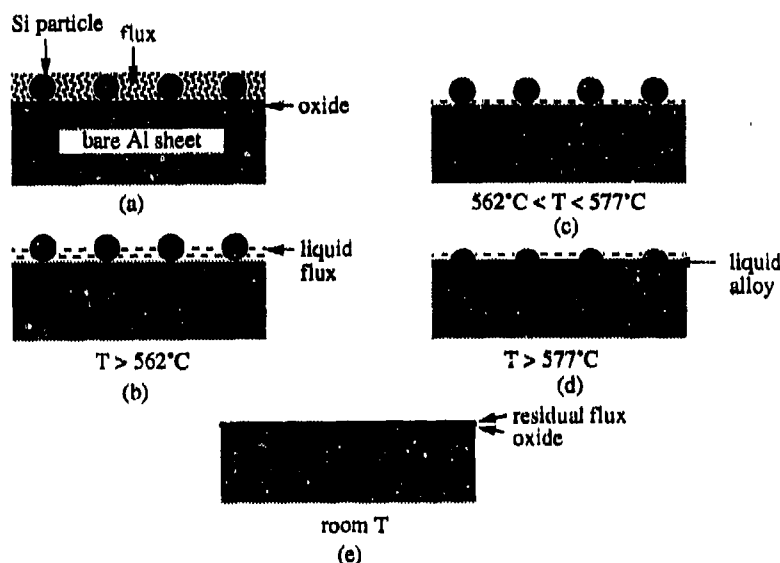


Figure 1. Successive steps in the novel brazing process:

- (a) deposition of a Si/flux powder mix on the aluminum surface; the Si particle dimensions range from  $\sim 1$  to  $100\text{ }\mu\text{m}$ , the flux particle dimensions do not exceed  $\sim 1\text{ }\mu\text{m}$ .
- (b) melting of the flux at  $\sim 562^{\circ}\text{C}$  and dissolution of surface oxide films,
- (c) at  $562^{\circ}\text{C} < T < 577^{\circ}\text{C}$ , solid-state diffusion of Si into aluminum
- (d) at  $T > 577^{\circ}\text{C}$ , rapid dissolution of Si to form localized pools of filler metal of near-eutectic composition, followed by coalescence of liquid-metal pools,
- (e) end of filler metal generation and solidification.

was dried in a circulating air oven.

In the work reported below, the efficacy of the brazing technique was assessed by assembling the test components in the desired joint configuration, heating the assembly in a nitrogen furnace at the selected temperature for a time interval not exceeding two minutes, and examining the brazed joint(s) after cooling. All brazed joints were produced by coating only one of the contacting surfaces with Si/flux powder.

#### Aluminum/Aluminum Joints

The novel brazing technique may be used with any aluminum alloys, provided the Mg content of the alloy is smaller than  $\sim 0.1\text{ wt}\%$  [7]. Figure 2(a) shows a metallurgical cross-section from a typical joint formed between two AA3003 aluminum sheet specimens (composition: Si 0.6, Fe 0.7, Cu 0.05-0.2, Mn 1.0-1.5, Zn 0.1 wt%, balance Al). In this example, only the sheet shown horizontally in the figure was coated with the Si/flux mix. Brazing was carried out at  $600^{\circ}\text{C}$ . Note the uniformity of the fillet. The dark needle-like particles in the fillet are Si particles precipitated from solution during cooling. For comparison, Fig. 2(b) shows a metallurgical cross-section obtained from a joint similar to that illustrated in Fig. 2(a) but formed by conventional brazing at  $600^{\circ}\text{C}$ . In that joint, the vertical AA3003 specimen was joined to a coupon of AA3003 clad with AA4045 alloy [3] (AA4045 composition: Si 9-11, Fe 0.8, Cu 0.3, Mn 0.05, Mg 0.05, Zn 0.1, Ti 0.2, balance Al) and filler liquid was generated on melting of that alloy. The fillets in the two figures are essentially identical.

One attractive feature of the new brazing process is a capability for introducing additional materials into the Si/flux mix to enhance selected properties of the joined components. For example, the addition of Zn powder was found to lead to diffusion of Zn into the component surfaces without adversely affecting the generation of Al-Si filler material [7]. The introduction of Zn by this method was found to provide sacrificial corrosion-protection for the joined aluminum surfaces [7].

#### Aluminum/Cu Joints

Aluminum/Cu joints were brazed by the novel technique using the Si/flux brazing mix. The mechanism of filler metal generation in this system will be outlined below. Prior to brazing, the copper and aluminum component (AA1100, composition (Si + Fe) 0.93, Cu 0.05-0.2, Mn 0.05, Zn 0.1 wt%, balance Al) were both

cleaned chemically. The aluminum surface was coated with Si/flux powder using a water-based slurry. Typical surface coverages by Si and flux were respectively  $\sim 8 \text{ g m}^{-2}$  and  $25 \text{ g m}^{-2}$ . Brazing was carried out by heating to  $584^\circ\text{C}$  in nitrogen gas to melt the flux, and then reducing the temperature to below  $548^\circ\text{C}$  as quickly as possible by cutting off power to the furnace and increasing the nitrogen gas flow. Figure 2(c) shows a typical metallographic cross-section obtained from an aluminum/Cu lap joint. Note the presence of a

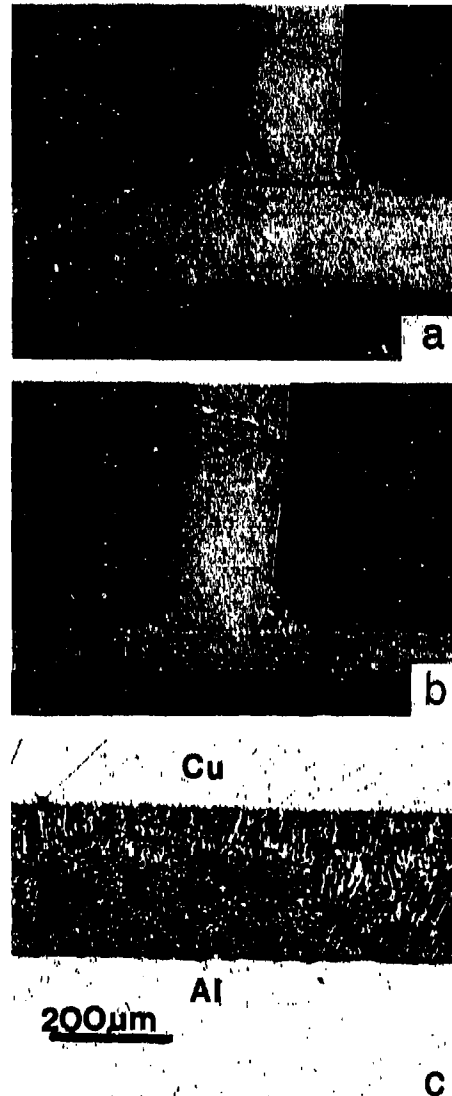


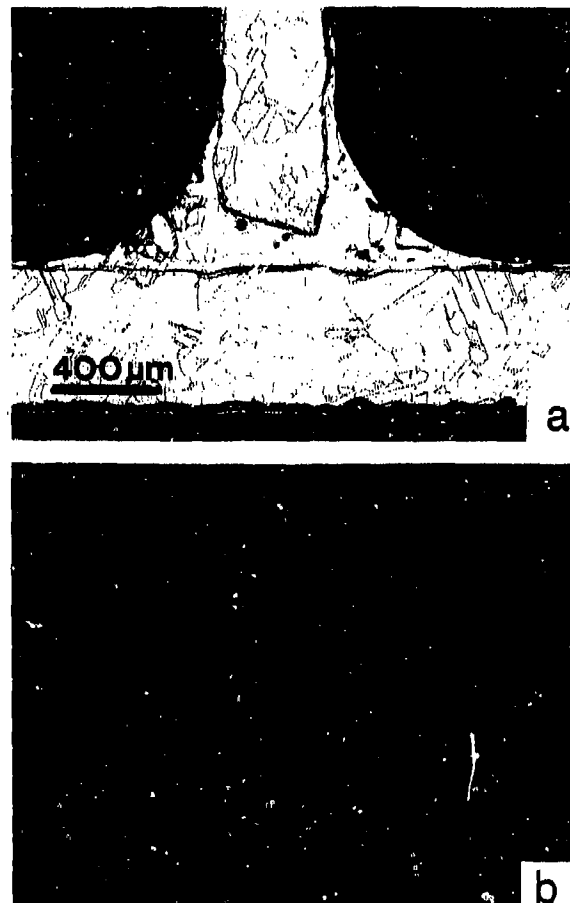
Figure 2. (a) metallurgical cross-section from a typical AA3003 joint.  
 (b) metallurgical cross-section from a joint formed by conventional brazing wherein the vertical component was joined to a coupon of AA3003 clad on both sides with AA4045.  
 (c) metallographic cross-section from an aluminum/Cu lap joint.

relatively wide layer consisting of Al-Cu-Si solid solution and intermetallic particles at the interface [8]. Exposure of the joint to temperatures higher than  $-548^{\circ}\text{C}$  for time intervals exceeding  $\sim 1$  minute led to excessive dissolution of Cu into the aluminum sheet. This dissolution stems from the large solubility of Cu in Al in that temperature range [4].

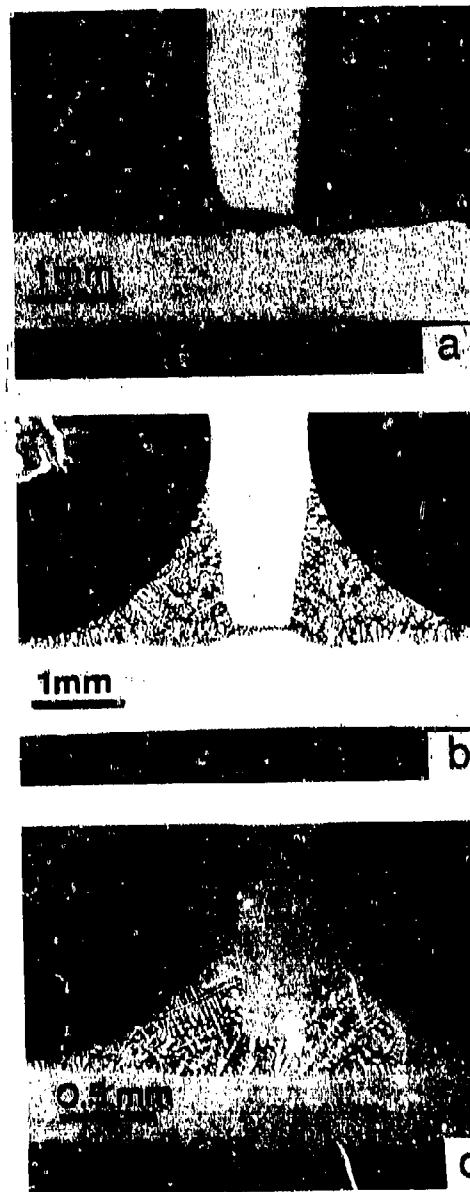
Brazing of an aluminum/Cu joint in the presence of Si occurs by initial dissolution of Si into aluminum to form a layer of Al-Si eutectic liquid at a temperature exceeding  $577^{\circ}\text{C}$  as explained previously; wetting of the Cu surface by the molten eutectic metal then leads to Cu dissolution to generate a molten ternary alloy. Because of this filler formation mechanism, aluminum/Cu joints could not be brazed at temperatures lower than  $577^{\circ}\text{C}$  i.e. below the eutectic temperature of the Al-Si system.

#### Cu/Cu and Cu/brass joints

Joining of Cu/Cu and Cu/brass joints was also successfully carried out using the novel brazing technique. The brass consisted of 70/30 Cu-Zn material of commercial purity. After chemical cleaning [7], the brazing mix was deposited from a water- or isopropyl alcohol-based slurry to generate typical surface coverages of Si and flux of  $\sim 10$  and  $30\text{ g m}^{-2}$  respectively. Brazing was carried out at an elevated temperature as the eutectic reaction between Cu and Si occurs at  $803^{\circ}\text{C}$  [4]. It was found that excellent fillets were formed in Cu/Cu and Cu/brass joints by heating for a few minutes respectively at  $900^{\circ}\text{C}$  and at  $876^{\circ}\text{C}$  in nitrogen



3. Metallographic cross sections from typical brazed joints: (a) Cu/Cu; (b) Cu/brass (Cu coupon is horizontal). The Si/flux mix was deposited on the horizontal metal surface.



4. Metallographic sections of:
- (a) a AA1100 aluminum joint brazed with Cu/flux,
  - (b) a AA1100 aluminum joint brazed with Ge/flux,
  - (c) a Cu/Cu joint brazed with Ge/flux powder.
- The Si/flux powder was deposited on the horizontal metal surface.



gas. Here again, the brazing temperature was significantly above the Cu-Si eutectic temperature to induce rapid generation of filler metal. Metallographic cross sections from typical brazed joints are illustrated in Fig. 3. Note the excellent fillet geometry.

#### BRAZING WITH METALS OTHER THAN SI

Although the work reported above has focused on Si as the intermediary material for brazing, the brazing technique may use other elements to generate filler metal. The only requirement is that these elements form a relatively low-temperature eutectic alloy with at least one of the metals in the joint. Several elements such as Cu, Ge, Zn, La, Ca, Ba etc., form a low-temperature eutectic with Al [4]. However use of these metals for brazing aluminum may not always be desirable [7] since, for example, some of these metals are chemically unstable in air. Similarly for Cu/Cu joining, the selection of an intermediary metal from Ge, La, Nd, Sb, Se, Sr etc., all of which form low-temperature eutectics with Cu, requires careful consideration [7]. In the following, the use of brazing elements other than Si is illustrated only to show the broad applicability of the principles on which the novel brazing process is based.

Figures 4(a) and (b) show metallographic sections of AA1100 aluminum joints brazed respectively with Cu/flux and Ge/flux powder mixes. The Cu- and Ge-containing powders were deposited from an isopropyl alcohol-based and an aqueous slurry respectively to yield surface coverages of  $46 \text{ g m}^{-2}$  for Cu and  $15 \text{ g m}^{-2}$  for Ge. The Cu/flux and Ge/flux weight ratios were respectively 1:1 and 1:2. Brazing was carried out at  $600^\circ\text{C}$  in nitrogen gas as described earlier. Note that metallurgical bonds are formed in the two cases. As mentioned earlier, the filler metal formed with the Cu and Ge powders stems from the eutectic reaction with Al at  $548^\circ\text{C}$  and  $420^\circ\text{C}$  [4] in each case respectively. In both cases, the joints were heated to  $600^\circ\text{C}$  to cause melting of the flux. As expected, the fillet in Fig. 4(a) consists of a Cu-Al solid solution interdispersed with intermetallic particles such as  $\text{CuAl}$ . The dark particles in the fillet shown in Fig. 4(b) consist of Ge precipitates.

Figure 4(c) shows a metallographic section from a typical Cu/Cu joint brazed with Ge/flux powder. The brazing mix was deposited from the aqueous slurry mentioned above. Brazing was carried out in nitrogen gas at  $700^\circ\text{C}$  to take advantage of the Ge-Cu eutectic reaction at  $644^\circ\text{C}$  [4] to generate filler metal. Although some porosity is evident in the fillet, the metallurgical bond was found to be excellent.

#### SUMMARY AND CONCLUSIONS

This paper has reported on a novel brazing technique for aluminum. The brazing process uses the *in situ* formation of filler metal by the eutectic reaction of an intermediary metal powder with the core-metal surface. The requirement on the intermediary metal is that the temperature of the eutectic reaction be appreciably lower than the melting point of the core material. The brazing technique also requires the use of a non-corrosive flux [1,2] to remove surface oxide films from the components to be joined. With aluminum, the brazing technique has been shown to be successful using Si, Cu or Ge as intermediary metals. The technique cannot be used for joining aluminum alloys containing Mg in a concentration as small as ~0.1 weight % [7].

Examples of Cu/Cu and Cu/brass joints brazed using mixtures of flux and Si or Ge powders show that the underlying principles of the novel brazing technique are widely applicable. Thus it should be possible to braze a variety of metals using an appropriate intermediary material i.e. a material capable of forming a low-temperature eutectic with the core material. For example, brazing of Ni or Ni-rich alloys may be carried out using Si, Ge, Sm etc powders since eutectic reactions of these elements with Ni occur at temperatures of ~  $963^\circ\text{C}$ ,  $762^\circ\text{C}$ ,  $570^\circ\text{C}$  etc respectively [4]. In principle, there are no constraints to using any compatible combination of core materials and intermediary metals for brazing. In practice, constraints may arise from such factors as the reactivity of the intermediary metal in air or in the slurry, the formation of brittle intermetallics, the cosmetic properties of the joint etc. For the brazing of Al alloys, these constraints are clearly avoided by the use of intermediary metals such as Si or Ge, which are relatively inert in air and water. Finally, the flux must be capable of stripping surface oxide films from the core materials of interest at the brazing temperature.

#### ACKNOWLEDGEMENTS

The authors are grateful to D. Lauzon and to the metallographic and electron optics sections of the Kingston R&D Centre of Alcan International Ltd for providing technical assistance during the course of this work.

#### REFERENCES

1. W.E. Cooke, T.E. Wright and J.A. Hirschfield, SAE Int. Congr., Detroit, Technical Paper Series 780300 (1978).
2. D.G.W. Claydon and A. Sugihara, SAE Int. Congr., Detroit, Technical Paper Series 830021 (1983).
3. P.E. Fortin, W.M. Kellerman, F.N. Smith, C.J. Rogers and M.J. Wheeler, SAE Int. Congr., Detroit, Technical Paper Series 852228 (1987).
4. *Binary Alloy Phase Diagrams*, T. B. Massalski Ed., ASM International (1990).
5. Roland, S. Timsit, U.S. Patent No. 5,100,048 (31 March 1992).
6. D.J. Field and N.I. Steward, SAE Int. Congr., Detroit, Technical Paper Series 870186 (1987).
7. R.S. Timsit and B.J. Janeway, to be published (1993).
8. *Ternary Alloys*, S. G. Petzow and G. Effenberg Eds., ASM International (1992).

---

**PART VI**

---

**Joining and Adhesion in  
Electronic Materials**

## INDIRECT BONDED METALLIZATION OF ALUMINUM NITRIDE

M. GRANT NORTON

Washington State University, Department of Mechanical and Materials Engineering, Pullman, WA 99164

### ABSTRACT

The use of aluminum nitride (AlN) as a substrate and packaging material for microcircuit applications is of present interest due to its many advantageous physical properties. A limitation to the widespread use of AlN is the lack of an adequate metallization system. The most common method of achieving high-integrity metallized ceramics is through the use of indirect-bonded metallizations. A wide range of intermediate bonding materials are used, for example glasses, oxide mixtures, and active metals. In this paper, the indirect-bonded metallization of AlN will be reviewed and discussed. Requirements which must be considered in producing successful metallizations include: wetting of the substrate and the metal by the intermediate phase and the reactivity between the intermediate phase and the substrate. The reactions which occur in many of the systems considered can be predicted by examination of thermodynamic data.

### INTRODUCTION

Aluminum nitride (AlN) has produced a great deal of interest as a substrate material for microcircuit packaging applications due to its high thermal conductivity [1-6]. The thermal conductivity of presently available AlN substrates is as high as  $260 \text{ Wm}^{-1}\text{K}^{-1}$ . The thermal conductivity of 96%  $\text{Al}_2\text{O}_3$ , the most widely used substrate material, is in the range  $10\text{-}30 \text{ Wm}^{-1}\text{K}^{-1}$ . In the most simple approach to application AlN will replace surface-mount and pin-grid-array modules where substantial benefit may accrue from its order of magnitude better thermal conductivity. Structures with large heat sinks are already required to meet the present thermal specifications of some optical components. Since these thermal specifications determine the reliability of the components, significant improvements may be achieved by being able to specify a lower device temperature through the use of AlN. AlN also has a number of other physical properties that render it interesting for packaging applications: close coefficient of thermal expansion (CTE) match to silicon, high electrical resistivity, and moderately low dielectric constant [7,8].

A limitation in the more widespread use of AlN has been the lack of an adequate metallization system. For example, the limited availability of compatible thick film material systems has restricted the production of hybrid circuits based on AlN to low volume applications. The metallization system is required for mounting of the integrated circuit, for interconnection to other circuit components and in the case of ceramic packages for joining the package base and lid. Metallization can be classified into two major types—direct bonded and indirect bonded. Direct-bonded metallization is achieved without the use of a second or intermediate phase, for example, by pressing together very flat mating surfaces to achieve diffusion bonding [9-11]. The most common method of achieving high-integrity metallized ceramics is through the use of indirect-bonded metallizations. A wide range of intermediate bonding materials are used such as glasses, oxide mixtures and active metals. A number of different indirect-bonded metallization systems have been developed for oxide ceramics, principally  $\text{Al}_2\text{O}_3$ . These systems will be discussed and their application to the metallization of AlN reviewed. Whatever the process, the basic requirements for strong bonding are the achievement of intimate contact between the two materials, the conversion of these surfaces into a chemically-bonded interface, and the ability of this interface to accommodate CTE mismatch stresses generated during cooling after fabrication or temperature changes in operational conditions.

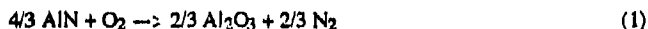
### THICK FILM METALLIZATION

This technique utilizes a conductor ink which contains a metal powder, a bonding agent, and an organic vehicle/solvent system which has well-defined rheological properties. The ink is screen printed onto the substrate, dried and fired to produce a conductive metal layer. The firing temperature is usually in the range  $700\text{-}950^\circ\text{C}$ . There are two primary methods used to achieve

adhesion between a thick film conductor and a ceramic substrate, these are frit bonding and reactive bonding [12,13]. For reactive-bonded metallizations, the intermediate materials are generally oxides which, during firing, form mixed-oxide phases or liquid eutectic phases at the interface. Bonding occurs by the reduction of the oxides and solid solution into the metal. The most common method of achieving adhesion is frit bonding, which involves the addition of 2-10wt% glass powder relative to the metal. During firing the glass should wet the substrate and penetrate to some extent into the metal network. The development of an interlocking glass-ceramic and glass-metal structure is desirable for good adhesion because it provides mechanical interlocking in addition to chemical bonding between phases. To achieve the required microstructure at the conductor-substrate interface it is necessary for the glass to have the appropriate surface tension and viscosity during the firing process, and for it to wet the substrate. The glasses are often high-lead borosilicates, a typical composition being 63wt% PbO-25wt% B<sub>2</sub>O<sub>3</sub>-12wt% SiO<sub>2</sub>. A number of review articles are available which discuss thick film materials and processes, the reader should refer to these for an overview of this technology [12-14].

#### AlN/Glass Interactions.

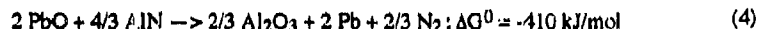
The interaction between typical high-lead borosilicate glasses and AlN results in three phenomena [15]. At temperatures above 670°C bubble formation occurs, indicating a reaction between the glass and the ceramic. At higher temperatures (> 900°C) dewetting of the ceramic by the glass and the formation of metallic spheres was evident. These effects were observed for glasses fired in either nitrogen or oxygen atmospheres. Because of these reactions most commercially available thick film materials are not suitable for use with AlN. The reactions which occur, for example between PbO and AlN, can be explained with reference to an Ellingham diagram [16]. An Ellingham diagram is a graphical representation of free energy data. The free energy of formation of several oxides used in glass manufacture is shown as a function of temperature in figure 1. The line for the oxidation reaction of AlN has also been included in figure 1.



At a given firing temperature, say 850°C (1123K), the Gibbs free energies of the following reactions are:



Therefore, the reaction:



is favorable as written, leading to evolution of nitrogen gas and the formation of lead. These products have been confirmed by performing the reaction in a sealed crucible and monitoring the gaseous emissions using gas chromatography. Nitrogen evolution was found to become significant above about 700°C and continue as the temperature was increased. The solid products were identified by x-ray diffraction (XRD).

The relative positions of the  $\Delta G^0$  versus T lines for the metal oxidation reaction and the AlN oxidation reaction allows predictions to be made about the stabilities of various oxides in contact with AlN. At a given temperature, any oxide whose free energy lies above that of AlN will oxidize the AlN while at the same time itself being reduced by the AlN. Any oxide whose  $\Delta G^0$  lies below that for the oxidation of AlN (i.e., more negative  $\Delta G^0$ ), at a given temperature, will be stable in contact with AlN. The free energy of formation of several common glass constituents lies above the line for AlN oxidation. Similar studies have been performed with other glass systems in contact with AlN, for example manganese oxide containing glasses [17]. These results also agreed well with the predictions based on the use of Ellingham diagrams.

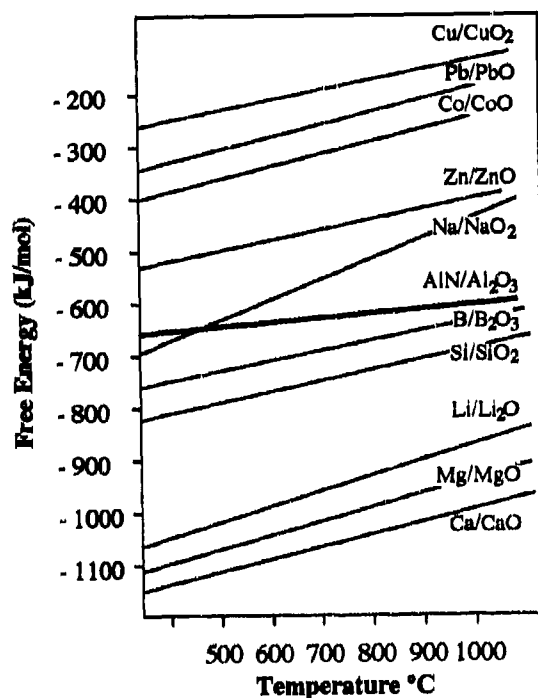


Figure 1. Gibbs free energies for selected reactions as a function of temperature. The lines represent reactions of the form  $2 \text{Pb(s)} + \text{O}_2(\text{g}) = 2 \text{PbO(s)}$ .

Using the data in figure 1 a model glass (in the  $\text{Li}_2\text{O-B}_2\text{O}_3$  system) was formulated which was compatible with AlN. A glass of the composition 20 mol%  $\text{Li}_2\text{O}$ -80 mol%  $\text{B}_2\text{O}_3$  has comparable rheological properties to a high-lead borosilicate glass [18]. In addition to chemical compatibility, a further requirement is that the glass wets the ceramic surface during the firing process. The wettability of a material is evaluated by measuring the contact angle,  $\theta$ , between the peripheral surface of a small sessile drop of the molten material and the horizontal surface of the ceramic substrate. A number of studies have evaluated the wettability of oxide ceramics by glasses and metals [e.g., 19-22] and the wettability of nitride ceramics by molten metals [e.g., 23-26]. Far fewer studies have examined the wettability of nitride ceramics by glasses [27-29].

The contact angle of the 20 mol%  $\text{Li}_2\text{O}$ -80 mol%  $\text{B}_2\text{O}_3$  glass on  $\text{Al}_2\text{O}_3$  and AlN substrates was determined in both air and nitrogen ambients [30]. In air, the glass behaved similarly on both substrates—in the latter case presumably due to oxidation of the surface. In nitrogen, instantaneous wetting of the AlN by the glass was not observed, however, a time-dependent contact angle was found. Time-dependent contact angles have been observed in metal/nitride-ceramic couples, e.g.,  $\text{Al/Si}_3\text{N}_4$ ,  $\text{Al/AlN}$ , and  $\text{Al-In/AlN}$  [23,25] and in many other systems, e.g., lead borosilicate glasses on ruthenium dioxide [31], polymer melts on aluminum, mica and Teflon [32], and water on glass and molten copper on iron [33].

Time-dependent contact angles are indicative of reaction-driven spreading. When a reaction occurs between the liquid and the solid, the free energy of reaction per unit interfacial area and unit time enhances the driving force for wetting [34,35]. In the case of the lithium borate glass on AlN and  $\text{Al}_2\text{O}_3$  the rate of reaction involving the glass and the oxide surface is faster than the corresponding reaction between the glass and the nitride surface. For high-lead borosilicate glasses on  $\text{Al}_2\text{O}_3$  substrates it has been found that significant quantities of the

substrate can be dissolved into the glass during the firing process of the film [36-38]. This interaction leads to an improvement in the adhesion of the metal [39]. Dissolution of AlN was found to occur in the lithium borate glass at typical processing times and temperatures, however the dissolution rate was lower than that observed for the dissolution of  $\text{Al}_2\text{O}_3$  in high-lead borosilicate glasses [30].

Further research is warranted to understand the reactions occurring between various glasses and AlN substrates. A recent study has evaluated the use of low-lead containing oxide glasses in thick film resistor ink formulations for AlN [40]. The glass contained only 6wt% PbO and based on the release of nitrogen the extent of the reaction between the PbO and AlN was limited. However, the most promising approach lies in the development of new compatible bonding systems specifically designed for use with AlN substrates [e.g., 41].

One particular type of glass system that may find application in this area is the oxynitrides [e.g., 42]. These glasses have been of considerable interest in recent years and a number of review articles on the subject have appeared [e.g., 43-47]. Oxynitride glasses are known to wet and adhere to nitrogen ceramics, for example in metallizing silicon nitride and in joining silicon nitride components [27,28,42]. Some preliminary studies have demonstrated that oxynitride glasses wet AlN substrates but because of the high glass transition temperature ( $T_g$ ) of the compositions fabricated, it was not ascertained if complete spreading would occur [30]. Oxynitride glasses have different physical properties from their oxide counterparts, a result of the substitution of trivalent nitrogen for bivalent oxygen in the glass structure. The extra bond offered by the nitrogen produces a tighter, more highly cross-linked glass structure. For example, an increase in  $T_g$  is often noted in an oxynitride glass compared to an oxide glass of the same cation ratio [48,49]. The increase in  $T_g$  being proportional to nitrogen concentration. Other changes in physical properties include a decrease in the CTE and an increase in the viscosity of the glass [50]. Although the majority of research work on oxynitride glasses has considered materials having high  $T_g$ , some studies have examined glasses with lower  $T_g$  [51-53].

#### AlN/Oxide Interactions.

Thermodynamic stability criteria can also be used to identify possible oxide additives for use as adhesion promoters in reactive-bonded thick film materials [54]. Cadmium and copper oxides are the most widely used additives in thick film materials for oxide ceramics. During firing, diffusion of the cations into the substrate (normally  $\text{Al}_2\text{O}_3$ ) occurs thereby forming mixed oxides (spinel) or a liquid eutectic phase which promotes adhesion of the metal film. Bonding to the metal occurs by reduction and solid solution into the metal. These oxides are added at the level of 0.1-1wt% relative to the metal powder. For AlN substrates, no such reactive bonders have been developed. The reactivity of some oxides with AlN has been examined by calcining oxide/AlN mixtures at high temperatures in nitrogen and then identifying the products using XRD [54]. A summary of these results is shown in Table I. Some preliminary studies have indicated that the addition of reactive oxides, e.g.,  $\text{CoO}$ , to a standard copper thick film formulation can lead to significant improvements in adhesion of the metal to AlN; compared to the adhesion of a similar formulation without the reactive oxide.

Table I. Reaction products of AlN + oxide

Oxide	Main Product	Side Product
CaO	CaO, AlN	$\text{Ca}_{12}\text{Al}_{14}\text{O}_{33}$ , $\text{Ca}_3\text{Al}_2\text{O}_6$
SiO	$\text{Sr}_3\text{Al}_2\text{O}_6$ , AlN	
BaO	$\text{Ba}_3\text{Al}_2\text{O}_6$ , AlN	$\text{Ba}_4\text{Al}_2\text{O}_4$
$\text{V}_2\text{O}_5$	$\text{V}_2\text{O}_5$	$\alpha\text{-Al}_2\text{O}_3$
MnO	MnO, AlN	
CoO	Co, CoO, $\text{Co}_3\text{O}_4$ , $\text{CoAl}_2\text{O}_4$ , AlN, $\text{Al}_2\text{O}_3$	
NiO	Ni, NiO, AlN	
$\text{Cu}_2\text{O}$	Cu	AlN
CuO	Cu, AlN	
ZnO	ZnO, AlN	$\text{ZnAl}_2\text{O}_4$
CdO	AlN	AlON, CdO, Cd

## REFRACTORY METALLIZATION

Traditionally this process employs molybdenum or tungsten and 'debased'  $\text{Al}_2\text{O}_3$ . The molybdenum is applied to the surface as a powder, often mixed with manganese oxide, and fired in a reducing atmosphere with a controlled dew point so that the Mn is present as MnO and Mo as the metal [55]. The MnO reacts with both the ceramic grains and the liquid glassy phase [56]. The glassy phase from the  $\text{Al}_2\text{O}_3$  migrates into the metal powder under the influence of capillary forces and bonds the metal particles to each other and to the  $\text{Al}_2\text{O}_3$  surface, producing a wettable surface layer. In the case of pure  $\text{Al}_2\text{O}_3$  and oxides without binder phases, it is necessary to add glasses to the metallizing mixtures [57]. The Mo coating is generally electroplated with Ni to provide a clean and continuous surface as well as one on which an applied braze would easily spread. A similar process is used for W metallization.

Commercially available AlN substrates are produced to be as pure as possible and contain only a very small amount of second phase material. Therefore for metallization using the molybdenum-manganese system a glass must be added to the metallizing mixture. It has been shown that manganese oxide ( $\text{MnO}_2$ ) is unstable in contact with AlN at typical metallization temperatures—resulting in the formation of nitrogen gas [17]. Transmission electron microscopy (TEM) studies of Mo/Mn and W metallizations on AlN have shown that complex reaction interfaces are formed [58,59]. The major bonding mechanism was determined to be grain boundary penetration of the glass into the substrate. There was also evidence for chemical bonding via the dissolution of AlN by a Al-Si-Mn glass phase and subsequent precipitation of a complicated sequence of precipitates.

## THIN FILM METALLIZATION

Thin film metallization involves the evaporation or sputtering of thin metal films onto a ceramic surface. It has been demonstrated that a sequence of layers of different metals is required for optimum film properties [60]. The first layer is usually a refractory metal such as Ti, Cr or NiCr; this layer provides adhesion to the ceramic. These elements are reactive and bond through redox reactions with the substrate. The second layer acts as a diffusion barrier. This material will usually be a noble metal, preferably Pt or Pd. The top layer will be the metal of choice for the particular application, for example, Au for wire bonding, Ni or Ag-Pd for solderability. Cross-section TEM studies of a Au/Pt/Ti thin film metallization on AlN have indicated that the bonding mechanism appears to involve interdiffusion across the metal/ceramic interface with the formation of TiN,  $\text{Al}_2\text{O}_3$ , and  $\text{TiAl}_3$  [58]. These reaction products can be predicted by examination of free energy data and are consistent with phases produced during active metal brazing of AlN.

## BRAZING

A braze must react with and reach chemical equilibrium at the interfaces with both the metal and ceramic components [34]. Metal systems are generally compatible, resulting in wetting and solution/diffusion bonding of the braze with the metal component. Conventional braze alloys, for example Ag-Cu, Au-Ni and Ag-Cu-Zn, generally do not, however, wet ceramics. They do not react with the ceramic since the oxidation potentials of Cu and Ag are less than that of Al. The interface energy can be lowered when there are strong forces of chemical attraction. The free energy of the reaction contributes to the driving force for wetting [34,61,62]. Liquid metals have much higher surface energies than most ceramic oxides, and therefore the interfacial energy is high so that most liquid metals do not wet and spread on ceramics unless special efforts are made [63].

Two general approaches have been used in the development of metal brazes for use with ceramic oxides. In one method, active metals such as titanium or zirconium are added to the metal; these effectively reduce the interfacial energy by their strong chemical attraction to the oxide and enhance the wetting behavior [64]. For example, brazes to be used directly with ceramics generally have a small percentage of an active metal, e.g., Ti, added [65]. The high oxidation potential of the Ti causes it to undergo a redox reaction with the ceramic (typically  $\text{Al}_2\text{O}_3$ ) which results in the spreading of the braze and formation of an oxide compound at the interface which is compatible with both phases, producing a chemical bond at the interface [66]. Several studies have demonstrated the effectiveness of small amounts of an active metal in increasing the wettability of both oxide [67] and nonoxide ceramics [42,68-72]. In the other

method, the surface of the ceramic is activated by application of a suitable metal hydride, for example,  $\text{TiH}_2$  [73]. The hydride decomposes at a temperature below the brazing temperature and the Ti undergoes a redox reaction with the ceramic at the interface to form a bond, and the bulk Ti sinters to form a wettable coating [74,75]. Other techniques may be used for the deposition of titanium coatings on the surface of ceramic samples prior to brazing, for example chemical-vapor deposition [76]. The interfacial reactions which occur during the brazing of nonoxide ceramics using either an active metal braze or by preactivating the ceramic surface with an active metal can also be explained by reference to an Ellingham diagram. An example of the latter case is discussed below.

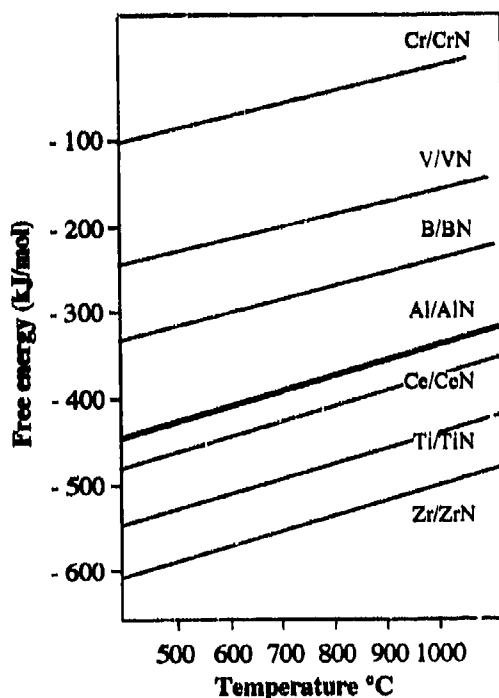
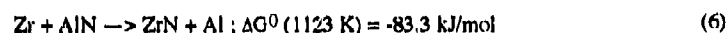
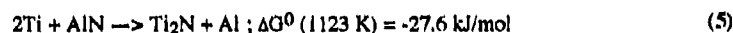


Figure 2. Gibbs free energies of formation of selected nitrides as a function of temperature. The lines represent reactions of the form  $2 \text{Zr (s)} + \text{N}_2 \text{(g)} = 2 \text{ZrN (s)}$ .

In this particular example, the AlN surface was activated by the in-situ decomposition of a metal hydride [77]. The choice of suitable metals can be made by reference to a standard free energy diagram for the formation of metal nitrides [78], as illustrated in Figure 2. Metals whose nitrides have lower free energies of formation than AlN will be suitable as active metals, for example titanium and zirconium. The decomposition of the metal hydride results in the formation of an active metal species. For  $\text{TiH}_2$  the decomposition reaction is believed to occur at  $\sim 340^\circ\text{C}$  with the subsequent reaction between the titanium and AlN occurring in the temperature range  $500\text{--}700^\circ\text{C}$  [77]. The products, identified by XRD, for reactions between  $\text{TiH}_2$  and AlN and between  $\text{ZrH}_2$  and AlN are shown in Table II. The reactions between Ti and Zr with AlN are thermodynamically favoured as shown below [79]:





Thus the overall reactions are proposed:



The intermetallic phases ( $\text{Ti}_3\text{Al}$  and  $\text{Zr}_3\text{Al}$ ) are formed by reaction between the free aluminum and either the titanium or zirconium, respectively. The formation of intermetallic phases during reaction of Ti and AlN has been reported by other authors although the composition of the intermetallics varies between the different studies [80,81]. Interfacial microstructures associated with the active metal brazing of AlN with a Ag-Cu-Ti alloy have been examined using TEM [82]. It was found that a layered series of reaction products was formed: TiN was found adjacent to the AlN and a complex  $\eta$ -type  $(\text{Ti,Cu,Al})_6\text{N}$  phase was found further from the substrate.

Table II. Phases identified in hydride/ceramic reaction

Reactants	Products
$\text{TiH}_2, \text{AlN}$	AlN $\text{Ti}_2\text{N}$ $\text{Ti}_3\text{Al}$
$\text{ZrH}_2, \text{AlN}$	AlN $\text{ZrH}_2$ $\text{Zr}_3\text{Al}$ ZrN

The general requirements for brazing to AlN are that (i) there must be a chemical reaction occurring at the interface between the braze and the substrate surface, and (ii) the CTE of the joining materials must be similar to avoid residual stresses being generated in cooldown from the brazing temperature. Also, it is necessary to control the brazing ambient to avoid direct reaction between the active metal and the gaseous atmosphere and to control the amount of active metal to avoid the formation of excessively thick interfacial layers. The design of brazes for nitride ceramics continues to be an active area of materials research [83].

It has been observed that metals that do not form stable nitrides can also be joined to AlN [84]. The reactions which occur can, in many cases, be correlated with thermodynamic predictions of the reaction products. An important consideration in these studies has been the nitrogen activity. In some microelectronic applications, metals such as Ti, Zr, and Ta are not attractive as conductors since they easily form stable oxides. Some preliminary studies of the interaction of non-oxygen (non-nitrogen) active metals with AlN have been reported. In particular, reactions between AlN and the metals Pt and Pd, and the alloys Pd-Ni and Pd-Ag were studied. In the case of Pt/AlN, for example, the following reactions were considered [84]:



The reaction only proceeds if the temperature is  $\geq 1390 \text{ K}$ . For the reaction to proceed at lower temperatures the nitrogen activity has to be lower than 1. Although some thermodynamic calculations have been performed on the use of non-nitride forming metals with AlN, more work has to be done to explain the AlN-metal reaction and to clarify the morphology of the

reaction layer. This work is especially required in the bonding of metal foils to AlN where the thermodynamic conditions are not fulfilled and the interfacial layer consists of unknown phases.

## SURFACE MODIFICATION

Preoxidizing of AlN substrates has been shown to be successful in providing a compatible surface for a number of existing metallization technologies. For example, the direct-bond copper (DBC) process, which has been developed for  $\text{Al}_2\text{O}_3$  [85] can work well when used with oxidized AlN substrates [86-89]. The process requires an inert atmosphere with a controlled  $\text{O}_2$  pressure. The necessary reaction to provide the adhesion between the oxide and the copper is the formation of a copper-oxide eutectic phase ( $\text{CuAlO}_2$ ) at the interface which is compatible with both the ceramic and the metal. For the metallization of AlN using the DBC process, the oxidation reaction is performed at temperatures  $>1100^\circ\text{C}$ . At these temperatures the predominant oxidation product is  $\alpha\text{-Al}_2\text{O}_3$ . The thickness of the oxide layer is an important factor in determining the adhesion strength of the copper to the AlN. If the layer is too thick then crack generation is observed during cooling, following bonding. This cracking is due to thermal stress caused by the differences in the CTE of AlN,  $\text{Al}_2\text{O}_3$ , and Cu. If the oxide layer is too thin then it will be dissolved completely in the Cu-O eutectic. The peel strength of copper films was found to be a maximum when the  $\text{Al}_2\text{O}_3$  layer was 1-2  $\mu\text{m}$  thick.

Another factor that can influence the adhesion of applied metallizations is the surface roughness of the substrate. It has been well documented that the adherence of thick film materials on  $\text{Al}_2\text{O}_3$  is enhanced by interfacial roughness, presumably due to the formation of interlocking structures [90-92]. Although surface roughness can contribute to adhesion it often appears to be a secondary factor. Surface roughness has been shown to be a factor in the adhesion of metal films to AlN. The etching of AlN substrates by NaOH solution increased the surface roughness and enabled the formation of Ni-P films on the surface which had high adhesion strengths [93,94]. The adhesion mechanism was attributed to the formation of interlocking surface structures through the selective etching of the substrate by NaOH. The adhesion of a commercially available Ag/Pt thick film material to AlN has also been attributed to surface roughness [95].

Recently a new technique for the selective metallization of AlN has been reported [96]. This technique utilizes an excimer laser to activate the AlN surface which results in the decomposition of AlN and the formation of an Al film on the substrate surface. The irradiated areas can then be electroless plated using Au, Ni or Cu. This technique has been used for writing a copper pattern into alumina substrates where the activation mechanism is reported to be similar [97].

## FUNDAMENTAL STUDIES

In studies of metallization behavior and reactions between intermediate phases and AlN, the intrinsic interactions may not be observed. Polycrystalline AlN substrates often contain second phase materials formed as a result of liquid-phase sintering, and almost always contain some oxygen on the surface or in the bulk. Therefore, the interactions observed may be one or a combination of the following: (i) interaction with AlN, (ii) interaction with the second phases, (iii) interaction with oxygen. Although it is necessary to determine the interactions between commercially available AlN substrates, which contain a number of different phases, and various intermediate materials, it is also important to study the intrinsic interactions between various materials (intermediates and metals) and AlN. Recently examination of the reactions between borosilicate glass and  $\text{Al}_2\text{O}_3$  have been performed using sapphire substrates [98]. Similar studies using AlN would be more difficult because high quality single crystal AlN substrates are not available. In x-ray photoelectron spectroscopy (XPS) studies of the bonding of Cu to  $\text{Al}_2\text{O}_3$  and Cu to AlN, thin films were used as the substrates for deposition [99,100]. A number of techniques have been shown to produce high purity, single phase AlN films [e.g., 101-103]. One of the advantages of thin film deposition for producing AlN is that the crystallographic orientation of the film can be changed. For example, AlN films produced by pulsed-laser deposition were oriented either with the (0002) plane of the film and the (1 $\bar{1}$ 02) plane of the substrate parallel or with the (10 $\bar{1}$ 0) plane of the film parallel to the (1 $\bar{1}$ 02) plane of the substrate. These different orientations were produced by changes in the deposition parameters.

Initial studies have demonstrated how these films can be used in studying the interaction between glasses and AlN [104]. It is possible to deposit glass or metal layers directly onto the AlN films without breaking the vacuum during the different depositions; thus avoiding any possible contamination of the AlN surface. Examination of the interface structure can be performed by TEM using samples prepared in a cross sectional geometry.

Recently, a new specimen preparation technique was developed for the study of surface reactions and thin film effects in AlN using TEM [105,106]. The technique uses specially prepared electron-transparent thin foils which act as substrates. The preparation of these substrates involves a high temperature annealing step in nitrogen which produces relatively large crystallographic terraces within the individual grains of a polycrystalline material as illustrated in figure 3. The abrupt variations in intensity in the image are due to discrete changes in the thickness of the specimen due to the presence of macroscopic steps between the facets. The traces of two sets of terrace edges can be clearly distinguished; one running horizontally in the image, the other at an angle of  $\sim 30^\circ$ . Relatively wide, low-index terraces may be formed by this technique, depending on the initial geometry of the grain. These terraces provide ideal surfaces for studying the metallization and reactions of AlN. For example, by heat-treating these annealed TEM specimens in the proximity of a metal source in a controlled environment, small metal particles can be deposited on the surface of the AlN. The metal/AlN interactions can be observed using the electron microscope. The same sample may, with care, be examined and then redeposited upon many times to follow the metallization process.

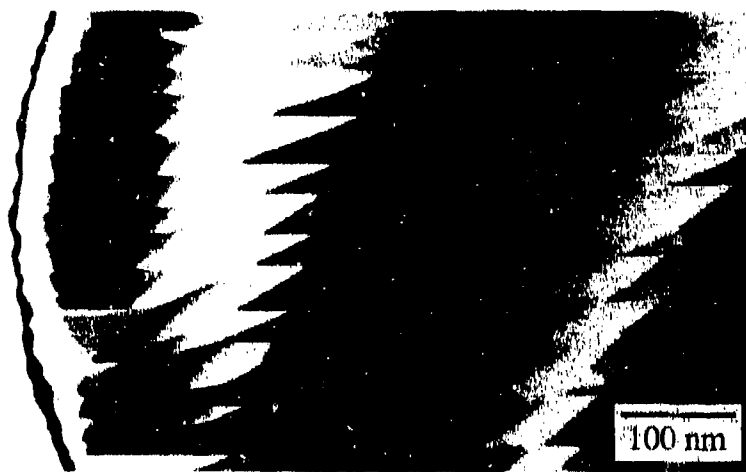


Figure 3. Bright-field image of pre-thinned AlN TEM sample after annealing at  $1800^\circ\text{C}$  for 10 mins.

## CONCLUSION

In conclusion, a number of studies have investigated the indirect-bonded metallization of AlN substrates. These studies have shown that high-quality joints can be obtained between AlN and various metals. In all cases the choice of intermediate material is very important and these choices can be made based on thermodynamic considerations. Further studies are however needed to understand in detail the interfacial reactions which occur between the ceramic and the intermediate material, as these interactions are important in developing high adhesion interfaces.

## REFERENCES

1. F. Aldinger and W. Werdecker, IEEE Trans. **CHMT** 7, 399 (1984)
2. Y. Kurokawa, K. Utsumi, H. Takamizawa, T. Kamata, and S. Noguchi, *ibid*, **CHMT** 8, 247 (1985)
3. N. Kuramoto, H. Taniguchi, and I. Aso, *ibid*, **CHMT** 9, 386 (1986)
4. S.G. Konsowski, J.A. Olenick, and R.D. Hull, Proceedings of the International Symposium on Microelectronics (International Society for Hybrid Microelectronics 1985) p. 213
5. R.R. Tummala, in: Advances in Ceramics vol. 26, edited by M.F. Yan (American Ceramic Society 1987) p. 3
6. N. Kuramoto, H. Taniguchi, and I. Aso, Amer. Ceram. Soc. Bull. **68**, 883 (1989)
7. E.S. Dettmer and H.K. Charles, Jr., in: Advances in Ceramics vol. 26, edited by M.F. Yan (American Ceramic Society 1987) p. 87
8. D.D. Marchant and T.E. Nemecek, in: Advances in Ceramics vol. 26, edited by M.F. Yan (American Ceramic Society 1987) p. 19
9. K. Suganuma, T. Okamoto, M. Koizumi, and M. Shimada, J. Amer. Ceram. Soc. **68**, C334 (1985)
10. J.T. Klomp, Amer. Ceram. Soc. Bull. **51**, 683 (1972)
11. M. Rühle, K. Berger, and W. Mader, J. Microsc. Spectrosc. Electron. **11**, 163 (1986)
12. R.W. Vest, Amer. Ceram. Soc. Bull. **65**, 631 (1986)
13. L.C. Hoffman, Amer. Ceram. Soc. Bull. **63**, 572 (1984)
14. J.R. Larry, R.M. Rosenberg, and R.O. Uhler, IEEE Trans. **CHMT** 3, 211 (1980)
15. M.G. Norton, J. Mater. Sci. Lett. **9**, 91 (1990)
16. R.A. Swallir, in: Thermodynamics of Solids 2nd. ed. (John Wiley and Sons, New York 1972) p. 116
17. E.Y. Luh, J.H. Enloe, L.E. Dolhert, J.W. Lau, A.L. Kovacs, and M.R. Ehlert, IEEE Trans. **CHMT** 14, 538 (1991)
18. O.V. Mazurin, M.V. Streltsina, and T.P. Shvaiko-Shvaikovskaya, in: Handbook of Glass Data (Elsevier, Amsterdam 1983) and references therein.
19. J.E. Comoforo and R.K. Hursh, J. Amer. Ceram. Soc. **35**, 130 (1952)
20. S.J. Hitchcock, N.T. Carroll, and M.G. Nicholas, J. Mater. Sci. **16**, 714 (1981)
21. M.G. Nicholas, T.M. Valentine, and M.J. Walto, J. Mater. Sci. **15**, 2197 (1980)
22. Yu. Naidich, Prog. Surface Membrane Sci. **14**, 353 (1981)
23. R. Sangiorgi, M.L. Muolo, and A. Passarone, in: High Tech Ceramics edited by P. Vincenzini (Elsevier, Amsterdam 1987) p. 415
24. S.K. Rhee, J. Amer. Ceram. Soc. **53**, 639 (1970)
25. M. Naka, M. Kubo, and I. Okamoto, J. Mater. Sci. Lett. **6**, 965 (1987)
26. S.K. Rhee, J. Amer. Ceram. Soc. **53**, 386 (1970)
27. R.E. Loehman, in: Surfaces and Interfaces in Ceramic and Ceramic-Metal Systems edited by J.A. Pask and A.G. Evans (Plenum Press, New York 1981) p. 701
28. M.L. McCartney, R. Sinclair, and R.E. Loehman, J. Amer. Ceram. Soc. **68**, 472 (1985)
29. M.G. Norton, J. Mater. Sci. **26**, 2322 (1991)
30. M.G. Norton, PhD thesis, University of London, 1989
31. R.W. Vest, Conduction Mechanisms in Thick-Film Microcircuits, Final Technical Report, Purdue Research Foundation Grant Nos. DAHC-15-70-G7 and DAHC-15-73-G8, ARPA Order No. 1642 (1975)
32. H. Schonhorn, H.L. Frisch, and T.W. Kwei, J. Appl. Phys. **37**, 4967 (1966)
33. M. Yokota, N. Moto-oka, A. Hara, and H. Mitani, Trans. Jpn. Inst. Met. **21**, 645 (1980)
34. J.A. Pask, Amer. Ceram. Soc. Bull. **66**, 1587 (1987)
35. I.A. Aksay, C.E. Hoge, and J.A. Pask, J. Phys. Chem. **78**, 1178 (1974)
36. W.S. Machin and R.W. Vest, in: Materials Science Research, edited by H. Palmour III, R.F. Davis, and T.M. Hare, vol. 11 (Plenum Press, New York 1976) p. 243
37. M. Prudenziati, B. Morten, L. Moro, G. Ruffi, E. Argentino, and C. Jachetti, Proceedings 6th. European Hybrid Microelectronics Conf. (International Society for Hybrid Microelectronics-United Kingdom 1987) p. 95
38. Y. Nakamura, Intl. J. Hybrid Microelectron. **4**, 168 (1981)

39. M. Prudenziati, B. Mörten, and M.L. Brigatti, *Active and Passive Elect. Comp.* **12**, 41 (1985)
40. Y. Kurihara, S. Takahashi, K. Yamada, T. Endoh, and K. Kanai, *IEEE Trans. CHMT* **14**, 199 (1991)
41. C.V. Cox, M.J. Hutfless, K. Allison, and D.L. Hankey, *Intl. J. Hybrid Microelectron.* **10**, 8 (1987)
42. R.E. Loehman and A.P. Tomsia, *Amer. Ceram. Soc. Bull.* **67**, 375 (1988)
43. S. Sakka, *Ann. Rev. Mater. Sci.* **16**, 29 (1986)
44. R.E. Loehman, in: *Treatise on Materials Science and Technology* vol. 26 Glass IV edited by M. Tomozawa and R.H. Doremus (Academic Press, London 1985)
45. S. Hampshire, R.A.L. Drew, and K.H. Jack, *Phys. Chem. Glasses* **26**, 182 (1985)
46. D.R. Messier, *Revue de Chimie Minerale* **22**, 518 (1985)
47. R.E. Loehman, *J. Non-Cryst. Solids* **56**, 123 (1983)
48. R.E. Loehman, *J. Amer. Ceram. Soc.* **62**, 491 (1979)
49. G.H. Frischat and C. Shrimpf, *J. Amer. Ceram. Soc.* **63**, 714 (1980)
50. P.E. Jankowski and S.H. Risbud, *J. Amer. Ceram. Soc.* **65**, C29 (1982)
51. Y. Luping, F. Quaxin, H. Guanqing, and L. Jiazhi, *J. Non-Cryst. Solids* **56**, 167 (1983)
52. G.H. Frischat, W. Krause, and H. Hübenthal, *J. Amer. Ceram. Soc.* **67** C10 (1984)
53. H. Unuma and S. Sakka, *J. Mater. Sci. Lett.* **6**, 996 (1987)
54. H.-G. Burkhardt, H. Vavra, and M.G. Norton, *Proceedings of the 7th. European Hybrid Microelectronics Conf. (International Society for Hybrid Microelectronics-Germany 1989)*
55. E.A. Hayduk, Jr., *Solid State Technol.* **1985**, 321
56. D.M. Mattox and H.D. Smith, *Amer. Ceram. Soc. Bull.* **64**, 1363 (1985)
57. M.E. Twentyman, *J. Mater. Sci.* **10**, 765 (1975)
58. A.D. Westwood and M.R. Notis, *Mater. Res. Soc. Symp. Proc.* **108**, 331 (1988)
59. A.D. Westwood and M.R. Notis, *Mater. Res. Soc. Symp. Proc.* **154**, 479 (1989)
60. W. Werdecker, *Proceedings 5th. European Hybrid Microelectronics Conf. (International Society for Hybrid Microelectronics-Italy 1985)* p. 472
61. R.E. Loehman, *Amer. Ceram. Soc. Bull.* **68**, 891 (1989)
62. F.G. Yost and A.D. Romig, Jr., *Mater. Res. Soc. Symp. Proc.* **108**, 385 (1988)
63. W.D. Kingery, H.K. Bowen, and D.R. Uhlmann, in: *Introduction to Ceramics*, 2nd. ed. (John Wiley and Sons, New York 1976) p. 208
64. M.G. Nicholas and R.M. Crispin, *Ceram. Eng. Sci. Proc.* **10**, 1602 (1989)
65. H. Mitzuhara and E. Huebel, *Weld. J.* **65**, 43 (1986)
66. M.G. Nicholas, *Br. Ceram. Trans. J.*, **85**, 144 (1986)
67. A. Tomsia, Z. Feipeng, and J.A. Pask, *Amer. Ceram. Soc. Bull.* **63**, 473 (1984)
68. A.P. Tomsia, J.A. Pask, and R.E. Loehman, *Ceram. Eng. Sci. Proc.* **10**, 1631 (1989)
69. Y. Kurihara, S. Takahashi, S. Ogihara, and T. Kurosu, *IEEE Trans. CHMT* **15**, 361 (1992)
70. A.-P. Xian, X.M. Xue, and Z.Y. Si, *J. Mater. Sci. Lett.* **10**, 246 (1991)
71. A.-P. Xian, *J. Mater. Sci.* **28**, 1019 (1993)
72. R.K. Brow, R.E. Loehman, A.P. Tomsia, and J.A. Pask, in: *Advances in Ceramics* vol. 26 edited by M.F. Yan (American Ceramic Society 1987)
73. R.J. Bondley, *Electronics*, **20**, 97 (1947)
74. M.G. Nicholas and D.A. Mortimer, *Mater. Sci. and Technol.* **1**, 657 (1985)
75. N. Iwamoto, Y. Makino, and H. Miyata, *Ceram. Eng. Sci. Proc.* **10**, 1761 (1989)
76. M.L. Santella, *Adv. Ceram. Mater.* **3**, 457 (1988)
77. M.G. Norton, J.M. Kajda, and B.C.H. Steele, *J. Mater. Res.* **5**, 2172 (1990)
78. J.M. Blocher, Jr., in: *High-Temperature Materials and Technology* edited by I.E. Campbell and E.M. Sherwood (John Wiley and Sons, New York 1967)
79. O. Kubaschewski and E.L. Evans, in: *Metallurgical Thermodynamics* 3rd ed. (Pergamon Press, New York 1958)
80. R. Beyers, R. Sinclair, and M.E. Thomas, *J. Vac. Sci. Technol.* **B2**, 781 (1984)
81. A.D. Westwood and M.R. Notis, *Advances in Ceramics*, **26**, 171 (1989)
82. A.H. Carim, *J. Mater. Res.* **4**, 1456 (1989)
83. J.R. McDermid and R.A.L. Drew, *J. Amer. Ceram. Soc.* **74**, 1855 (1991)
84. J.T. Klomp, A.J.C. van de Ven, and M. Monneraye, *Coll. de Phys.* **51**, C1-745 (1990)

85. J.F. Burgess, C.A. Neugebauer, and G. Flanagan, *J. Electrochem. Soc.* **122**, 688 (1975)
86. P. Tsuge-Weiss and J. Gobrecht, *Mater. Res. Soc. Symp. Proc.* **40**, 399 (1985)
87. T. Takahashi, N. Iwase, A. Tsuge, and M. Nagata, in: *Advances in Ceramics* vol. 26 edited by M.F. Yan (American Ceramic Society 1987) p. 159
88. N. Iwase, K. Anzai, K. Shinozaki, O. Hirao, T.D. Thanh, and Y. Sugiura, *IEEE Trans. CHMT* **8**, 253 (1985)
89. W.L. Chiang, V.A. Greenhut, D.J. Shanefield, I. Salvati, and R.L. Moore, *Ceram. Eng. Sci. Proc.* **12**, 2105 (1991).
90. T.T. Hitch, *J. Electron. Mater.* **3**, 553 (1974)
91. P.F. Becher and J.S. Murday, *J. Mater. Sci.* **12**, 1095 (1977)
92. P.F. Becher and W.L. Newell, *J. Mater. Sci.* **12**, 90 (1977)
93. T. Osaka, H. Nagata, E. Nakajima, I. Koiwa, and K. Utsumi, *J. Electrochem. Soc.* **133**, 2345 (1986)
94. T. Osaka, T. Asada, E. Nakajima, and I. Koiwa, *J. Electrochem. Soc.* **135**, 2578 (1988)
95. A.A. Mohammed and S.J. Corbett, *Proceedings of the International Symposium on Microelectronics (International Society for Hybrid Microelectronics 1985)* p. 218
96. H. Esrom, *Mater. Res. Soc. Symp. Proc.* **204**, 457 (1991)
97. A.J. Pedraza, M.J. Godbole, M.J. DeSilva, and D.H. Lowndes (1993 unpublished)
98. J.-H. Jean and T.K. Gupta, *J. Mater. Res.* **7**, 2514 (1992)
99. F.S. Ohuchi, R.H. French, and R.V. Kasowski, *J. Appl. Phys.* **62**, 2286 (1987)
100. F.S. Ohuchi and M. Kohyama, *J. Amer. Ceram. Soc.* **74**, 1163 (1991)
101. M.G. Norton, P.G. Kotula, and C.B. Carter, *J. Appl. Phys.* **70**, 2871 (1991)
102. F.S. Ohuchi and P.E. Russell, *J. Vac. Sci. Technol. A* **5**, 1630 (1987)
103. X. Li and T.L. Tansley, *J. Appl. Phys.* **68**, 5369 (1990)
104. M.G. Norton, P.G. Kotula, J. Li, S. McKernan, K.P.B. Cracknell, C.B. Carter, and J.W. Mayer, *Mater. Res. Soc. Symp. Proc.* **226** (1991)
105. S. McKernan, M.G. Norton, and C.B. Carter, *Proceedings of the XII International Congress for Electron Microscopy*, 350 (1990)
106. M.G. Norton, S. McKernan, and C.B. Carter, *Mater. Res. Soc. Symp.* **225** (1991)

## A JOINING TECHNIQUE USING MULTILAYER LEAD-INDIUM-GOLD COMPOSITE DEPOSITED IN HIGH VACUUM

CHIN C. LEE, CHEN-YU WANG, YI-CHIA CHEN, AND GORAN MATIJESEVIC  
University of California, Department of Electrical and Computer Engineering, Irvine, CA 92717

### ABSTRACT

A joining technique for electronic devices has been developed. This technique uses a lead-indium-gold multilayer composite solder deposited directly on GaAs wafers in high vacuum to prevent indium oxidation. The gold layer on the composite further protects the indium layer from oxidation in atmosphere. The GaAs dies are bonded to a gold-coated alumina substrate at a process temperature of 250°C. Nearly perfect joints are achieved as verified by a scanning acoustic microscope (SAM). SEM and EDX results indicate that the alloy joint consists of  $\text{AuIn}_2$  grains embedded in an In-Pb solid solution phase, as predicted from the Au-In-Pb phase diagram. Compared to lead-tin solder, indium-lead solder has been shown by others to exhibit much better fatigue resistance and have much less of a scavenging effect. Thermal shock as well as shear tests confirm that a good die attach is obtained with the lead-indium-gold composite.

### INTRODUCTION

The semiconductor device package serves the multiple purposes of mechanical support, environmental protection, heat dissipation, and electrical connection. Reliable die bonding is a necessity for a good IC package. Commonly used bonding media include metal-filled organic adhesives and glasses, hard solders, and soft solders. Hard solders have excellent fatigue resistance and a high thermal conductivity. Due to elastic rather than plastic deformation, hard solders retain the stresses caused by the thermal expansion mismatch among the parts joined and may fracture in extreme cases. Soft solders have a high degree of plastic strain capability and can therefore deform to release the stresses developed. Soft solders, on the other hand, incur thermal fatigue and creep movement. The most commonly used soft solders are tin-lead alloys of various compositions. Regardless of the wide and popular use, tin-lead solders do have significant thermal fatigue. Furthermore, they exhibit a scavenging effect when the molten solder with a high tin content dissolves the gold film and quickly forms brittle gold-tin intermetallic compounds. Since electrodes are frequently gold plated, the rapid gold-tin interdiffusion in either the liquid or solid state can degrade bonding quality and thus requires careful evaluation.

In spite of its seldom use in the industries, In-Pb solder has been shown to exhibit much better thermal fatigue lifetime than Pb-Sn solder [1-3]. Furthermore, molten In-Pb alloy dissolves gold much more slowly than Pb-Sn alloy, thus greatly reducing the scavenging effect [4]. Accordingly, the In-Pb alloy appears to be a worthwhile subject to study for electronic packaging. Fig. 1(a) displays the In-Pb phase diagram [5]. The In-Pb binary system is quite simple in that indium and lead form continuous solid solutions except for the alloy with an indium composition ranging from 54 wt.% to 78 wt.% where a separate phase  $\alpha_1$  is present.

To examine how the In-Pb alloy scavenges less gold than the Pb-Sn alloy, we turn to the Au-In-Pb phase diagram. Fig. 1(b) exhibits the isopleth for the 50In/50Pb alloy to Au taken from the Au-In-Pb ternary phase diagram [6]. As we can see from this figure, at 250°C the 50In/50Pb solder needs to dissolve only 1 wt.% Au to produce solid  $\text{AuIn}_2$  intermetallic. In the case of 37 wt.% Pb-Sn solder, approximately 13 wt.% Au must be dissolved before a solid  $\text{AuSn}_2$  can form [7]. Since these solid intermetallic compounds can protect the Au layer from further dissolution, 50In/50Pb solder scavenges gold much more slowly than Pb-Sn solder.

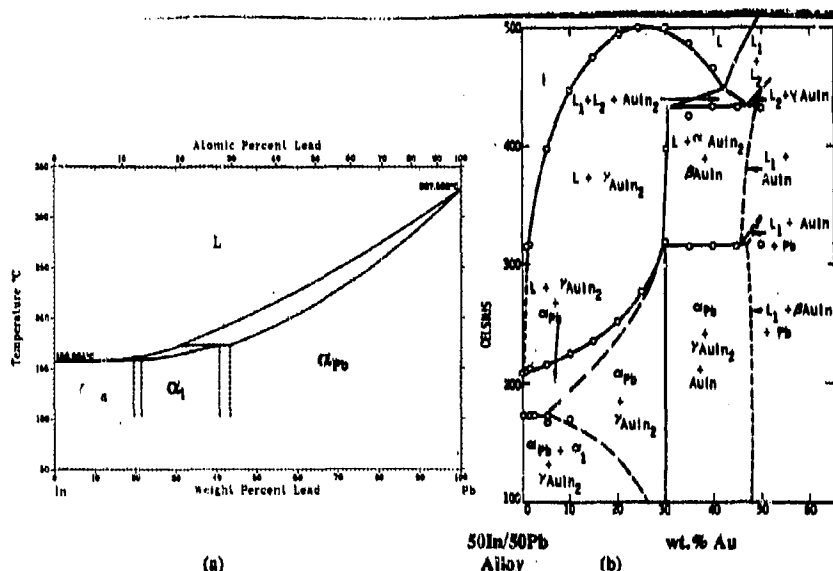


Fig. 1 (a) Phase diagram of indium-lead binary system [5]; (b) The isopleth from 50In/50Pb alloy to Au [6].

Oxidation of solders presents a major difficulty in producing high quality die attach joints [8,9]. The oxide forms a solid film on top of the molten solder solution, which prevents the solution from achieving a bond with the device die or the package. In common practice, the oxide film is broken down by a scrubbing action in the bonding process. However, the scrubbing motion itself may induce voids and inhomogeneity in the bonding layer. To inhibit oxidation in the In-Pb solders, we have developed a method of using multiple layers of Cr, Pb, In, and Au deposited in high vacuum directly on the object to be joined. Cr improves the adhesion on the object. The outer gold layer of the Cr-Pb-In-Au composite forms  $AuIn_2$  immediately upon evaporation that protects the inner In and Pb layers from oxidation. This has been proven to be effective with the Cr-Sn-Au and the Cr-In-Au composites previously reported that produced high quality Au-Sn and Au-In alloy joints [10-12].

We report here the use of a Pb-In-Au multilayer composite solder for bonding at a processing temperature of 250°C. Using the composite solder, GaAs dies have been successfully bonded to alumina substrates without the use of flux. High quality joints have been obtained as verified by a scanning acoustic microscope (SAM). The resulting bonding layers are found to be uniform and homogeneous. SEM and EDX studies reveal the grain structure and the composition of the alloy formed.

## PRINCIPLE

From Fig. 1(b), it is seen that all alloys containing from 0 to 30 wt.% Au will solidify to form solid alloys consisting of three phases:  $\alpha_{Pb}$ , indium-rich  $\alpha_1$ , and  $AuIn_2$  compound. The  $\alpha_{Pb}$  phase is a solid solution of In in Pb. The  $\alpha_1$  phase is characterized as an fct structure with a c/a ratio of 0.93, as compared to an fct structure of indium with a c/a ratio of 1.075 to 1.078 [6]. There is no evidence that  $AuIn_2$  intermetallic compound produces joint embrittlement



while some claims are made that the formation of the  $\text{Au}_3\text{In}_4$  intermetallic compound might embrittle the joint [13,14]. Therefore, by restricting the amount of gold in the composite solder, the formation of  $\text{Au}_3\text{In}_4$  is prevented, thus precluding the joint from becoming brittle.

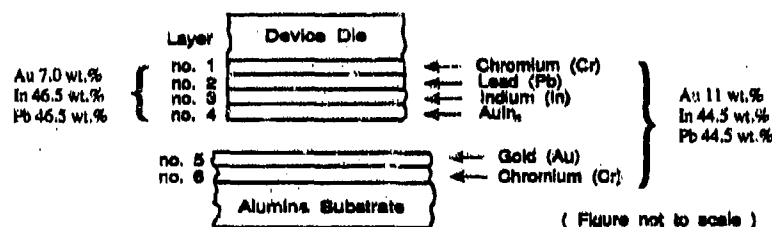


Fig. 2 The composite structure after deposition of a thin outer gold layer on the indium-lead layers. The gold layer forms  $\text{AuIn}_2$  at the outer surface of the composite solder.

Fig. 2 shows the multilayer composite design. In fabrication, chromium and lead are first deposited on the GaAs wafer, followed by the deposition of indium and an outer gold layer in one vacuum cycle to prevent oxidation of the indium layer (layer no. 3). The chromium layer (layer no. 1) enhances the adhesion of lead layer to the die. Right after deposition, room temperature interdiffusion occurs so that the outer gold layer (layer no. 4) forms  $\text{AuIn}_2$  very fast [15]. This layer inhibits contact of the pure indium layer with oxygen when the composite is exposed to air. The alumina substrate is deposited with chromium and gold where the chromium layer is present to enhance adhesion.

In the bonding process, the die and substrate are brought into contact with a static pressure and heated to  $250^\circ\text{C}$  in a hydrogen atmosphere. For the ternary system of Au-In-Pb, indium has the lowest melting temperature ( $157^\circ\text{C}$ ). The indium layer of the composite thus melts first as the specimens are heated above the indium melting point. As the indium layer melts, it dissolves the lead layer (layer no. 2) and breaks up the  $\text{AuIn}_2$  layer (layer no. 4). The composition of the Pb-In-Au composite shown in Fig. 2 is designed so that at  $250^\circ\text{C}$  it becomes a mixture of a liquid solution and  $\text{AuIn}_2$  as indicated in the isopleth of Fig. 1(b). This mixture in turn wets and dissolves the gold layer on the substrate to form a joint. When the temperature is reduced to room temperature, the mixture solidifies to form an alloy joint that contains three phases:  $\alpha_{\text{Pb}}$ , indium-rich  $\alpha_1$ , and  $\text{AuIn}_2$  as determined from Fig. 1(b).

## FABRICATION PROCESS

Chromium, lead, indium and gold are deposited directly on the polished side of the GaAs wafer in high vacuum with the thicknesses of  $300 \text{ \AA}$ ,  $3.9 \text{ \mu m}$ ,  $6.2 \text{ \mu m}$ ,  $0.35 \text{ \mu m}$ , respectively. After deposition, the backside of the die loses the gold color indicating the formation of  $\text{AuIn}_2$  which protects the inner In and Pb layers from oxidation. The multilayer composite is designed to have equal weight percentage of In and Pb. If the composite were to form a uniform alloy, it would have 7 wt.% of gold. The alumina substrate is coated with  $300 \text{ \AA}$ -thick chromium and  $0.22 \text{ \mu m}$ -thick gold layers. If the gold layer on the substrate and the composite on the GaAs die together form a uniform alloy, it would have 11 wt.% gold. After deposition, the GaAs wafers are cleaved into dies of  $2 \text{ mm} \times 3 \text{ mm}$  in size.

The die is placed on the substrate which is then laid on a graphite boat. Static pressure is applied to the die using a plate forced down with compression springs. This is to ensure complete contact between the die and the substrate surfaces to be joined. Static pressure in the range from 40 to 60 PSI was found to be low enough not to damage the die while achieving good contact. The boat is then loaded into a process furnace. The assembly is heated in a hydrogen atmosphere to  $250^\circ\text{C}$  within 10 minutes with a dwell time above  $240^\circ\text{C}$  of 5

minutes. Afterward, the boat is pulled out and cooled down to room temperature within 20 minutes. High quality bonds were achieved using this technique.

### EXPERIMENTAL RESULTS

To examine the bonding quality, a transmission scanning acoustic microscope (SAM) [8] is used to image the specimen. With the operating frequency of 130 MHz, the SAM has a spatial resolution of 25  $\mu\text{m}$ , with dark areas corresponding to voids. Fig. 3 shows the SAM image of a specimen that is well bonded using the composite solder. Due to the resolution limit, voids smaller than 25  $\mu\text{m}$  may exist in the bonding that are not seen in the SAM image but we speculate that such small voids would have little effect on the quality of the joint.

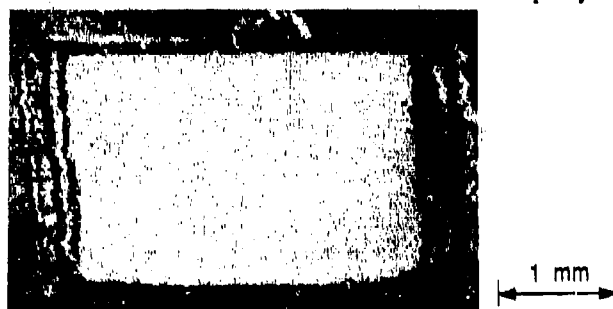


Fig. 3 SAM image of a 2 mm x 3 mm GaAs die bonded on a gold-coated alumina substrate.

In order to form a basic model of the bonding process, we studied thickness uniformity, alloy composition, and grain structure of the bonds. Several specimens were cut into cross sections, polished, and examined with an optical microscope and a scanning electron microscope (SEM) with an energy dispersive X-ray (EDX) spectrometer. Fig. 4 exhibits the SEM image of the cross section of one specimen. As we can see from the picture, the bonding layer is quite homogeneous and uniform with a thickness of 3.6  $\mu\text{m}$ . There are two distinct phases, one with blocky grains that is embedded in the second phase. EDX study reveals that the blocky phase is  $\text{AuIn}_2$  with a composition of 55 wt.% In and 45 wt.% Au, very close the  $\text{AuIn}_2$  stoichiometry. The other phase was found to be a solution of lead and indium with composition of 48 wt.% In and 52 wt.% Pb. This In-Pb phase is the  $\alpha_{\text{Pb}}$  phase shown in Figure 1.

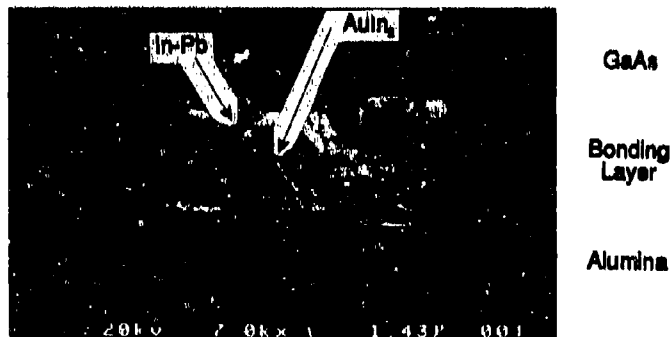


Fig. 4 SEM image of the cross section of the specimen showing the bonding layer.

To further study the interface between the GaAs die and the bonding layer, the GaAs die was sheared off. The remaining bonding layer on the alumina substrate is shown in Fig. 5(a). The joint broke at two different interfaces. One, marked "C", is inside the joint and shown to the right of the picture. The left side of the specimen broke at the interface of the GaAs die and the bonding layer, which is marked "D". In region "D", the entire bonding layer remains on the alumina substrate. Fig. 5(b) displays the top view of the left part of Fig. 5(a). The top layer is a solid solution of In and Pb with the same texture as the In-Pb solution identified in the cross-sectional picture. Through the holes in the top layer, we observe grains of about 1  $\mu\text{m}$  in size corresponding to the blocky grains of  $\text{AuIn}_2$  in Fig. 4. At the border between the two layers in Fig. 5(a), we can also see these grains directly underneath the top layer.

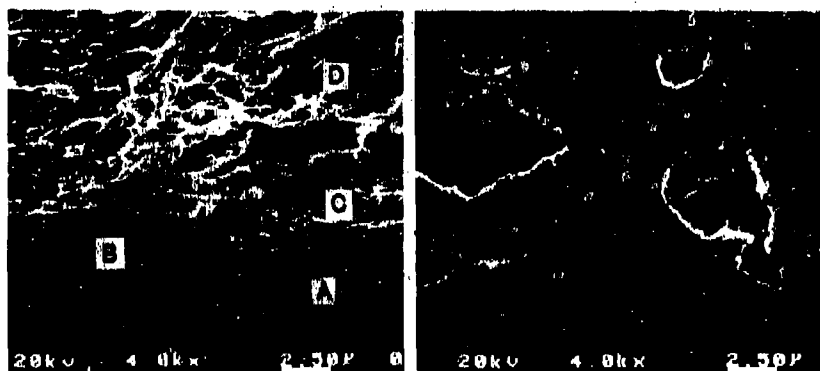


Fig. 5 (a) SEM image of the bonding layer after GaAs die is sheared off - A: alumina cross section, B: joint cross section, C: broken interface inside the joint, D: interface of GaAs and the joint; (b) top view SEM image of the bonding layer with GaAs die removed.

During the bonding process, the indium layer melts first, breaks up the  $\text{AuIn}_2$  and dissolves the lead layer to form a mixture of liquid solution and solid  $\text{AuIn}_2$  intermetallic. Due to the pressure applied, some liquid solution is squeezed out of the bonding area. The bonding layer thickness is thus less than that of the original multilayer composite. Furthermore, it appears that the solid intermetallic  $\text{AuIn}_2$  is kept in the remaining solution in the bond area and forms the blocky grains embedded in the In-Pb solution upon solidification. EDX data shows that the composition of the material squeezed out of the die area is close to that of the In-Pb phase inside the joint.



Fig. 6 (a) SAM image of the specimen before thermal shock test; (b) SAM image of the same specimen after 10 cycles of thermal shock test.

To test the reliability of the joint, thermal shock testing was carried out. The temperature extremes of  $-196^{\circ}\text{C}$  (liquid nitrogen) and  $160^{\circ}\text{C}$  (boiling cyclohexanol) were used with a dwell time of 2.5 minutes. After ten cycles, the specimens were examined under the SAM to determine whether any bonding degradation occurred. Fig. 6 shows the SAM image before and after the thermal shock test. As we can see from the picture, the bonding quality does not degrade after ten cycles of the thermal shock test.

Shear test was carried out on several samples according to the MIL-STD-883C. The samples passed the test for 1.25 X the rated shear strength while the die attach area exhibited evidence of adhesion across the whole die. In the case of a sample where some edge voids were seen on the SAM, the same bonding pattern was determined when the die was sheared off. Samples of die bonding which were not perfect due to unevenly applied pressure during the bonding process also exhibited good adhesion and passed the shear test.

## SUMMARY

A lead-indium-gold composite solder for bonding electronic devices was developed. The composite is deposited directly on GaAs wafers in high vacuum. Bonding of 2 mm x 3 mm dies to alumina substrates gave nearly perfect joints as determined by the scanning acoustic microscope. SEM and EDX studies on the cross sections of the bonding layer reveal the basic bonding mechanism and identify the two phases present as  $\text{AuIn}_2$  intermetallic and the In-Pb solid solution. The thermal shock and shear tests showed that good die attach was obtained. Accordingly, it seems realistic that we could control the strength and fatigue properties of the joint by designing a proper ratio of the  $\text{AuIn}_2$  and the In-Pb phases. This method is valuable in application where a soft solder of high fatigue lifetime, with small gold scavenging effect, and a well-controlled thickness is required.

## REFERENCES

1. C.R. Jackson, *Circuits Manufacturing* 13 (1), 40-41 (1973).
2. L.S. Goldmann, R.J. Herdzik, N.G. Koopman, and V.C. Marcotte, *Proc. 27th Electronic Compon. Conf.*, (IEEE, New York, NY, 1977), pp. 25-29.
3. R.T. Howard, *IBM J. Res. Develop.* 26, 372 (1982).
4. F.G. Yost, *Gold Bulletin* 10, 2 (1977).
5. J.P. Nabot and I. Ansara in *Binary Alloy Phase Diagrams*, Vol. 3, edited by T.B. Massalski (ASM International, Metals Park, Ohio, 1990), pp. 2269-2271.
6. M.M. Karnowsky and F.G. Yost, *Metallurgical Trans. A* 7A, 1149 (1976).
7. F.G. Yost, in *Proc. International Microelectronics Symp.*, (Vancouver, B.C., Canada, 1976), pp. 61-66.
8. G.S. Matijasevic and C.C. Lee, *J. of Electronic Mater.* 8, 327 (1989).
9. G.S. Matijasevic, C.Y. Wang and C.C. Lee, *IEEE Trans. Compon., Hybrids, and Manuf. Technol.* 13, 1128 (1990).
10. C.C. Lee, C.Y. Wang and G.S. Matijasevic, *IEEE Trans. Compon., Hybrids, and Manuf. Technol.* 14, 407 (1991).
11. C.Y. Wang and C.C. Lee, in *Proc. 42nd Electronic Compon. and Technol. Conf.*, (IEEE, New York, NY, 1992), pp. 502-507.
12. C.C. Lee, C.Y. Wang, G.S. Matijasevic, and S.S. Chen, in *Electronic Packaging Material Science VI*, edited by P.S. Ho, K.A. Jackson, C.-Y. Li, and G.F. Lipscomb (Mater. Res. Soc. Proc. 264, Pittsburgh, PA 1992), pp. 305-310.
13. D.M. Jacobson and G. Humpston, *Gold Bulletin* 22, 9 (1989).
14. F. Yost, F.P. Ganyard, and M.M. Karnowsky, *Metallurgical Trans. A* 7A, 1141 (1976).
15. J. Bjøntegaard, L. Buene, T. Finstad, O. Lønne, and T. Olsen, *Thin Solid Films* 101, 253 (1983).

## WAFER BONDING FOR HYBRID CIRCUIT TECHNOLOGY USING SOLID-STATE REACTIONS

Z. Ma<sup>a)</sup>, G.L. Zhou<sup>a)</sup>, T.C. Shen<sup>a)</sup>, M.E. Lin<sup>a)</sup>, K.C. Hsieh<sup>b)</sup>, L.H. Allen<sup>a)</sup>, and H. Morkoç<sup>a)</sup>

a) Coordinated Science Laboratory, University of Illinois, Urbana, IL 61801.

b) Department of Electrical and Computer Engineering, University of Illinois, Urbana, IL 61801.

### ABSTRACT

In this study, we report a new wafer bonding technique for the integration of GaAs- and InP-based optical devices with prefabricated Si electronic devices in hybrid circuit technology. This technique uses a Au-Ge eutectic alloy as the bonding materials between GaAs and Si wafers, and between InP and Si wafers. This process takes advantage of the low temperature solid-state reactions at GaAs/Au-Ge, InP/Au-Ge, and Si/Au-Ge interfaces. The bonding was carried out by annealing the samples at 280-300°C in an alloying furnace. The reliability of the joined wafers was evaluated by both cleavage test and standard thermal cycling test. The joining interfaces were characterized by scanning electron microscopy and transmission electron microscopy. The results reveal that the bonding is achieved by low temperature reactions at the GaAs/Au-Ge and InP/Au-Ge interfaces as well as solid-phase epitaxial regrowth at the Si interfaces. The joined structure has very good integrity.

### INTRODUCTION

The rapid progress in hybrid circuit technology has stimulated considerable efforts in the integration of micro-optic components with the optoelectronic and microelectronic circuitry, and integration of digital and analog microelectronics with optoelectronic components [1-3]. To realize this, heteroepitaxial growth of device-quality GaAs, InP, and related materials on Si substrates with low threading dislocation density has been motivated [4-6]. Significant results have been achieved in improving the minority-carrier lifetime in these epitaxial films by introducing strained-layer superlattice and various buffer layers to reduce the threading dislocation density.

Recently, Lo *et al.*[7] demonstrated an alternative approach to optoelectronic integration for InP-based materials on GaAs substrates using the so-called bonding by atomic rearrangement (BAR) method. This method involves high temperature annealing and requires precise crystallographic alignment of InP and GaAs. To overcome these problems, Venkatasubramanian *et al.*[8] used Au as the bonding material and developed an eutectic-metal bonding (EMB) method by making use of the low temperature eutectics of Au-Si and Au-GaAs. But their bonding process involves liquid-phase reaction. In this work, we have explored a new bonding

technique, which utilizes a commercial Au-Ge low temperature eutectic alloy as the bonding materials.

#### EXPERIMENTAL PROCEDURE

(100) oriented GaAs, InP, and Si wafers were used in this study. After a standard degreasing procedure, the wafers were chemically cleaned in buffered HF. A commercial Au-Ge eutectic alloy was used as the adhesion material. The Au-Ge films were deposited onto the cleaned GaAs, InP, and Si substrates using a thermal evaporator. The Au-Ge-coated samples were then stacked face-to-face, i.e., GaAs/Au-Ge/Si and InP/Au-Ge/Si, in intimate physical contact. The bonding process was carried out by annealing at 280~300°C for 0.5 hr in an alloying furnace. The strength and reliability of the joined structure were evaluated by a simple cleavage test as well as standard thermal cycling experiments. The joining interfaces were also examined by scanning electron microscopy (SEM) as well as transmission electron microscopy (TEM) equipped with x-ray microanalysis.

#### RESULTS AND DISCUSSION

Figures 1(a) and 1(b) show cross-sectional scanning electron micrographs (SEM) for the joined samples of GaAs on Si and InP on Si, respectively. The cross-section samples were prepared by cleaving with a diamond scribe. The adhesion is seen to be fairly uniform across the entire regions under inspection. Also, the original physical points of contact can not be distinguished after bonding, implying that atomic rearrangement occurred during annealing. Only limited reactions are observed at the interfaces. To obtain more detailed pictures about the bonding process, we further characterized the joined regions of the samples using transmission

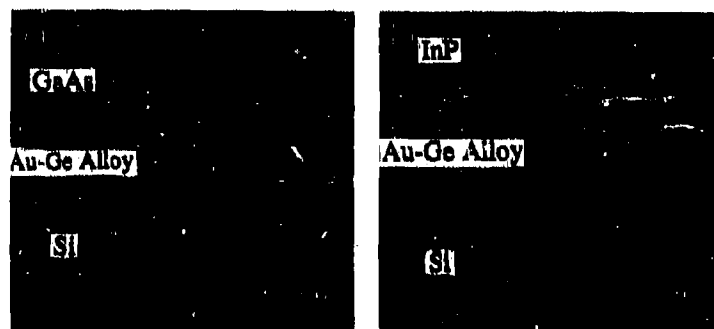


Figure 1. Cross-sectional SEM micrographs of the joined wafers (a) GaAs/Au-Ge/Si and (b) InP/Au-Ge/Si.

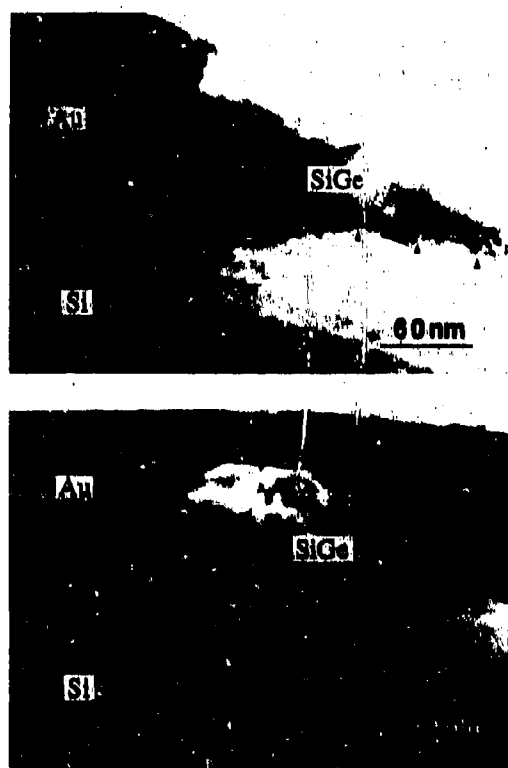


Figure 2. XTEM micrographs of the joining interfaces (a) CuAu/Au-Ge/Si and (b) InP/Au-Ge/Si.

electron microscopy equipped with x-ray microanalysis. Since the preparation of TEM specimens involves both diamond-blade cutting and mechanical polishing down to about 40  $\mu\text{m}$ , the preparation itself provides the initial stress test for the strength of the adhesion. Figures 2(a) and 2(b) are cross-sectional TEM micrographs corresponding to Figs. 1(a) and 1(b), respectively. In both cases, it is seen that the initially codeposited Au-Ge eutectic alloy separates into Au(Ge) and Ge regions during annealing. It is deduced that the incorporation of Ge in the Au films largely suppresses the further dissolution of Si into the Au. This is expected in view of their simple eutectic phase diagrams where no stable compounds exist [9]. More interesting is that after phase separation, the Ge grows epitaxially onto the Si substrate. This is clearly shown in a high-resolution TEM micrograph (Fig. 3). X-ray microanalysis indicates that this epitaxially regrown region contains only a small amount of Si, which is believed to be initially dissolved in Au and then incorporated in the epitaxial film during regrowth [10]. The strain contrast is also seen in the image and is due to the large lattice mismatch between the epitaxially regrown region and the Si substrate (the interface is delineated by a set of arrows).

Similar to previous studies on Au-Ge contacts to GaAs [11-12], interfacial reactions are very limited at our annealing temperatures. The major reaction products at this interface are Au-rich Au-Ga compounds, which were identified by TEM diffraction analysis. At the InP/Au-Ge interface, In-rich In-Au compounds are found. The detailed phase identification is under way.

Based upon our microstructural characterizations, we believe that the bonding is achieved by the low temperature solid-state reactions occurring at these interfaces as well as the solid-

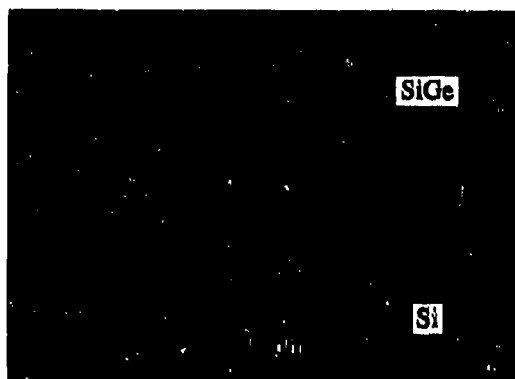


Figure 3. High-resolution XTEM micrograph showing solid-phase epitaxial regrowth of Ge-rich SiGe alloy to the Si substrate. The strain contrast shown is due to the lattice mismatch between the regrown SiGe and Si substrate.

phase epitaxial regrowth of Ge-rich SiGe to the Si substrate. The presence of Ge in initial Al<sub>x</sub> film not only suppresses the dissolution of Si into Au but also acts as a buffer layer between the joining materials through the heteroepitaxial regrowth owing to the close lattice constants and linear thermal expansion coefficients between Ge and GaAs or InP.

To evaluate the strength and reliability of the joined wafers, we also performed a thermal cycling experiment with a temperature ramp from -50°C to 150°C for 15 cycles. The bonded wafers show very good mechanical integrity after the thermal cycling test even though there were further reactions at the GaAs/Au-Ge and InP/Au-Ge interfaces, as revealed by cross-sectional SEM observations. Residual elastic strain generated during cycling is confined within the interface region and the Si substrate. This simple wafer bonding technique is governed by the low temperature solid-state reactions and shows promise in designing new substrates for heteroepitaxial growth as well as in realizing the integration of GaAs- and InP-based optical devices with prefabricated Si electronic devices in hybrid circuit technology.

## SUMMARY

We have presented a low temperature wafer bonding technique, which involves the low temperature reactions as well as solid-phase epitaxial regrowth, for the integration of GaAs- and



InP-based optical devices with Si microelectronic components. The Au-Ge eutectic alloy as the bonding material not only suppresses the interfacial reactions but also enhances the bonding strength through heteroepitaxial growth. Both simple mechanical tests and thermal cycling tests confirm good mechanical integrity of the joined structure.

#### ACKNOWLEDGEMENTS

The authors (Z.Ma and L.H.Allen) would like to acknowledge the funding support from the Joint Services Electronics Programs (JSEP) under contract N00014-90-J-1270 and a grant from the Petroleum Research Fund ACS-PRF#25422-G5. The authors (G.L.Zhou, T.C.Shen, M.E.Lin, and H.Morkoç) would like to thank the funding support from ONR under grant # N00014-92-J-1258 and acknowledge Dr.Y.S. Park as the technical monitor. Some of the materials characterization were carried out in the Center for Microanalysis of Materials at University of Illinois, which is supported by the Department of Energy.

#### REFERENCES

1. J.L. Jewell, Y.H. Lee, A. Scherer, S.L. McCall, N.S. Olson, J.P. Harbison, and L.T. Florez, *Opt. Eng.* **29**, 210 (1990).
2. C.J. Hasnain, J.R. Wullert, J.P. Harbison, L.T. Florez, and N.G. Stoffel, *Appl. Phys. Lett.* **58**, 31 (1991).
3. R.P. Bryan, W.S. Fu, and G.R. Olbright, *Appl. Phys. Lett.* **62**, 1230 (1993).
4. N.A. El-Masry, J.C.L. Tarn, and S.M. Bedair, *Appl. Phys. Lett.* **55**, 1442 (1989).
5. M. Yamaguchi, M. Sugo, and Y. Itoh, *Appl. Phys. Lett.* **53**, 2293 (1988).
6. H. Cheng, J.M. Depuydt, J.E. Potts, and T.L. Smith, *Appl. Phys. Lett.* **52**, 147 (1988).
7. Y.H. Lo, R. Bhat, D.M. Hwang, M.A. Koza, and T.P. Lee, *Appl. Phys. Lett.* **58**, 1961 (1991).
8. R. Venkatasubramanian, M.L. Timmons, T.P. Humphreys, B.M. Keyes, and R.K. Ahrenkiel, *Appl. Phys. Lett.* **60**, 886 (1992).
9. *Binary Alloy Phase Diagrams*, ed. T.B. Massalski, ASM, Ohio, 1986.
10. Z. Ma, Y. Xu, and L.H. Allen, *Appl. Phys. Lett.* **61**, 225 (1992).
11. T. Kim and D.D.L. Chung, *Mat. Res. Soc. Symp. Proc.* **54**, 437 (1986).
12. T.S. Kuan, P.E. Batson, T.N. Jackson, H. Rupprecht, and E.L. Wilkie, *J. Appl. Phys.* **54**, 6952 (1983).

# Author Index

- Ahmad, Ifikhar, 119  
 Allen, L.H., 241  
 Anders, André, 205  
 Anders, Simone, 205  
 Arunajatesan, S., 131  
  
 Blue, Craig A., 143  
 Brow, R.K., 77  
 Brown, Ian G., 205  
  
 Campbell, G.H., 61  
 Cannon, R.M., 109  
 Card, J.C., 109  
 Carim, A.H., 71, 131  
 Chen, S.J., 163  
 Chen, Yi-Chia, 235  
 Chow, Peter, 205  
 Coombs, A.W., 61  
  
 Dauskardt, R.H., 109  
 Deve, Herve E., 103  
 Devletian, J.H., 151, 163  
 Dogan, C.P., 169, 183  
 Drevet, B., 15  
 Dunford, David V., 39  
  
 Eustathopoulos, N., 15  
  
 Gerberich, William W., 103  
 Goldstein, J.I., 77  
 Gould, J., 163  
  
 Hackney, S.A., 89  
 Halvarsson, Mats, 83  
 Hawk, J.A., 151, 169, 183  
 Hong, T., 3  
 Howe, James M., 27  
 Hsieh, K.C., 241  
  
 Intrator, James B., 95  
  
 Janeway, B.J., 215  
 Johnson, G.W., 61  
  
 Kelkar, G.P., 71  
 Kelly, B.E., 61  
 Khan, Parwaz A.A., 137  
 King, Wayne E., 61  
  
 Lee, Chin C., 235  
 Lin, Chien-Li, 103  
  
 Lin, M.E., 241  
 Lin, Ray Y., 143  
  
 Ma, Z., 241  
 Matljasevic, Goran, 235  
 McCarty, E.D., 89  
 Messler, Jr., Robert W., 177  
 Moore, G.A., 197  
 Morkog, H., 241  
  
 Nelson, John C., 103  
 Norden, Hans, 83  
 Norton, M. Grant, 223  
  
 Orling, Timothy T., 177  
  
 Paul, Anand J., 137  
 Petty, A.V., 183  
  
 Rabin, B.H., 197  
 Rawers, J.C., 183  
 Reitz, T.C., 61  
 Ritchie, R.O., 109  
  
 Saha, S.K., 77  
 Schwartz, D.S., 163  
 Shen, T.C., 241  
 Silbergliitt, Richard, 119  
 Skowronek, Charles J., 103  
 Smith, J.R., 3  
 Spear, K.E., 71  
 Srolovitz, D.J., 3  
 Stoner, S.L., 61  
 Suganuma, Katsuaki, 51, 209  
  
 Timsit, Roland S., 215  
  
 Varadan, V.K., 131  
 Vuorinen, Sakari, 83  
  
 Wang, Chen-Yu, 235  
 Wang, Hsin-Fu, 103  
 Wien, W.L., 61  
 Wilson, D.M., 61  
 Wilson, R.D., 151, 169  
 Wisbey, Andrew, 39  
  
 Ylin, T.Y., 131  
  
 Zhou, G.L., 241

## Subject Index

- activity diagram, 71
- adhesion, 3, 15, 205
- Al, 39, 169, 209, 215
- Al<sub>4</sub>C<sub>3</sub>, 131
- Al-Fe, 169
- AlN, 223
- Al<sub>2</sub>O<sub>3</sub>, 83
- analytical model, 151
- Au-Ge eutectic alloy, 241
- bending tests, 103
- bimaterial interfaces, 89, 109
- bonding, 15, 95, 223
- borate glass, 77
- boride precipitates, 77
- brazing alloys, 71
- capacitor discharge welding (CDW), 163, 169
- carbon, 95
- casting, 209
- ceramic-metal interfaces, 15, 27, 51, 61, 89, 103, 109, 131
- composites, 103, 137
  - carbon-carbon, 205
  - intermetallic-ceramic, 183
  - layered, 183
  - metal matrix, 39, 137
  - titanium matrix, 143
- contact angle, 15
- diffusion, 131
  - bonding, 39, 61
- direct joining, 119
- discontinuously reinforced Al alloys, 163
- dislocations, 89
- electron probe microanalysis (EPMA), 131
- eutectic, 215
- first principles study, 3
- flash welding (FW), 163
- flux, 215
- fracture, 27, 109
- functionally gradient materials, 177
- glass-copper, 109
- glasses, 223
- grain boundaries, 61
- graphite, 95
- high-temperature synthesis, 177
- hybrid
  - circuit technology, 241
  - heating, 119
- image stress, 89
- In-Pb alloy, 235
- interface(s), 15, 61, 71, 89, 103, 109, 209, 223
- interfacial
  - fracture energy, 27
  - layer, 77
  - structure, 27
- intermetallics, 39, 177, 183
- internal heating, 119
- joining affected zone, 143
- lasers, 137
- local shear strength, 89
- mechanical properties, 197
- metal/
  - ceramic interfaces (see ceramic-metal interfaces)
  - oxide, 15
  - metallization, 95, 223
  - metals, 177, 215
  - microwave joining, 119, 131
  - Mo/MoSi<sub>3</sub>, 3
  - multilayers
    - alumina coatings, 83
    - composite solder, 235
- orientation relationships, 83
- packaging, 223
- phase diagram, 235
  - ternary, 71
- plasma deposition, 205
- pressure, 209
- processing, 197
- pushout tests, 103
- rapid
  - infrared joining, 143
  - solidification, 151
- RBSC, 119
- reaction sequences, 71
- reactivity, 15
- reliability, 51
- scanning acoustic microscope (SAM), 235
- self-propagating high-temperature synthesis (SHS), 177, 183
- SiC, 197
  - (Hexoloy™), 119
  - reinforcements, 163
  - SiC/Al interfaces, 131
  - 2009/SiC/15w, 163
  - 8009/SiC/11p, 163
  - SiC/Al/SiC, 131
  - slip traces, 89
  - soldering, 95
  - solid-
    - phase epitaxial regrowth, 241
    - state reactions, 241

stainless, 209  
standoff distance, 89  
stress corrosion, 109  
subcritical crack growth, 109  
substrate, 223  
surface roughness, 51

thermal  
  expansion mismatch, 51  
  shock testing, 235  
thick film, 95  
Ti, 39, 77  
  alloys, 143

TiAl, 183  
TiAlV, 143  
transmission electron microscopy (TEM), 83,  
  89, 131, 169

ultra-high speed photography, 151  
unjoined area, 51

wafer bonding, 241  
wetting, 15, 223  
Widmanstätten structures, 143